

University of Alberta

**THE USE OF MICROFLUIDICS
FOR MULTIPLEXED PROTEIN ANALYSIS**

by

Yujuan Hua

A thesis submitted to the Faculty of Graduate Studies and Research
in partial fulfillment of the requirements for the degree of

Doctor of Philosophy

Department of Chemistry

©Yujuan Hua
Spring 2010
Edmonton, Alberta

Permission is hereby granted to the University of Alberta Libraries to reproduce single copies of this thesis and to lend or sell such copies for private, scholarly or scientific research purposes only. Where the thesis is converted to, or otherwise made available in digital form, the University of Alberta will advise potential users of the thesis of these terms.

The author reserves all other publication and other rights in association with the copyright in the thesis and, except as herein before provided, neither the thesis nor any substantial portion thereof may be printed or otherwise reproduced in any material form whatsoever without the author's prior written permission.

Examining Committee

D. Jed Harrison, Chemistry

Charles A. Lucy, Chemistry

Liang Li, Chemistry

Jonathan G. C. Veinot, Chemistry

Christine M Szymanski, Biological Sciences

David Sinton, Mechanical Engineering, University of Victoria

Abstract

The research presented in this work explores the application of microfluidics to the field of proteomics through the design of a multi-channel microfluidic platform and the investigation of individual components of the system. The design of this microfluidic device allows the integration of several protein sample preparation steps for automated electrospray ionization mass spectrometric (ESI-MS) analysis, including protein separation, fractionation and collection, preconcentration and cleanup, and protein digestion.

In order for the multi-channel system to function properly, I first evaluated each individual component of the device. Several areas were explored: (i) optimization of polymer monolith for solid-phase extraction (SPE) preconcentration; (ii) investigation of cationic coatings for microchannel surface modification to facilitate positive electrospray of peptides and proteins for chip-MS coupling; (iii) combination of the hydrophobic monolith and the PolyE-323 coating in a single channel device for on-chip SPE and on-bed tryptic digestion with on-line coupling to ESI-MS.

Multiplexed microfluidic devices for protein analysis, which integrate a series of microfluidic features, were then designed, built and tested. The multiplexed microfluidic architecture employed a separation channel, a fractionator, an array of microchambers to accommodate monolithic polymer for SPE preconcentration, and an elution channel for the detection of eluted sample using fluorescence detector or mass spectrometer. The performance of the

multiplexed devices for integration of multiple analytical steps was explored with sequential fractionation, collection, and elution of fluorescent sample, evaluating the ability to trap and release individual fractions without cross-contamination.

Thorough analysis of each of the individual components on the multiplexed microfluidic platform provides valuable insights into the design of such systems, which brings us closer to our final goal of a proteomic processing microchip.

Acknowledgement

There are many people I'd like to thank for their help and support during the last five years. First and foremost, I would like to express my great and sincere gratitude to my supervisor, Prof. Jed Harrison. He introduced me to this interesting and exciting field of microfluidics and provided me with insightful guidance and support throughout the course of my research. I also thank him for his patience and encouragement during the difficult periods of my research work. His great kindness made my research experience here truly enjoyable and unforgettable.

Many thanks go to the DJH group members both past and present. Special thanks to Dr. James Bao for his instructive suggestion and discussions. Thank Dr. Svetlana Sapelnikova, Dr. Abebaw Jemere, Jing Wen, Dr. Dolores Martinez, Dr. Zhen Wang, Dr. Yong Zeng, Dr. Mei He, Dr. Eric Flaim, Josh Wasylycia, Qingye Lu, Neda Nazemifard, Wenmin Ye, and Ledi Wang for their help and friendship. Thank Arlene Figley and Lin Ferguson for their help in organizing many things in the group.

I give sincere thanks to my committee members, Dr. Charles A. Lucy, Dr. Jonathan G. C. Veinot, Dr. Liang Li, Dr. Michael Deyholos, Dr. Christine M. Szymanski, and Dr. David Sinton for their support in my candidacy exam and final oral exam.

I am grateful for the help from the support staff in electronic shop, machine shop, general office and Nanofab. Special thanks to Kim Nguyen-Do, who gave me a lot of help in building electronic devices.

Finally, I'd like to express my sincere thanks to my family: my beloved husband and my daughter, my parents, and my parents-in-law. Great and special

thanks to my husband, Yu Bai, for his patience, care, understanding, and love.
Thanks to my daughter, Ruijie Bai, for being such a lovely and clever baby and
for the pleasures she gave me. Without their support, I never would have made it
this far.

Table of Contents

Chapter 1 Introduction

1.1 Project Aim	2
1.2 Proteomics on a Chip	2
1.3 Microchip-MS Interface.....	13
1.3.1 Direct Spray from the Chip.....	14
1.3.2 Spray from Attached Capillary Emitters.....	15
1.3.3 Spray from Microchip Integrated Electrospray Emitters.....	16
1.3.4 Microchip-MS Coupling via MALDI.....	16
1.3.5 Multispray	17
1.4 Sheath Flow Technology and Its Application.....	19
1.5 Background	20
1.5.1 Microfabrication	20
1.5.1.1 Photolithography.....	20
1.5.1.2 Wet Etching	20
1.5.2 Electroosmotic Flow	22
1.5.3 Porous Polymer Monolith.....	24
1.5.4 Electrospray ionization	28
1.6 Thesis Outline	29
1.7 References.....	31

Chapter 2

Preparation and Characterization of Porous Polymer

Monoliths and the Evaluation of SPE Performance

2.1 Introduction.....	38
2.2 Experimental Section.....	39
2.2.1 Chemicals and Materials.....	39
2.2.2 Microchip Design and Fabrication.....	40

2.2.3	Preparation of Monolithic Polymer	43
2.2.4	Instrumentation	45
2.2.5	Microchip Operation	46
2.3	Results and Discussion	47
2.3.1	Control of Surface Chemistries.....	47
2.3.2	Control of Porous Properties.....	48
2.3.2.1	Porogenic Solvent System	50
2.3.2.2	Initiator Type	53
2.3.2.3	Effect of Exposure Time on Polymer Structure.....	54
2.3.2.4	Optimized Monolith Recipes and Pore Size Measurement	55
2.3.3	Effect of Chip Design on the Monolithic Polymer	59
2.3.3.1	Exposure Window Size.....	59
2.3.3.2	Bed Dimensions and Beds with Posts.....	60
2.3.4	Evaluation of SPE Performance.....	63
2.3.4.1	On-Chip SPE of BODIPY	63
2.3.4.2	Protein Adsorption onto the Monolithic Bed.....	68
2.3.4.3	Effect of Eluent Composition	69
2.3.4.4	Durability of the Monoliths and Recovery of Glass Chips.....	71
2.4	Conclusion	72
2.5	References.....	73

Chapter 3

Microchannel Surface Modification with Cationic Coatings for On-Line Coupling of Microchip to Electrospray Mass Spectrometry

3.1	Introduction.....	76
3.2	Experimental Section	78
3.2.1	Materials and Instrumentation	78
3.2.2	Synthesis of PolyE-323.....	80

3.2.3	Microchannel Coating Procedure.....	80
3.3	Results and Discussion	83
3.3.1	Evaluation of Four Cationic Coatings.....	83
3.3.1.1	EOF Measurement	83
3.3.1.2	Coating Stability and Reproducibility	83
3.3.1.3	Effect of Methanol Concentration on EOF Mobility	85
3.3.1.4	Comparison of Four Cationic Coatings	87
3.3.2	Compatibility of PolyE-323 Coating with ESI-MS	88
3.3.2.1	Electrospray Performance	88
3.3.2.2	Background Tests on PolyE-323 Coated Channels	90
3.3.2.3	On-line CE-MS	92
3.3.3	CE Separation in PolyE-323 Coated Capillaries	95
3.3.3.1	Separation of Peptides and Proteins.....	95
3.3.3.2	Effect of Polymerization Mixture on PolyE-323 Coating	98
3.3.3.3	Separation of Cytochrome <i>c</i> Digests.....	100
3.4	Conclusions.....	103
3.5	References.....	103

Chapter 4

Solid-Phase Extraction and Enzymatic Digestion of Proteins on Porous Polymer Monolith with On-Line Coupling to ESI-MS

4.1	Introduction.....	107
4.2	Experimental Section	109
4.2.1	Chemicals and Materials.....	109
4.2.2	Instrumentation	110
4.2.3	Microchip-ESI Interface Construction.....	112
4.2.3.1	Device and Joint Preparation for Coupling Chip to ESI-MS. 112	
4.2.3.2	Preparation of Capillary ESI Tips.....	115
4.2.4	Monolith Preparation and Chip Operation.....	118

4.3 Results and Discussion	120
4.3.1 On-Chip Solid-Phase Extraction of Proteins	120
4.3.1.1 Adsorption and Elution of Standard Proteins	120
4.3.1.2 Different Cytochrome <i>C</i> Loads.....	124
4.3.2 On-Bed Digestion of Proteins.....	127
4.3.2.1 Melittin.....	128
4.3.2.2 Cytochrome <i>c</i>	131
4.3.2.3 BSA.....	139
4.3.2.4 Myoglobin.....	143
4.4 Conclusion	145
4.5 References.....	147
4.6 Appendix.....	149

Chapter 5

Electrokinetically Controlled Fractionator and Collector with Photopatterned Monolithic Polymer Beds for Protein

Analysis

5.1 Introduction.....	157
5.2 Chip Design	159
5.2.1 Design Considerations	159
5.2.2 Final Chip Design	161
5.3 Impedance Simulation and Theoretical Calculation	166
5.4 Experimental Section.....	173
5.4.1 Chip Fabrication.....	173
5.4.2 Experimental Setup.....	174
5.4.2.1 Single Wavelength Detection System.....	174
5.4.2.2 Multi-Wavelength Detection System.....	175
5.5 Results and Discussion	178
5.5.1 Fabricated Devices.....	178
5.5.2 Fractionation and Collection.....	178

5.5.2.1 Measuring the Mobility of Fluorescein.....	178
5.5.2.2 Study of Sheath Effect on PolyE-323 Coated Devices.....	180
5.5.2.3 Study of Sheath effect on Devices with Monolithic Beds	191
5.5.2.4 Automatic Fractionation Using Three Delivery Sequences...	203
5.5.2.5 Theoretical Calculation of Pressure-Induced Flow.....	209
5.5.3 Elution.....	216
5.5.3.1 Study of Elution Profile	217
5.5.3.2 Sequential Elution with Single Wavelength Detection.....	222
5.5.3.3 Sequential Elution with Multi-Wavelength Detection.....	227
5.6 Conclusion	251
5.7 References.....	253

Chapter 6 Conclusions and Future Work

6.1 Summary of the Thesis	256
6.2 Future Work	258
6.2.1 Improvement of Fractionation Process	258
6.2.2 Device Re-design for Sequential Elution.....	260
6.2.3 Separation in Sample Channel	261
6.2.4 Protein Digestion on Polymer Beds	262
6.2.5 Protein Identification	263
6.3 References.....	264

List of Tables

Chapter 2

Table 2.1	The compositions of polymerization mixtures and reaction conditions for the preparation of monolithic polymer beds	49
-----------	--	----

Chapter 3

Table 3.1	EOF measurements for four cationic coating and the coating stability and reproducibility	83
Table 3.2	Molecular weights (<i>MW</i>) and isoelectric points (<i>pI</i>) of the model peptides and proteins.....	96
Table 3.3	Separation of peptides and proteins on PolyE-323 coated capillaries	98
Table 3.4	Effect of Polymerization Mixture on PolyE-323 Coating	100

Chapter 4

Table 4.1	Three different cytochrome c loads.	124
Table 4.2	Peptide fragments of melittin.....	129
Table 4.3	Observed cytochrome c and myoglobin charge states.....	149
Table 4.4	Trypsin autodigestion peaks	150
Table 4.5	Cytochrome c peptides from on-bed tryptic digestion.....	150
Table 4.6	Cytochrome c peptides from tryptic digestion in free solution.....	151
Table 4.7	BSA peptides from on-bed tryptic digestion.	152
Table 4.8	BSA peptides from tryptic digestion in free solution	153
Table 4.9	Myoglobin peptides from thermal denatured solution digestion	155

Chapter 5

Table 5.1	Detailed channel dimensions of Device A, B, C, D, and E	163
Table 5.2	Simulation results for Device B when four collection channels were grounded separately	184
Table 5.3	Simulation results for Device C when the third collection channel was grounded at different sheath voltages	190
Table 5.4	Calculated and observed sample stream width for Device D when six collection channels were grounded separately	195
Table 5.5	Comparison of sample stream width in Device D and E	198
Table 5.6	Geometric form factors F for each segment of Device B	210
Table 5.7	Comparison of pressure-induced flows and EOF flows for delivery of fluids into one collection channel.	213
Table 5.8	Comparison of pressure-induced flows and EOF flows for delivery of fluids into all eight collection channels.....	216
Table 5.9	Peak area reproducibility in the sequential elution	226

Chapter 6

Table 6.1	Summary of digestion products detected by ESI/MS resulting from on-bed digestion and solution phase digestion	257
-----------	---	-----

List of Figures

Chapter 1

Figure 1.1	Multicolumn Microdevice for Protein Processing.....	6
Figure 1.2	Integrated and modular microsystem for protein analysis.....	7
Figure 1.3	Two-dimensional MEKC-CE and OCEC-CE separation system.....	9
Figure 1.4	2-D separation platform combining IEF with gel electrophoresis ..	10
Figure 1.5	On-line IEF-CGE 2-D separation device.....	12
Figure 1.6	A centrifugal CD for high-throughput MALDI-MS	13
Figure 1.7	On-line microfluidic chip MALDI interface	17
Figure 1.8	Microfluidics systems for multiplexed ESI-MS analysis	18
Figure 1.9	Isotropic wet etching profile.....	21
Figure 1.10	Schematic illustration of the principle of electroosmotic flow.....	23
Figure 1.11	The monomers and crosslinkers used for the preparation of monoliths.....	27

Chapter 2

Figure 2.1	Schematic illustrating the device fabrication process.....	42
Figure 2.2	Device layout and the setup for photo-initiated polymerization	44
Figure 2.3	Laser-induced fluorescence detection	46
Figure 2.4	Monoliths prepared with different porogenic solvents.....	51
Figure 2.5	Effect of porogenic solvent on edge resolution.....	51
Figure 2.6	Monoliths prepared with different porogen-to-monomer ratios.....	53
Figure 2.7	SEM images of monoliths prepared with different initiators	54
Figure 2.8	Monoliths prepared with different exposure times.....	55
Figure 2.9	Monoliths prepared with different META concentrations	56
Figure 2.10	Micrographs of the monoliths prepared with two optimized recipes	57
Figure 2.11	Pore size distribution profile of bulk neutral monolith	58
Figure 2.12	Schematic illustrating the exposure window aligned with the bed .	59

Figure 2.13	The designs and expected etched results for devices with posts	60
Figure 2.14	Microscopic images of the fabricated beds with posts	61
Figure 2.15	Optical micrographs of the monoliths prepared in beds.....	61
Figure 2.16	Capacity determination for the neutral hydrophobic monolith	63
Figure 2.17	Elution traces with increasing sample loading times	66
Figure 2.18	Elution traces with various BODIPY concentrations	66
Figure 2.19	Fluorescence intensity profile during sample loading and elution..	67
Figure 2.20	Dynamic protein adsorption process onto a monolithic bed	68
Figure 2.21	Effect of eluent composition on elution	70
Figure 2.22	Durability of monoliths	71

Chapter 3

Figure 3.1	Synthesis and structure of PolyE-323.....	80
Figure 3.2	Coating procedure for triple layer PB-DS-PB coating	81
Figure 3.3	Bilayer structure of 2C ₁₄ DAB surfactant coating.....	82
Figure 3.4	Run-to-run stability of EOF in a PolyE-323 coated channel.....	84
Figure 3.5	Long-term stability of EOF in a PolyE-323 coated channel	85
Figure 3.6	Effect of MeOH concentration on the magnitude and stability of EOF	86
Figure 3.7	TICs and mass spectra from constant infusion of bradykinin and cytochrome c from a PolyE-323 coated device	89
Figure 3.8	TICs from continuous infusion of Bradykinin in buffers with different MeOH percentages.....	90
Figure 3.9	Background tests on PolyE-323 coated channels.....	91
Figure 3.10	Electrokinetic injection of sample	93
Figure 3.11	TIC for the separation of two peptides	94
Figure 3.12	Electrochromatograms of CE separation of peptides and proteins .	97
Figure 3.13	CE separations of peptides and proteins after the PolyE-323 coating was exposed to the polymerization mixture.....	99
Figure 3.14	Electrochromatograms for CE separation of peptide digests of cytochrome c at different protein-to-enzyme ratio	102

Figure 3.15	Electrochromatograms for CE separation of cytochrome c digests with different digestion time	102
-------------	--	-----

Chapter 4

Figure 4.1	Schematic diagram of the sheathless microchip ESI-MS interface.	112
Figure 4.2	Drilling procedures for microchip/ESI-MS coupling.....	113
Figure 4.3	TICs and mass spectra for on-chip SPE preconcentration and elution of cytochrome c and myoglobin.....	122
Figure 4.4	TIC and mass spectrum for preconcentration and elution of BSA	123
Figure 4.5	Three different cytochrome c loads	125
Figure 4.6	Breakthrough curve for sample capacity measurement.....	126
Figure 4.7	TIC and mass spectrum for on-bed tryptic digestion of melittin...	129
Figure 4.8	EICs of the three tryptic peptide components of melittin.....	130
Figure 4.9	TICs and mass spectra obtained during each step of on-bed digestion of cytochrome c.....	133
Figure 4.10	EICs for several of the most intense cytochrome c peptides.....	134
Figure 4.11	ESI mass spectrum for solution digestion of cytochrome c	136
Figure 4.12	On-bed tryptic digestion of BSA.....	140
Figure 4.13	EICs for several of the most intense Tryptic BSA peptides	140
Figure 4.14	ESI mass spectrum for solution digestion of BSA	142
Figure 4.15	On-bed tryptic digestion of myoglobin	143
Figure 4.16	ESI mass spectra of myoglobin solution digest.....	144

Chapter 5

Figure 5.1	Schematic diagrams of the fractionator-ESI/MS interface.....	160
Figure 5.2	Mask design for five multi-channel devices.....	162
Figure 5.3	The detailed structure of Device B	163
Figure 5.4	Cartoon illustrating the pinched sample stream profile.....	167
Figure 5.5	Schematic layout of the optical connection part for two PMTs	175
Figure 5.6	Schematic drawing of experimental setup.....	176

Figure 5.7	Final platform assembled for multi-wavelength detection	177
Figure 5.8	Images of fractionation zones of the five fabricated devices	178
Figure 5.9	The layout of the microchip for determination of analyte mobility	179
Figure 5.10	Determination of mobility of fluorescein	179
Figure 5.11	Sample stream flow profiles with no sheath flow protection	180
Figure 5.12	Sheath images of focused fluorescein stream into individual channels.....	181
Figure 5.13	Intensity profiles extracted from sheath images for Device B	182
Figure 5.14	Simulation result for the fourth collection channel of Device B...	183
Figure 5.15	Intensity profiles at difference positions of a sample stream entering into the fourth collection channel of Device B	186
Figure 5.16	Signal intensity profiles with normalized intensity	186
Figure 5.17	Signal intensity distributions at the initial state, position 4 and 5.	187
Figure 5.18	Comparison of extracted signal intensity profiles to the theoretically predicted distribution curves for position 4 and position 5.....	188
Figure 5.19	Images and extracted intensity profiles at different sheath voltages for Device C	189
Figure 5.20	Simulation results for the third collection channel of Device C....	189
Figure 5.21	Schematic illustrating exposure window aligned with the bed	192
Figure 5.22	The transparency mask for UV exposure and the mask design of chip.....	192
Figure 5.23	Image of monoliths prepared in a 6-channel Device D.....	193
Figure 5.24	Sheath flow tests on Device C with monolithic beds	195
Figure 5.25	Sheath effect at different focus voltages for Device D and E	197
Figure 5.26	Intensity profiles at different sheath voltages.....	197
Figure 5.27	Variation of sample stream width versus sample field strength....	199
Figure 5.28	Dynamic dye adsorption process.....	201
Figure 5.29	Selective adsorption of dye into a specific polymer bed	202
Figure 5.30	Electrical fractionation system	203
Figure 5.31	Sequential fractionation with Mode A.....	205

Figure 5.32	Sequential fractionation with Mode B.....	206
Figure 5.33	Sequential fractionation with Mode C.....	206
Figure 5.34	Comparison of the three switching modes in terms of the potential leakage during switches between adjacent relays	207
Figure 5.35	Frames extracted from a video illustrating the leakage during switch from L4 to R1 in switching mode B	208
Figure 5.36	Frames extracted from a video illustrating the leakage during switch between left and right channels in Mode C.....	208
Figure 5.37	Simulation scheme of the pressure induced hydrodynamic flow for one channel	214
Figure 5.38	Simulation scheme of the pressure induced hydrodynamic flow for eight channels.....	215
Figure 5.39	Voltage program for sequential elution.....	217
Figure 5.40	Elution stream profiles with no spatial confinement.....	218
Figure 5.41	Elution stream profiles with focus voltages on sheath channels ...	219
Figure 5.42	Elution stream profiles when focusing voltage on the channel downstream of the desired collection channel	220
Figure 5.43	Elution profiles at different focus voltages at the sheath channels	221
Figure 5.44	Sequential elution from an 8-channel Device B.....	224
Figure 5.45	Reproducibility study for sequential elution in Device D.....	226
Figure 5.46	Experiment designed for sample carryover evaluation	228
Figure 5.47	Chemical structure, adsorption spectrum and emission spectrum of Fluorescein.....	229
Figure 5.48	Chemical structure, adsorption spectrum and emission spectrum of Carboxy SNARF-1.....	230
Figure 5.49	Interface of the LabVIEW program for collecting data with the multi-wavelength detection system.....	232
Figure 5.50	Optimization of sampling frequency and averaging rate, and overall writing frequency for data collection.....	233
Figure 5.51	Signal-response curve.....	234
Figure 5.52	Electronic leakage of signal from CH0 to CH2.....	235

Figure 5.53	Electronic leakage of signal from CH2 to CH0.....	236
Figure 5.54	Plot of electrical leakage in the undesired channel as a function of input signal intensity	236
Figure 5.55	Traces of the green and red fluorescence detected with constant infusion of fluorescein solution at difference concentrations	238
Figure 5.56	Quantification of optical and electrical leakage into red fluorescence channel	239
Figure 5.57	Traces of red and green fluorescence obtained with constant infusion of carboxy SNARF solution at difference concentrations	240
Figure 5.58	Quantification of optical and electrical leakage into green fluorescence channel	241
Figure 5.59	Sequential elution from an 8-channel Device B with multi-wavelength detection	242
Figure 5.60	Elution traces of two repetitive runs showing the sequential elution of fluorescein and SNARF.....	243
Figure 5.61	Graphical interpretation of possible presence of sample carryover of Carboxy SNARF for elution of fluorescein	245
Figure 5.62	Graphical interpretation of possible presence of sample carryover of Fluorescein for elution of Carboxy SNARF	246
Figure 5.63	CCD images illustrating that the focus streams are guided to the top two grounded collection channels.....	249
Figure 5.64	PSpice simulation scheme for the case when dye solution is delivered from the first collection channel reservoir	250

Chapter 6

Figure 6.1	Procedure of sample flow pause experiment.....	259
Figure 6.2	Microfluidic device with three outlet channels	261
Figure 6.3	Microchip-ESI/MS interface	264

List of Abbreviations

AA	acrylamide
ACN	acetonitrile
AIBN	azobisisobutyronitrile
AMPS	2-acrylamido-2-methyl-1-propanesulfonic acid
BODIPY	4,4-difluoro-1,3,5,7,8-pentamethyl-4-bora-3a,4-diaza-s-indacene
BSA	bovine serum albumin
BMA	butyl methacrylate
2C ₁₄ DAB	Dimethylditetradecylammonium bromide
C18	octadecylsilyl
CD	compact disk
CCD	charged coupled device
CE	capillary electrophoresis
CZE	capillary zone electrophoresis
CIEF	capillary isoelectric focusing
CLOD	concentration detection limit
CMC	critical micelle concentration
2D-GE	two-dimensional gel electrophoresis
DMABP	4-(dimethylamino)benzophenone
DMPAP	2,2-dimethoxy-2-phenylacetophenone
DS	dextran sulfate sodium salt
DTT	dithiothreitol
DVB	divinylbenzene
EDMA	ethylene dimethacrylate
EIC	extracted ion chromatogram
EOF	electroosmotic flow
EPM	electrophoretic mobility
ESI	electrospray ionization
ESI-MS	electrospray ionization mass spectrometry

FASS _____ field amplified sample stacking
 FITC _____ fluorescein isothiocyanate
 FITC-BSA _____ bovine serum albumin-fluorescein isothiocyanate conjugate
 GE _____ gel electrophoresis
 GMA _____ glycidyl methacrylate
 HPLC _____ high performance liquid chromatography
 i.d. _____ internal diameter
 IEF _____ isoelectric focusing
 IMAC _____ immobilized metal affinity chromatography
 ITP _____ isotachopheresis
 LC _____ liquid chromatography
 LIF _____ laser-induced fluorescence
 MC _____ missed cleavage
 MALDI _____ matrix-assisted laser desorption ionization
 MeOH _____ methanol
 MEKC _____ micellar electrokinetic chromatography
 META _____ [2-(methacryloyloxy)ethyl]trimethylammonium chloride
 MET-OX _____ methionine oxidized
 MS _____ mass spectrometry
 MS/MS _____ tandem mass spectrometry
 MW _____ molecular weight
 m/z _____ mass-to-charge ratio
 OCEC _____ open-channel electrochromatography
 o.d. _____ outer diameter
 ODS _____ octadecylsilyl
 PB _____ polybrene
 PDMS _____ Polydimethylsiloxane
 PI _____ isoelectric point
 RPLC _____ reverse phase liquid chromatography
 PMT _____ photomultiplier tube
 PR _____ photoresist

RSD _____ relative standard deviation
SDS-PAGE _____ sodium dodecyl sulfate polyacrylamide gel electrophoresis
SPE _____ solid phase extraction
SEM _____ scanning electron microscope
TIC _____ total ion chromatogram
UV _____ ultraviolet
VDMA _____ 2-vinyl-4,4-dimethylazlactone
 μ -TAS _____ Micro Total Analysis Systems

List of Symbols

Å _____	10^{-10}	η _____	viscosity
n _____	10^{-9}	N _____	plate number
μ _____	10^{-6}	D _____	diffusion coefficient
m _____	10^{-3}	R _____	resistance
c _____	10^{-2}	ρ _____	electrical resistivity
k _____	10^3	A _____	cross-sectional area
g _____	gram	V _____	voltage
h _____	hour	I _____	current
Hz _____	hertz	t _____	time
m _____	meter	δ _____	double layer thickness
M _____	molar	ζ _____	zeta potential
min _____	minute	q _____	charge
s _____	second	r _____	radius
W _____	watts	σ^2 _____	variance
V _____	volts	σ _____	standard deviation
AFU _____	arbitrary fluorescence unit	H _____	plate height
m/z _____	mass-to-charge		
cps _____	counts per seconds		
amu _____	atomic mass unit		
l _____	length		
w _____	width		
d _____	depth		
Q _____	volumetric flow rate		
F _____	geometric form factor		
μ _____	electrophoretic mobility		
v _____	velocity		
E _____	electric field		
ϵ_r _____	dielectric constant		

Chapter 1

Introduction

1.1 Project Aim	2
1.2 Proteomics on a Chip	2
1.3 Microchip-MS Interface.....	13
1.3.1 Direct Spray from the Chip.....	14
1.3.2 Spray from Attached Capillary Emitters.....	15
1.3.3 Spray from Microchip Integrated Electrospray Emitters.....	16
1.3.4 Microchip-MS Coupling via MALDI.....	16
1.3.5 Multispray	17
1.4 Sheath Flow Technology and Its Application.....	19
1.5 Background	20
1.5.1 Microfabrication	20
1.5.1.1 Photolithography.....	20
1.5.1.2 Wet Etching	20
1.5.2 Electroosmotic Flow	22
1.5.3 Porous Polymer Monolith.....	24
1.5.4 Electrospray ionization	28
1.6 Thesis Outline	29
1.7 References.....	31

1.1 Project Aim

The field of “lab-on-a-chip” has experienced rapid growth in recent years in response to the demand for high-speed, sensitive, high-throughput, and automated analysis methods for proteomics applications. Its combination with mass spectrometry (MS) provides a powerful, information-rich analytical technique. It was with this in mind that this project was undertaken. The focus of this thesis is the application of micro total analysis systems (μ TAS) to the field of proteomics research. In my thesis work, I have attempted to build a multiplexed microfluidic platform, which will be coupled on-line by electrospray to a mass spectrometer for detection and identification of protein samples. This device integrates a number of protein sample preparation steps for automated MS analysis, including protein separation, fractionation and collection, preconcentration and cleanup, and protein digestion. Due to the complexity and wide dynamic range of proteins in real samples, tedious sample preparation procedures are required prior to MS analysis. Many examples of microfluidic systems have been developed to facilitate sample preparation and sample introduction for MS-based analysis. In this chapter, I will give a review on the development of protein sample pre-treatment techniques in microfabricated systems and some background knowledge relevant to what will be discussed in the following chapters.

1.2 Proteomics on a Chip

The proteome is the entire collection of proteins in an organism, a phrase coined in an analogy to the genome, which incorporates all the genes in an

organism [1]. Proteomics involves the large-scale study of proteins expressed in cells under defined conditions, including their structure and function. The field is divided into three branches: profiling proteomics, which detects and identifies all proteins present in a biological sample, preferably quantitatively; functional proteomics, which explores protein function; and structural proteomics, which studies tertiary protein structure [2]. The focus of this thesis is profiling proteomics. It is hoped that by profiling all proteins expressed in an organism, tissue or cell, some connection can be made between protein expression and the onset of disease or response to stressors, which is critical for developing effective diagnostic techniques and disease treatments in the future. However, analysis of the proteome is a far more daunting task than analysis of the genome, as protein chemistry, reactivity and function is much more complicated than is that of DNA. First, an organism's genome is more or less constant, while the proteome differs from cell to cell and from time to time. Second, proteins carry dynamic and static modifications that are not apparent from genomic information. In addition, proteins expressed within a cell exist in variable abundances with a dynamic range covering five orders of magnitude [3]. Moreover, no protein amplification technique analogous to the polymerase chain reaction (PCR) exists.

With these overwhelming challenges in proteomic research, great stress is placed on the development of new analytical techniques for protein profiling. The most traditional and to date most successful analytical approach to complex protein sample analysis utilizes two-dimensional gel electrophoresis (2-D GE) followed by MS identification [4]. Briefly, a protein mixture is separated by

isoelectric focusing (IEF) in the first dimension on the basis of the protein's isoelectric points (pI), and then further separated in the second dimension based on their molecular weights. The resulting gel is stained in order to visualize the protein spots. The spots are then excised, destained and enzyme-digested. The resulting peptides are extracted from the gel and analyzed by MS for peptide mass mapping. A review of this technique was presented by Issaq *et al.* [5]. Despite the success of this technique, it has several shortcomings, including being slow and expensive to automate, poor reproducibility, limited dynamic range, and relatively low sensitivity, due mostly to the types of visualization methods used.

Besides this established technology, new tools are receiving attention. One of these is microfluidics, the science and technology of manipulating and processing small amounts of fluids in channels with dimensions on the micrometer-scale. The “lab-on-a-chip” technologies or micro total analysis system (μ TAS) have received significant attention since the concept was introduced at the beginning of the nineties [6, 7]. The key elements that contribute to the development of this technology are miniaturization, automation, integration, and portability. The miniaturization of a conventional system to a lab-on-a-chip affords a large number of advantages. The small sample processing volume in a microfluidic device reduces the sample and reagent consumption as well as process waste, consequently lowering the cost of analysis. The small dimensions associated with the chip allow for faster analysis and improved analytical performance due to short diffusion distances and fast heat dissipation. The smaller channel size also has the potential to yield higher mass sensitivity as the injection and detection

volumes can be minimized. The compactness of the μ TAS systems creates opportunities for portability, making it ideal for applications such as on-site security or environmental monitoring and point-of-care diagnostics. The ability to repeatedly pattern microfluidic features on the same device lends itself to densely arrayed, multiplexed fluid networks, permitting the analysis of multiple samples in parallel and increasing sample throughput. The most obvious advantages of μ TAS is the capacity to integrate multiple sample processing steps on a single microchip, thereby offering the potential to create fully automated systems with high throughput.

The initial chip designs consisted of microchannels in cross geometries, with a long separation channel intersected by a sample injection channel, which enables sample injection, pretreatment, and electrophoresis separation [8, 9]. Driven by the need for automated and high-throughput analytical techniques, the trends in lab-on-a-chip technology development have been toward more complex microfluidic networks which can incorporate a variety of functional elements on a single platform [10-18]. Many examples of increasingly integrated devices combining various steps for application to the field of proteomics have been reported. Several reviews of the application of microfluidics to proteomics are available [19-26]. The following discussion will focus on examples in which multiple processing steps have been integrated on a chip.

The Regnier group [27] reported a microfluidic system that integrated three analytical dimensions of sample pretreatment and separation, including tryptic digestion, isolation of histidine-containing peptides using copper(II)-immobilized

metal affinity chromatography [Cu(II)-IMAC], and reversed-phase capillary electrochromatography of the selected peptides (Figure 1.1). The microdevice was made in polydimethylsiloxane (PDMS), and microfabricated frits A and B were used to retain the trypsin-derivatized beads and Cu(II) loaded IMAC sorbent, respectively. The performance of this system was evaluated using FITC-BSA as a model system to explore the possibility of combining trypsin digestion, affinity selection, and reversed-phase separation for proteomic analysis. However, this device was used with fluorescence detection, and the coupling of this system to ESI-MS remains questionable due to buffer and reagent compatibility.

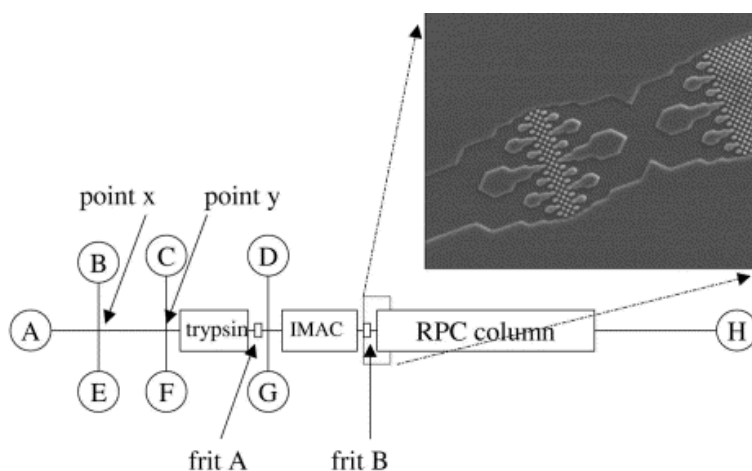


Figure 1.1 Scheme of the multicolumn microfluidic device for protein processing, adapted from [27].

In a more comprehensive and flexible approach, Li and coworkers built up an integrated and modular microsystem for proteomics application [28], which consisted of an autosampler, a large channel for C18 reverse phase packing or other types of affinity media enabling affinity selection of target peptides, an array of separation channels and an interface to ESI-MS via an electrospray tip for identification (Figure 1.2). A conventional gel was used to achieve protein separation. Selected spots were excised and placed in a 96-well plate for in-gel

digestion. Digested samples were then transferred to the microchip using an autosampler, followed by steps involving preconcentration, desalting, injection, separation, and MS identification. The application of this device was demonstrated for the analysis of trace-level tryptic peptides obtained from gel-isolated proteins of human prostatic cancer cell extracts.

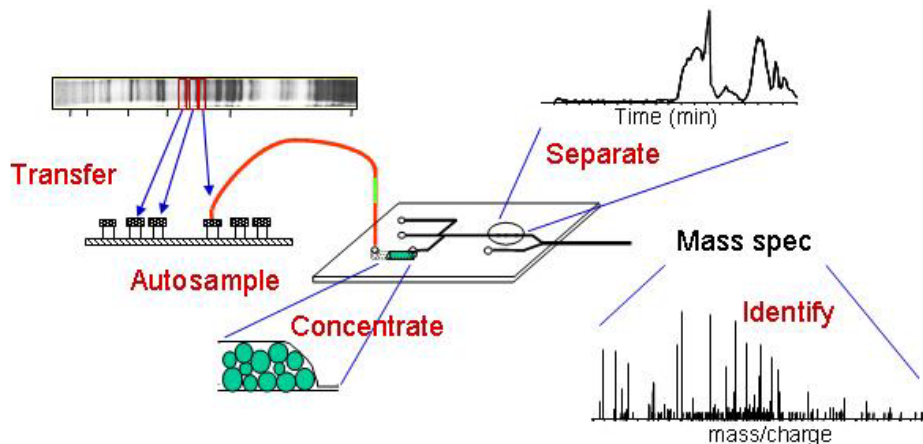


Figure 1.2 Schematic representation of a microfluidic system used for protein analysis, adapted from [28].

Microfluidic devices with a dual function containing a solid-phase extractor and an enzymatic microreactor were demonstrated by Peterson *et al.* [29]. The devices were fabricated from a 25-mm-long porous monolith prepared within a 50- μm -i.d. capillary. Photografting with irradiation through a mask was used to selectively functionalize a 20-mm-long portion of a monolith, introducing reactive groups to enable the subsequent attachment of trypsin. The other 5 mm of unmodified hydrophobic monolith served as a solid-phase extractor. A capillary with a pulled needle tip was used as an electrospray emitter, coupling the device to MS. The use of this dual-function device was demonstrated in both SPE-digestion and digestion-SPE flow directions. Both approaches significantly improved the sequence coverage for the digested protein.

The vast number of proteins and the large variation in their relative abundance in biological samples present a major analytical challenge for proteomics. Thus separation techniques with high peak capacity and excellent resolving power are critically needed. 2D-GE is one of the techniques that has enormous separation resolution; typically 3000-5000 different protein spots can be detected in a single 2D gel image. Great efforts have been made to develop alternative multi-dimensional separations to match the performance of conventional 2D-GE. A variety of chromatographic and electrophoretic approaches, including high pressure liquid chromatography (HPLC), isoelectric focusing (IEF), gel electrophoresis (GE), microchip capillary electrophoresis (CE), and micellar electrokinetic chromatography (MEKC) have been combined in various ways to achieve multi-dimensional separations on microfluidic devices [30, 31].

The first chip-based demonstration was reported by the Ramsey group, who combined MEKC with open-channel CE in a glass device for peptide separation [32]. The MEKC–CE device operates by rapidly sampling and analyzing effluent from the first dimension in the second dimension. The peak capacity was estimated to be around 500–1000. They improved the device design in following efforts by lengthening the channel of the first dimension [33]. The microchip layout is shown in Figure 1.3a, in which a 19.6-cm-long serpentine channel was used for MEKC, followed by CE in a 1.3-cm-long channel. The turns in the serpentine channel were asymmetrically tapered to minimize geometrical contributions to band broadening, resulting in an increased peak capacity of 4200.

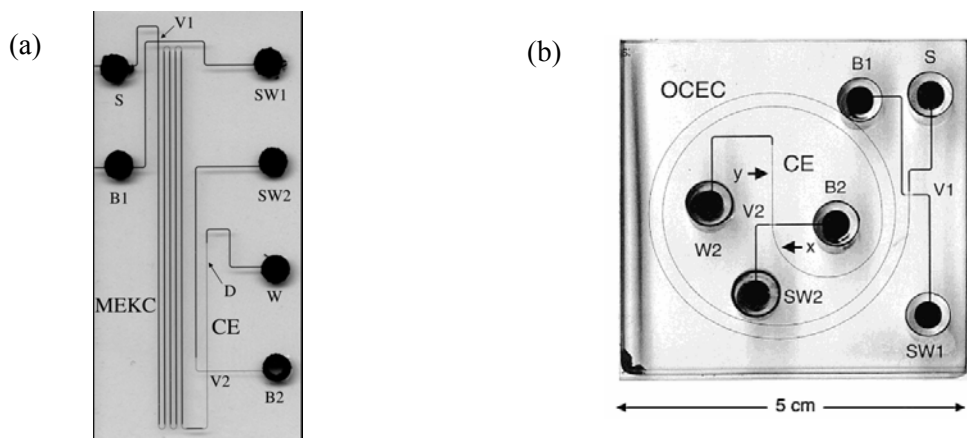


Figure 1.3 (a) Image of a microchip with a serpentine channel for two-dimensional separations coupling MEKC and CE, adapted from [33]; (b) Two-dimensional OCEC/CE separation system with a spiral channel design, adapted from [34].

Gottschlich *et al.* dealt with the challenge of geometric dispersion or “racetrack” effect by utilizing a spiral channel geometry with a large radius of curvature [34]. 2-D separation was achieved using open-channel electrochromatography (OCEC) as the first dimension and CE as the second dimension. The device layout is shown in Figure 1.3b, in which a 25-cm separation channel with spiral geometry for OCEC was chemically modified with octadecylsilane and coupled to a 1.2-cm straight channel for CE.

The 2-D separations discussed above were performed in devices with two intersecting channels. Although very impressive results have been obtained in these studies, fundamental limitations exist. First, separation in the second dimension must be faster than that in the first dimension. Second, not all fractions in the first dimension are transferred to the second dimension, leading to loss of sample information.

To improve the quantitative transfer of sample, devices consisting of one channel intersecting with an array of channels were developed for 2-D separation.

Li *et al.* [35] integrated denaturing IEF and SDS gel electrophoresis in a microfluidic channel network fabricated in polycarbonate. The plastic device consisted of one 1-cm-long channel for IEF and ten 4-cm-long channels for the second dimension as shown in Figure 1.4a. Rather than sequentially sampling protein analytes eluted from IEF, focused proteins are electrokinetically transferred into an array of orthogonal microchannels and further resolved by SDS gel electrophoresis in a parallel format. Since there was no physical barrier to prevent diffusion from taking place, contamination between the liquid media of the first and second dimensions was possible.

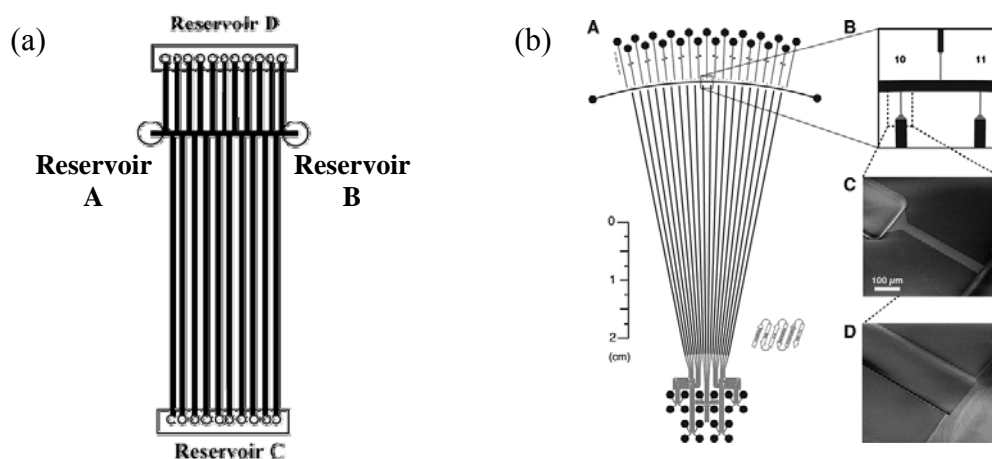


Figure 1.4 (a) Schematic of 2-D protein separation platform combining non-native IEF with SDS gel electrophoresis, adapted from [35]; (b) Design of the 2-D protein analyzer consisting of a single, arced channel for first dimension IEF interfaced with 20 longer channels for second-dimension native gel electrophoresis, adapted from [36].

Emrich *et al.* [36] have tackled the interface problem in IEF-CE by designing a microfluidic geometry to minimize the diffusion at the junctions between the dimensions. The device consisted of a 3.75-cm-long channel in an arch shape for the first dimension of IEF and twenty 6.9-cm-long channels for native gel electrophoresis in the second dimension, as is shown in Figure 1.4b. At the

interface, a short segment of channels with a total cross-sectional area 65 times smaller than that of the separation channels were used to connect the first and second dimension. This smaller-channel interface prevented separation media of the two dimensions from mixing with each other.

Das and coworkers offered an alternative solution to the interfacing problem by placing photo-polymerized pseudo-valves of polyacrylamide gel at the regions of channel intersection [37]. The layout of the device is shown in Figure 1.5a. It consisted of one 15-mm-long channel for IEF and 29 parallel channels 65 mm long for polyacrylamide gel electrophoresis (PAGE). Fabrication of pseudo-valves was achieved by photo-initiated, *in situ* gel polymerization. The gel pseudo-valves offered a simple method to reduce diffusional mixing without hindering the electrokinetic transfer of the focused proteins from the first to the second dimension.

In a similar fashion, DeVoe's research group exploited *in situ* photo-polymerized polyacrylamide gel plugs to separate two different separation media in a PMMA chip [38]. Figure 1.5b shows the schematic diagram of the device, which consisted of one IEF channel and five parallel CGE channels. Discrete gel plugs provided hydrodynamic resistance to the bulk flow and formed a barrier to prevent diffusion, while simultaneously allowing the passage of charged proteins in the microchannel network.

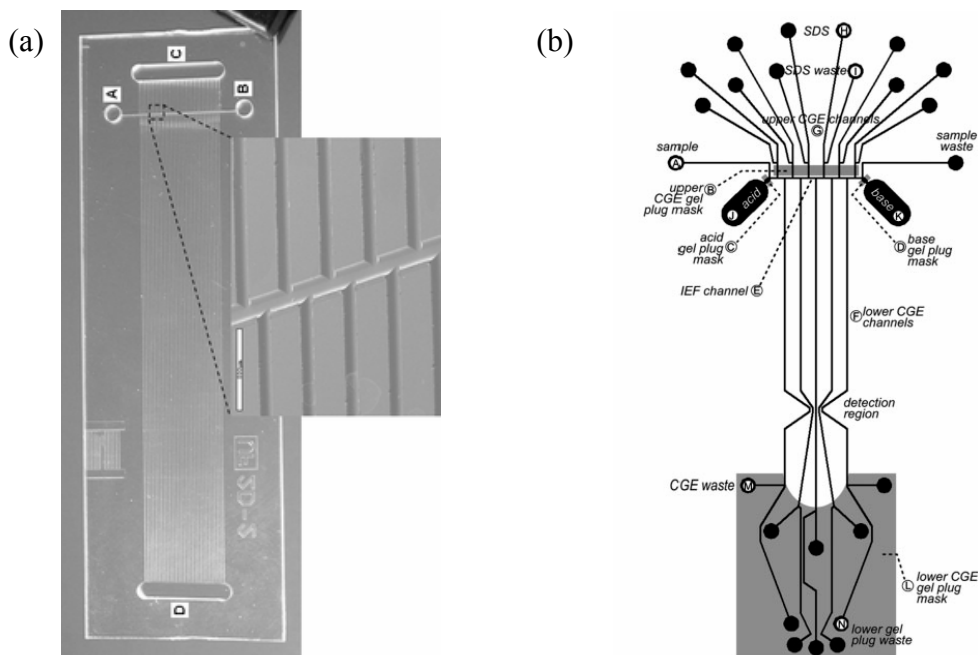


Figure 1.5 (a) Picture of a plastic device for 2-D protein separation. Channel AB is for IEF and channels CD are for PAGE; adapted from [37]; (b) Schematic diagram of an on-line IEF-CGE 2-D separation device; adapted from [38].

An attractive feature of lab-on-a-chip technology is the ability to accommodate multiple identical microfluidic patterns on the same device, permitting the analysis of multiple samples in parallel. Gustafsson *et al.* [39] described the high-throughput microfluidic processing of protein digests integrated with MALDI-MS within a compact disk (CD) format. The CD-based technology takes advantage of centrifugal force induced by rotation of a microfluidic disk to manipulate fluids in the microstructures. The CD microfluidic system comprised 96 sample processing lines placed radially on the chip, enabling parallel preparation of 96 samples. Each processing line performed one or more sample preparation steps: sample preconcentration, affinity selection, desalting and digestion. After processing, the samples were collected in small spots at the end of each working line and the CD was inserted into a MALDI-MS for high-

throughput screening. This system is being commercialized by Gyros AB (Uppsala, Sweden) [40].

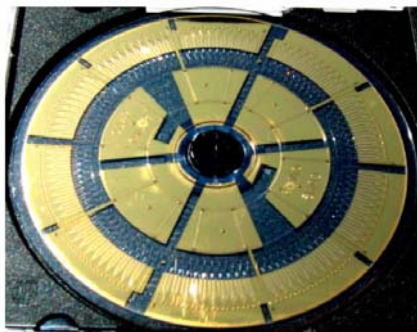


Figure 1.6 Photograph of a centrifugal CD for high-throughput MALDI-MS, adapted from [39].

1.3 Microchip-MS Interface

MS has become a central analytical technique for protein identification in proteomics. It offers several advantages including high sensitivity, high throughput, and the ability to offer a separation dimension according to m/z , as well as providing mass and structure information. Electrospray ionization (ESI) and matrix-assisted laser desorption/ionization (MALDI) are the two most widely used ionization methods for proteomics. ESI is a flow-based ionization technique, where the liquid sample flowing out from a channel can be directly sprayed from the emitter to generate gas-phase ions, making it an ideal ionization source for on-line coupling of microfluidic devices to MS. MALDI, in contrast, is a solid-state technique in which a laser vaporizes a mixture of sample and matrix that has been deposited on a metal target plate. Thus on-line coupling of microchips with MALDI is more difficult than with ESI. In the following discussion, I will focus on the microchip-ESI interface, and several examples of chip-MALDI coupling

will be described.

A large number of designs for electrospray emitters have been developed to facilitate the coupling of microfluidic device to MS [41-47]. These methods can be broadly classified based on how the electrospray is generated, including: (i) direct spray from exposed channels [48-53]; (ii) spray from capillary tips attached to the chip channel [54-63]; and (iii) spray from microchip integrated emitters [64-72].

1.3.1 Direct Spray from the Chip

The first interface of a microfluidic chip with MS was reported by Karger's and Ramsey's groups [48, 49], in which the spray was generated from the flat edge of an exposed channel in a glass chip. The design is attractive because it does not require any complex machining and the outlet can be formed simply by dicing the chip. However, the performance of direct-from-chip spray is limited by eluent spreading at the interface due to the nontapered geometry and the hydrophilic properties of the substrate. Direct solutions to this problem have included coating the exit surface with a hydrophobic reagent [48, 49] or pneumatically assisting the droplet formation [73]. One creative strategy for overcoming this problem was recently reported by Bedair *et al.* [53], who constructed a polymeric monolith at the edge of an open channel, which resulted in stable ionization from the pores of the monolith.

1.3.2 Spray from Attached Capillary Emitters

The problems associated with direct spray from the chips prompted the development of an alternative geometry for interfacing microfluidics with MS: using a capillary coupled to a chip as the electrospray emitter, as first introduced by Figeys *et al.* [54]. The link between the device and the capillary was made by gluing a teflon sleeve to the edge of the device and inserting a capillary into the sleeve. This design suffered from difficulties in capillary alignment. In order to attach a capillary at the end of a hard substrate device, Zhang and coworkers made use of double-etching to build a wide channel, into which the capillary was inserted [74]. The procedure was reproducible but time-consuming, and a significant dead volume was produced at the interconnection. In another design, our group [63] demonstrated that a capillary could be fitted to the chip by drilling a hole at the edge. The dead volume created with a conical-shaped carbide bit was effectively removed using a flat-tipped drill bit. With this low dead volume connection, the band-broadening associated with the capillary/chip junction was eliminated and separations on the chip were preserved.

The electrospray voltage can be controlled separately at the point where the liquid is emitted, using either a liquid junction [75] or conductive coating materials, such as gold [76, 77] and carbon-black [78-80] on the emitter surface to provide electrical contact. Although these interfaces offered sensitive and stable ESI-MS performance, they are difficult to construct, the drilling process needs skill to obtain a precise channel alignment, and great care needs to be taken to prevent glass shards produced during drilling from entering the microchannel.

1.3.3 Spray from Microchip Integrated Electrospray Emitters

Electrospray emitters can be constructed in the microfluidic chip itself. The fabrication of polymeric microchip devices with integrated electrospray emitters has been described in many reports. For example, Kameoka *et al.* [67] described a triangular tip integrated in a microfluidic channel and interfaced to ESI-MS. A triangular-shaped thin polymer tip was formed by lithography and etching. A microfluidic channel was embossed in a cyclo olefin substrate using a silicon master. The triangular tip was aligned with the channel and bonded between the channel plate and a flat plate to create a microfluidic channel with a wicking tip protruding from the end. In other approaches, electrospray emitters were fabricated from polyimide by plasma etching [81], from SU-8 epoxy resin by photolithography and dicing [82], from polycarbonate by laser ablation [83], from poly(dimethylsiloxane) by casting [68, 84] and from poly(methylmethacrylate) by injection molding [85]. Batch-generation of microchips with integrated electrospray emitters can result in improved emitter reproducibility and the potential of simple, disposable devices.

1.3.4 Microchip-MS Coupling via MALDI

MALDI is typically carried out in a vacuum on crystallized sample spots containing matrix and analyte. Thus coupling MALDI to microfluidic chips is usually done in an off-line arrangement, in which fractions are collected from a separation column and deposited on a sample target [86]. On-line coupling of microfluidic devices to MALDI is challenging, but can be achieved using

continuous flow [87] or mechanical interfaces [88]. The coupling of microfluidic separations with a rotating ball interface was reported by Murray's group [88]. Hot-embossed PMMA chips were constructed with a sharp V-shaped tip at the channel exit, as depicted in Figure 1.7. The tip was positioned against the surface of the rotating ball and the eluent from the microchip was deposited onto it. Matrix was in-line added to the sample spot and the ball rotated into the vacuum for MALDI MS detection.

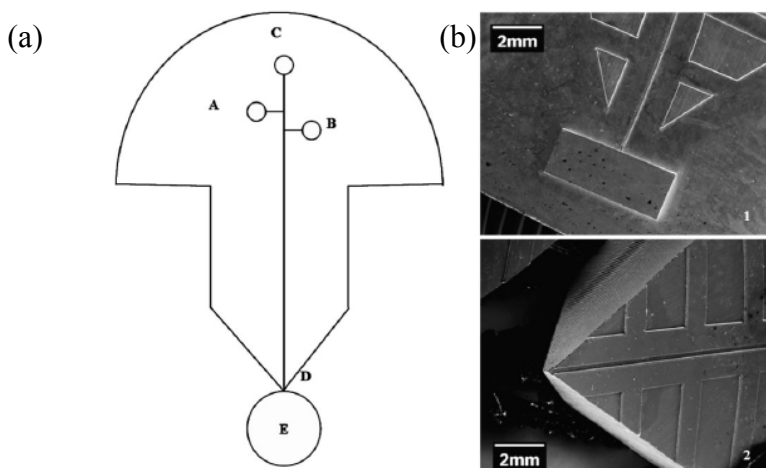


Figure 1.7 (a) Schematic of an on-line microfluidic chip MALDI interface using a rotating ball inlet. A, sample inlet reservoir; B, sample waste reservoir; C, buffer reservoir; D, channel exit; E, rotating ball; Separated samples are deposited onto the ball through direct contact of chip. (b) Scanning electron microscopy images: 1, brass mold master; 2, a hot embossed PMMA chip. Adapted from [88]

1.3.5 Multispray

Multiplexing is another aspect of chip-MS coupling that has attracted increasing attention. The first example [48] of multiplexing in chip-MS coupling involved spraying directly from the edge of the chip, utilizing a six-channel device with six separate spray orifices (Figure 1.8a). The parallel multiple-

channel microchip system allowed ESI-MS analysis of different samples in one chip without cross-contamination.

Another multi-channel device design with an array of electrospray tips was developed by Liu *et al.* [89]. In this work, they showed a 96-well epoxy-resin microplate. Each sample well was connected to a dedicated microchannel, and 96 electrospray capillary emitters were inserted into the exit of the channels (Figure 1.8b). Each tip was sequentially positioned in front of the MS sampling orifice. This design allowed a high throughput analysis and avoided the risk of sample carryover.

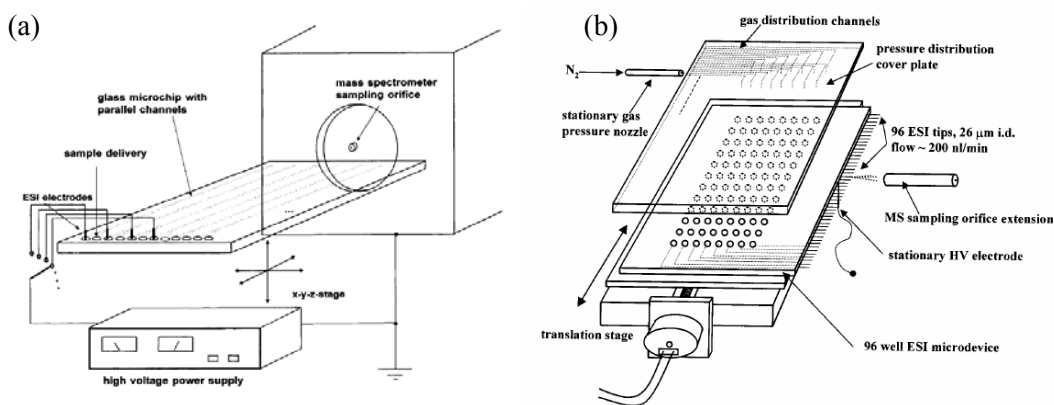


Figure 1.8 (a) Scheme of a microfluidics system for multiplexed ESI-MS analysis, adapted from [48]; (b) Schematic diagram of the 96-channel microdevice with 96 independent electrospray tips, adapted from [89].

Microfabricated electrospray nozzles with high aspect ratio were constructed on the planar surface of a silicon substrate using deep reactive ion etching [90, 91]. This procedure allowed for the creation of a large number of ESI nozzles in parallel, with similar performance to that of microspray capillaries. The multi-electrospray nozzle chip is now available commercially (Nanomate, Advion, Ithaca, NY). Despite the success of this technique, the on-line coupling of such a

device with upstream sample preparation such as protein separation and tryptic digestion is not straightforward, which may hinder its use in proteomics.

1.4 Sheath Flow Technology and Its Application

Sheath flow is a particular type of laminar flow in which one layer of fluid, typically a sample stream or particle stream, is surrounded by another layer of fluid (sheath stream) on more than one side. Microfluidic sheath flow devices have been reported, using either hydrodynamic focusing [92] or electrokinetic focusing [93]. The basic design for performing sample focusing using sheath flow involves three channels intersecting each other. One channel is used to introduce a sample stream in a continuous fashion, while sheath streams are delivered from two side channels, confining the sample stream. Sheath flow is a widely used technique for a variety of applications, including particle counting, flow cytometry, waveguiding, and flow control. In particle counting and flow cytometry applications [94, 95], the sheath flow prevents particles from coming into contact with the walls, minimizing loss of particles or cells to the channel wall. It also serves to focus the particles or cells into the center of the channel, allowing for easy counting or measurement through optical or other means. By incorporation of transverse spatial confinement of the sample, the probe volume of the detector can be reduced and scatter induced by refractive index changes at the wall boundary is eliminated. These advantages permit more sensitive measurements compared with on-column detection [96].

1.5 Background

1.5.1 Microfabrication

1.5.1.1 Photolithography

Glass microchips are traditionally fabricated using standard photolithography techniques with photomasks for design transfer, and wet chemical etching for structure formation. The photomask that contains the design for the microfluidic features such as channels and chambers, is created using software such as L-Edit.

For a photolithographic process, the theoretical resolution limit (i.e., the minimum resolved dimension) is given by:

$$b_{\min} = \frac{3}{2} \sqrt{\lambda \left(s + \frac{z}{2} \right)} \quad (1.1)$$

where b_{\min} is the minimum feature size, λ is the wavelength of exposing light, z is the photoresist thickness and s is the distance between the mask and the photoresist during exposure. In contact printing, the photomask is pressed against the resist-covered wafer with pressure or vacuum, thus s is zero. With λ of 365 nm and a 1.2 μm thick resist, the minimum line width is 0.7 μm . Smaller features can be obtained using alternative lithographic techniques, such as Deep UV and e-beam lithography.

1.5.1.2 Wet Etching

Glass can be etched in HF containing solution with the reaction:



The product is water soluble, resulting in an etched glass substrate.

An important issue is that wet etching of glass by HF is isotropic, meaning that the glass structure is etched at the same rate in all directions. This results in a channel with a flat bottom and a circular arc edge with a radius d (depth of the channel) or a D-shaped channel, as illustrated in Figure 1.9.

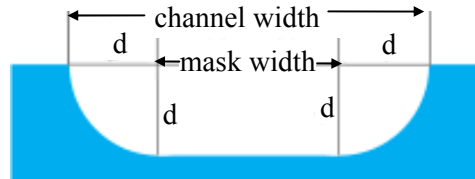


Figure 1.9 Schematic illustration of channel cross section profile resulting from isotropic wet etching.

As a result of the isotropic nature of the etching, undercutting of the mask layer by the same distance as the etch depth creates a top channel width larger than that in the mask design. The widening at the top of the channel must be taken into account when designing the device and when determining the etching depth. For example, two adjacent features need to be more than $20\ \mu\text{m}$ apart in the mask for a $10\ \mu\text{m}$ deep etch to be possible. While the isotropic etching limits the possible feature size that can be obtained on a substrate, it can be of advantage in two aspects. First, it provides a straightforward and fast method for estimating the channel depth d by:

$$d = (W - W_M) \quad (1.3)$$

Where W is the etched channel width at the top and can be measured under a microscope and W_M is the original channel width in the mask design. Exact measurement of the etch depth can be obtained using a profilometer, if necessary. Secondly, the isotropic etching can be utilized for the fabrication of a weir structure (a shallower region in the channel) for retaining beads. Briefly, in the

chip mask, a line is designed across the channel, and thus is left unexposed during the lithographic process. As the two channel segments are etched, the line between them is undercut from both sides. The final height of the weir can be tuned through the control of the width of the line in the initial mask design.

1.5.2 Electroosmotic Flow

One of the critical issues in a microfluidic system is the technique used to transport fluid in the microchannel. In an electrokinetically driven system, the bulk fluid flows are generated utilizing electroosmosis. Electroosmosis refers to the movement of liquid induced by an electric field along a charged surface, creating a bulk flow.

When brought into contact with an ion-containing solvent, many materials will develop a surface charge. In the case of a capillary or microchannel, the negative charge on the inner wall is a result of deprotonation of silanol groups in a buffer solution with $\text{pH} > 2$. The surface charge, in turn, will influence the distribution of ions in the nearby solution, creating what is called the electric double layer. The cause of EOF is the electrical double layer formed at the surface/solution interface: consisting of a compact layer and a diffuse layer. As shown in Figure 1.10, ions in solution, of opposite charge to that of the surface (counter-ions, cations in this case), are attracted towards the wall of the channel and partially neutralize the negative charge on the surface. These cations lack hydration and form an immobilized compact layer, termed a Stern layer or the inner Helmholtz plane (IHP). The remaining negative charge is neutralized by

solvated cations in the next layer. The plane of closest approach of the hydrated cations to the surface is the outer Helmholtz plane (OHP), which delimits the compact portion of the double layer. In the diffuse part of the double layer, both hydrated cations and anions are present in this region, with an excess of cations over anions.

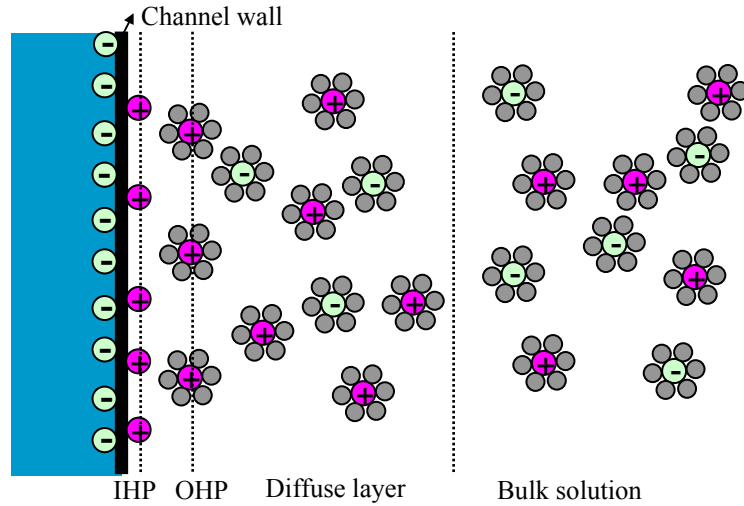


Figure 1.10 Schematic illustration of the principle of electroosmotic flow.

Upon application of an electric field, the solvated cations in the diffuse double layer move toward the cathode, and owing to viscous drag, the momentum is transported to the adjacent liquid, resulting in a bulk liquid flow, named electroosmotic flow (EOF). Electrophoretic mobility for the EOF is defined by:

$$\mu_{EOF} = -\frac{\varepsilon_0 \varepsilon_r \zeta}{\eta}$$

where ζ is zeta potential, the electric potential at the plane of shear, which is the plane that separates mobile fluid from the stagnant fluid, ε_0 is the permittivity of vacuum, and ε_r and η are the dielectric constant and the viscosity of the electrolyte solution.

EOF depends solely on the interaction between the liquid within the channel and the applied electric field, and is a preferred approach for fluid manipulation in microfluidic devices due to the following advantages over pressure-drive flow: (i) no external device with moving parts is required, making the design and fabrication much simpler; (ii) the profile of EOF is generally flat, contributing to high separation efficiencies in separations; and (iii) the flow in a multiplexed microfluidic device with complex channel networks can be easily controlled by switching voltages.

However, the chemical properties of microchannel surface play an important role in the EOF properties. Since the silanol groups on the inner surface are dissociated to form $-\text{SiO}^-$ when the solution $\text{pH} > 2$, the channel exposes a hydrophobic, negatively charged, pH dependent surface. These features can be problematic, especially when analyzing biomolecules like proteins, due to analyte-wall interactions. Analytes are easily adsorbed onto the surface by interactions such as hydrophobic interaction, electrostatic interaction, hydrogen bonding, which cause poor reproducibility due to the variations in the surface properties. A successful strategy to overcome analyte adsorption problems is to modify the microchannel internal wall.

1.5.3 Porous Polymer Monolith

Porous polymer materials, known as monoliths, were introduced in the late 1980s and early 1990s to be used as new chromatographic separation media in HPLC to address some of the well-known drawbacks of packed particulate

sorbents [97, 98]. In a simplified way, a monolith can be roughly considered as a single large “particle” containing a network of interconnected pores, which provides this material high permeability. In addition, the porous structure also accelerates mass transfer within the separation medium since all of the mobile phase must flow through the pores. Thus polymer monoliths have been widely explored as an attractive alternative to packed particulate stationary phase in chromatography.

Polymer monoliths are typically prepared by *in situ* polymerization of a mixture composed of a monomer, cross-linker, porogenic solvent, and an initiator. Polymerization is initiated either thermally [99] or by UV light [100]. Recently introduced UV-initiated polymerization enables the formation of monolithic polymers within specific regions of a microfluidic device using photolithographic techniques. The mechanism of monolith formation through photo-initiation can be described as follows. When the mixture is exposed to UV light, the initiator decomposes and liberates free radicals that initiate the reaction. As the polymer chains grow, their solubility in the reaction mixture decreases and the polymer chains precipitate to form nuclei. The nuclei further increase their size and associate in clusters. As the polymerization proceeds further, in the later stages of polymerization, the clusters are large enough to come into contact with their neighbors and form an interconnected matrix, and the final morphological structure is created. This process results in a two-phase system consisting of a white-colored continuous solid monolith and inert liquid porogens filling the pores.

Different functional parts of the microfluidic system may require monolithic polymers with different surface chemistries. For example, chromatographic separations using the reversed-phase mode or solid-phase extractions of nonpolar compounds from aqueous solutions will require monolithic material with a hydrophobic chemistry, whereas monoliths used in electrochromatography must contain charged functional groups to generate EOF that drives the solution through the column. In applications such as enzyme immobilization, monoliths containing reactive functional groups where the enzyme can be attached should be used. The surface chemistries can be easily controlled by choosing different monomers, and a broad variety of monomers is available to achieve the desired surface chemistries.

A few examples of monomers (1-8) and cross-linkers (9, 10) that have been used for the preparation of polymer monoliths are shown in Figure 1.11. These monomers cover a broad variety of surface chemistries including hydrophilic (1, 2), hydrophobic (3, 4), reactive (5, 6), and ionizable (7, 8) functionalities. The porosity and hydrodynamic properties of the monolithic materials can be adjusted to serve the desired functions in different applications. Key variables such as the composition of the polymerization mixture and the reaction conditions allow the tuning of porous properties of the monoliths over a broad range.

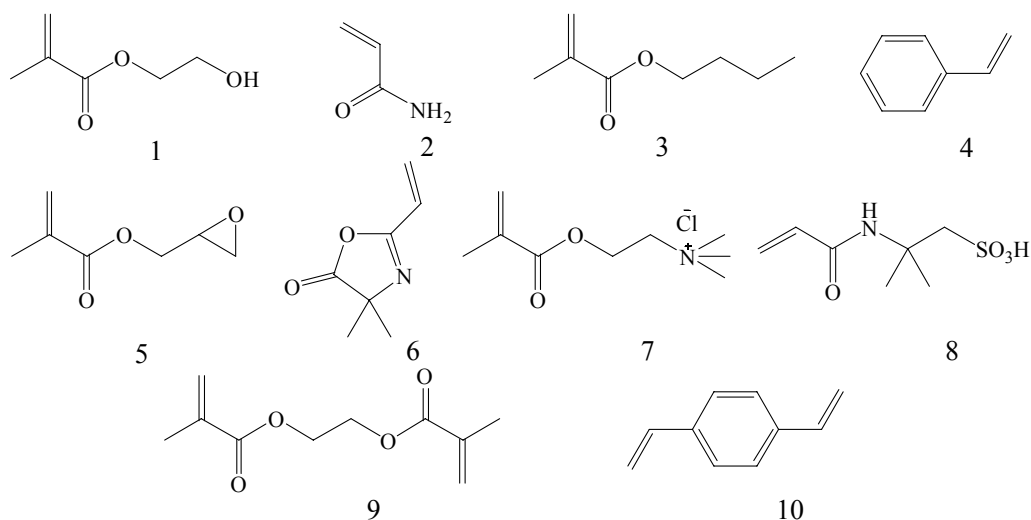


Figure 1.11 Examples of monomers (1-8) and cross-linkers (9, 10) used for the preparation of monoliths, 1. 2-hydroxyethyl methacrylate (HEMA), 2. acrylamine (AA), 3. butyl methacrylate (BMA), 4. styrene, 5. glycidyl methacrylate (GMA), 6. 2-vinyl-4,4-dimethylazlactone (VDMA), 7. 2-(methacryloyloxy)ethyl trimethyl ammonium chloride (META), 8. 2-acrylamido-2-methyl-1-propanesulfonic acid (AMPS), 9. ethylene dimethacrylate (EDMA), 10. divinylbenzene (DVB).

Although the polymer monoliths were first introduced to use as a stationary phase in HPLC, these monolithic materials have found a broad variety of applications in many areas such as solid-phase extraction [101], electrochromatography [102], enzyme immobilization [103], molecular recognition [104], heterogeneous catalyst [105], and combinatorial chemistry [106]. The driving force behind their development is the distinct advantages that monoliths hold. They are easy to prepare, the monolith fills the entire column by polymerization *in situ*, often via a one-step process, eliminating the need for retaining frits, and thus avoids any potential band broadening caused by the frit. Their properties such as porosity, surface area and functionality can be readily tailored.

1.5.4 Electrospray ionization

Electrospray ionization (ESI) is a solution-based technique used in mass spectrometry for producing ions, through which ions present in solution can be transferred to the gas phase. The phenomenon of electrospray was first described by Zeleny in 1917, where he captured the first time-lapse images of the dynamic liquid meniscus at the tip of a glass capillary [107]. Dole and co-workers were the first to attempt to use electrospray to produce gas phase ions in 1968 [108]. Electrospray ionization mass spectrometry (ESI-MS) was first introduced by Yamashita and Fenn in 1984 [109]. Since then, ESI-MS has gained widespread attention and applications in this area have risen dramatically over the last decades.

When a high voltage is applied between the capillary tip and a counter electrode, the charged liquid exits the capillary and builds up charges at the liquid surface. The shape of the solution surface changes and forms a cone, named a Taylor cone. At high enough electric field, the cone becomes unstable and generates a liquid filament jet, from which separate charged droplets form. These charged droplets undergo solvent evaporation and shrink, while the charge remains constant, resulting in an increase in the surface charge intensity. When the charge density at the droplet surface reaches a critical value (the Rayleigh limit) and coulombic repulsion of the ions overcomes the surface tension, a so-called coulombic explosion occurs and several even smaller droplets are formed, each carrying a fraction of the original droplets surface charge. The process of solvent evaporation, droplet contraction and coulombic explosions is repeated

until extremely small droplets containing only one ion form, and further evaporation will lead to conversion to gas phase ions.

Electrospray ionization shows a number of unique advantages: first, it is a soft ionization process, so intact molecular ions are observed; second, ESI allows production of multiply-charged ions. This results in the ability of analyzing very high molecular weight species using most available mass analyzers. Furthermore, ESI is an atmospheric pressure process, making it easy to use and interface with separation techniques.

1.6 Thesis Outline

In Chapter 2, we present the preparation of porous polymer monoliths within the microchannels and their application for on-chip solid-phase extraction and preconcentration. The preparation of the monolithic material is achieved by photo-initiated copolymerization of butyl methacrylate with ethylene dimethacrylate. The polymerization conditions, including porogenic solvent content, initiator type, and UV exposure time are investigated systematically, in order to optimize the composition of the monoliths for SPE preconcentration.

In Chapter 3, four physically adsorbed coatings are investigated and their performance is compared in terms of stability, reproducibility, EOF properties, resistance towards organic modifier, and compatibility with sheathless ESI-MS.

Chapter 4 demonstrates an on-chip SPE and on-bed digestion system, which is coupled on-line to ESI-MS for peptide mass mapping. On-bed digestion was performed by capturing protein sample onto a hydrophobic monolithic support,

then followed by flowing a trypsin solution over the adsorbed protein. The microchannel surface was coated with a cationic polymer, polyE-323 in order to electrokinetically pump fluids through the microdevice and facilitate positive electrospray. The function of this system is evaluated in terms of the SPE behavior and digestion performance using several standard proteins.

Chapter 5 focuses on the design and fabrication of an electrokinetically controlled fractionator and collector with multiple collection channels, and the integration of monolithic polymers within this multi-channel device. The performance of this microfluidic device as a platform for integration of multiple analytical steps is investigated by sequential fractionation, retention, and elution of fluorescent samples to evaluate the ability to capture and release individual fractions without cross-contamination.

Chapter 6 summarizes the previous chapters and briefly discusses the future work. New ideas and chip designs for further development are presented.

1.7 References

- 1 James, P. *Quarterly Reviews of Biophysics* **1997**, *30*, 279–331.
- 2 Qoronfleh, M.W. *Journal of Biomedicine and Biotechnology* **2004**, *3*, 121–123.
- 3 Corthals, G. L.; Wasinger, V. C.; Hochstraser, D. F.; Sanchez, J. C. *Electrophoresis* **2000**, *21*, 1104–1115.
- 4 Beranova-Giorgianni, S. *Trends Anal. Chem.* **2003**, *22*, 273–281.
- 5 Issaq, H. J.; Conrads, T. P.; Janini, G. M.; Veenstra, T. D. *Electrophoresis* **2002**, *23*, 3048–3061.
- 6 Manz, A.; Graber, N.; Widmer, H. M. *Sensors and Actuators B* **1990**, *B1*, 244–248.
- 7 Manz, A.; Miyahara, Y.; Miura, J.; Watanabe, Y.; Miyagi, H.; Sato, K. *Sensors and Actuators B* **1990**, *B1*, 249–255.
- 8 Harrison, D. J.; Manz, A.; Fan, Z. H.; Ludi, H.; Widmer, H. M. *Anal. Chem.* **1992**, *64*, 1926–1932.
- 9 Harrison, D. J.; Glavina, P. G.; Manz, A. *Sensors and Actuators B* **1993**, *10*, 107–116.
- 10 Vilkner, T.; Janasek, D.; Manz, A. *Anal. Chem.* **2004**, *76*, 3373–3385.
- 11 Dittrich, P. S.; Tachikawa, K.; Manz, A. *Anal. Chem.* **2006**, *78*, 3887–3907.
- 12 West, J.; Becker, M.; Tombrink, S.; Manz, A., *Anal. Chem.* **2008**, *80*, 4403–4419.
- 13 Bruin, G. J. M. *Electrophoresis* **2000**, *21*, 3931–3951.
- 14 Thorsen, T.; Maerkl, S. J.; Quake, S. R. *Science* **2002**, *298*, 580–584.
- 15 Hong, J. W.; Quake, S. R. *Nat. Biotechnol.* **2003**, *21*, 1179–1183.
- 16 Whitesides, G. M. *Nature* **2006**, *442*, 368–373.
- 17 Melin, J.; Quake, S. R. *Annu Rev Biophys Biomol Struct.* **2007**, *36*, 213–231.
- 18 Hong, J. G.; Edel, J. B.; Demello, A. I. *Drug Discovery Today* **2009**, *14*, 134–146.
- 19 Llion, N.; Rohner, T. C.; Dayon, L.; Arnaud, I. L.; Damoc, E.; Youhnovski, N.; Wu, Z. Y.; Roussel, C.; Jossierand, J.; Jensen, H.; Rossier, J. S.; Przybylski, M.; Girault, H. H. *Electrophoresis* **2003**, *24*, 3533–3562.

- 20 Mouradian, S. *Current Opinion in Chemical Biology* **2002**, *6*, 51–56.
- 21 Lazar, I. M.; Grym, J.; Foret, F. *Mass Spectrom. Rev.* **2006**, *25*, 573–594.
- 22 Harrison, D. J.; Oleschuk, R. D.; Thibault, P. *Lab-on-a-Chip: Miniaturized Systems for (Bio)Chemical Analysis and Synthesis*, **2003**, 249–270.
- 23 de Mello, A. J.; Beard, N. *Lab on a Chip* **2003**, *3*, 11N–19N.
- 24 Schasfoort, R. B. M. *Expert Rev. Proteomic* **2004**, *1*, 123–132.
- 25 Song, S.; Singh, A. K. *Anal. Bioanal. Chem.*, **2006**, *384*, 41–43.
- 26 Sueyoshi, K.; Kitagawa, F.; Otsuka, K. *J. Sep. Sci.* **2008**, *31*, 2650–2666.
- 27 Slentz, B. E.; Penner, N. A.; Regnier, F. E. *J. Chromatogr. A* **2003**, *984*, 97–107.
- 28 Li, J. J.; LeRiche, T.; Tremblay, T. L.; Wang, C.; Bonneil, E.; Harrison, D. J.; Thibault, P. *Mol. Cell. Proteomics* **2002**, *1*, 157–168.
- 29 Peterson, D. S.; Rohr, T.; Svec, F.; Frechet, J. M. J. *Anal. Chem.* **2003**, *75*, 5328–5335.
- 30 Tia, S.; Herr, A. E. *Lab on a Chip* **2009**, *9*, 2524–2536.
- 31 Chen, H.; Fan, Z. H. *Electrophoresis* **2009**, *30*, 758–765.
- 32 Rocklin, R. D.; Ramsey, R. S.; Ramsey, J. M. *Anal. Chem.* **2000**, *72*, 5244–5249.
- 33 Ramsey, J. D.; Jacobson, S. C.; Culbertson, C. T.; Ramsey, J. M. *Anal. Chem.* **2003**, *75*, 3758–3764.
- 34 Gottschlich, N.; Jacobson, S. C.; Culbertson, C. T.; Ramsey, J. M. *Anal. Chem.* **2001**, *73*, 2669–2674.
- 35 Li, Y.; Buch, J. S.; Rosenberger, F.; DeVoe, D. L.; Lee, C. S. *Anal. Chem.* **2004**, *76*, 742–748.
- 36 Emrich, C. A.; Medintz, I. L.; Chu, W. K.; Mathies, R. A. *Anal. Chem.* **2007**, *79*, 7360–7366.
- 37 Das, C.; Zhang, J.; Denslow, N. D.; Fan, Z. H. *Lab on a Chip* **2007**, *7*, 1806–1812.
- 38 Liu, J.; Yang, S.; Lee, C. S.; DeVoe, D. L. *Electrophoresis*, **2008**, *29*, 2241–2250.
- 39 Gustafsson, M.; Hirschberg, D.; Palmberg, C.; Jornvall, H.; Bergman, T.

- Anal. Chem.* **2004**, *76*, 345–350.
- 40 Hirschberg, D.; Jagerbrink, T.; Samskog, J.; Gustafsson, M.; Stahlberg, M.; Alvelius, G.; Husman, B.; Carlquist, M.; Jornvall, H.; Bergman, T. *Anal. Chem.* **2004**, *76*, 5864–5871.
- 41 Oleschuk, R. D.; Harrison, D. J. *Trends in Anal. Chem.* **2000**, *19*, 379–388.
- 42 Limbach, P. A.; Meng, Z. J. *Analyst*, **2002**, *127*, 693–700.
- 43 Zhang, S.; Van Pelt, C. K. *Expert Rev. Proteomic* **2004**, *1*, 449–468.
- 44 Sung, W. C.; Makamba, H.; Chen, S. H. *Electrophoresis* **2005**, *26*, 1783–1791.
- 45 Foret, F.; Kusy, P. *Electrophoresis* **2006**, *27*, 4877–4887.
- 46 Lee, J. H.; Soper, S. A.; Murraya, K. K. *J. Mass. Spectrom.* **2009**, *44*, 579–593.
- 47 Koster, S.; Verpoorte, E. *Lab on a Chip* **2007**, *7*, 1394–1412.
- 48 Xue, Q. F.; Foret, F.; Dunayevskiy, Y. M.; Zavracky, P. M.; McGruer, N. E.; Karger, D. L. *Anal. Chem.* **1997**, *69*, 426–430.
- 49 Ramsey, R. S.; Ramsey, J. M. *Anal. Chem.* **1997**, *69*, 1174–1178.
- 50 Lion, N.; Gobry, V.; Jensen, H.; Rossier, J. S.; Girault, H. H. *Electrophoresis* **2002**, *23*, 3583–3588.
- 51 Lion, N.; Gellon, J.-O.; Jensen, H.; Girault, H. H. *J. Chromatogr. A* **2003**, *1003*, 11–19.
- 52 Wang, Y. X.; Cooper, J. W.; Lee, C. S.; DeVoe, D. L. *Lab on a Chip* **2004**, *4*, 363–367.
- 53 Bedair, M. F.; Oleschuk, R. D. *Anal. Chem.* **2006**, *78*, 1130–1138.
- 54 Figeys, D.; Ning, Y.; Aebersold, R. *Anal. Chem.* **1997**, *69*, 3153–3160.
- 55 Lazar, I. M.; Ramsey, R. S.; Sundberg, S.; Ramsey, M. J. *Anal. Chem.* **1999**, *71*, 3627–3631.
- 56 Chan, J. H.; Timperman, A. T.; Qin, D.; Aebersold, R. *Anal. Chem.* **1999**, *71*, 4437–4444.
- 57 Pinto, D. M.; Ning, Y. B.; Figeys, D. *Electrophoresis* **2000**, *21*, 181–190.
- 58 Chen, S. H.; Sung, W. C.; Lee, G. B.; Lin, Z. Y. *Electrophoresis* **2001**, *22*, 3972–3977.

- 59 Deng, Y. Z.; Henion, J.; Li, J. J.; Thibault, P.; Wang, C.; Harrison, D. J. *Anal. Chem.* **2001**, *73*, 639–646.
- 60 Zhang, B. L.; Foret, F.; Karger, B. L. *Anal. Chem.* **2001**, *73*, 2675–2681.
- 61 Ssenyange, S.; Taylor, J.; Harrison, D. J.; McDermott, M. T. *Anal. Chem.* **2004**, *76*, 2393–2397.
- 62 Dahlin, A. P.; Wetterhall, M.; Liljegren, G.; Bergstrom, S. K. *Analyst* **2005**, *130*, 193–199.
- 63 Bings, N. H.; Wang, C.; Skinner, C. D.; Colyer, C. L.; Thibault, P.; Harrison, D. J. *Anal. Chem.* **1999**, *71*, 3292–3296.
- 64 Schilling, M.; Nigge, W.; Rudzinski, A.; Neyer, A.; Hergenroder, R. *Lab on a Chip* **2004**, *4*, 220–224.
- 65 Xie, J.; Miao, Y.; Shih, J.; Tai, Y. C.; Lee, T. D. *Anal. Chem.* **2005**, *77*, 6947–6953.
- 66 Licklider, L.; Wang, X. Q.; Desai, A.; Tai, Y. C.; Lee, T. D. *Anal. Chem.* **2000**, *72*, 367–375.
- 67 Kameoka, J.; Orth, R.; Ilic, B.; Czaplewski, D.; Wachs, T.; Craighead, H. G. *Anal. Chem.* **2002**, *74*, 5897–5901.
- 68 Svedberg, M.; Veszelei, M.; Axelsson, J.; Vangbo, M.; Nikolajeff, F. *Lab on a Chip* **2004**, *4*, 322–327.
- 69 Freire, S. L. S.; Yang H.; Wheeler, A. R. *Electrophoresis* **2008**, *29*, 1836–1843.
- 70 Kim, W.; Guo, M.; Yang, P.; Wang, D. *Anal. Chem.* **2007**, *79*, 3703–3707.
- 71 Hoffmann, P.; Haeusig, U.; Schulze, P.; Belder, D. *Angew. Chem. Int. Ed.* **2007**, *46*, 4913–4916.
- 72 Yin, N. F.; Killeen, K.; Brennen, R.; Sobek, D. *Anal. Chem.* **2005**, *77*, 527–533.
- 73 Wachs, T.; Henion, J. *Anal. Chem.* **2001**, *73*, 632–638.
- 74 Zhang, B.; Liu, H.; Karger, B. L.; Foret, F. *Anal. Chem.* **1999**, *71*, 3258–3264.
- 75 Zhang, B.; Foret, F.; Karger, B. L. *Anal. Chem.* **2000**, *72*, 1015–1022.
- 76 Barnidge, D. R.; Nilsson, S.; Markides, K. E.; Rapp, H.; Hjort, K.; *Rapid*

- Commun. Mass Spectrom.* **1999**, *13*, 994–1002.
- 77 Barnidge, D. R.; Nilsson, S.; Markides, K. E. *Anal. Chem.* **1999**, *71*, 4115–4118.
- 78 Chang, Y. Z.; Chen, Y. R.; Her, G. R.; *Anal. Chem.* **2001**, *73*, 5083–5087.
- 79 Rohner, T. C.; Rossier, J. S.; Girault, H. H. *Anal. Chem.* **2001**, *73*, 5353–5357.
- 80 Zhu, X.; Thiam, S.; Valle, B. C.; Warner, I. M. *Anal. Chem.* **2002**, *74*, 5405–5409.
- 81 Gobry, V.; van Oostrum, J.; Martinelli, M.; Rohner, T. C.; Reymond, F.; Rossier, J. S.; Girault, H. H. *Proteomics* **2002**, *2*, 405–412.
- 82 Le Gac, S.; Arscott, S.; Rolando, C. *Electrophoresis* **2003**, *24*, 3640–3647.
- 83 Tang, K. Q.; Lin, Y. H.; Matson, D. W.; Kim, T.; Smith, R. D. *Anal. Chem.* **2001**, *73*, 1658–1663.
- 84 Kim, J. S.; Knapp, D. R. *J. Am. Soc. Mass Spectrom.* **2001**, *12*, 463–469.
- 85 Svedberg, M.; Pettersson, A.; Nilsson, S.; Bergquist, J.; Nyholm, L.; Nikolajeff, F.; Markides, K. *Anal. Chem.* **2003**, *75*, 3934–3940.
- 86 Hsieh, S.; Dreisewerd, K.; van der Schors, R. C.; Jimenez, C. R.; Stahl-Zeng, J.; Hillenkamp, F.; Jorgenson, J. W.; Geraerts, W. P. M.; Li, K. W. *Anal. Chem.* **1998**, *70*, 1847–1852.
- 87 Brivio, M.; Tas, N. R.; Goedbloed, M. H.; Gardeniers, H. J. G. E. *Lab on a Chip* **2005**, *5*, 378–381.
- 88 Musyimi, H. K.; Guy, J.; Narcisse, D. A.; Soper, S. A.; Murray, K. K. *Electrophoresis* **2005**, *26*, 4703–4710.
- 89 Liu, H.; Felten, C.; Xue, Q.; Zhang, B.; Jedrzejewski, P.; Karger, B. L.; Foret, F. *Anal. Chem.* **2000**, *72*, 3303–3310.
- 90 Schultz, G. A.; Corso, T. N.; Prosser, S. J.; Zhang, S. *Anal. Chem.* **2000**, *72*, 4058–4063.
- 91 Dethy, J. M.; Ackermann, B. L.; Delatour, C.; Henion, J. D.; Schultz, G. A. *Anal. Chem.* **2003**, *75*, 805–811.
- 92 Lee, G. B.; Hung, C. I.; Ke, B. J.; Huang, G. R.; Hwei, B. H. *J. Micromech. Microeng.* **2001**, *11*, 567–573.

- 93 Jacobson, S. C.; Ramsey, J. M. *Anal. Chem.* **1997**, *69*, 3212–3217.
- 94 Schrum, D. P.; Culbertson, C. T.; Jacobson, S. C.; Ramsey, J. M. *Anal. Chem.* **1999**, *71*, 4173–4177.
- 95 Hung, C. I.; Ke, B. J.; Huang, G. R.; Hwei, B. H.; Lai, H. F.; Lee, G. B. *J. Fluids Eng.* **2001**, *123*, 672–679.
- 96 Skinner, C. D. *Electrophoresis* **2009**, *30*, 372–378.
- 97 Hjerten, S.; Liao, J. L.; Zhang, R. *J. Chromatogr.* **1989**, *473*, 273–275.
- 98 Tennikova, T. B.; Svec, F.; Belenkii, B. G. *J. Liquid Chromatogr.* **1990**, *13*, 63–70.
- 99 Peters, E. C.; Petro, M.; Svec, F.; Frechet, J. M. J. *Anal. Chem.* **1997**, *69*, 3646–3649.
- 100 Tan, A.; Benetton, S.; Henion, J. D. *Anal. Chem.* **2003**, *75*, 5504–5511.
- 101 Yu, C.; Davey, M. H.; Svec, F.; Frechet, J. M. J. *Anal. Chem.* **2001**, *73*, 5088–5096.
- 102 Faure, K.; Albert, M.; Dugas, V.; Cetier, G.; Ferrigno, R.; Morin, P.; Rocca, J. L. *Electrophoresis* **2008**, *29*, 4948–4955.
- 103 Peterson, D. S.; Rohr, T.; Svec, F.; Frechet, J. M. J. *Anal. Chem.* **2002**, *74*, 4081–4088.
- 104 Matsui, J.; Kato, T.; Takeuchi, T.; Suzuki, M.; Yokoyama, K.; Tamyia, E.; Karube, I. *Anal. Chem.* **1993**, *65*, 2223–2224.
- 105 Cybulski, A.; Moulijn, J. A. *Catal. Rev. Sci. Eng.* **1994**, *36*, 179–270.
- 106 Tripp, J. A. ; Svec, F.; Frechet, J. M. J. *J. Comb. Chem.* **2001**, *3*, 216–323.
- 107 Zeleny, J. *Physical Review* **1917**, *10*, 1–6.
- 108 Dole, M.; Mack, L. L.; Hines, R. L.; Mobley, R. C.; Ferguson, L. D.; Alice, M. B. *Journal of Chemical Physics* **1968**, *49*, 2240–2249.
- 109 Yamashita, M.; Fenn, J. B. *J. Phys. Chem.* **1984**, *88*, 4671–4675.

Chapter 2

Preparation and Characterization of Porous Polymer Monoliths and Evaluation of SPE Performance

2.1 Introduction.....	38
2.2 Experimental Section.....	39
2.2.1 Chemicals and Materials.....	39
2.2.2 Microchip Design and Fabrication.....	40
2.2.3 Preparation of Monolithic Polymer	43
2.2.4 Instrumentation	45
2.2.5 Microchip Operation.....	46
2.3 Results and Discussion	47
2.3.1 Control of Surface Chemistries.....	47
2.3.2 Control of Porous Properties.....	48
2.3.2.1 Porogenic Solvent System	50
2.3.2.2 Initiator Type	53
2.3.2.3 Effect of Exposure Time on Polymer Structure.....	54
2.3.2.4 Optimized Monolith Recipes and Pore Size Measurement	55
2.3.3 Effect of Chip Design on the Monolithic Polymer	59
2.3.3.1 Exposure Window Size.....	59
2.3.3.2 Bed Dimensions and Beds with Posts.....	60
2.3.4 Evaluation of SPE Performance.....	63
2.3.4.1 On-Chip SPE of BODIPY	63
2.3.4.2 Protein Adsorption onto the Monolithic Bed.....	68
2.3.4.3 Effect of Eluent Composition	69
2.3.4.4 Durability of the Monoliths and Recovery of Glass Chips.....	71
2.4 Conclusion	72
2.5 References.....	73

2.1 Introduction

Microchip systems enable the integration of multiple sample handling steps [1–3]. Sample preconcentration is a critical step in sample preparation, and it is generally required for analysis of low abundance or trace level analytes to overcome the detection-limit problem or to get rid of potential interferences [4]. This is even more important in the case of microchip-based applications given the low sample loading capacity of the microfluidic chip format.

To date, sample preconcentration within microchips has been performed by many methods, such as field amplified sample stacking (FASS) [5–7] and isotachopheresis (ITP) [8]. In these electrophoretic preconcentration techniques, two or more buffers with different conductivities are involved to generate a spatial variation of electric field strength. Focusing and preconcentration is based upon the changes of migration velocity of the analytes between different zones, allowing charged analytes to be stacked at the buffer boundaries into sharp, narrow bands. Although these methods are simple and are easy to implement in microfluidic systems pumped by electrokinetic forces, their concentration efficiencies are ultimately limited by the maximum sample volume that can be introduced into the system (usually smaller than the total channel volume).

In contrast, solid-phase extraction (SPE) allows the loading of multiple column volumes of sample into the devices as the analytes are adsorbed onto a stationary phase [9, 10]. In addition to the significant enhancement in sample concentration, this sorption based technique can also be used for sample clean-up to remove matrix interferences. Thus, SPE is extremely useful when complex

matrices are analyzed. SPE can be easily integrated into a microfluidic system by coating the channel wall with sorption phase [11], packing beads into microchannels [12, 13], or using an *in situ* polymerized monolith [14–16]. *In situ* polymerized monoliths have their distinct advantages. They can be prepared easily and rapidly in a microchannel with no need for retaining frits. The porous properties and surface chemistries can be easily controlled by changing the composition of the initial monomer solution and the polymerization conditions. More importantly, UV-initiated polymerization enables the formation of monoliths at multiple locations in a microdevice simultaneously by using a mask to expose the desired regions. This feature is of great importance for multi-channel device applications.

In this chapter, I describe the efforts to prepare monolithic polymer beds within microfluidic devices by UV-initiated polymerization. We systematically investigated a wide variety of polymerization mixture compositions and reaction conditions in order to obtain ideal monoliths for SPE for protein preconcentration, which should have low flow resistance and high loading capacity. The monolithic polymers were characterized by scanning electron microscopy (SEM) and were evaluated in terms of SPE performance.

2.2 Experimental Section

2.2.1 Chemicals and Materials

Butyl methacrylate (BMA), [2-(methacryloyloxy)ethyl]trimethylammonium chloride (META), azobisisobutyronitrile (AIBN), ethylene dimethacrylate

(EDMA), 4-(dimethylamino)benzophenone (DMABP), 2,2-dimethoxy-2-phenylacetophenone (DMPAP), toluene, hexane, 1-octanol, methanol, 1-propanol, 1,4-butanediol, cyclohexanol, acetonitrile (ACN) were purchased from Sigma-Aldrich Chemical Co. (Milwaukee, WI, USA). Benzoin was obtained from General Intermediates of Canada (Edmonton, AB, Canada). BMA and EDMA were purified by passing through basic alumina columns (mesh 650, activity I) to remove the inhibitor. Alumina Basic was from Fisher Scientific (Canada). BODIPY 493/503 (4,4-difluoro-1,3,5,7,8-pentamethyl-4-bora-3a,4-diaza-s-indacene) was from Molecular Probes (Eugene, OR, USA), and was prepared as a 0.1 mM stock solution in HPLC grade methanol. FITC-BSA (Bovine serum albumin-fluorescein isothiocyanate conjugate) was purchased from Sigma-Aldrich. All aqueous solutions were prepared using ultrapure water purified from a Milli-Q purification system (Millipore, Bedford, MA, USA) and filtered with 0.2 μm pore size filters (Millipore, Bedford, MA).

2.2.2 Microchip Design and Fabrication

A simple straight microchannel (56 μm wide, 3.5 cm long and 20 μm deep) was used in this study. Typically, when preparing monolithic polymers in a microdevice, the inner walls of the microchannel were vinylized with a bifunctional silanization reagent to enable covalent attachment of the monolith [14]. However, in our case, the monolith can not be anchored to the channel wall because we need to modify the channel surface with a cationic coating for positive ion electrospray coupling to a mass spectrometer, as will be described in Chapter

3. To help retain the monolith in the desired place, a widened bed (140 μm wide) was designed in the channel and the photo-initiated polymerization is confined in this region using a mask. For better retainment of the monolith, we also designed a post at the outlet of the bed in some devices. The design and fabrication of these posts will be discussed in Section 2.3.3.2.

The microfluidic devices were fabricated in the Nanofab at the University of Alberta using standard photolithography and wet chemical etching techniques, as described in the literature [17]. The entire process is illustrated in Figure 2.1. A 4" \times 4" Corning 0211 glass substrate (600 μm thick, Precision Glass and Optics, CA, USA) was cleaned in a piranha solution (3:1 mixture of H_2SO_4 and H_2O_2) for 15 min (Figure 2.1a), thoroughly rinsed with water, dried and loaded into the Lesker, two-target sputtering system (Kurt J. Lesker Company, Clairton, PA, USA). With the system under vacuum ($\sim 1.5 \times 10^{-6}$ Torr), 30 nm chrome and 150 nm gold were sputtered (Figure 2.1b) successively (parameters: 7 mTorr argon, Cr: 300 W for 3 min, Au: 75 W for 18 min). The photoresist (HPR 504, OCG Microelectronic Materials, Cheshire, MA, USA) was spin-coated onto the Cr/Au glass wafer (Solitec, 500 rpm for 10 s, 4000 rpm for 40 s) (Figure 2.1c). After soft-baking at 115 $^\circ\text{C}$ for 30 min in a Blue M Oven and leaving at room temperature for rehydration (15 min), the substrate was aligned with the photomask using the mask aligner (ABM Inc., Scotts Valley, CA, USA) and exposed to UV light (365 nm for 4 s) (Figure 2.1d). The photoresist was then developed in Microposit 354 Developer (Shipley, Newton, MA, USA) for 25 s to remove the exposed photoresist (Figure 2.1e). This was followed by gold etching ($\text{KI}:\text{I}_2$ at 4:1 in H_2O)

and chrome etching (HNO_3 , $(\text{NH}_4)_2\text{Ce}(\text{NO}_3)_6$ and H_2O , Arch Chemicals, Inc., Norwalk, CT, USA) in the areas that are not protected by photoresist (Figure 2.1f). Finally, the glass wafer was etched in a glass etching solution ($\text{H}_2\text{O}:\text{HF}:\text{HNO}_3$, 66:20:14) to the desired depth to generate the microchannels (Figure 2.1g). The glass etching proceeded at a rate of $\sim 1.5 \mu\text{m}/\text{min}$ in the 0211 glass. The remaining photoresist was removed using acetone. The gold and chrome layers were completely removed using the gold and chrome etchants, respectively (Figure 2.1h).

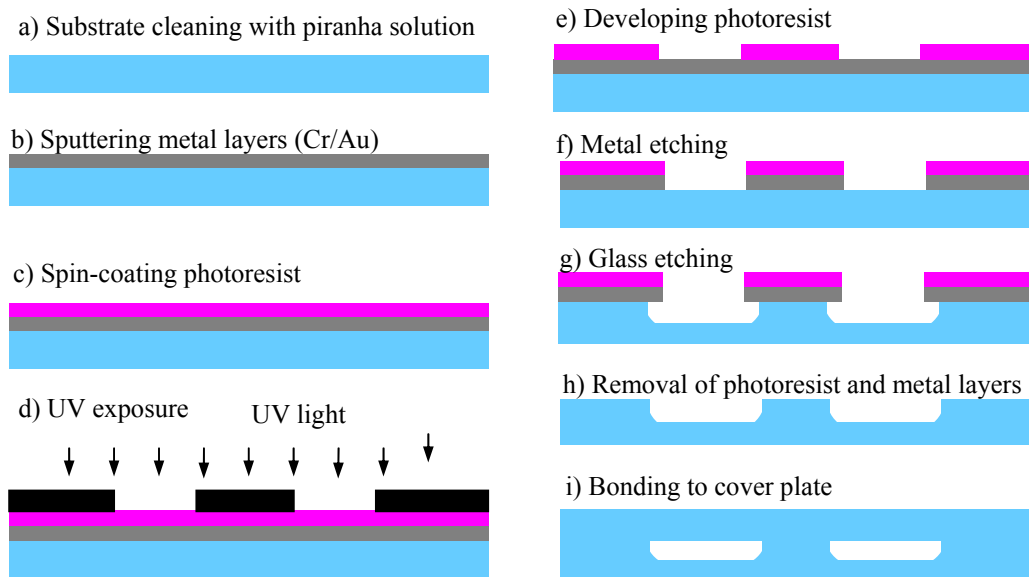


Figure 2.1 Schematic illustrating the device fabrication process.

Access holes were drilled in the cover plate using a 1.5 mm diameter drill bit (Lee Valley, Ottawa, ON, Canada) to allow for the fluidic and electric contacts. A $4'' \times 4''$ Corning 0211 glass was mounted on a thick support glass wafer using Crystalbond (#509, Aremco Products Inc., Valley Cottage, NY, USA), in order to reduce the amount of break-out as the drill passed through the glass. After drilling (Model 7010, Servo Products Company), the 0211 glass was removed from the

support wafer by heating on a hot plate, which softens the Crystalbond, and then immersed in an acetone bath for removal of the Crystalbond. For bonding of the microchannel-containing glass substrate to the cover plate, both were immersed in a piranha solution for 20 minutes. After thorough rinsing with water, both wafers were mounted on a ring holder and loaded into a high pressure washer (Micro Automation 2066, settings: 5 rinse cycles, 10 dry cycles). The top and bottom wafers were then aligned and pressed gently together to start the cold bonding. After this initial cold bonding process, the two wafers were irreversibly bonded in a thermal bonding oven (settings: room temperature to 440 °C at 10 °C/min hold 30 min, 440 °C to 473 °C at 2 °C/min hold 30 min, 473 °C to 592 °C at 2 °C/min hold 6 hours, 592 °C to 473 °C at 4 °C/min hold 30 min) (Figure 2.1i). This process served to form covalent bonding between adjacent silanol groups on opposing wafers. After thermal bonding, pipette tips were cut and attached on the microdevice using epoxy glue to act as reservoirs.

2.2.3 Preparation of Monolithic Polymer

The functional monomers, cross-linker and porogenic solvents were purged with nitrogen for 5 min individually to remove dissolved oxygen before mixing with an initiator. The microchip channel was filled with the polymerization mixture by capillary force and sealed with tape. Figure 2.2 shows the device layout and the setup for photo-initiated polymerization.

The chip was aligned with a transparency mask which had an open window to confine the UV-initiated polymerization within a specific region. The

polymerization reaction was initiated by exposing the microchip to UV light from a UV transilluminator equipped with six 312 nm, 15 W tubes (TS-312R, Spectronics corporations, Westbury, NY). After exposure, the monolith formed was rinsed with a methanol/water mixture (50%:50%, v/v) to remove the unreacted components from its pores. When not in use, the monolithic beds were stored in buffer solution to prevent the monolith from drying out. If not, the dried monoliths will trap bubbles which are very difficult to remove.

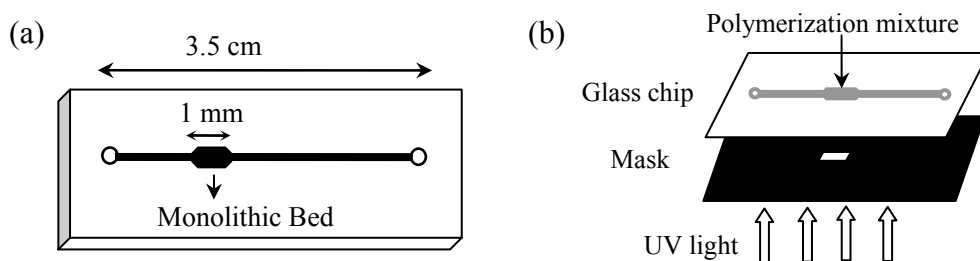


Figure 2.2 (a) Microfluidic chip layout showing a single channel with a 1 mm long bed; (b) Schematic of the experimental setup for photo-initiated polymerization.

The monolith structures were inspected using a LEO 1430 scanning electron microscope (SEM) (Leo, Oberkochen, Germany). Capillaries or glass microchips were cut to expose the cross-sections of the monolithic polymers. Most SEM micrographs were obtained within a capillary, because capillaries are easy to cut with a ceramic capillary cutter, while glass chips have to be cut with a Dicing Saw. Moreover, fabrication of a glass chip is time-consuming and expensive; it is not practical to cut the microchannel to take SEM micrographs for each monolith sample. Monolithic polymer beds in chips were also inspected under an optical microscopy to evaluate the edge resolution of the monolith. A syringe pump (Harvard Apparatus PHD2000, Instech Laboratories, Inc., Plymouth Meeting, PA USA) was used to pump liquid through the monolithic polymers at various flow

rates to check their permeability and mechanical strength in certain range of flow rate. The pore size distribution of bulk monolithic materials was determined using mercury intrusion porosimetry (Autopore IV 9500, Micromeritics). Bulk polymers for the pore size measurement were prepared in glass vials under identical conditions, and then extracted with methanol and dried in vacuum overnight.

2.2.4 Instrumentation

To evaluate the SPE performance, a laser-induced fluorescence (LIF) detection system was used (Figure 2.3). The microchip assembly was placed above an inverted confocal epiluminescent microscope on an X-Y translation stage. Excitation light from an argon ion laser (488 nm, operated at 4 mW Model 2214-105L, Uniphase, San Jose, CA) was reflected by a dichroic mirror (505DRLP, Omega Optical), and then focused on the device using a 25 \times , 0.35 N.A. microscope objective (Leitz Wetzlar, Germany). The fluorescence emission was collected by the same objective, passed through the dichroic mirror and focused by a tube lens onto a 200 μ m pinhole. The signal was filtered by a bandpass filter (530DF30, Omega Optical) and recorded with a photomultiplier tube (PMT) (Hamamatsu HC-120-05). The PMT was biased at 500 V and the analog signal was amplified (10^7 gain trans-impedance amplifier), filtered (active 25 Hz Butterworth filter, house built), and converted to digital data with a National Instruments LAB PC 1200 board and recorded with a LabVIEW program at a writing frequency of 50 Hz.

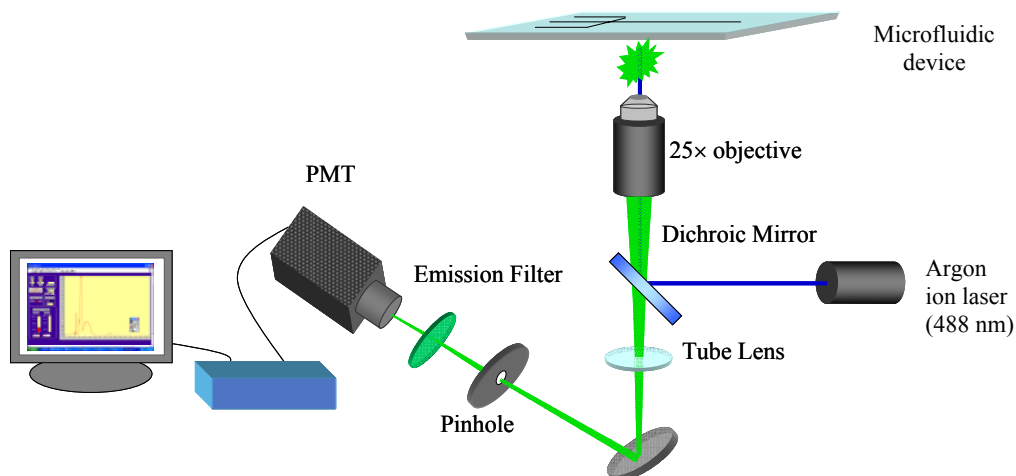


Figure 2.3 The setup for Laser-induced fluorescence (LIF) detection.

A power supply, referred to as the blue box, provided the high voltages necessary for chip operation. It contains a computer controlled 10 kV and three manually controlled (+/-) 3 kV power supplies and several computer controlled relays. Electrical contact with the reservoirs was made through platinum wires. In-house written LabVIEW programs (National Instruments, Austin, TX) were used for computer control of the voltage application and for data acquisition.

2.2.5 Microchip Operation

Most microfluidic systems relied on two types of fluid transport: pressure-driven flow and electrokinetically-driven flow. Both driving forces were used in the studies in this chapter. For pressure-driven flow, the liquids were driven through the device with a syringe pump. A nanoport was attached to connect the device with the syringe pump through a capillary. For electrokinetically-driven flow, the fluid flows were generated by applying an electric field to induce electroosmotic flow (EOF). To generate an anodal EOF, the channel surface was

modified with a cationic coating. A detailed description of the steps involved in channel modification will be presented in Section 3.2.3.

For solid-phase extraction studies with LIF detection, BODIPY was used as the low molecular weight probe and FITC-BSA was used as a protein probe. Stock probe solution was diluted to the desired concentrations in loading buffer (10 mM NH₄Ac, pH 8.0). After equilibrating the channel and bed with the loading buffer, sample was loaded onto the monolithic bed by applying pressure or voltage for a certain time. Following a buffer flush step, elution buffer was placed in the reservoir to release samples adsorbed on the bed. The fluorescence detector was positioned downstream of the monolithic bed. The total capacity of the SPE bed was estimated from the breakthrough curve by continuously pumping probe solution through the monolithic bed. Fluorescence signal was monitored before and after the monolithic bed in separate runs.

2.3 Results and Discussion

2.3.1 Control of Surface Chemistries

Monoliths with a variety of surface functionalities can be readily prepared because of the versatility of monomers. In our work, hydrophobic monoliths were prepared using butyl methacrylate (BMA) as the functional monomer to enable solid-phase extraction in the hydrophobic mode. To facilitate the applications of monoliths in an electrokinetically pumped system, an ionizable monomer, [2-(methacryloyloxy)ethyl]trimethylammonium chloride (META), was added into the starting mixture as a co-monomer to provide the monoliths with positively-

charged functionalities. All the monoliths prepared in this work were cross-linked with a divinyl monomer, ethylene glycol dimethacrylate (EDMA), which provides the material with high mechanical strength and contributes to the formation of the porous structure.

2.3.2 Control of Porous Properties

Porous properties are also very important in all applications of polymer monoliths. Because mobile phase must flow through the monoliths, the first concern is permeability of the monolith to liquids, which depends completely on the size of their pores. A monolith with very small pores would likely be damaged by the extremely high pressures required for flow. Low flow resistance can be achieved with large-pore materials. However, many applications such as SPE also require a large surface area in order to achieve a high loading capacity. This large surface area is generally a feature of porous materials with small pores. Therefore, the overall porous properties of the monolith must be carefully tailored in order to find a balance between the contradictory requirements of low flow resistance and high capacity.

The porous properties of the monoliths can be controlled by many variables, including composition of the porogenic solvent, porogen-to-monomer ratio, initiator type, cross-linker concentration, reaction time, and radiation power. Here we explored a broad range of polymerization conditions in order to design suitable monolithic materials for our applications. All the polymerization conditions are listed in Table 2.1.

Table 2.1 The compositions of polymerization mixtures and reaction conditions for the preparation of monolithic polymer beds

No.	BMA (g)	EDMA (g)	Charged monomer(g)	Initiator (mg)	Porogenic solvents (g)	Exposure time	Polymer property
1	0.36	0.24		AIBN: 6	Methanol: 1.26 Hexane: 0.54	3 h	Non-uniform
2	0.36	0.24		AIBN: 6	Methanol: 0.45 Hexane: 0.45	3 h	Im-permeable
3	0.36	0.24		Benzoin: 6	Methanol: 0.9	8 min	Bad edges
4	0.36	0.24		Benzoin: 6	Octanol: 0.6	8 min	High resistance
5	0.36	0.24		Benzoin: 6	Octanol: 0.9	8 min	Good
6	0.36	0.24		Benzoin: 6	Octanol: 1.2	8 min	Sparse structure
7	0.36	0.24		Benzoin: 6	Octanol: 1.8	8 min	Collapse
8	0.36	0.24		Benzoin: 6	Octanol: 2.4	8 min	No reaction
9	0.36	0.24		DMPAP: 6	Octanol: 0.9	8 min	Bad edges
10	0.36	0.24		DMABP: 6	Octanol: 0.9	8 min	Bad edges
11	0.36	0.24		Benzoin: 6	Decanol: 0.9	8 min	High resistance
12	0.36	0.24		Benzoin: 6	1-Propanol: 0.63 1,4-Butandiol:0.27	8 min	Bad edges
13	0.36	0.24		Benzoin: 6	1-Propanol: 0.63 1,4-Butandiol:0.18 H ₂ O: 0.09	8 min	Bad edges
14	0.36	0.24	*META/ H ₂ O: 0.09	Benzoin: 6	Octanol: 0.81	8 min	Im-permeable
15	0.36	0.24	META/ H ₂ O: 0.09	Benzoin: 6	Octanol: 0.36 Toluene: 0.45	8 min	No reaction
16	0.36	0.24	META/ H ₂ O: 0.09	Benzoin: 6	Octanol: 0.63 Toluene: 0.18	8 min	No reaction
17	0.36	0.24	META/ H ₂ O: 0.09	Benzoin: 6	1-Propanol: 0.54 1,4-Butandiol:0.27	8 min	Bad edges
18	0.36	0.24	META/ H ₂ O: 0.09	Benzoin: 6	1-Propanol: 0.54 1,4-Butandiol:0.27	4 min	Good
19	0.36	0.24	META/ H ₂ O: 0.12	Benzoin: 6	1-Propanol: 0.54 1,4-Butandiol:0.27	4 min	High Resistance
20	0.36	0.24	META/ H ₂ O: 0.18	Benzoin: 6	1-Propanol: 0.54 1,4-Butandiol:0.27	4 min	High resistance
21	0.36	0.24	META/ H ₂ O: 0.09	Benzoin: 6	1-Propanol: 0.63 1,4-Butandiol:0.18	4 min	higher Resistance than #18
22	0.36	0.24	META/ H ₂ O: 0.09	Benzoin: 6	1-Propanol: 0.72 1,4-Butandiol:0.09	4 min	Im-permeable
22	0.36	0.24	META/ H ₂ O: 0.09	Benzoin: 6	1-Propanol: 0.45 1,4-Butandiol:0.36	4 min	Bad edges

* META/H₂O: solution of 0.2 g META (75% solution in water) in 1.8 g H₂O

2.3.2.1 Porogenic Solvent System

Among the variables to adjust the porous properties, porogenic solvent is the most effective. Many reported porogenic solvent systems were used to prepare polymer monoliths with large pores. A highly porous monolith with a pore size of 19.5 μm was prepared by Yu *et al.* [14] using methanol and hexane together as the porogen. This large pore size provides a monolith with low flow resistance, allowing the use of high flow rates without mechanical damage. This monolith was used as a starting point for our studies; the monolith was prepared in a 50- μm -i.d. capillary (#1 in Table 2.1). The SEM image in Figure 2.4a shows that the monolith formed has a deformed structure: the interconnected globules aggregated to form a thick coating layer on the surface with a big through-pore in the center. Similar structural deformation of monoliths in confined space has been reported previously [18, 19].

Pure methanol is another porogenic system that has been used widely for the preparation of large-pore materials. The use of methanol results in a more uniform monolith with large globules and large throughpores (Figure 2.4b). However, this monolith grew across the interface defined by the exposure window, leading to bad edge resolution (Figure 2.5a). The growth of the polymer beyond the bed region into the narrow channel in our microfluidic device will increase the flow resistance significantly, or even worse, plug the channel. The bad edge of the monolith may be attributed to the diffusion of free radicals into the non-irradiation region [20].

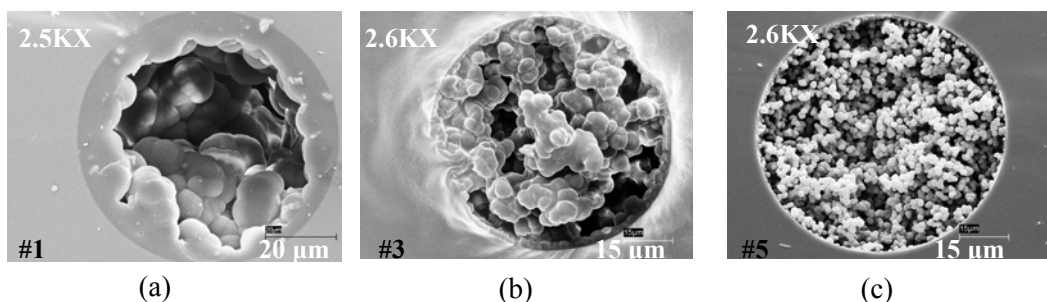


Figure 2.4 SEM images of monoliths prepared with different porogenic solvents, (a) methanol and hexane, (b) methanol, (c) octanol, corresponding to polymer #1, #3 and #5 in Table 2.1, respectively.

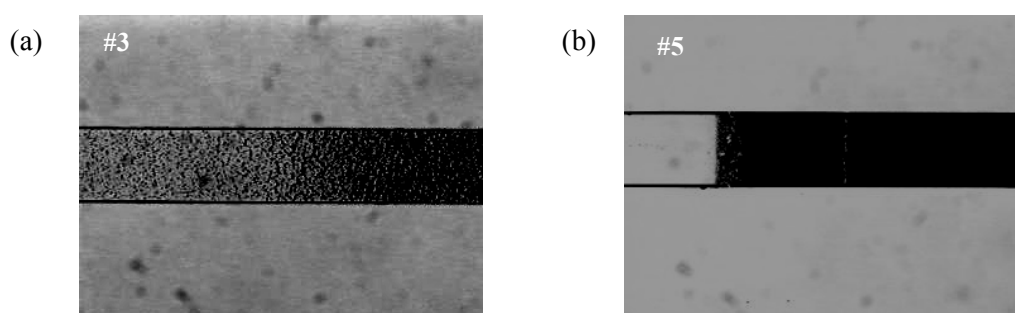


Figure 2.5 Effect of porogenic solvent on edge resolution. Top views of the edges of the monoliths prepared with methanol (a), octanol (b), corresponding to polymer #3 and #5 in Table 2.1.

In contrast to using methanol, edges can always be sharply defined when octanol is used as porogenic solvent (Figure 2.5b). This bed edge difference might be related to the viscosity of the solvent. Octanol has much higher viscosity (7.21 cP) compared to methanol (0.544 cp), thus the dissolved free radicals will have a smaller diffusion coefficient in octanol. The diffusion distance of free radicals in methanol over the exposure time is estimated to be ~ 4 times that in octanol. The monolith prepared with octanol has uniform porous structure, as is shown in the SEM micrograph in Figure 2.4c. Compared to the monolith prepared with methanol (Figure 2.4b), the morphology of this monolith is characterized by small microglobules and small voids (pores) between them.

Given the small pore size, the permeability of this octanol-produced monolith was tested using a syringe pump to generate flow at various flow rates. Within a flow rate range of 0.05–3 $\mu\text{L}/\text{min}$, solution can be pumped through the polymer bed without causing mechanical breakage of the monolithic material. With higher flow rate, the monolith starts to break at the edges, forming small pieces, or it is compressed to form voids deep within the bed.

Many other porogenic systems were tested in an effort to produce a monolith with larger pores (#11, #12, #13 in Table 2.1). All these recipes afford porous monoliths with relative small pore size, and polymers #12 and #13 have ill-defined edges.

Besides the type of porogenic solvent, the porogen ratio in the mixture also plays an important role in controlling the porous properties. The pore-producing solvents do not react during polymerization and remain trapped within the monolithic structure. Once the polymerization is completed, the volume originally occupied by the solvents represents the pore volume. In theory, high porosity can be obtained by simply increasing the percentage of the solvents in the mixture.

Various porogen-to-monomer ratios were tested in an attempt to obtain a larger pore size. Monoliths were prepared according to #4, 5, 6, 7, and 8 in Table 2.1, which used octanol as porogen at various porogen ratios (50 wt% - 80 wt%). With a solvent content in the range of 50 wt% - 75 wt%, all the polymers prepared have uniform structures, as shown in Figure 2.6. The monolith prepared with a solvent content of 60 wt% gave desirable flow resistance and permeability to liquids. A flow rate of 3 $\mu\text{L}/\text{min}$, corresponding to a linear flow velocity of 24 mm/s, was

achieved with no mechanical damage to the monolith. Further increase in the solvent ratio (67 and 75 wt%) led to the formation of monoliths with sparse structures and reduced mechanical strength. With 80 wt% solvent in the mixture, there is no observed polymerization reaction. So the optimal porogen ratio in the polymerization mixture for this BMA-based neutral monolith is 60 wt%.

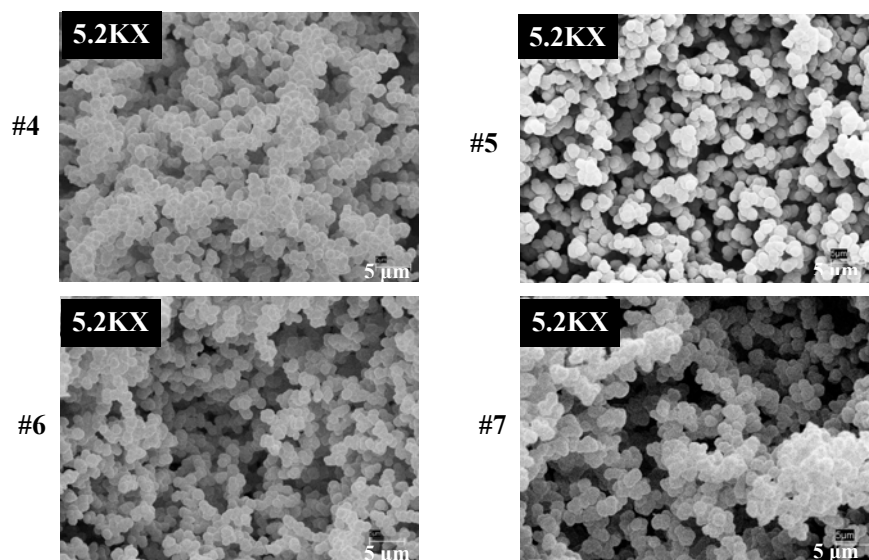


Figure 2.6 SEM images of monoliths prepared with porogen ratio of 50%, 60%, 67%, and 75%, corresponding to polymer #4, #5, #6, and #7 in Table 2.1, respectively.

2.3.2.2 Initiator Type

Four photo-initiators, AIBN, benzoin, DMPAP, and DMABP were used to investigate the effect of initiator on the polymerization reaction. AIBN is a good thermal initiator by thermal decomposition. Although it can also be used as photo-initiator, the polymerization process is slow, typically requiring several hours for the reaction to complete (#1 and #2 in Table 2.1). This longer reaction time will lead to heating and, consequently, to thermal polymerization in the unexposed region. The other three initiators are all good photo-initiators, and monoliths

initiated with these three initiators have uniform porous structures, as shown in Figure 2.7. However, obvious differences have been observed in their edge resolution. Benzoin-initiated monolith has sharp and well-defined edges. The monoliths prepared with DMPAP and DMABP grew beyond the irradiation region, resulting in diffused edges.

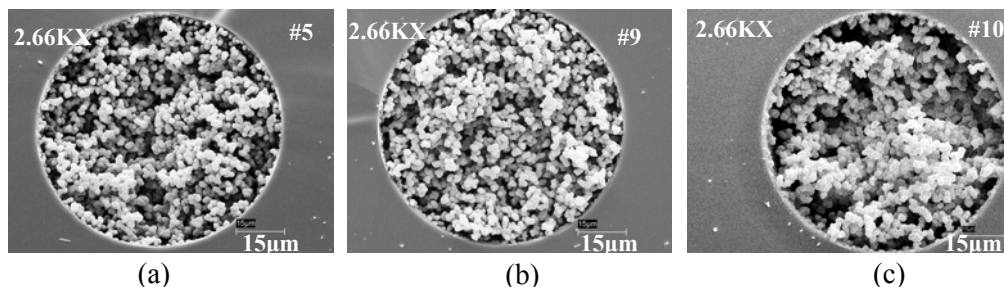


Figure 2.7 SEM images of monoliths prepared with different initiators, (a) benzoin, (b) DMPAP, (c) DMABP, corresponding to polymer #5, #9 and #10 in Table 2.1.

2.3.2.3 Effect of Exposure Time on Polymer Structure

Polymerization mixture #5 in Table 2.1 was used to study the effect of exposure time on the polymer structure. No polymer was observed within a microchannel with a reaction time of less than 4 min, at which point a white solid monolith started to appear. Exposure times of 4 min and 6 min resulted in monoliths with sparse structures (Figure 2.8a and b), which are fragile and application of pressure can lead to collapse. A longer reaction time gave a much denser structure, as shown in Figure 2.8c and d. No significant difference in porous structures was observed under a microscope for a reaction time longer than 8 min, indicating the conversion of monomer reaches a plateau after a certain exposure time. However, longer exposure times resulted in deterioration in the edge resolution (Figure 2.8d). A possible explanation for this is free-radical

polymerization is an exothermic process. With longer reaction time, the heat generated will accumulate and dissipate to the solution adjacent to the irradiation region, leading to heat induced polymerization at the interface. Therefore, 8 min was taken as the optimal UV exposure time for this neutral monolith, and was used for the following experiments.

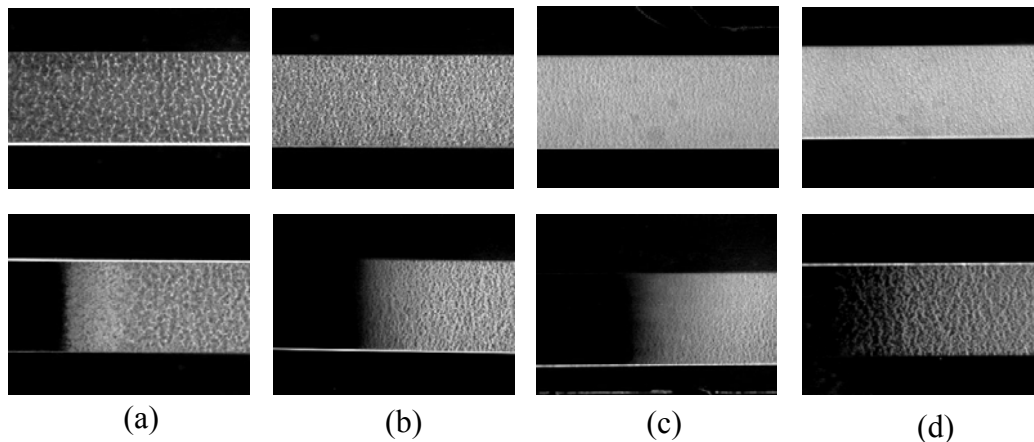


Figure 2.8 Microscopic images showing the polymer structures (top) and edges (bottom) of the monoliths prepared with different exposure times using #5 in Table 2.1. (a) 4 min, (b) 6 min, (c) 8 min, (d) 10 min.

2.3.2.4 Optimized Monolith Recipes and Pore Size Measurement

When new monolith recipes are developed, several factors are taken into account as optimization criteria. The monolith must have uniform structure and reproducible properties; the porosity should be high enough to make the monoliths permeable under reasonable pressure; the polymer edge must be sharp and well defined as a diffused edge tends to break and form small fragments.

After an extensive study of polymerization conditions, octanol has proved to be a good porogen for the preparation of a BMA-based neutral hydrophobic monolith that met the above requirements (#5 in Table 2.1). The addition of new monomer may affect the phase-separation process and require re-optimization of

polymerization conditions. Similar optimization studies were thus conducted for the preparation of positively-charged monoliths through the addition of META. Using pure octanol as a porogen leads to a monolith with very dense structure and high flow resistance. After testing a variety of porogenic solvents, the binary porogenic system 1-propanol/1,4-butanediol proved to be well suited for the preparation of the positively-charged monolith containing META in terms of porous properties and edge resolution. Various parameters, including the concentration of the META monomer, the ratio 1-propanol to 1,4-butanediol and reaction time were studied in order to optimize the composition of the monolithic columns (#14–#23 in Table 2.1).

The SEM images in Figure 2.9 show the effect of META concentration on the porosity, in which the monoliths were prepared with 0.45%, 0.6%, and 0.9% META (percentage of META in the polymerization mixture), corresponding to #18, 19, 20 in Table 2.1. The increase in META concentration in the mixture resulted in a significant decrease in pore size. This is consistent with the results reported in the literature [21]. It is likely the high polarity of META may have an effect on the phase separation process and consequently on the pore formation.

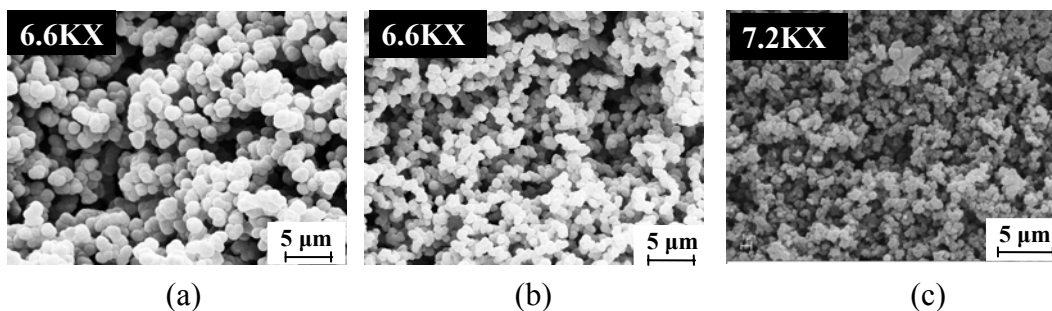


Figure 2.9 SEM images of monoliths prepared with different META concentrations, (a) 0.45%, (b) 0.6%, and (c) 0.9%, corresponding to polymer #18, #19 and #20 in Table 2.1.

The optimized recipes for these two monoliths (neutral and positively-charged) are listed in Table 2.1 as #5 and #18. These monolith precursor solutions were found to produce monoliths with uniform pore structures, sharply defined edges, and reproducible properties. Figure 2.10a shows the top views of the monolithic polymers prepared in a 1- mm-long bed. Figure 2.10b shows the SEM micrographs of the cross-sections of microchannels containing photopatterned monoliths. The characteristic shape of the glass channel is due to isotropic etching. The polymer monoliths are cast uniformly over the cross section of the channel with no gap between the polymer and the channel wall. SEM images with higher magnification in Figure 2.10c show the uniform distribution of polymer microglobules and pores.

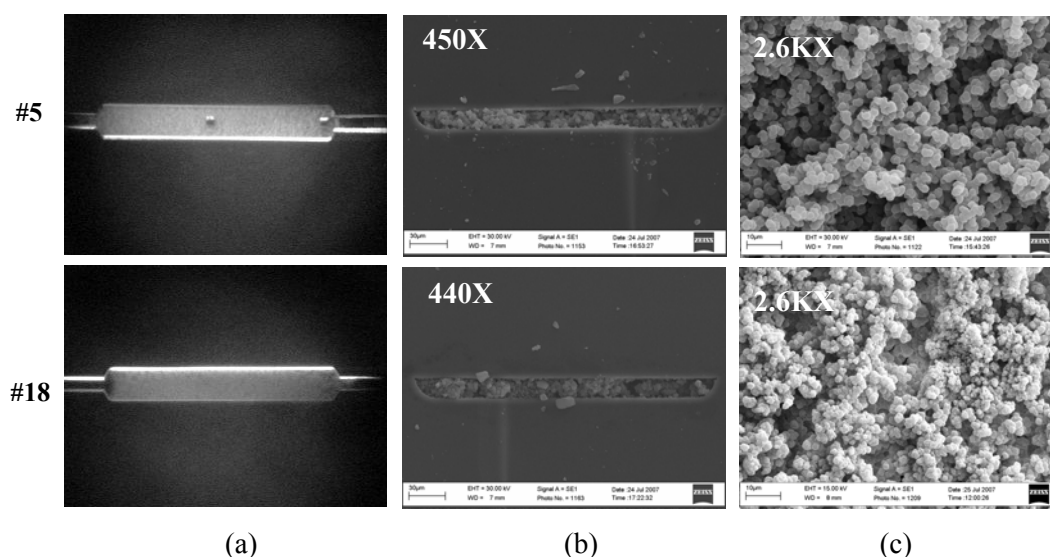


Figure 2.10 (a) Optical micrographs of the monolithic polymers prepared in beds; (b) SEM images of the cross-section of the monoliths; (c) Higher magnification SEM images showing the details of nodules and pores for polymer #5 and #18 in Table 2.1.

The pore size of bulk neutral monolith was measured using mercury intrusion porosimetry and Figure 2.11 shows the pore size distribution profile. The average

pore size of the bulk material is 950 nm, and the porosity is 62.4%. It is worth noting these values were determined using monoliths in the dry state while the monoliths are typically used in a solvated state, and hence, the porous properties of the wet polymer may be different. In addition, the small amount of monoliths in a microchannel made it very difficult to measure the porous properties of the monoliths produced in the channel. Instead, the polymers were prepared in glass vials in order to obtain the sample size required for mercury intrusion porosimeter (~0.5 g). The difference between large scale and small scale reactions could also result in difference in pore structures [18, 22].

Although these two monoliths have relative small pore size, they exhibit sufficient permeability and mechanical stability, allowing transport of liquid through the monoliths at reasonable operational pressures generated by a syringe pump. A flow rate of up to 3 $\mu\text{L}/\text{min}$ can be achieved without damaging the monoliths.

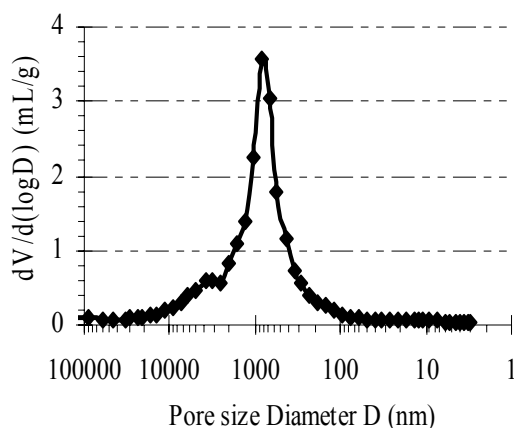


Figure 2.11 Pore size distribution of bulk neutral monolith (#5 in Table 2.1).

2.3.3 Effect of Chip Design on the Monolithic Polymer

2.3.3.1 Exposure Window Size

A transparency mask, produced by a high resolution laser printer, was used to define the exposure window. Two transparency masks with different window sizes were printed and tested. Figure 2.12 shows the schematic of the exposure window aligned with the bed. On mask A, the exposure window size has the same dimension as the final fabricated bed (140 μm wide and 1 mm long). On mask B, the window is widened from 140 μm to 4 mm while the length is kept constant.

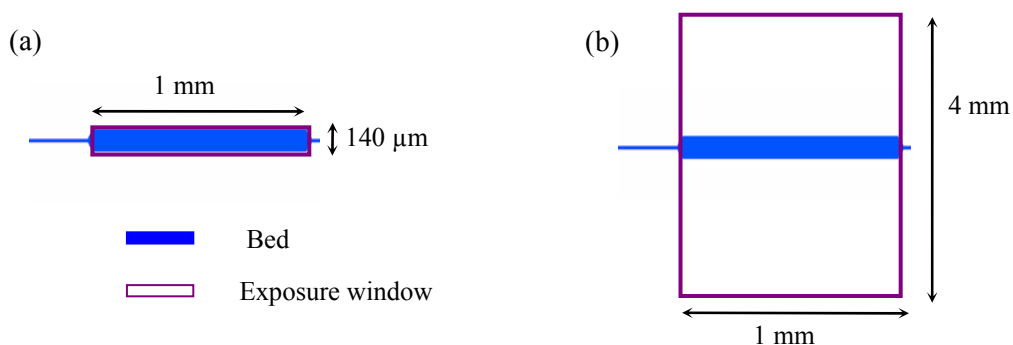


Figure 2.12 Schematic illustrating the exposure window aligned with the fabricated bed. (a) Transparency mask A; (b) Transparency mask B.

With Mask A, a longer exposure time is required to initiate the polymerization reaction, possibly owing to the poor collimation of the transilluminator. With a much wider window in mask B, monolithic polymer filled up the entire bed within 8 min for the neutral monolith. However, with a 1-mm long window for a 1-mm bed, there is a great chance the monolith will form in the narrow channel if the alignment between the chip and the transparency mask is not absolutely perfect. In our later experiments, an exposure window with a length slightly shorter than the length of the bed was used for UV exposure for easy alignment (e.g., a 1.5-mm window for a 2-mm bed).

2.3.3.2 Bed Dimensions and Beds with Posts

Covalent attachment of monoliths to the channel wall cannot be achieved in our system since we need to modify the channel with a cationic coating to reverse the EOF, as will be described in Chapter 3. To retain the monolith in the desired place, an enlarged bed was designed in the microchannel. The bed structure includes gradually tapering inlet and outlet geometries with 100 μm and 16 μm wide at its wide and narrow end, connecting the bed with the narrow channel. To investigate the effect of bed dimensions on the reaction, beds with length from 80 to 1000 μm were designed in the mask. In an effort to help retain the monolith in the bed region, we designed a square post at the outlet of the bed in several devices. The design of post accounted for the isotropic etching characteristic of glass wet etching. The post is designed to be 30 $\mu\text{m} \times 30 \mu\text{m}$ in the etched device, so in the mask it should be 70 $\mu\text{m} \times 70 \mu\text{m}$. Several post-mask designs were made to test the effect of post location. The designs and the expected etched results are shown in Figure 2.13, while the actual etched products are shown in Figure 2.14.

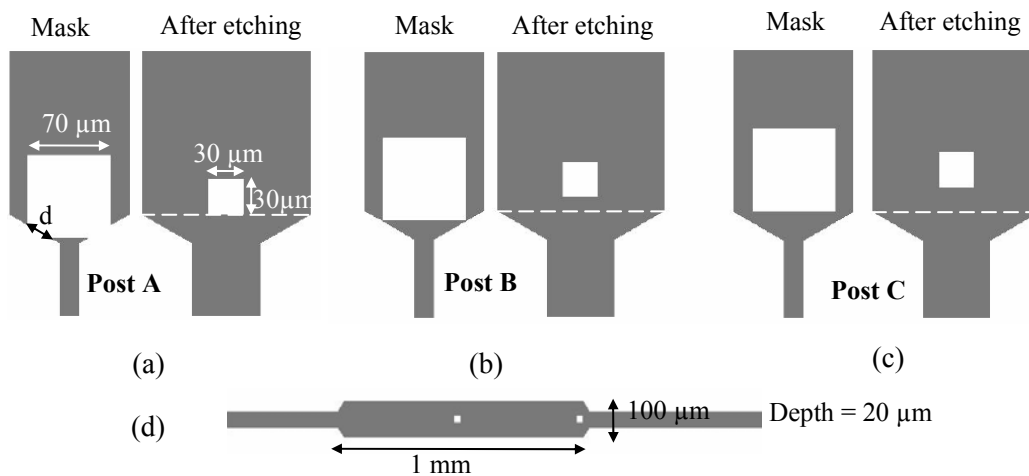


Figure 2.13 Schematic of the design and expected etched results for devices with post (a) Design A; (b) Design B; (c) Design C; (d) The mask layout of a bed with posts.

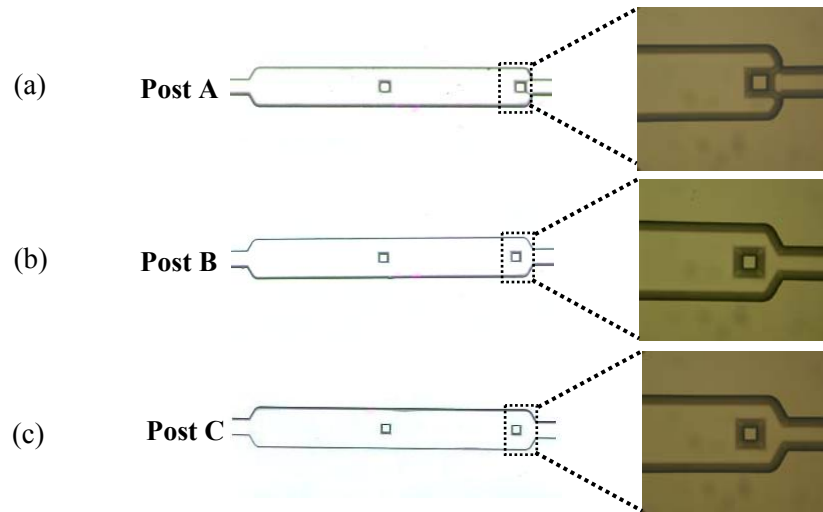


Figure 2.14 Microscopic images of the fabricated beds with posts at the outlet and the enlarged views of the post region, (a) Design A; (b) Design B; (c) Design C.

The fabrication of posts with these three designs was successful; the posts are all uniform squares. For Design A, the channel at the junction looks darker because it is shallower than other places, due to the isotropic etching.

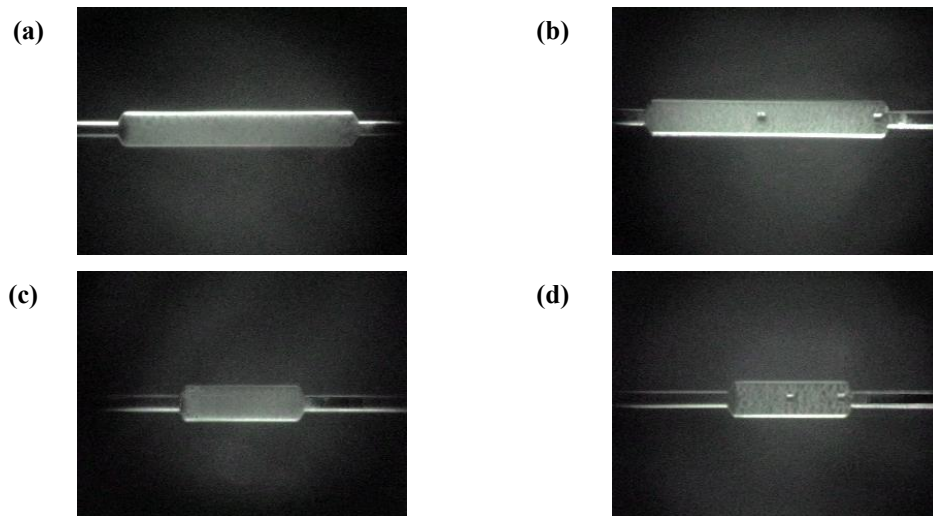


Figure 2.15 Optical micrographs of the monolithic polymers prepared in beds; (a) 1- mm-long bed without posts; (b) 1-mm-long bed with posts; (c) 0.5-mm-long bed without posts; (d) 0.5-mm-long bed with posts.

Neutral monoliths were prepared in these beds according to the optimized #5 in Table 2.1. The monolith formed easily in 500- μm and 1-mm-long beds (Figure 2.15), while there is no monolith observed in beds with a length of 200 μm or less.

In our work, the UV light exposure region is defined by a transparency mask, this method works well for preparation of relatively large monoliths. However, there are some challenges if we try to decrease the monolith size in smaller microchannels or reduce the bed length. The theoretical resolution of a monolithic polymer bed is limited optically as follows [23]:

$$2b_{\min} = 3\sqrt{\lambda(s + z/2)}$$

where $2b_{\min}$ is the resolution limit, λ is the illuminating wavelength, s is the distance between mask and the polymer surface, and z is polymer thickness. For photopatterning of monolith in our chip, λ is 312 nm, s is 600 μm , which is the thickness of the glass wafer and z is the depth of the channel, 20 μm . This leads to a theoretical resolution limit of 40 μm . We observed a practical resolution limit of ~ 200 μm , indicating there are other factors that limit the ability to pattern a monolith below 200 μm . One of these factors could be that the UV light from the transilluminator is not well collimated, and the light passing through the short exposure window (≤ 200 μm) may not be intense enough to generate efficient monomer conversion. To evaluate this, a polymerization reaction was done using better collimated UV light from a mask aligner. Polymer did form within a 200- μm -long bed, although the monolith formed has a sparse structure. No polymer was observed in an even shorter bed. The use of an intense UV laser may confer

higher resolution in photodefinition of smaller size monolith, but this was not tested.

2.3.4 Evaluation of SPE Performance

2.3.4.1 On-Chip SPE of BODIPY

BODIPY is a non-polar dye showing a high affinity to the BMA-based monolith in an aqueous environment and is an excellent fluorophore. Thus it was chosen as the starting analyte to investigate the SPE performance of the monolithic column.

To determine the total capacity of the SPE bed, breakthrough curves were obtained by continuously delivering 1 μM BODIPY solution through the neutral hydrophobic monolithic bed at a flow rate of 2 $\mu\text{L}/\text{min}$ using a syringe pump. The fluorescence of BODIPY was recorded downstream of the bed to obtain a breakthrough curve (Figure 2.16, curve 2). In order to correct the time needed for the analyte to reach the bed, fluorescent signal was also monitored at the inlet of

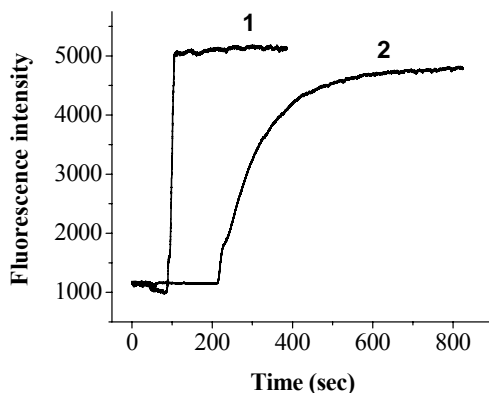


Figure 2.16 Capacity determination for the neutral hydrophobic monolith from breakthrough curve. Conditions: probe solution: 1 μM BODIPY in 10 mM NH_4Ac , flow rate: 2 $\mu\text{L}/\text{min}$. Fluorescence intensity was measured at the inlet (1) and outlet (2) of the monolithic bed. The monolith was prepared according to #5 in Table 2.1.

the bed (Figure 2.16, curve 1). The breakthrough time is taken as time needed for signal downstream of the bed to reach 50% of its maximum, less the time required for the dye to reach the inlet of bed.

The overall capacity of the hydrophobic column as calculated from the breakthrough curve is 7.6 pmol, representing a specific capacity of 2.9 mmols per liter of monolithic bed volume. This calculated capacity is comparable to values reported for monoliths in the literature [14, 24, 25]. The relative standard deviation (RSD) of sample capacities calculated from 5 different monolithic SPE beds was 6.8%, indicating the relatively reproducible SPE properties of these monoliths.

Compared to other SPE materials, the monolithic column gives loading capacity 5 orders of magnitude larger than that reported for a C18 coated open-tubular SPE microchip device [11], which is clearly due to the much higher surface area. However, the adsorption capacity of the monolithic column is comparable to a C18 particle packed column [13], even though the surface area is typically smaller than porous particle packed columns. One possible explanation is the accessible surface area of the monolithic column was larger than that of the packed column, most likely due to the differences in the structure of the pore network. However, the extraction capacity of an SPE system depends on a number of factors including the nature of the probe, and surface chemistry of SPE phase. As each measurement used a different probe and a different SPE phase, the comparisons to the literature are not exact.

To evaluate the SPE behavior of the monolithic bed under electrokinetic flow, adsorption and elution of BODIPY were performed on a device modified with a cationic coating PolyE-323 and positively-charged monolith containing META (#18 in Table 2.1) was used in order to be compatible with the coated channel. A discussion of the PolyE-323 coating including the coating procedure, properties and performance will be presented in Chapter 3.

The experimental procedure is as follows. First, diluted BODIPY sample was placed in the sample reservoir and negative voltage was applied on this reservoir with the other reservoir grounded. The EOF was directed toward the grounded reservoir, carrying BODIPY sample onto the SPE bed. Second, aqueous buffer was flushed through the channel for 1 min to wash sample remaining within the channel onto the bed. Finally, the concentrated BODIPY sample was eluted using buffer at high organic content (10 mM NH₄Ac with 60% ACN) with the same voltage as during sample loading.

Two sets of experiments with different sample loading times and various sample concentrations were performed to investigate the quantitative performance of this SPE bed. A 0.5 nM BODIPY solution was concentrated for varying preconcentration times, the elution traces were monitored downstream of the bed (Figure 2.17a). Figure 2.17b shows a plot of the integrated peak areas of the eluted sample versus sample loading times, which gives a linear relationship ($R^2 = 0.9965$).

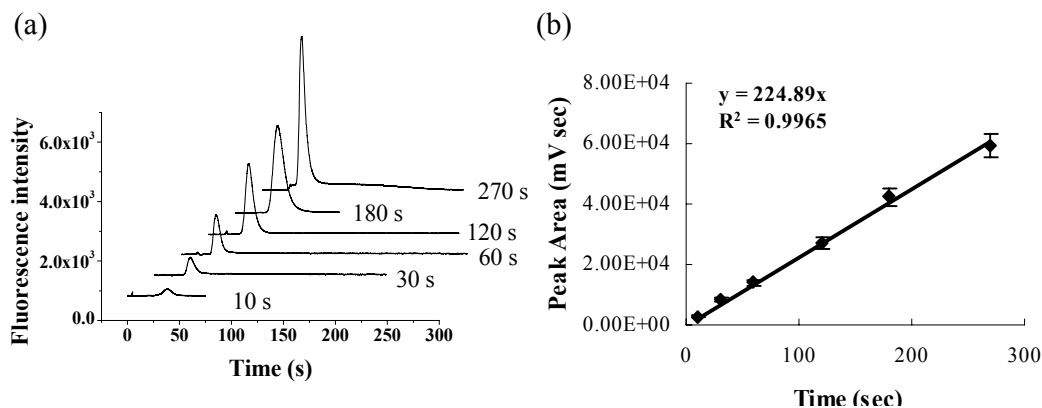


Figure 2.17 (a) Solid phase extraction with increasing sample loading times for BODIPY. Each trace is an individual run labeled with the loading time. Traces are offset by 60% in the y axis and 40% in the x axis. (b) Variation of peak areas with enrichment times. Sample loading: 2.0 kV with 10 mM NH₄Ac (pH 8.0), elution: 2.0 kV with 60% ACN/10 mM NH₄Ac. Concentration of BODIPY is 0.5 nM. The microchannel was modified with PolyE-323 cationic coating. The positively-charged monolith was prepared according to #18 in Table 2.1.

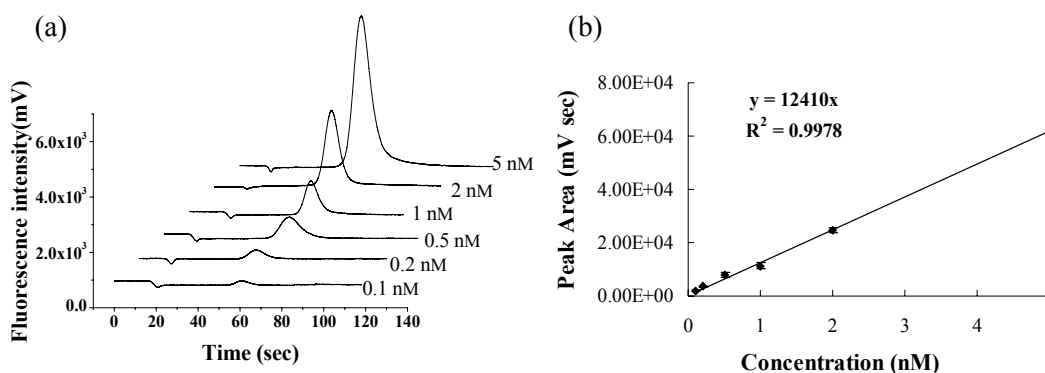


Figure 2.18 (a) Elution profiles with various BODIPY concentrations at fixed preconcentration time. (b) The calibration curve between the resulting peak areas versus sample concentrations. The preconcentration time is 30 s. The other conditions were the same as those in Figure 2.17.

In experiments using different concentrations of sample, peak areas plotted versus sample concentrations also yielded a linear response across a concentration range of 0.1-5 nM (Figure 2.18). For a 30 s preconcentration time, a concentration detection limit (CLOD, S/N =3) was estimated to be 4 pM by linear extrapolation of the data in Figure 2.18, compared to a CLOD of 50 pM for BODIPY without preconcentration.

In these experiments, no noticeable sample breakthrough was observed during sample loading. The linear relationship also indicated that we were far below the breakthrough volume of the bed under these conditions. The SPE experimental results also showed reproducible extraction and elution of the analyte (the RSD of integrated peak area of eluted BODIPY were 3.8-5.5%, $n = 4$).

Figure 2.19 shows a preconcentration experiment using a dilute 20 pM BODIPY solution. Trace 1 shows the detection signal for a 30 min BODIPY loading with the PMT located before the polymer bed. A slight increase of fluorescence signal resulting from the sample entering the detector region can be seen at point a. Trace 2 shows the elution peak following the 30 min preconcentration.

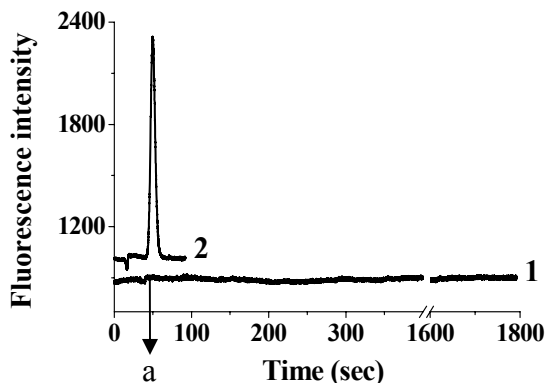


Figure 2.19 Fluorescence intensity profiles during sample loading and elution. Trace 1 represents sample loading of 20 pM BODIPY in 10 mM NH_4Ac . Trace 2 represents the elution of the preconcentrated analyte using 10 mM $\text{NH}_4\text{Ac}/60\%$ ACN. Both loading and elution were performed by applying 1.0 kV. Two trace are offset by 5% in the y axis. The microchannel was modified with PolyE-323 cationic coating. The positively-charged monolith was prepared according to #18 in Table 2.1.

The preconcentration factor can be calculated by dividing the volume of the sample solution flowing through the monolith in the loading step by the volume of the eluted peak, which is product of the peak width in time and the flow rate. For

the elution peak in Figure 2.19, the estimated concentration factor is ~ 105 . Further increasing the preconcentration time would enhance the signal and give higher concentration enhancement.

2.3.4.2 Protein Adsorption onto the Monolithic Bed

Although the fluorescent dye BODIPY is a good probe to evaluate the SPE behavior of the monolithic bed, practical applications of such SPE beds are likely to involve quite different compounds. Our goal is a microfluidic system for protein analysis, which requires an element allowing capture of proteins from its dilute solution, followed by enzymatic digestion of the adsorbed proteins. Therefore, the concentrating ability of the hydrophobic monolith for proteins was tested using a common protein, FITC-BSA. A highly concentrated BSA solution

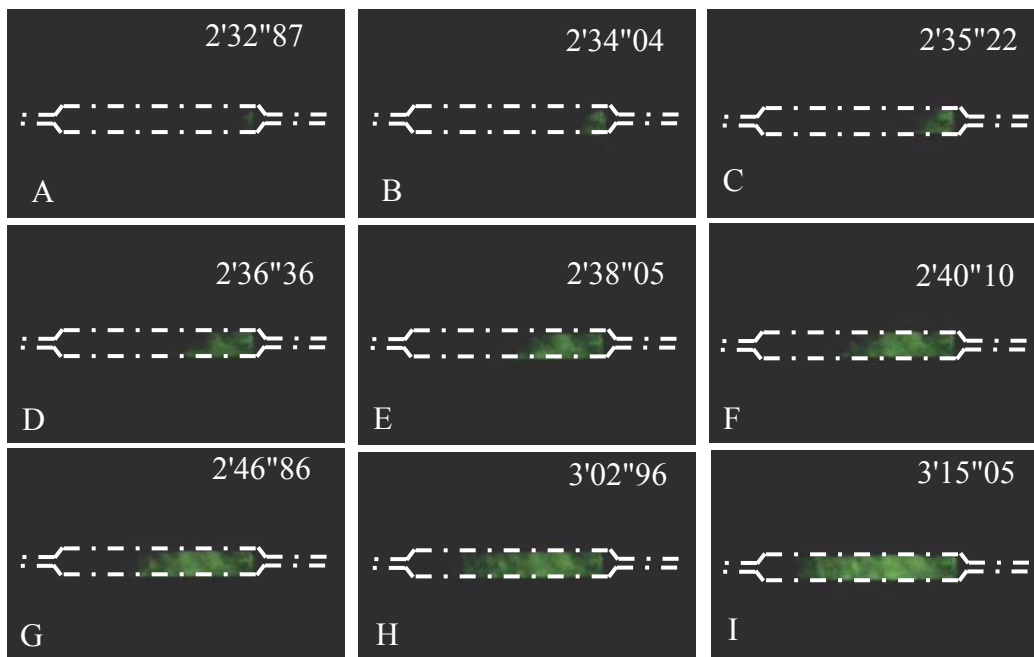


Figure 2.20 Frames extracted from a video illustrating the dynamic protein adsorption process onto a monolithic bed over 1 min sample loading. The channel and bed are outlined with white line for clarity. The microchannel was coated with PolyE-323. The monolith is positively-charged containing META.

(1 mg/mL) was driven to the monolithic polymer bed and adsorbed, and the adsorption process was recorded with a CCD camera. Figure 2.20 presents a series of extracted frames from a video illustrating the dynamic protein adsorption process onto the monolith. The laser spot was expanded to cover the entire bed region. The monolith emitted strong fluorescence as the protein was adsorbed on it.

2.3.4.3 Effect of Eluent Composition

An important issue in any reusable microfluidic device is the sample carryover from a previous experiment; therefore, particular attention was paid to the completeness of the elution. The effect of eluent composition on elution was explored; FITC-BSA solution was electrokinetically transported through the monolith, and release of the probe from the monolithic bed was monitored by measuring the fluorescence intensity. The eluents were prepared by mixing acetonitrile (ACN) with the NH_4Ac buffer in different proportions. The volume ratio of ACN is varied while the concentration of NH_4Ac is kept constant at 10 mM. Figure 2.21a shows the elution traces with different ACN concentrations. After that, a stronger eluent with 80% ACN is used to further release the remaining adsorbed probe, as shown in Figure 2.21b.

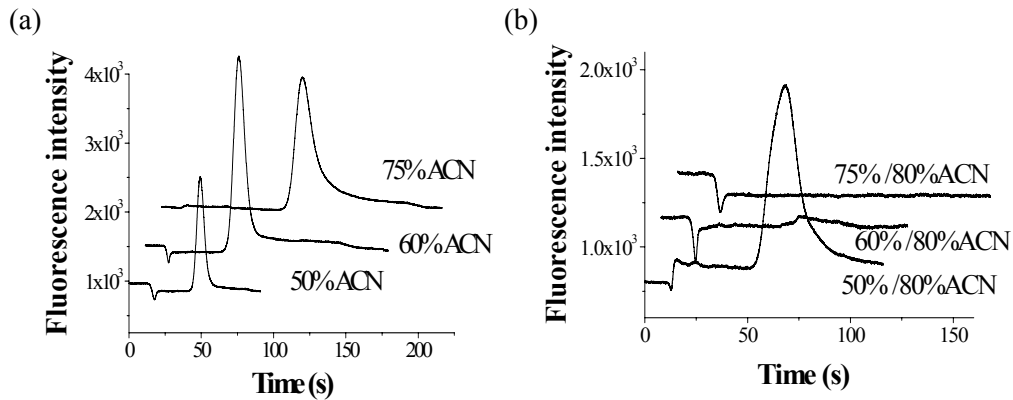


Figure 2.21 Effect of eluent composition on elution. (a) Elution traces with eluents containing different ACN concentrations (25% -75%); (b) Further elution with a stronger eluent containing 80% ACN. Protein loading: 0.01 mg/ml FITC-BSA in 10 mM NH_4Ac buffer; elution: 10 mM NH_4Ac /25%-80% ACN. The microchannel was modified with PolyE-323 cationic coating. The positively-charged monolith was prepared according to #18 in Table 2.1.

Figure 2.21b shows that eluent containing 25% ACN is not sufficient to completely elute the adsorbed protein. For a bed eluted with 60% ACN, a further elution with 80% ACN displays a very small peak. The residual protein was estimated from the intensity to be less than 3% of the total loaded protein sample. A second elution with 80% ACN eluent after 75% ACN did not exhibit fluorescence that could be detected. Also, no detectable residual fluorescence for the monolith itself after elution with 75% ACN provided further proof on the absence of remaining probe on the beds. However, the current dropped dramatically after introducing 75% ACN eluent into the channel, due to the decrease in conductivity. In addition, a higher ratio of ACN gives a higher tendency to deteriorate the cationic coating. Therefore, eluent containing 60% ACN was used in subsequent experiments. To eliminate sample carryover from run to run, a pulse of 75% ACN eluent was used after each experiment to remove residual sample.

2.3.4.4 Durability of the Monoliths and Recovery of Glass Chips

The durability of the monolith is another important characteristic in evaluating an SPE column. To test the long-term stability of the concentrators, a large number of measurements described above were carried out using a single microfluidic chip containing the monolithic polymer, and then the SPE bed was again inspected with optical microscopy. Figure 2.22 shows the comparison of images of the polymer beds before and after running experiments for several days. No obvious voids or collapse are formed in the monolith, demonstrating the durability of the monolithic bed.

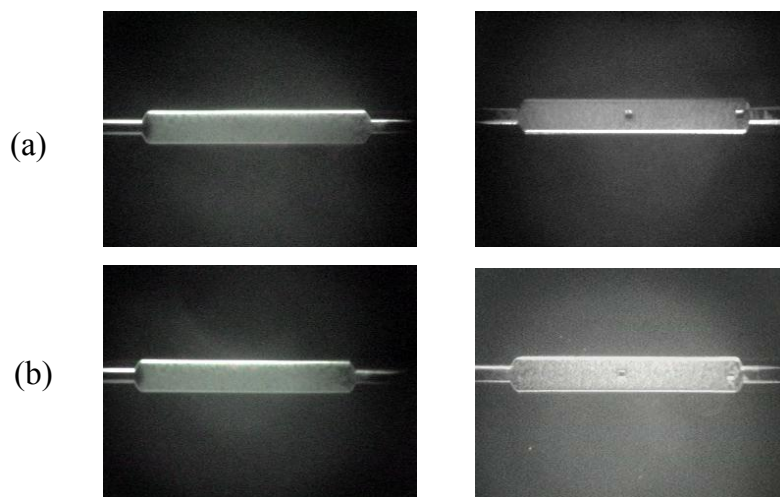


Figure 2.22 Durability of monoliths. Images of monolithic beds (a) before running experiments and (b) after several days of use.

Experiments were also performed on devices with and without posts in the bed. The results showed that flows driven by pressure or EOF will not dislodge the monolithic polymers in either case. Even in a device without the post design, the monolithic polymer is retained well in the bed region. One explanation is the monolith formed acts as a single entity and is unlikely to be dislodged from the bed region due to the restriction of the narrow channels. Given the possibility that

these posts will distort the fluid flow and introduce extra band broadening effect, beds with no posts were used in our later designs.

The monolithic polymer can be completely removed from the channels by thermal incineration to regenerate the glass microchips [20], if necessary, e.g., in case of degradation of the monolith due to drying, irreversible adsorption of impurities or clogging by particulates. The thermal incineration protocol for complete removal of the monolithic material involved washing the channel thoroughly with Milli-Q water, and heating in an oven using the same temperature program for glass bonding to decompose the monolith, followed by incubating the channel in 0.2 M NaOH overnight to refresh the glass surface. This method regenerated a clean glass chip that could be used for photopatterning of new monolithic polymers.

2.4 Conclusion

Photo-initiated polymerization within microchannels is a straightforward approach for preparation of monolithic polymer materials with a broad range of surface chemistries and porous properties. Here, we demonstrated the preparation of monolithic polymer with hydrophobic chemistry within a single-channel microfluidic device by copolymerization of butyl methacrylate (BMA) with ethylene dimethacrylate (EDMA). The EDMA monomer serves as the crosslinking agent, whereas BMA plays the role of the methacrylate monolith backbone. An ionizable monomer, META, was added as co-monomer to provide charged functionalities to support EOF that drives fluid flow through the column.

The polymerization mixture compositions and reaction conditions were systematically investigated in order to optimize the monoliths for solid-phase extraction and preconcentration. The SPE performance of the monolithic beds was evaluated in terms of adsorption capacity, concentration enhancement, elution efficiency, durability and reproducibility. By integrating tapered geometries at the beginning and end of an enlarged channel acting as bed, monoliths can be spatially retained without the need for covalent attachment of the polymer to the channel wall. Single channel components will comprise a portion of more complex microfluidic systems designed for multiple function integration and parallel sample processing in proteomics research. The information gathered in this chapter provides guidance for photo-patterning robust and uniform monolithic polymer beds at multiple locations in a multi-channel device with parallel functional elements; therefore it lays the groundwork for the development of multiplexed microfluidic systems for protein analysis.

2.5 References

- 1 Lichtenberg, J.; de Rooij, N. F.; Verpoorte, E. L. *Talanta* **2002**, *56*, 233–266.
- 2 Hong J.; Edel J. B.; deMello A. J. *Drug Discovery Today* **2009**, *14*, 134–146.
- 3 Freire, S. L.; Wheeler, A. R. *Lab on a Chip* **2006**, *6*, 1415–1423.
- 4 Armenta, J. M.; Gu, B.; Thulin, C. D.; Lee, M. L. *J. Chromatogr. A* **2007**, *1148*, 115–122.
- 5 Jacobson, S. C.; Ramsey, J.M. *Electrophoresis* **1995**, *16*, 481–486.
- 6 Li, J.; Wang, C.; Kelly, J. F.; Harrison, D. J.; Thibault, P. *Electrophoresis* **2000**, *21*, 198–210.
- 7 Lichtenberg, J.; Verpoorte, E.; de Rooij, N. F. *Electrophoresis* **2001**, *22*, 258–271.

- 8 Zhang, B.; Liu, H.; Karger, B. L.; Foret, F. *Anal. Chem.* **1999**, *71*, 3258–3264
- 9 Thurman, E. M.; Mills, M. S. *Solid-Phase Extraction: Principles and Practice*; Wiley: New York, **1998**.
- 10 Schaller, D.; Hilder, E. F.; Haddad, P. R. *Anal. Chim. Acta* **2006**, *556*, 104–111.
- 11 Kutter, J. P.; Jacobson, S. C.; Ramsey, J. M. *J. Microcolumn Sep.* **2000**, *12*, 93–97.
- 12 Oleschuk, R. D.; Shultz-Lockyear, L. L.; Ning, Y.; Harrison, D. J. *Anal. Chem.* **2000**, *72*, 585–590.
- 13 Jemere, A. B.; Oleschuk, R. D.; Ouchen, F.; Fajuyigbe, F.; Harrison, D. J. *Electrophoresis* **2002**, *23*, 3537–3544.
- 14 Yu, C.; Davey, M. H.; Svec, F.; Frechet, J. M. J. *Anal. Chem.* **2001**, *73*, 5088–5096.
- 15 Yu, C.; Svec, F.; Frechet, J. M. J. *Electrophoresis* **2000**, *21*, 120–127.
- 16 Svec, F. *J. Chromatogr. B* **2006**, *841*, 52–64.
- 17 Fan, Z. H.; Harrison, D. J. *Anal. Chem.* **1994**, *66*, 177–184.
- 18 Kanamori, K.; Yonezawa, H.; Nakanishi, K.; Hirao, K.; Jinnal, H. *J. Sep. Sci.* **2004**, *27*, 874–886.
- 19 He, M.; Zeng, Y.; Sun, X.; Harrison, D. J. *Electrophoresis* **2008**, *29*, 2980–2986.
- 20 Throckmorton, D. J.; Shepodd, T. J.; Singh, A. K. *Anal. Chem.* **2002**, *74*, 784–789.
- 21 Yu, C.; Xu, M.C.; Svec, F.; Frechet, J.M.J. *Journal of Polymer Science: Part A: Polymer Chemistry* **2002**, *40*, 755–769.
- 22 Geiser, L.; Eeltink, S.; Svec, F.; Frechet, J. M. J. *J. Chromatogr. A* **2007**, *1140*, 140–146.
- 23 Madou, M. *Fundamentals of Microfabrication*; CRC Press: Boca Raton, **1997**.
- 24 Tan, A.; Benetton, S.; Henion, J.D. *Anal. Chem.* **2003**, *75*, 5504–5511.
- 25 Yang, Y.; Li, C.; Lee, K.H.; Craighead, H.G. *Electrophoresis* **2005**, *26*, 3622–3630.

Chapter 3

Microchannel Surface Modification with Cationic Coatings for On-Line Coupling of Microchip to Electrospray Mass Spectrometry

3.1 Introduction.....	76
3.2 Experimental Section.....	78
3.2.1 Materials and Instrumentation	78
3.2.2 Synthesis of PolyE-323.....	80
3.2.3 Microchannel Coating Procedure.....	80
3.3 Results and Discussion	83
3.3.1 Evaluation of Four Cationic Coatings.....	83
3.3.1.1 EOF Measurement	83
3.3.1.2 Coating Stability and Reproducibility	83
3.3.1.3 Effect of Methanol Concentration on EOF Mobility.....	85
3.3.1.4 Comparison of Four Cationic Coatings	87
3.3.2 Compatibility of PolyE-323 Coating with ESI-MS	88
3.3.2.1 Electrospray Performance.....	88
3.3.2.2 Background Tests on PolyE-323 Coated Channels	90
3.3.2.3 On-line CE-MS	92
3.3.3 CE Separation in PolyE-323 Coated Capillaries	95
3.3.3.1 Separation of Peptides and Proteins.....	95
3.3.3.2 Effect of Polymerization Mixture on PolyE-323 Coating	98
3.3.3.3 Separation of Cytochrome <i>c</i> Digests.....	100
3.4 Conclusions.....	103
3.5 References.....	103

3.1 Introduction

A major issue in a microfluidic system is the manipulation of fluid flows in the microchannels [1, 2]. There are two fundamental ways of mobilizing fluids in microfluidic systems: pressure-driven flow and electrokinetically-driven flow. In pressure driven flow, fluids are pumped by external devices such as syringe pumps or pneumatic pressure. The second method utilizes the phenomenon of electroosmotic flow (EOF) and uses electric fields to induce electrokinetic pumping. In contrast to the conventional pressure-driven mode, electrokinetic fluid pumping is a more convenient and preferable way to direct fluids on a microfabricated device due to its many advantages, including easy operation with no need for solid moving parts, plug flow profile, and the ability to control fluid flow in a complex channel network by switching voltages. However, EOF is highly dependent on the surface charge of the channel walls, and consequently is sensitive to changes in the physical state of the channel surface. In analysis of biomolecules such as proteins, the surface properties might change due to analyte-wall interactions. Therefore, the poor reproducibility arising from variability in EOF must be addressed for protein applications. A successful approach to reduce analyte adsorption is chemical modification of the channel inner surface.

When microfluidic devices are coupled on-line to electrospray mass spectrometry (ESI-MS), there is a need to continuously deliver solution to a charged ESI emitter to maintain a stable electrospray. For MS detection in a positive ion mode, an acidic buffer will be used to facilitate the formation of positively-charged ions. At low pH values, the silanol groups on the channel

surface are protonated and EOF is significantly reduced. In addition, to generate a positive electrospray, the emitter must be biased at a positive potential relative to the entrance to the MS. A commonly used strategy for delivering fluids from a device to the ESI emitter by EOF involves modification of the microchannel surface with a cationic coating, which allows the use of a negative potential at the channel reservoir upstream and a positive potential at the emitter to produce anodal EOF towards the MS.

The selection of a coating for protein analysis in an electrokinetically-driven microchip system coupled with a sheathless ESI-MS involves a number of factors. First, the coating must generate an EOF of sufficiently high magnitude to maintain a stable electrospray. In addition, the coating should not bleed from the surface into the MS, as that produces a high background signal and may interfere with analyte detection. Furthermore, the coating should be compatible with the background electrolyte and solvent. An organic modifier is usually added to the background buffer to improve the electrospray performance, and a substantial modifier is often used as an SPE eluent.

Two commonly used approaches for cationic coating are covalently bonded coatings and physically adsorbed polymeric coatings [3–5]. Covalently bonded coatings are usually achieved via bifunctional silylating reagents to permanently shield the silanol groups and anchor the polymer coating to the wall, which is often a laborious and time-consuming procedure. In contrast, physically adsorbed polymeric coatings are attractive due to their versatility and simplicity. A wide range of cationic polymers, such as polybrene (PB) [6–10], polyethyleneimine

(PEI) [9, 11–14], poly(diallyldimethyl ammonium chloride) (PDADMAC) [9, 15–17], chitosan [18, 19], polyarginine [20] have been used as microchannel wall coatings. However, bleeding from the columns can be a problem with these materials.

In this chapter, four physically adsorbed coatings were examined, including the triple layer PB–Dextran sulfate (DS)–PB coating [21, 22], a double-chained cationic surfactant coating [23, 24], a commercially available coating reagent kit, and a recently reported polyamine coating, PolyE-323 [25, 26]. These coatings were investigated and compared in terms of stability, reproducibility, EOF properties, and resistance towards organic modifier. The results showed that the PolyE-323 coating yielded the best performance and satisfactorily met all the criteria for sheathless ESI-MS. Since monoliths will be prepared in the coated channel in later application, PolyE-323 coating was also evaluated for compatibility with the polymerization mixture.

3.2 Experimental Section

3.2.1 Materials and Instrumentation

Polybrene (PB), dextran sulfate sodium salt (DS), epichlorohydrin, 1,2-bis(3-aminopropylamino)ethane, and dimethylditetradecylammonium bromide (2C₁₄DAB) were purchased from Sigma-Aldrich. The commercial coating kit Ultratrol™ HR was obtained from Target Discovery, Inc (Palo Alto, CA, USA). Peptide standards methionine enkephalin, bradykinin (fragment 1–5), leucine enkephalinamide acetate salt, angiotensin II human, and somatostatin, and the

proteins carbonic anhydrase from bovine erythrocytes, lysozyme from chicken egg white, cytochrome *c* from horse heart, ribonuclease A from bovine pancreas, and α -chymotrypsinogen A from bovine pancreas were purchased as lyophilized powders from Sigma and used without further purification. Analyte stock solutions were prepared by dissolving peptides or proteins in Milli-Q water at a concentration range of 1–2 mg/ml. The analyte solutions were stored at -20°C and adjusted to room temperature prior to use. BODIPY 493/503 was from Molecular Probes (Eugene, OR, USA) and was used as the neutral EOF marker. Formic acid was from Fluka and LC-MS grade methanol was from Riedelde Haen. Water was purified with Milli-Q purification system (Millipore, Bedford, MA, USA). All aqueous solutions were filtered through 0.2 μm Nylon syringe filters (Chromatographic Specialties Inc. Brockville, Canada). Fused-silica capillaries of 50 μm i.d. \times 365 μm o.d. were obtained from Polymicro Technologies.

All CE-UV experiments were carried out using P/ACE 5010 (Beckman Instruments, Inc., Fullerton, CA) with UV detection at 200 nm. CE separations were performed under reversal polarity with an anodal EOF in PolyE-323 coated capillaries. MS work was done using a PE/Sciex API 150 EX single quadrupole mass spectrometer (Perkin-Elmer/Sciex, Concord, ON, Canada). A full description of the construction of the microchip-ESI interface and ESI-MS operation parameters will be presented in Chapter 4.

3.2.2 Synthesis of PolyE-323

Synthesis of PolyE-323 followed a previously reported procedure [25]. In short, in a 250 ml round-bottom flask, 17.65 g (0.1 mol) of 1,2-bis(3-aminopropylamino)ethane was mixed with 20 g Milli-Q water, and 9.3 g (0.1 mol) epichlorohydrin was added dropwise with vigorous magnetic stirring. The flask was sealed and reaction mixture was continuously stirred for 48 h at room temperature. 100 g Milli-Q water was added and the reaction was continued for 1 week to equilibrate. The synthesis generates a viscous, light yellow, alkaline solution with a polymer concentration of 19 % (w/w), given by the polymer synthesis stoichiometry, schematically depicted in Figure 3.1. After synthesis, the polymer solution is stored in darkness at 8 °C and used without further purification. The coating solution was prepared by diluting the polymer solution with Milli-Q water to give a polymer concentration of 7.5% (w/w) and adjusting to pH 7 with 1 M acetic acid.

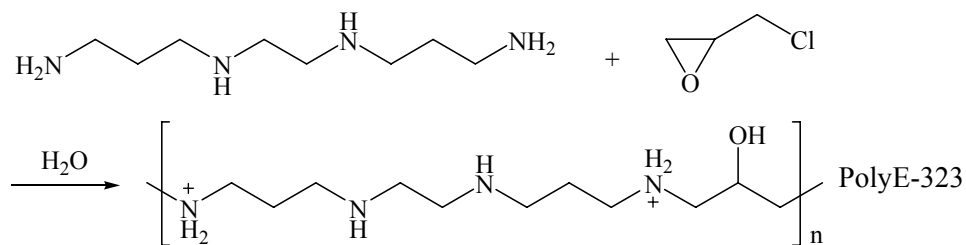


Figure 3.1 Synthesis and structure of PolyE-323. The polymer is depicted at a degree of protonation of 50%.

3.2.3 Microchannel Coating Procedure

For the triple layer PB–DS–PB coating [21], the channel was first rinsed with 1 M NaOH for 30 min and Milli-Q water for 15 min in order to activate the

silanol groups on the surface. After preconditioning, the channel was flushed with 10% PB solution for 15 min to form the first layer of cationic coating, and then the channel was rinsed with 3% DS solution for 15 min to coat the second layer. Finally, 10% PB solution was rinsed over the anionic layer for 15 min. This procedure of successive coating resulted in a triple layer of PB–DS–PB on the channel walls and the water rinsing between each step is critical. The chemical structure of the coating reagents and the schematic illustrating the coating procedure are showed in Figure 3.2.

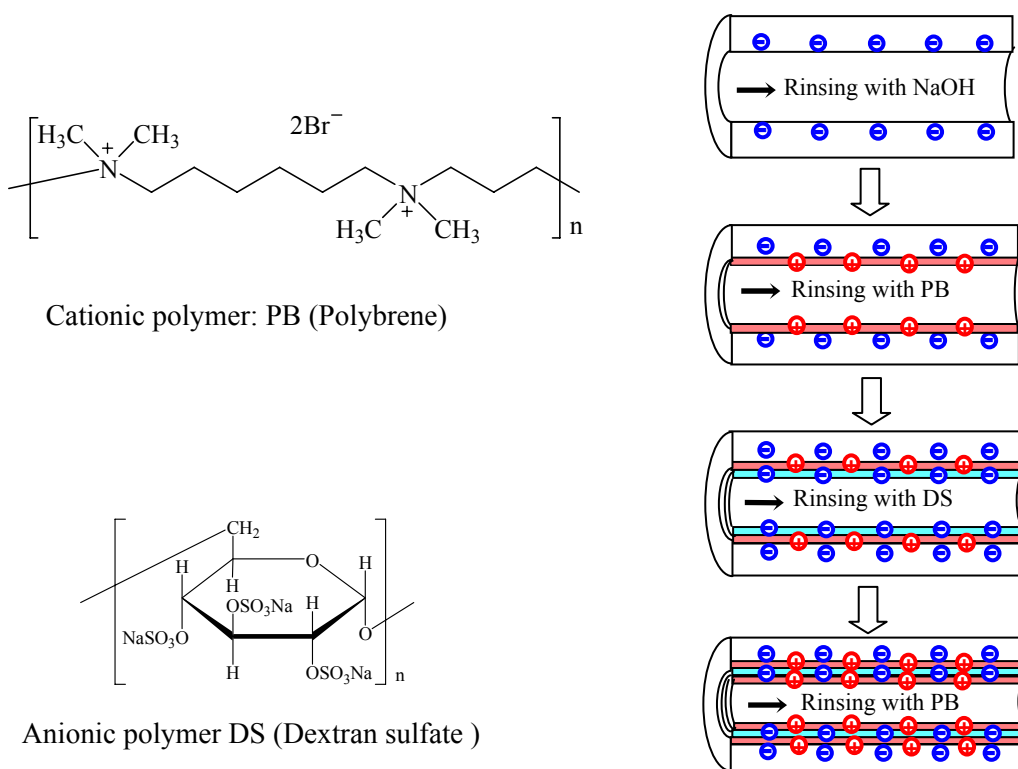


Figure 3.2 Chemical structures of PB and DS, and the coating procedure for triple layer PB–DS–PB coating.

For the other three coatings, the coating procedure is a simple three-step rinsing protocol comprising deprotonation of surface silanol groups with NaOH, a

30 min rinse with the respective coating reagent, and a final rinse with buffer to remove excess coating solution.

The double-chained surfactant 2C₁₄DAB is only slightly soluble in water due to the long hydrocarbon chains; thus a sonicate/stir cycle method is applied according to a previous report [24] when preparing the 2C₁₄DAB solution. The surfactant solution was sonicated at 50°C for 20 min, followed by stirring for 10 min at room temperature. This sonicate/stir cycle was repeated until a clear solution was obtained. Here the surfactant is present in the solution at a concentration higher than the critical micelle concentration (CMC), so the free surfactant will aggregate and form a bilayer structure on the channel wall, as demonstrated in Figure 3.3.

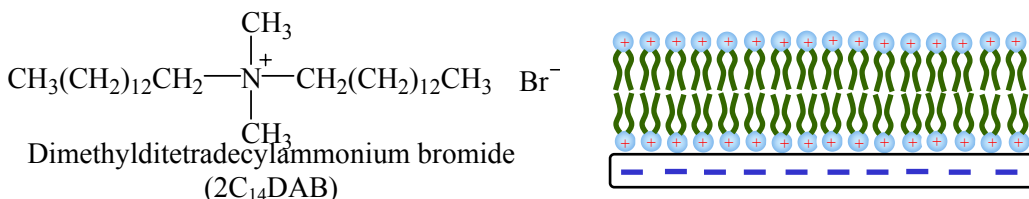


Figure 3.3 Chemical structure of 2C₁₄DAB surfactant and schematic illustrating the bilayer structure formed at the channel surface.

All rinsing was performed by applying a vacuum to the buffer waste reservoir with the other reservoirs filled with the rinsing solution. The capillary electro spray tips were coated following the same procedure using a syringe pump. For CE-UV experiments, a 3-mm detection window was made by burning off the external polyimide coating before capillary coating. The capillary was assembled into the capillary cartridge and coated using the rinsing ability of the CE instrument.

3.3 Results and Discussion

3.3.1 Evaluation of Four Cationic Coatings

3.3.1.1 EOF Measurement

The EOF generated by the four cationic coatings discussed above was measured using a double-T injector device [27]. BODIPY in 10 mM NH₄Ac buffer (pH 8.0) was used as the neutral EOF marker. An electrokinetic injection was conducted for 10 s with -0.5 kV at the sample reservoir, sample waste grounded, and buffer and waste reservoirs left floating. Sample was then delivered into the main channel with 1 kV applied between buffer and waste reservoirs, and push back voltages of 250 V at the sample and sample waste reservoirs. The fluorescence detector was positioned 1.5 cm from the double-T intersection. From the time required for BODIPY to reach the detector and the electrical field used, the EOF mobility was calculated. The magnitudes of the EOF measured for all four coatings are listed in Table 3.1.

Table 3.1 EOF measurements for four cationic coatings and the coating stability and reproducibility.

	Reversed μ_{EOF}	run-to-run %RSD (n = 80)	day-to-day %RSD (n = 20)	chip-to-chip %RSD (n = 6)
PB-DS-PB	$4.97 \times 10^{-4} \text{cm}^2/\text{V s}$	1.8%	1.4%	2.2%
UltraTrol™	$2.19 \times 10^{-4} \text{cm}^2/\text{V s}$	3.5%	3.8%	4.1%
Surfactant	$8.31 \times 10^{-4} \text{cm}^2/\text{V s}$	2.0%	2.5%	2.5%
PolyE-323	$4.22 \times 10^{-4} \text{cm}^2/\text{V s}$	1.4%	1.9%	1.8%

3.3.1.2 Coating Stability and Reproducibility

The lifetime of the four coatings was investigated by performing 80 successive EOF measurements in a day without regenerating the coatings, and the

coating stability was evaluated on the basis of the change of EOF. The reservoirs were refreshed with new buffer every 10th run in order to minimize problems with buffer depletion and electrolysis, which would alter buffer pH and consequently change EOF. The relative standard deviations (RSDs) of EOF for all four coatings are listed in Table 3.1 as run-to-run stability ($n = 80$). As an example, Figure 3.4a shows the electropherograms of the first 5 and last 5 runs of EOF measurement in a PolyE-323 coated channel. The EOF values measured are almost constant for the 80 consecutive runs with an RSD of 1.4% (Figure 3.4b), indicating a high stability of the EOF generated by this coating.

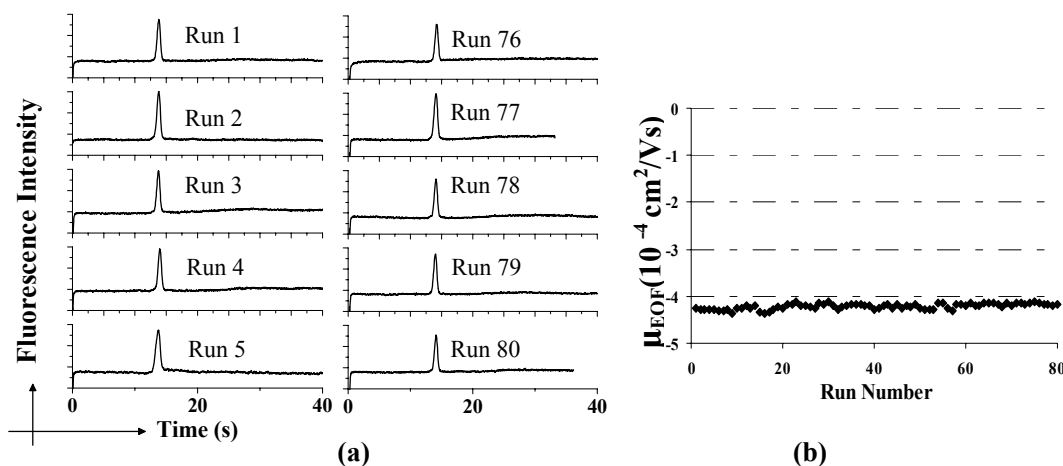


Figure 3.4 Run-to-run stability of EOF measured within a PolyE-323 coated channel. (a) Electropherograms of the first 5 and last 5 EOF measurement; (b) EOF measured within a PolyE-323 modified channel for 80 successive runs. Neutral EOF marker: BODIPY in 10 mM NH_4Ac buffer (pH 8.0).

The long-term stability of these coatings was determined over 20 days without any regeneration of the coating. Ten successive runs were performed in a single chip each day for 10 consecutive days. After Day 10 the coated channel was stored for 10 days in the running buffer and EOF was measured again. The RSDs of EOF measured over this 20-day period are presented in Table 3.1 as day-to-day stability. Figure 3.5 illustrates a fairly stable EOF during the investigation of

PolyE-323 coating. The average values of the EOF measured in the first-day and the last-day are $4.23 \pm 0.03 \times 10^{-4} \text{ cm}^2 \text{ V}^{-1} \text{ s}^{-1}$ (0.7% RSD, $n = 10$) and $4.11 \pm 0.06 \times 10^{-4} \text{ cm}^2 \text{ V}^{-1} \text{ s}^{-1}$ (1.4% RSD, $n = 10$), respectively. The average EOF for the total 20-day measurements is $4.16 \pm 0.08 \times 10^{-4} \text{ cm}^2 \text{ V}^{-1} \text{ s}^{-1}$ (1.9% RSD, $n = 110$).

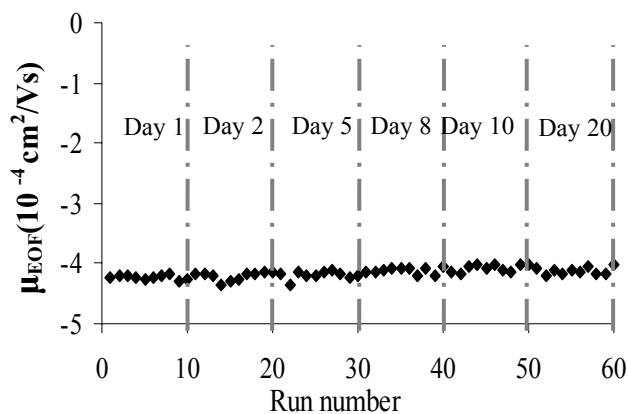


Figure 3.5 Long-term stability of EOF measured within a PolyE-323 modified channel. The measurements were performed in a 20-day period with ten successive runs each day. Sample: BODIPY; Running buffer: 10 mM NH_4Ac buffer (pH 8.0).

In order to investigate the reproducibility of the coating procedures, six chips were coated on different days for each coating. The EOF was calculated from ten consecutive injections of the neutral dye for each chip and the RSDs of EOF measured for six chips of all four coatings are summarized in Table 3.1 as chip-to-chip reproducibility.

3.3.1.3 Effect of Methanol Concentration on EOF Mobility

The surface coating must tolerate the use of organic modifiers in order to be compatible with sheathless ESI-MS. In addition, in an integrated system, high organic solvent content buffers will be used for the elution of adsorbed proteins or peptides. Microchannels modified with these four coatings were thus evaluated

for compatibility with methanol (MeOH) and acetonitrile (ACN), two modifiers commonly used in ESI-MS. EOF was measured in NH_4Ac buffers containing various amounts of MeOH or ACN. Figure 3.6a shows the dependence of EOF on MeOH concentration in MeOH/aqueous mixtures for a PolyE-323 coated device. The reversed EOF decreases with increasing percentage of MeOH to a minimum ($\sim 60\%$ MeOH) and then increases slightly. This change has the same tendency as the variation of dielectric constant to viscosity ratio (ϵ/η) versus percentage of MeOH (Figure 3.6b), which is calculated from literature values [28].

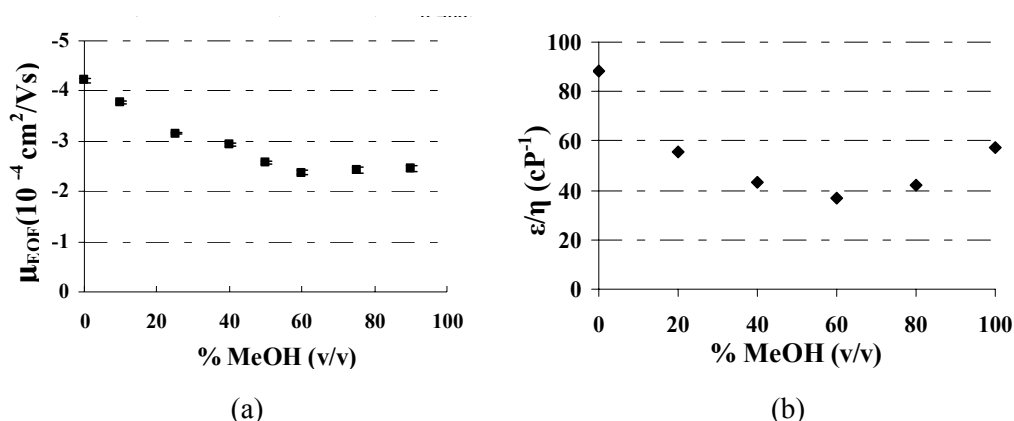


Figure 3.6 Effect of MeOH concentration on the magnitude and stability of EOF generated with PolyE-323 coating. (a) Dependence of EOF on MeOH concentrations. Measurements at each MeOH concentration were repeated for 15 times. Error bars are within symbols unless shown. Running buffer: 10 mM NH_4Ac (pH 8.0) buffer containing various amounts of MeOH. (b) Variation of dielectric constant to viscosity ratio (ϵ/η) versus percentage of MeOH.

Measurements at each MeOH concentration were repeated for 15 times, with RSDs in the range of 0.7%-2.4%. Channels coated with PolyE-323 show good performance with somewhat higher stability at lower MeOH concentrations (pure aqueous buffer, RSD = 0.7%), compared to higher MeOH concentrations in buffer (90% MeOH buffer, RSD = 2.4%). Similar results were obtained for buffers containing ACN.

For the PB–DS–PB coating and the UltraTrol™ coating, the dependence of EOF on MeOH concentration follows the same tendency as that of PolyE-323. And the EOF reproducibility at different MeOH concentrations ranges between 0.8% to 3.2% and 0.8% to 2.0% for PB–DS–PB and UltraTrol™ coating, respectively.

For the 2C₁₄DAB surfactant coating, the EOF decreases by about 12% over 15 successive runs of EOF measurement (~15 min) in a 20% MeOH buffer, indicating degradation of the bilayer structure on the channel surface. The coating degrades even more rapidly as the MeOH concentration increases. In buffers containing more than 60 % MeOH, no reversed EOF is observed, indicating a completely loss of positively-charged surfactant bilayer at the channel surface. This is consistent with the results reported by other researchers [29].

3.3.1.4 Comparison of Four Cationic Coatings

All four coatings demonstrate good performance in aqueous buffer in terms of stability and reproducibility, as shown in Table 3.1. The RSDs for EOF measured within-day and between-day are 1.4-3.5% and 1.4-3.8%, respectively, and chip-to-chip reproducibility ranges between 1.8-4.1%.

For the triple layer ionic-polymer PB–DS–PB coating, the coating procedure is time-consuming with the need for alternate rinses with positively and negatively charged polymers. This coating suffers from channel clogging problem even with careful water rinsing between each coating step. A tiny amount of residual PB or DS can form precipitate that leads to clogging. A problem

associated with the Ultratrol commercial coating reagent is that the EOF generated by this coating is too low to sustain a stable electrospray, especially in buffers with high organic content. The poor stability of 2C₁₄DAB surfactant coating in buffers containing organic solvent limits its application in our system. It turns out that only PolyE-323 satisfactorily met the criteria for sheathless ESI-MS: high enough anodal EOF to promote a stable electrospray; high stability with no observed degradation, strong tolerance to the use of organic modifier. Besides, the coating procedure is fast, simple and reliable. The evaluation of this coating for compatibility with sheathless ESI-MS will be described in detail in the next section.

3.3.2 Compatibility of PolyE-323 Coating with ESI-MS

3.3.2.1 Electrospray Performance

Long term electrospray stability tests were carried out to further characterize the performance of the PolyE-323 coating. In these experiments, a peptide, bradykinin (fragment 1-5), and a protein, cytochrome *c*, were dissolved in 5 mM formic acid buffer containing 25% MeOH. Samples were electrokinetically infused through a single straight microchannel to the electrospray tip and sprayed into the MS orifice. The electrospray was driven by the EOF generated in the PolyE-323 modified channel. The coating durability was evaluated based on signal variation in the total ion chromatograms (TICs) (Figure 3.7). The spray exhibits a stable current for more than 1 h with an RSD of 4.4% for Bradykinin (fragment 1-5) and 8.4% for cytochrome *c*. The stability of the signal over time

indicates a high stability of the EOF, and consequently a high stability of the coating. The mass spectra on the right side of Figure 3.7 show a single mass peak for bradykinin and a protein charge envelope for cytochrome *c*. The small spikes seen in the TICs could be due to the formation of air bubbles. Considering the high electric field at the ESI emitter during the electrospray process, some bubbles may form due to electrochemical reactions, causing some fluctuations in the current [30].

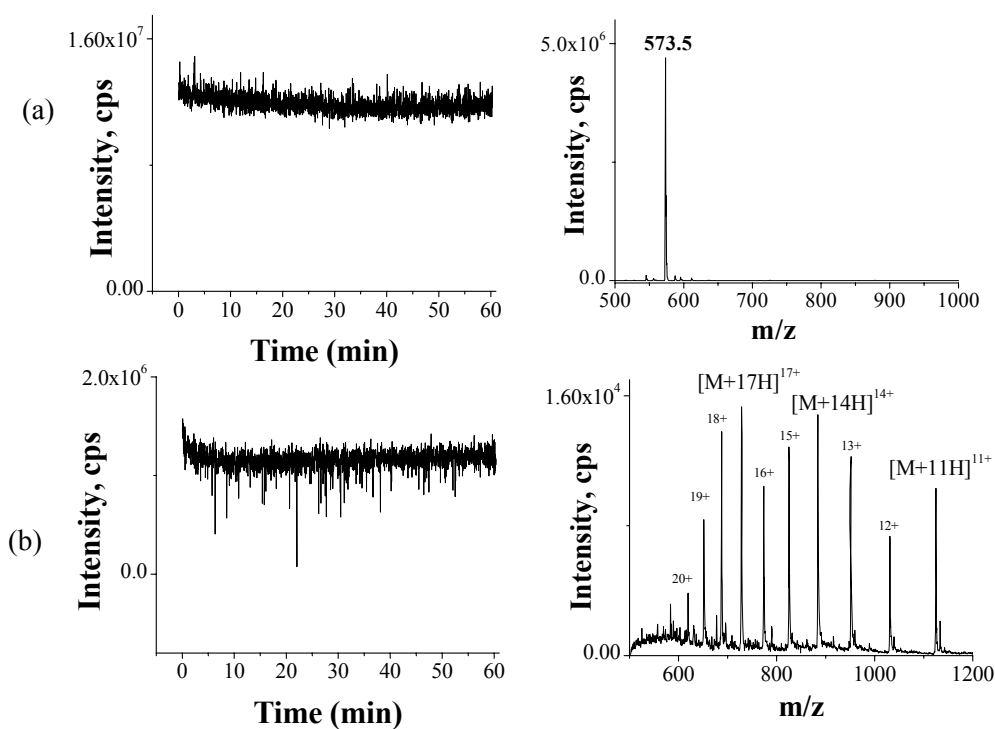


Figure 3.7 TICs and mass spectra from constant infusion of sample from a PolyE-323 coated device. (a) Bradykinin (fragment 1-5) ($87 \mu\text{M}$) and (b) Cytochrome *c* ($20 \mu\text{M}$) in 5 mM formic acid with $25\% \text{ MeOH}$. Applied voltage: -2 kV at sample reservoir, 3.2 kV at the electrospray tip.

As mentioned in Section 3.3.1.3, the addition of organic solvent will reduce the magnitude of EOF, which may result in unstable signal. Since buffers with high organic content are always required for analyte elution, the Bradykinin fragment dissolved in buffers containing different amount of MeOH was used for

infusion studies. The electrospray voltage at the tip was constant at 3.2 kV, while the voltage applied at the sample reservoir was varied from 0 to -4 KV with a step change of -1 kV each time. From the TICs in Figure 3.8, the signal is very stable for buffer with 25% and 50% MeOH for all the voltage combinations. For buffer containing 75% MeOH, although a continuous signal can still be obtained, the signal stability gets poorer, especially at lower voltage (0 kV). The signal intensity also drops dramatically, probably due to a decreased flow rate.

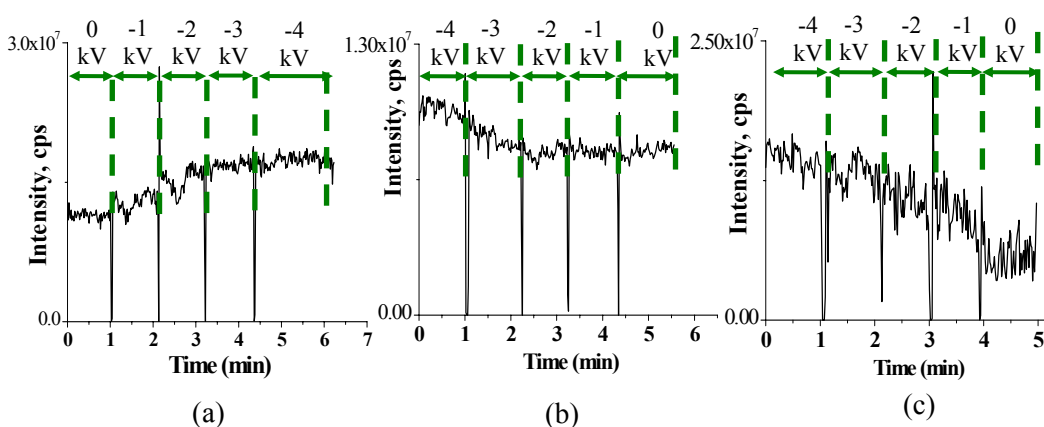


Figure 3.8 TICs from continuous infusion of Bradykinin (fragment 1-5) ($87 \mu\text{M}$ in 5 mM formic acid with different MeOH percentages). (a) 25% MeOH, (b) 50% MeOH, (c) 75% MeOH. Applied voltage: -4 to 0 kV at sample reservoir as labeled on the graph, 3.2 kV at the electrospray tip. The channel was modified with PolyE-323 cationic coating.

3.3.2.2 Background tests on PolyE-323 Coated Channels

In the experiments mentioned above, no masses corresponding to the bleeding of the polymer were detected in the mass spectra. However, it is possible that signal from a small amount of polymer leaching from the surface coating, if any, could be suppressed by the analyte ion signal and become undetectable. PolyE-323-coated channels were thus assessed by monitoring the channel eluent for 1 h with continuous infusion of sample-free buffer solution. Figure 3.9 shows the

TICs and mass spectra obtained for buffer containing 25%, 50% and 75% MeOH. The background signal is stable over time, indicating a high stability of the EOF.

From the mass spectra, most background signals are present in the lower m/z region (<200) and these signals originate from the buffer solution. The m/z range between 500 and 1000 is more important when ion interference is considered, as most signals we want to detect fall into this region. As highlighted by the dashed box in Figure 3.9b, almost no mass peaks were observed for 25% MeOH buffer, while a set of small peaks is observed for 50% and 75% MeOH buffer. Since we cannot deliver PolyE-323 polymer solution directly into MS with the risk of contaminating the ion source, it is difficult to determine whether these mass peaks are from polymer leaching from the coating.

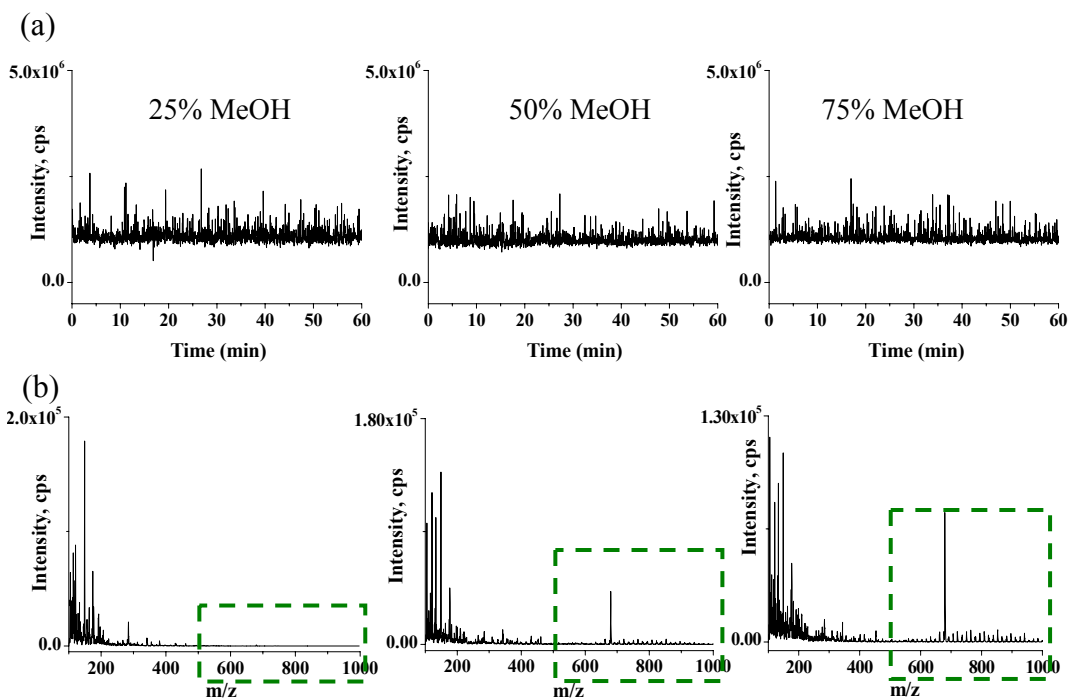


Figure 3.9 Background tests on PolyE-323 coated channels. (a) TICs from continuous infusion of buffer containing 25%, 50% and 75% MeOH. (b) The corresponding mass spectra. Applied voltage: -3 kV at sample reservoir and 3.2 kV at the electrospray tip.

A series of control experiments were performed to determine the source of the interfering peaks. One possible source is the PolyE-323 coating. Similar background tests were carried out on an uncoated device, and buffer solution was pumped through the channel using pressure driven flow with the aid of a syringe pump. The resultant mass spectra gave similar peak patterns, suggesting the background peaks are not from the coating polymer. Experiments using freshly prepared buffer resulted in the same background signal, ruling out the possibility that they are from dissolved components from the buffer container under high content of organic solvent. It was determined that this background signal was from the solvent filter. Signals obtained from unfiltered buffer are very clean, while signals from filtered buffer contain a set of peaks similar to those in Figure 3.9b. The Nylon filter we used is hydrophilic and only suitable for aqueous samples; the use of organic solvents likely dissolved some components from the filter. A filter with broad chemical compatibility for organic solvents and low extractable levels, such as polypropylene filter, should be used in subsequent experiments, or we should use high purity LC/MS solvents directly without filtration.

3.3.2.3 On-line CE-MS

Electrokinetic injection of sample was conducted using a device with a double-T injector [27], the device layout and relevant parameters are shown in Figure 3.10a. Sample was injected by applying -1.0 kV to sample reservoir, with the sample waste reservoir grounded for 10 s, and then the sample plug was

delivered to the MS by applying -2.0 kV at the buffer reservoir and 3.2 kV at the electrospray tip. The resulting TICs display a single peak for Methionine-enkephalin (Figure 3.10b) and cytochrome *c* (Figure 3.10c). Their corresponding mass spectrum is shown in the inset.

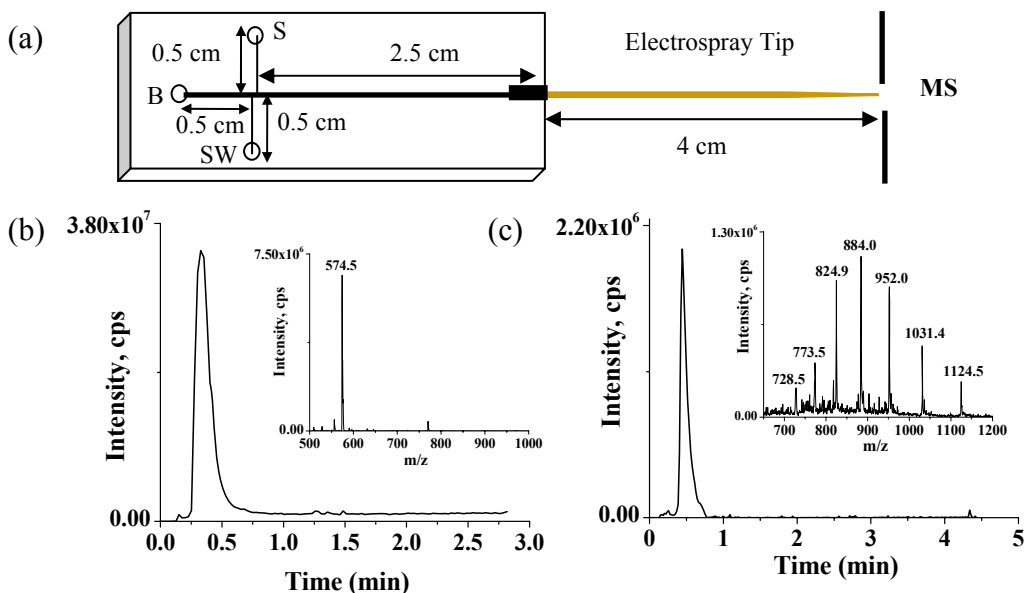


Figure 3.10 Electrokinetic injection of sample. (a) Schematic illustrating the microchip layout for ESI-MS with channel lengths labeled. The injector length (center to center distance) is 100 μm . Reservoirs: S, sample; B, buffer; SW, sample waste. TICs for electrokinetic injection of (b) methionine-enkephalin (174 μM) and (c) cytochrome *c* (20 μM). The inset is the corresponding mass spectrum. Conditions: Running buffer: 5 mM formic acid with 25% MeOH. Injection: S: - 1.0 kV, SW: grounded; separation: B: -2.0 kV, electrospray tip: 3.2 kV. The microchannel was modified with PolyE-323 cationic coating.

CE-ESI-MS separation of two peptides, methionine-enkephalin and Angiotensin II, was carried out in a PolyE-323 coated device and the TIC in Figure 3.11 displays two peaks. The two peaks are completely baseline resolved and the theoretical plate numbers are 1.5×10^4 and 1.2×10^4 plates/m with a separation length of 7 cm.

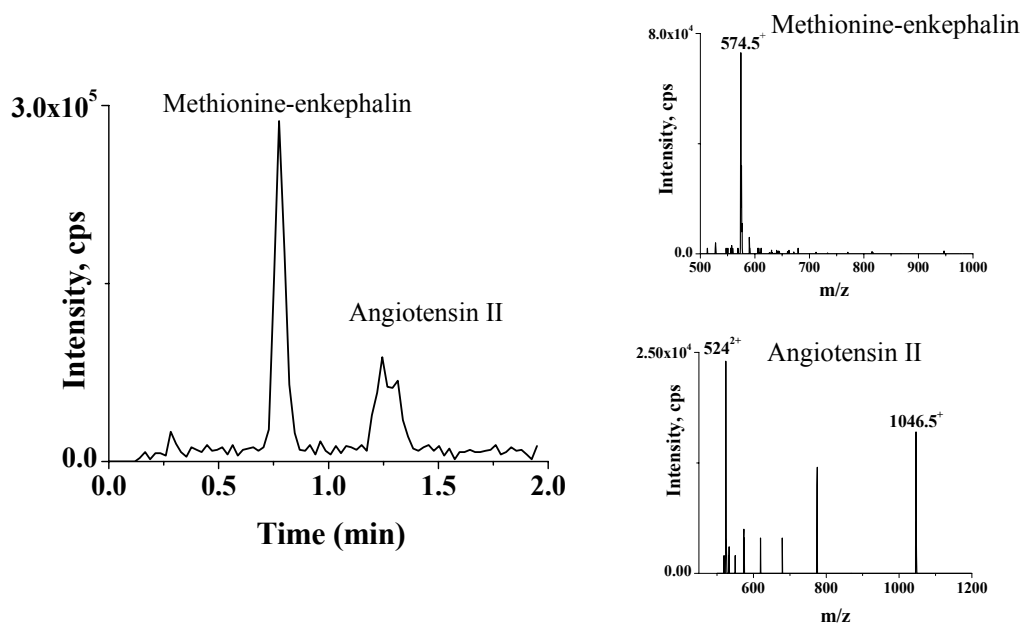


Figure 3.11 TIC for the CE separation of two peptides, methionine-enkephalin ($8.7 \mu\text{M}$) and Angiotensin II ($5.0 \mu\text{M}$) and the mass spectrum extracted from each peak. All the conditions are the same as those in Figure 3.10. The microchannel was modified with PolyE-323 cationic coating.

The relatively poor separation efficiencies could be attributed to three factors. First, the dead volume at the chip-ESI tip connection has the potential to act like a mixing chamber and contributes to band broadening. However, a low dead volume connection design described previously [31] was employed. Second, when performing CE-ESI-MS, the electrospray should not arise from a droplet at the tip, since the accumulation of liquid decreases the separation efficiency. A third factor is the injection sample plug. On chip-based electrophoretic separations, due to the very short separation distance, a short sample plug is essential to improve separation efficiency.

In the CE-ESI-MS separation experiment described above, the injection was conducted by applying a negative high voltage at the sample reservoir, with sample waste reservoir grounded and other reservoirs left floating, which is called

“no plug shaping” in the literature [32]. This injection mode will result in a sample plug extending out beyond the edges of the intersection, leading to an adverse effect in the separation performance. The sample plug can be better defined by applying additional voltages to the other reservoirs to drive buffer as well as sample into the sample waste reservoir, a mode called “full plug shaping” [32].

Another important issue in sample injection is the leakage of sample from side channels into the moving stream in the main channel during separation process. With no pushback voltages applied during separation in our CE-MS experiments, the leakage of sample into the separation channel would contribute to band broadening and result in poor separation efficiency. This leakage effect can be eliminated by applying bias voltage to the side reservoirs to push buffer back into the side channels during the separation.

Injection with full plug shaping and separation with pushback require another power supply to provide the extra voltages, and thus are not performed in our CE-ESI-MS separation experiment.

3.3.3 CE Separation in PolyE-323 Coated Capillaries

3.3.3.1 Separation of Peptides and Proteins

The anionic and hydrophobic feature of the silica capillary surface is well known as a problem in the analysis of biomolecules, especially basic proteins, due to analyte-wall interactions. One strategy to overcome this problem is the use of cationic coatings in combination with an acidic background electrolyte.

The performance of the PolyE-323 coating was investigated by separating peptides and proteins in a buffer solution with a pH below their *pI* value. Table 3.2 summarizes the molecular weights (*MW*) and isoelectric points (*pI*) of these peptides and proteins.

Table 3.2 Molecular weights (*MW*) and isoelectric points (*pI*) of the model peptides and proteins used.

Sample	<i>MW</i>	<i>pI</i>
Peptides		
Methionine enkephalin	537.7	5.78
Angiotensin II	1046.18	7.74
Leucine enkephalinamide	554.6	9.78
Somatostatin	1637.88	10.6
Proteins		
Carbonic Anhydrase	29.0 kDa	6.4
α -chymotrypsinogen A	25.6 kDa	8.97
Ribonuclease A	13.7 kDa	9.6
Cytochrome C	12.4 kDa	10.0-10.5
Lysozyme	14.3 kDa	11.4

Electrochromatograms of CE separation of four peptides and five proteins on a PolyE-323 coated capillary using CE-UV are shown in Figure 3.12 a and b, respectively. This cationic coating enables fast separation of basic peptides and proteins, completed in less than 6 min with efficiencies ranging between 3.8×10^5 and 5.0×10^5 plates/m with a total capillary length of 27 cm (Table 3.3). At pH 5, all these peptides and proteins have an overall positive charge, and thus analyte adsorption is greatly reduced on the polycationic surface.

Five injections were made for each sample without regenerating the cationic coatings. Excellent reproducibility of migration times was obtained, with low RSDs between 0 and 0.11% for all peptides and proteins (Table 3.3). The peak

area reproducibility was ranging between 1.4% and 3.5% RSD. The efficiency reproducibility was 1.3%–6.1%. The high degree of reproducibility suggests that very little peptide or protein is irreversibly adsorbed on the PolyE-323 coated surface. Clearly, the positively charged PolyE-323 coating not only generates anodal EOF, but also hinders analyte–wall interactions of basic protein analytes.

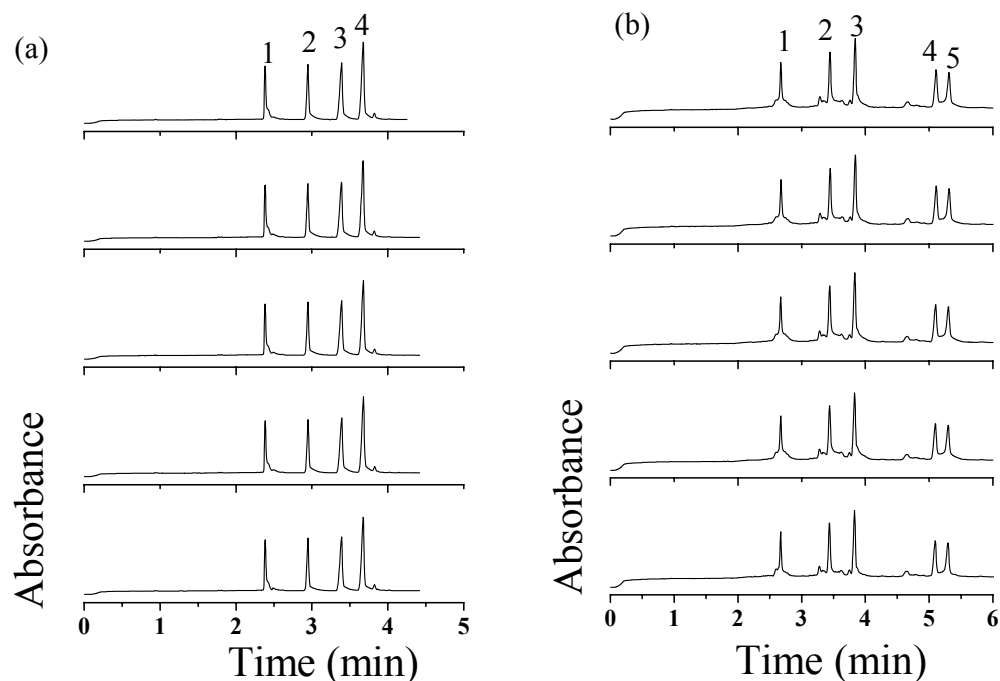


Figure 3.12 (a) Electrochromatograms of CE separation of four peptides on a PolyE-323 coated capillary. Peak identification: 1, Methionine Enkephalin; 2, angiotensin II; 3, Leucine enkephalinamide; and 4, Somatostatin. Peptide concentration: 0.2 mg/ml; (b) Electrochromatograms of CE separation of five proteins on a PolyE-323 coated capillary. Peak identification: 1, carbonic anhydrase; 2, α -chymotrypsinogen; 3, ribonuclease A; 4, cytochrome c; and 5, lysozyme. Protein concentration: 0.25 mg/ml; Conditions: Capillaries, 50 μm i.d., 365 μm o.d., 27 cm total length and 20 cm to the detection window; Pressure injection for 2 s; applied voltage of -10 kV; UV detection at 200 nm; background electrolyte: 50 mM ammonium acetate, pH 5.

Table 3.3 Separation of peptides and proteins on PolyE-323 coated capillaries. Average migration time and plate numbers of peptides and proteins, and their reproducibility in terms of migration time, plate number and peak area.

	Migration time t (min)	Plate number N /m	Reproducibility %RSD(n=5)		
			t	Peak area	N/m
Peptides					
Methionine Enkephalin	2.383	5.0×10^5	0	3.5	4.3
Angiotensin II	2.947	3.9×10^5	0	1.4	1.6
Leucine enkephalinamide	3.389	4.1×10^5	0.03	2.7	3.9
Somatostatin	3.675	5.0×10^5	0.05	1.6	6.1
Proteins					
Carbonic Anhydrase	2.670	3.8×10^5	0.06	1.4	2.0
α -chymotrypsinogen A	3.433	3.8×10^5	0.06	2.3	1.3
Ribonuclease A	3.827	4.2×10^5	0.08	2.0	2.7
Cytochrome C	5.083	4.4×10^5	0.11	2.7	3.6
Lysozyme	5.283	5.0×10^5	0.10	1.0	2.1

3.3.3.2 Effect of Polymerization Mixture on PolyE-323 Coating

Because the monolithic polymer is to be prepared in the PolyE-323 coated channel, it is necessary to determine if the PolyE-323 coating will be affected after coming into contact with the polymerization mixture. This was examined by comparing the CE separations of peptides and proteins before and after the cationic coating was brought into contact with the mixture. The coated capillary was rinsed with the polymerization mixture (#18 in Table 2.1 for the positively-charged monolith) for 1 min and the solution was left in the column for 8 min, the same condition as is used when preparing the monolith, but without exposure to UV light. CE analyses were then performed after rinsing the polymerization mixture out with water or a MeOH/water mixture. Using water and aqueous buffer for the rinse, the baseline is unstable, as shown in Figure 3.13a and c for

peptides and proteins. In contrast, rinsing with 50% MeOH followed by buffer produces a stable baseline (Figure 3.13b and d).

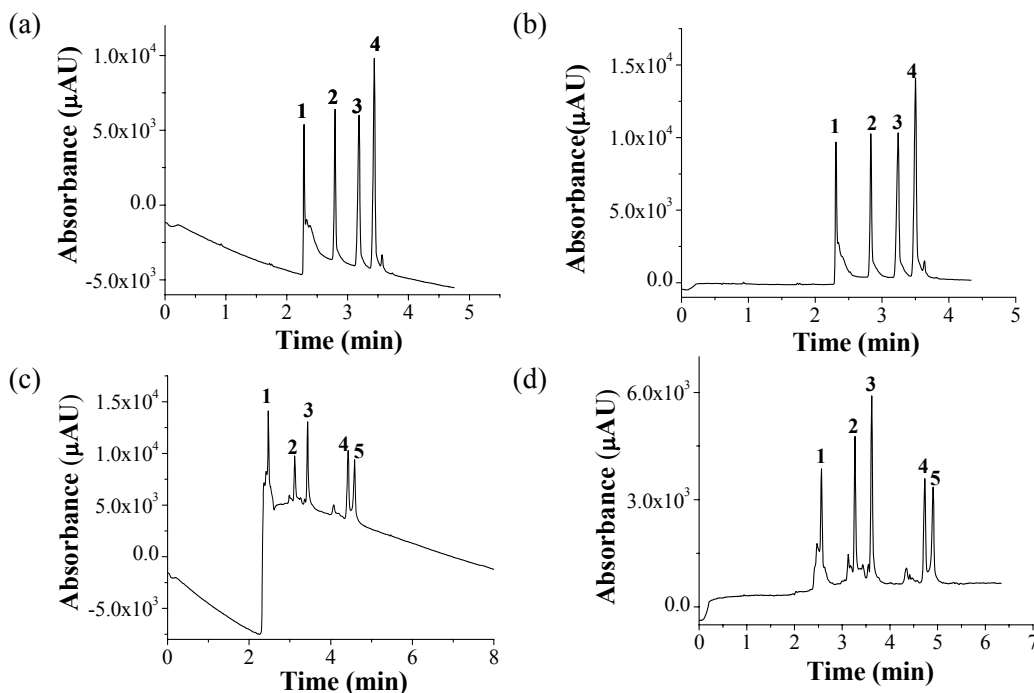


Figure 3.13 CE separations of four peptides (a), (b) and five proteins (c), (d) on a PolyE-323 coated capillary after the coating was brought into contact with the polymerization mixture. In (a) and (c), the mixture was rinsed out using water (5 min) followed by 50 mM NH₄Ac (2 min). In (b) and (d), the polymerization mixture was rinsed out using 50% MeOH (5 min) followed by 50 mM NH₄Ac (2 min). All the separation conditions and peak identifications are the same as those in Figure 3.12.

Comparing the separations before and after the coated capillary was exposed to the polymerization mixture (Figure 3.12 and Figure 3.13) shows that the migration times shift earlier after exposure. Comparing Table 3.3 and Table 3.4 shows a change of 2.8, 3.6, 4.0 and 4.4% for the four peptides and a change of 3.4, 3.9, 4.6, 5.7 and 5.8% for the five proteins. The shift in migration time may arise from adsorption of positively-charged META, which would increase the anodal EOF slightly. The efficiencies decrease slightly (4.0%-7.7% for peptides and 4.1%-8.4% for proteins), mostly due to the shift of migration time.

Table 3.4 Effect of polymerization mixture on PolyE-323 coating. Average migration time and plate numbers of peptides and proteins separated using PolyE-323 coated capillaries after the coating is exposed to polymerization mixture, and their reproducibility in terms of migration time, plate number and peak area.

	Migration time t (min)	Plate number N /m	Reproducibility %RSD(n=5)		
			t	Peak area	N/m
Peptides					
Methionine Enkephalin	2.316	4.8×10^5	0.06	2.8	6.8
Angiotensin II	2.842	3.6×10^5	0.20	3.4	3.6
Leucine enkephalinamide	3.252	3.9×10^5	0.25	5.0	6.2
Somatostatin	3.515	4.7×10^5	0.24	3.3	2.0
Proteins					
Carbonic Anhydrase	2.567	3.5×10^5	0.08	2.4	6.3
α -chymotrypsinogen A	3.280	3.5×10^5	0.06	5.0	1.6
Ribonuclease A	3.627	4.0×10^5	0.10	5.0	2.0
Cytochrome C	4.743	4.1×10^5	0.13	3.1	6.2
Lysozyme	4.920	4.7×10^5	0.15	4.3	2.7

Table 3.4 shows the RSDs (n=5) obtained for migration times, peak areas and efficiencies of each peptide and protein after exposure to the monomer mixture. The coating still shows high performance, with RSDs of 0.06-0.25% for the migration times and RSDs of 2.4-5.0% for peak areas. The results for efficiencies varied between 1.6 and 6.8% RSD, showing a random variation with no significant loss in efficiency throughout the study.

3.3.3.3 Separation of Cytochrome c Digests

The ability to perform protein analysis with the PolyE-323 coating was further evaluated through CE separation of tryptic digests of cytochrome c. Solution digestion was performed and the effect of cytochrome c-to-trypsin ratio and

digestion time on the digestion efficiency was studied. The cytochrome *c* peptides were prepared using the following procedure: a 10 μl protein sample, at a concentration ranging between 0.02 and 1 $\mu\text{g}/\mu\text{l}$ were mixed in vials with 2 μl of 100 mM NH_4HCO_3 and 1 μl of 0.2 $\mu\text{g}/\mu\text{l}$ trypsin, resulting in protein-to-enzyme ratios from 1:1 to 50:1 (w/w). The mixing solution was incubated at 37°C from 30 min to 2 h, and a portion of the digested sample was diluted in the running buffer (50mM NH_4Ac , pH 5) and injected into the coated capillary for separation.

The resulting electrochromatograms for the peptide fragments at different protein-to-enzyme ratios are shown in Figure 3.14. The peptide fragments from cytochrome *c* digestion are partially separated, and with higher protein enzyme ratio, more peptide peaks are detected. Two sets of peaks are worth noting in these chromatograms. First is the peak from the undigested intact protein (labeled with asterisks), which is only detected in the last two traces with a protein:trypsin ratio of 20:1 and 50:1. Second is the peak at about 2.6 min, which could be from trypsin autolysis products (indicated by arrows). With the increase of protein-to-enzyme ratio, the trypsin peak becomes smaller. These results are consistent with the known performance of trypsin digestion. Under our conditions, digestion using a cytochrome *c*-to-trypsin ratio of 10:1 produced the best digestion products, and thus was chosen for subsequent experiments.

Figure 3.15 shows CE separation of the solution digest of cytochrome *c* with different digestion times. A 2 h digestion period is sufficient to fully digest cytochrome *c* in free solution under the optimized conditions (protein-to-enzyme ratio 10:1).

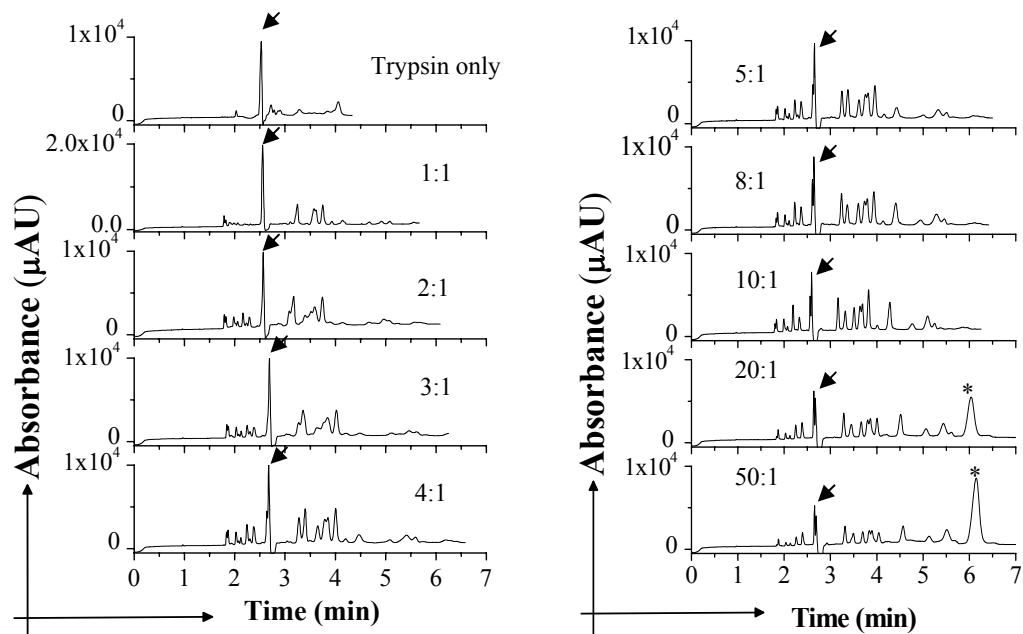


Figure 3.14 Electrochromatograms for CE separation of peptide digests of cytochrome *c* at different protein-to-enzyme ratio from 1:1 to 50:1. Intact cytochrome *c* peaks are denoted by asterisks and trypsin autolysis peaks are indicated with arrows. All the separation conditions are the same as those in Figure 3.12.

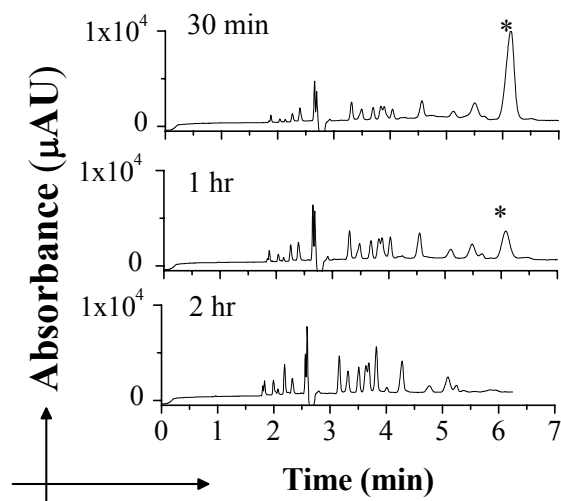


Figure 3.15 Electrochromatograms for CE separation of cytochrome *c* digests with different digestion time. Intact cytochrome *c* peaks are denoted by asterisks. All the separation conditions are the same as those in Figure 3.12.

3.4 Conclusions

In this work, the performance of four cationic coatings was evaluated in terms of EOF properties, durability, reproducibility, chemical stability, and compatibility with sheathless ESI-MS. A polyamine coating, PolyE-323 is shown to provide a stable, robust anodal EOF, which facilitates CE separation and detection of proteins and peptides in positive ESI-MS. The preparation of this coating is simple and straightforward, based on a simple rinsing procedure. The use of PolyE-323 coated capillaries allows fast separation of basic peptides and proteins, typically within a few minutes, with high efficiencies and good reproducibility. This excellent performance, which cannot be achieved with bare-fused silica capillaries, can be attributed to the stable EOF produced by the coating, as well as the elimination of analyte–wall interactions. Furthermore, the PolyE-323 coating was evaluated for compatibility with the monolith polymerization mixture. Contact of the surface coating with the monomer mixture leads to a small shift in analyte migration times, yet no obvious adverse effect in the analytical performance is observed.

3.5 References

- 1 Chen, L. X.; Lee, S.; Choo, J.; Lee, E. K. *J. Micromech. Microeng.* **2008**, *18*, 013001.
- 2 Laser, D. J.; Santiago, J. G. *J. Micromech. Microeng.* **2004**, *14*, R35–R64.
- 3 Doherty, E. A.; Meagher, R. J.; Albarghouthi, M. N.; Barron, A. E. *Electrophoresis* **2003**, *24*, 34–54.
- 4 Belder D.; and Ludwig M. *Electrophoresis*, **2003**, *24*, 3595–3606.
- 5 Dolnik, V. *Electrophoresis* **2004**, *25*, 3589–3601.

- 6 Yao, Y. J.; Khoo, K. S.; Chung, M. C. M.; Li, S. F. Y. *J. Chromatogr. A* **1994**, *680*, 431–435.
- 7 Dong, M.; Oda, R. P.; Strausbauch, M. A.; Wettstein, P. J.; Landers, J. P.; Miller, L. J. *Electrophoresis* **1997**, *18*, 1767–1774.
- 8 Li, M. X.; Liu, L.; Wu, J.-T.; Lubman, D. M. *Anal. Chem.* **1997**, *69*, 2451–2456.
- 9 Cordova, E.; Gao, J.; Whitesides, G. M.; *Anal. Chem.* **1997**, *69*, 1370–1379.
- 10 Pesek, J. J.; Matyska, M. T.; Swedberg, S.; Udivar, S. *Electrophoresis* **1999**, *20*, 2343–2348.
- 11 Amini, A.; Olofsson, I.-M. *J. Sep. Sci.* **2004**, *27*, 675–685.
- 12 Towns, J. K.; Regnier, F. E. *J. Chromatogr.* **1990**, *516*, 69–78.
- 13 Erim, F. B.; Cifuentes, A.; Poppe, H.; Kraak, J. C. *J. Chromatogr. A* **1995**, *708*, 356–361.
- 14 Nutku, M. S.; Erim, F. B. *J. High Resolut. Chromatogr.* **1998**, *21*, 505–508.
- 15 Wang, Y.; Dubin, P. L. *Anal. Chem.* **1999**, *71*, 3463–3468.
- 16 Morand, M.; Blass, D.; Kenndler, E. *J. Chromatogr. B* **1997**, *691*, 192–196.
- 17 Liu, Q.; Lin, F.; Hartwick, R. A. *J. Chromatogr. Sci.* **1997**, *36*, 126–130.
- 18 Sun, P.; Landman, A.; Hartwick, R. A. *J. Microcol. Sep.* **1994**, *6*, 403–407.
- 19 Yao, Y. J.; Li, S. F. Y. *J. Chromatogr. A* **1994**, *663*, 97–104.
- 20 Chiu, R. W.; Jimenez, J. C.; Monnig, C. A. *Anal. Chim. Acta* **1995**, *307*, 193–201.
- 21 Katayama, H.; Ishihama, Y.; Asakawa, N. *Anal. Chem.* **1998**, *70*, 5272–5277.
- 22 Haselberg, B.; de Jong, G. J.; Somsen, G. W. *J. Sep. Sci.* **2009**, *32*, 2408–2415.
- 23 Yassine, M. M.; Lucy, C. A. *Electrophoresis* **2006**, *27*, 3066–3074.
- 24 Yassine, M. M.; Lucy, C. A. *Anal. Chem.* **2005**, *77*, 620–625.
- 25 Hardenborg, E.; Zuberovic, A.; Ullsten, S.; Soderberg, L.; Heldin, E.; Markides, K. E. *J. Chromatogr. A* **2003**, *1003*, 217–221.
- 26 Ullsten, S.; Zuberovic, A.; Wetterhall, M.; Hardenborg, E.; Markides, K. E.; Bergquist, J. *Electrophoresis* **2004**, *25*, 2090–2099.
- 27 Harrison, D. J.; Manz, A.; Fan, Z. H.; Ludi, H.; Widmer, H. M. *Anal. Chem.* **1992**, *64*, 1926–1932.

- 28 Wright P. B.; Lister A. S.; Dorsey J. G. *Anal. Chem.* **1997**, *69*, 3251–3259.
- 29 Diress A. G.; Yassine M. M.; Lucy C. A. *Electrophoresis* **2007**, *28*, 1189–1196.
- 30 Yang, Y.; Li, C.; Kameoka, J.; Lee, K. H.; Craighead, H. G. *Lab on a Chip* **2005**, *5*, 869 – 876.
- 31 Bings, N. H.; Wang, C.; Skinner, C. D.; Colyer, C. L.; Thibault, P.; Harrison, D. J. *Anal. Chem.* **1999**, *71*, 3292–2396.
- 32 Shultz-Lockyear, L.L.; Colyer, C.L.; Fan, Z.H.; Roy, K.I.; Harrison, D.J. *Electrophoresis*, **1999**, *20*, 529–538.

Chapter 4

Solid-Phase Extraction and Enzymatic Digestion of Proteins on Porous Polymer Monolith with On-Line Coupling to ESI-MS

4.1 Introduction.....	107
4.2 Experimental Section.....	109
4.2.1 Chemicals and Materials.....	109
4.2.2 Instrumentation.....	110
4.2.3 Microchip-ESI Interface Construction.....	112
4.2.3.1 Device and Joint Preparation for Coupling Chip to ESI-MS.	112
4.2.3.2 Preparation of Capillary ESI Tips.....	115
4.2.4 Monolith Preparation and Chip Operation.....	118
4.3 Results and Discussion.....	120
4.3.1 On-Chip Solid-Phase Extraction of Proteins.....	120
4.3.1.1 Adsorption and Elution of Standard Proteins.....	120
4.3.1.2 Different Cytochrome <i>C</i> Loads.....	124
4.3.2 On-Bed Digestion of Proteins.....	127
4.3.2.1 Melittin.....	128
4.3.2.2 Cytochrome <i>c</i>	131
4.3.2.3 BSA.....	139
4.3.2.4 Myoglobin.....	143
4.4 Conclusion.....	145
4.5 References.....	147
4.6 Appendix.....	149

4.1 Introduction

The rapid expansion of proteomics has increased the demand for fast, sensitive and automated analysis methods. The combination of chip-based microfluidic system with mass spectrometry (MS) provides a powerful, information-rich analytical technique for proteomics applications [1-6]. On-line coupling of microchip to electrospray ionization mass spectrometry (ESI-MS) has, in particular, proven to be successful [7-9].

A fundamental step in sample preparation for protein identification by MS involves the digestion of proteins into peptides by a proteolytic enzyme, in most cases, by trypsin. Protein digestion by trypsin in free solution suffers from several drawbacks, such as low efficiency at low concentration and undesirable enzyme autodigestion [10]. The use of trypsin immobilized on a solid support offers several advantages including improved digestion speed, higher enzyme stability, fewer trypsin autolysis products, the possibility of repeated use, and ease of automation. To date, various supports have been reported for enzyme immobilization, such as silica [14] and polymeric particles [15, 16], silica [17, 18] and polymeric monolithic materials [19-21].

An alternative approach to improve the digestion efficiency of a diluted protein sample involves the adsorption of protein onto a hydrophobic support prior to digestion. Doucette *et al.* reported a bead-based protein digestion technique [22]. Proteins were first adsorbed onto reverse-phase chromatographic beads placed in a microcentrifuge tube, and then digested with trypsin solution while still bound to the beads. The resulting peptides were detected using

MALDI-TOF-MS by directly placing the beads on a MALDI target. They further improved this technique by packing the beads in a microcolumn [23], in which sample loading was accomplished by flowing protein solution through the packed beads, and the adsorbed protein is digested by flowing a trypsin solution through the microcolumn. The peptide fragments were subsequently released using high organic content buffer for detection by MALDI or ESI-MS.

In our work, digestion of immobilized protein sample with trypsin in solution phase was explored using polymer monolith as the solid support material. This method involves the adsorption of proteins onto the hydrophobic monolith, followed by digestion using buffered trypsin solution, and finally, peptide elution for ESI-MS analysis. In the multiplexed platform, the solid-phase extraction beds will first act as fraction collection traps to capture the separated proteins. In addition, sample enrichment before digestion on the SPE bed improves the digestion efficiency, which is critical for the digestion of low concentration samples. Moreover, the incorporation of SPE step prior to digestion allows for sample clean-up to remove matrix interferences. A problem associated with the digestion approach of using an immobilized trypsin microreactor is the buffer compatibility issue. For example, if the multiplexed system is used to process input from a CIEF column, some reagents or additives, such as the ampholyte are not compatible with trypsin digestion or ESI-MS. An incoming CIEF sample will contain proteins with a range of different local pHs, while trypsin will not function at acidic pH values. Using a SPE bed to capture the incoming protein samples, the undesired components can be easily removed by rinsing with buffer.

The use of photolithographic techniques to pattern the monolithic concentrators *in situ* is superior to methods using packed beads in a microchannel as it eliminates the tedious steps of frit fabrication and bead packing, and allows the preparation of SPE beds with better uniformity and reproducibility. Moreover, multiple monoliths can be simultaneously patterned in a microfluidic system to facilitate high-throughput sample preparation in parallel.

In this chapter, a single channel microfluidic device integrated with a solid-phase extraction (SPE) bed based on monolithic material was coupled on-line to ESI-MS for peptide mass mapping. The combination of the hydrophobic monolith developed in Chapter 2 and the PolyE-323 coating described in Chapter 3 was achieved in this device. META, a monomer with cationic groups was added to the monolith to match the EOF of the polyE-323 coating. The application of this device for on-chip SPE, on-bed tryptic digestion and protein identification was demonstrated for melittin, cytochrome *c*, myoglobin and bovine serum albumin (BSA).

4.2 Experimental Section

4.2.1 Chemicals and Materials

Melittin from honey bee venom (M.W. = 2846.46 g/mol), cytochrome *c* from horse heart (M.W. = 12,384 g/mol), myoglobin from horse heart (M.W. = 16,951 g/mol), bovine serum albumin (BSA, M.W. = 66,433 g/mol), trypsin from bovine pancreas, dithiothreitol (DTT), iodoacetamide, ammonium bicarbonate (NH₄HCO₃), acetonitrile (ACN, HPLC grade) were purchased from Sigma.

Formic acid was from Fluka and LC-MS grade methanol was from Riedel-de Haen. All aqueous solutions were prepared with Milli-Q water and filtered through 0.2 μm Nylon syringe filters (Chromatographic Specialties Inc. Brockville, Canada). The 2-propanol-based colloidal graphite used to coat the electrospray tip, consisting of approximately 5% proprietary thickener, 5% propylene glycol methyl ether, 5% *n*-butyl alcohol, 5% hexylene glycol, 50% 2-propanol, and 20% graphite, was obtained from Energy Beam Sciences (Agawam, MA).

4.2.2 Instrumentation

A PE/Sciex API 150 EX single quadrupole mass spectrometer (Perkin-Elmer/Sciex, Concord, ON, Canada) was used for the ESI-MS studies. All experiments were done in the positive ion mode. The experimental parameters were defined using the software accompanying the instrument: nebulizer gas = 0, curtain gas = 8, orifice = 35 V, focusing ring = 175 V, entrance quadrupole = -10 V, interquadrupole lens = -11 V, stubbies = -15 V, first resolving quadrupole = -11, deflector = -250 V, channel electron multiplier = 2,200 V. The distance from the electrospray tip to the orifice of the MS was 5-10 mm.

High voltage used to generate electrospray was supplied by the mass spectrometer to the ESI emitter by attaching a platinum wire to the conductive layer coated on the tip. Another power supply (referred to as blue box and described in Section 2.2.4), was used to provide the high voltages necessary for chip operation. Electrical contact with the reservoirs was made using platinum

wires. In-house written LabVIEW programs were used for computer control of the voltage application. In such a CE-ESI-MS system, two separate electrical circuits are involved: the first circuit is the CE electrical circuit, with inlet at the sample reservoir and outlet at the conductive ESI tip; the second circuit consists of the electrospray electrode and the MS inlet electrode. Thus the platinum electrode at the ESI emitter is shared by both circuits. The application of a conductive layer on the capillary tip helps to maintain the continuity of the electrophoresis circuit, while simultaneously provides the electrospray voltage. The optimal electrospray voltage varied from 3.2 to 3.5 kV, depending on the emitter performance and the flow rate.

For data acquisition, the mass spectrometer was scanned over the range m/z 500-1200, unless otherwise stated, with a step size of 0.5 amu and a dwell time of 1 ms. The results are presented in two ways: either as a total ion chromatogram (TIC) or as a mass-to-charge ratio (m/z) spectrum. The TIC represents the sum of all intensities in the range of m/z scanned, giving a count per second (c.p.s) versus time plot. Each time point in the TIC plot has an m/z spectrum associated with it, representing the m/z intensities at time t , shown as a c.p.s. versus m/z plot. These spectra can be extracted and averaged.

Peptides were identified by database searching using a combination of ExPASy (<http://us.expasy.org/>) and MS-Digest of Protein Prospector (<http://prospector.ucsf.edu/>). All search parameters are outlined in the Appendix. Sequence coverage is defined as the number of amino acid residues identified in the resulting peptides, divided by the total number of residues in the protein.

4.2.3 Microchip-ESI Interface Construction

4.2.3.1 Device and Joint Preparation for Coupling Chip to ESI-MS

Microfluidic devices with a simple straight microchannel (56 μm wide, 3.5 cm long and 20 μm deep) were used for the MS work in this chapter. An enlarged bed (140 μm wide and 1 mm long) was etched in the channel to accommodate the monolithic SPE bed (Figure 4.1a). The devices were fabricated using standard lithographic techniques, which have been described in Chapter 2. All the channels were etched into the bottom wafer, with access holes drilled in the top wafer for fluidic and electrical contact.

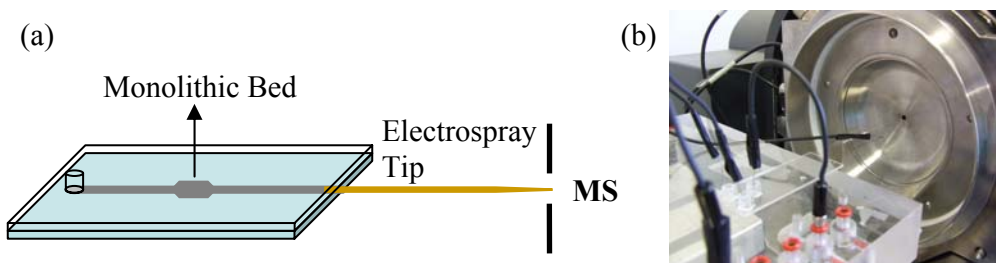


Figure 4.1 Schematic diagram of the sheathless microchip ESI-MS interface. (a) The microchip layout for ESI-MS. (b) Photograph showing experimental setup for coupling microchip to ESI-MS.

To facilitate the integration of microfluidic devices to ESI-MS, previous work done in this lab has reported a low dead volume junction enabling the direct insertion of ESI capillary tip to the chip device [24]. The construction of this low dead volume junction, which is essential for maintaining the separation efficiency achieved on chip, involves the drilling of a small hole into the edge of the device with a combination of pointed and flat-tipped drills. A capillary tip is then inserted into the drilled edge of the microdevice and serves as an electro spray emitter (Figure 4.1b). A detailed description of the procedure is illustrated in Figure 4.2 and described subsequently.

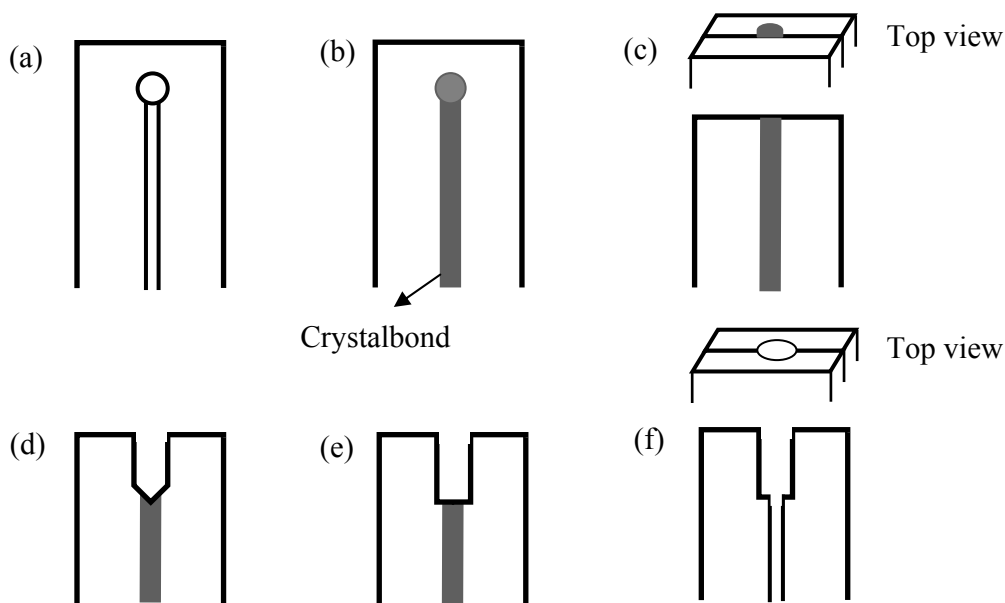


Figure 4.2 Drilling procedures for microchip/ESI-MS coupling. (a) The channel segment where the device was to be cut; (b) the microchannel was filled with Crystalbond; (c) the edge of the chip was cut, exposing the outlet channel; (d) a hole with conical-shaped bottom was drilled with a 368 μm pointed drill bit; (e) the bottom of the hole was flattened with a flat-tipped drill to reduce dead volume; (f) Crystalbond was removed from the channel.

First, the channel segment where the device was to be cut and drilled was filled with Crystalbond (#509, Aremco Products Inc.) in order to prevent glass shards produced during sawing and drilling from entering the microchannel. The device was placed on a hot plate (80 °C) and a drop of Crystalbond was put in the outlet reservoir, melted, and drawn into the microchannel using vacuum. The device was then cut perpendicularly with a diamond saw to expose the outlet channel at the end. The edge of the chip was polished with 220, 600, and 1200 grit silicon carbide abrasive paper to help visualize and locate the channel for easy alignment.

The device was mounted to a XY translation stage at the drilling station and positioned below the drill bit. Using a home-built microscope and side illumination, the drill bit (Kyocera Tycom) was aligned with the exposed channel.

A 368 μm drill bit (#29 series 225, TYCOM) was used for drilling to accommodate a 360 μm O.D. capillary tip. The drill (4000 RPM) was lowered until it started removing glass and created a small hole. The chip was then inspected to ensure that the small hole was centered on the channel, if not, the face was re-polished, and this process was repeated. The drill was raised from time to time during the drilling process, and a drop of water was placed on the edge for lubricating and cooling the drill bit until a hole of ~ 800 μm deep was obtained. The hole drilled with this commercial pointed drill bit has a conical-shaped bottom, which will introduce a significant dead volume at the capillary/chip connection. To reduce this volume, the pointed drill bit was replaced with a flat-tipped drill to create a flat-bottomed hole. The flat-tipped drills were prepared in-house by manually grinding the tip of the drill bit flat on silicon carbides abrasive paper.

The drilled end of the device was soaked in water overnight to allow the glass debris to settle out of the hole via gravity. After gentle heating, Crystalbond was removed from the channel by applying a vacuum to the drilled edge. For complete removal of the Crystalbond, acetone was pulled through the channel and the device was put in the thermal bonding oven overnight (settings as described in Section 2.2.2).

A capillary electrospray tip is then inserted into the flat-bottomed hole to create a low dead volume connection. The preparation of the capillary tip will be described in detail in the following section. In a system where the flow is driven electrokinetically, no obvious leakage at the microchip-capillary interface is

observed; therefore, there is no need to use epoxy or other adhesives to fix the tip. In case of degradation of conductive layer or tip clogging, the capillary tip can be easily removed and replaced, preserving the expensive microfluidic device.

4.2.3.2 Preparation of Capillary ESI Tips

In a sheathless ESI interface, the shape, size, and surface properties of the emitter are critical to obtain stable electrospray ionization. The production of gas-phase ions from ESI is more efficient when using a smaller sized emitter, thus, in most case the capillary electrospray emitters were pulled to form a tapered geometry, from which the liquid sprays to produce small, well-defined droplets. Several methods, including HF etching [25] and mechanical grinding [26], have been described for tapering the tip of a fused-silica capillary. In our study, the tip of the capillary was mechanically tapered to a fine point using a capillary puller. The polyamide coating was removed to create a small window in the middle of an 8-cm-long capillary (50 μm I.D., 360 μm O.D.). The capillary was then loaded into a capillary puller (P-2000 Laser Based Micropipette Puller, Sutter Instrument Company) with the window aligned with the laser; pulling resulted in a tapered end with a inner diameter around 3 μm (settings: Heat = 260, Velocity = 42, Delay = 30); the 3 μm tip was opened to around 10 μm by careful scratching with a ceramic capillary cutter.

On the other hand, a conductive coating material on the emitter outer surface is required to provide electrical contact for both electrospray and microchip operation. In our work, two coating materials, gold and colloidal graphite, were

employed as the conductive layer, and their stability and durability were compared.

Gold is the most commonly used conductive material on ESI emitters, and it is often sputtered onto the ESI tip using additional adhesive materials in order to enhance the stability. Briefly, the gold coating was formed by loading the tapered capillary ESI tips into the Lesker two-target sputtering system. With the system under vacuum (around 1.5×10^{-6} Torr), 30 nm chrome and 150 nm gold were sputtered on the tip surface. Although these chromium-gold coated fused silica capillary tips have been used extensively for sheathless ESI, this style of emitter is susceptible to degradation as a result of electrical discharge and electrochemical stress, and thus suffers from rather short lifetime. In our operation, tips coated with this procedure can only last about two to three days. The loss of the conductive coating is likely due to a loss of chromium adhesive layer under the gold film. Such a loss could occur via small defects or cracks in the gold layer through which the chromium layer is exposed to the electrolyte and electrochemically dissolved. The gold coating tends to flake off as the adhesive layer is oxidized. The loss of gold coating will render the tip unstable due to the degradation of electrical contact, and eventually the CE-ESI/MS operation becomes problematic. Furthermore, the production of these emitters requires special equipment and is often tedious, time-consuming, and expensive.

An alternative emitter coating using colloidal graphite, which was developed by Zhu and co-workers [27], was also explored in our work in an effort to prepare ESI emitters with higher durability. The procedure for applying the colloidal

graphite coating on the capillary tip is rather simple following the procedure described in the literature. Briefly, the tapered tip, approximately 4 cm in length, was cleaned with acetone to remove dust. The commercially available 2-propanol-based colloidal graphite was brushed gently on the tip to form a fine layer. To prevent clogging during the coating procedure, a low flow of nitrogen was applied through the capillary. The fabrication involves a single step and requires less than 2 min. Full cure properties develop in ~2 h at room temperature and then the tip is ready for use. Compared to a gold-coated capillary, fabrication of this emitter is simple, fast, and inexpensive. In addition, this emitter has higher durability and a longer lifetime of over one week. Although the attachment of a platinum electrode to the graphite-coated capillary tip would occasionally scratch the coating layer, this problem can be solved by re-coating the capillary tip with colloidal graphite.

An additional advantage of this emitter is the possibility of applying the conductive coating on capillaries which already have a derivatized inner surface. In contrast to methods that require curing at high temperature, the mild condition will be beneficial to capillary inner wall coatings, which are usually heat-sensitive and may spoil during high temperature curing. With this property, we adjusted the steps involved in preparation of the ESI tip by coating the inner surface of a long capillary with the PolyE-323 cationic polymer first; then cutting the coated capillary into 8-cm-long segments, and tapering them with the capillary puller to form the tip; and finally, applying the conductive coating on the sharpened tip. This method allows the derivatization of the inner surface of a batch of capillary tips at the same time, instead of treating them one by one. Moreover, it minimized

the probability of tip clogging during the inner wall coating process, which is another problem associated with the gold-coated capillary tips, as the tapered tip with a narrow opening is easily blocked by the sticky polymer coating reagent.

4.2.4 Monolith Preparation and Chip Operation

For all the studies in this chapter, the BMA-based monolithic polymer with a positively derivatized surface was prepared within the microchannel with #18 in Table 2.1 following the procedures described in Section 2.2.3. The optimization of the polymerization conditions for this positively-charged monolith containing META has been described in Section 2.3.2.4.

In order to create an anodal EOF to drive fluids through the microdevice and facilitate a positive electrospray, the inner surface of the microchannel and capillary tips were modified with the cationic polymer, polyE-323. Synthesis and coating of PolyE-323 were carried out as described previously in Section 3.2.3.

EOF flow rate generated by this coating can be estimated from the EOF mobility ($4.22 \times 10^{-4} \text{ cm}^2/\text{Vs}$ in a polyE-323 coated channel, from Section 3.3.1.1), the cross-sectional area of the microchannel ($9.48 \times 10^{-10} \text{ m}^2$), and the electric field in the channel. Because the microchannel and the capillary tip are two segments of different cross-sectional areas, the electric field in the microchannel is calculated from the fraction (0.45) of the applied voltage between the sample reservoir and the electrospray tip.

For SPE studies with MS detection, three standard proteins, cytochrome *c*, myoglobin, and BSA were tested. The proteins were dissolved in 5 mM formic

acid in siliconized microcentrifuge tubes to the desired concentrations. During the enrichment step, the protein solution was loaded in the sample reservoir and electrokinetically transported onto the monolithic polymer by applying -2.5 kV at the sample reservoir and 3.2 kV at the electrospray tip. EOF was calculated to be 0.21 $\mu\text{L}/\text{min}$ at this voltage combination. After this loading step, 5 mM formic acid buffer was pumped through the channel for 5 min to wash the sample that remained within the channel onto the bed. Finally, elution buffer replaced the aqueous buffer in the reservoir to release the concentrated sample for ESI-MS detection.

For off-chip digestion of protein in free solution, proteins were diluted in the digestion buffer (50 mM of NH_4HCO_3 , pH 8.0) to the desired concentrations. An aliquot of trypsin was added to the protein solution so that the protein-to-enzyme ratio was maintained at 10:1 (w/w). The mixed solution was incubated at 37 °C for 2 h, and then a portion of the digested sample was loaded in sample reservoir and delivered by electrokinetic infusion for ESI-MS analysis.

For on-chip protein digestion, the SPE bed was first saturated with the protein of interest (0.10 mg/mL Melittin, 0.124 mg/mL cytochrome c, and 0.33 mg/mL BSA, and 0.17 mg/mL myoglobin, all proteins were diluted in 5 mM formic acid) during sample loading step. 20 mM NH_4HCO_3 (pH 8.0) buffer was then introduced into sample reservoir and a 5 min buffer rinse was conducted to unbound protein in solution. The adsorbed protein was then digested by flowing 0.31 mg/mL trypsin solution in 20 mM NH_4HCO_3 through the column; a small volume of enzyme solution was left in the channel and digestion was allowed to

proceed under stop-flow conditions for 30 min. Following digestion, the column was washed with 5 mM formic acid for 5 min to remove trypsin solution left in the column, and finally tryptic peptides were eluted with 5 mM formic acid containing 60% ACN and detected by ESI-MS. The flows of solution in the channel during sample loading, buffer rinsing, trypsin delivering and elution were all driven by electrokinetic force, with -3 kV at the reservoir and 3.2 -3.5 kV on the electrospray tip.

BSA was reduced in solution to break disulfide bonds before digestion. 1 mL of 100 μ M BSA solution was mixed with 250 μ L of 45 mM DTT, and the reaction was allowed to proceed at 50 $^{\circ}$ C for 20 min. The cysteines were then capped to prevent reformation of disulfide bond using 250 μ L of 100 mM iodoacetamide with incubation at room temperature in the dark for a further 20 min.

4.3 Results and Discussion

4.3.1 On-Chip Solid-Phase Extraction of Proteins

4.3.1.1 Adsorption and Elution of Standard Proteins

In chapter 2, we demonstrated the potential of the hydrophobic monolithic SPE bed for protein preconcentration using fluorescently labeled BSA. Here, further tests were performed to ascertain the SPE behavior of the hydrophobic monolithic bed for proteins using three model proteins, cytochrome *c*, myoglobin, and BSA.

Studies were conducted in PolyE-323 coated single channel devices with a 1-mm-long hydrophobic monolithic polymer bed integrated in the microchannel. In

order to be compatible with the cationic coating which generates anodal EOF, the charge of the monolith was adjusted by adding the co-monomer META into the polymerization mixture to provide positive charged functionalities (#18 in Table 2.1). The optimization of polymerization conditions such as META concentrations for the preparation of this positively-charged monolith has been described in Section 2.3.2.4.

For the enrichment step, a protein sample dissolved in aqueous buffer was electrokinetically transported onto the monolithic bed. After rinsing the channel to remove nonbound proteins, buffer with 60% ACN was pumped through the channel to release sample from the monolithic bed. The elution traces were monitored by ESI-MS through the integrated electrospray tip.

The monolithic bed retains the protein well under aqueous conditions, while at high organic content, the protein partitions between the hydrophobic bed and elution buffer, resulting in the elution profiles shown in Figure 4.3a and b for cytochrome *c* and myoglobin, respectively. Comparing the two elution profiles, the myoglobin eluted later with a wider peak and significant tailing. In contrast, rapid desorption of cytochrome *c* results in a sharp elution peak with no tailing. The different elution behavior of cytochrome *c* and myoglobin can be attributed to the difference in their affinity to the hydrophobic surface, as myoglobin exhibits a more hydrophobic nature.

The representative m/z spectra for cytochrome *c* and myoglobin associated with protein elution peaks are shown on the right side in Figure 4.3. Both are characterized by an envelope of peaks, each peak representing a different charge

state of the analyte. Table 4.3 of the appendix shows the charge states and the associated m/z values for cytochrome *c* and myoglobin. Both proteins have a heme group in their structures: for myoglobin, the heme group is non-covalently bound to apo-myoglobin (myoglobin that lacks its heme group). The peak at 616.5 is from the heme group, and a set of peaks with multiple charges belongs to apo-myoglobin. While for cytochrome *c*, the heme group is covalently attached through cysteine residues at position 14 and 17, thus, no peak corresponding to the heme group is observed, and peaks represent the different cytochrome *c* charge states.

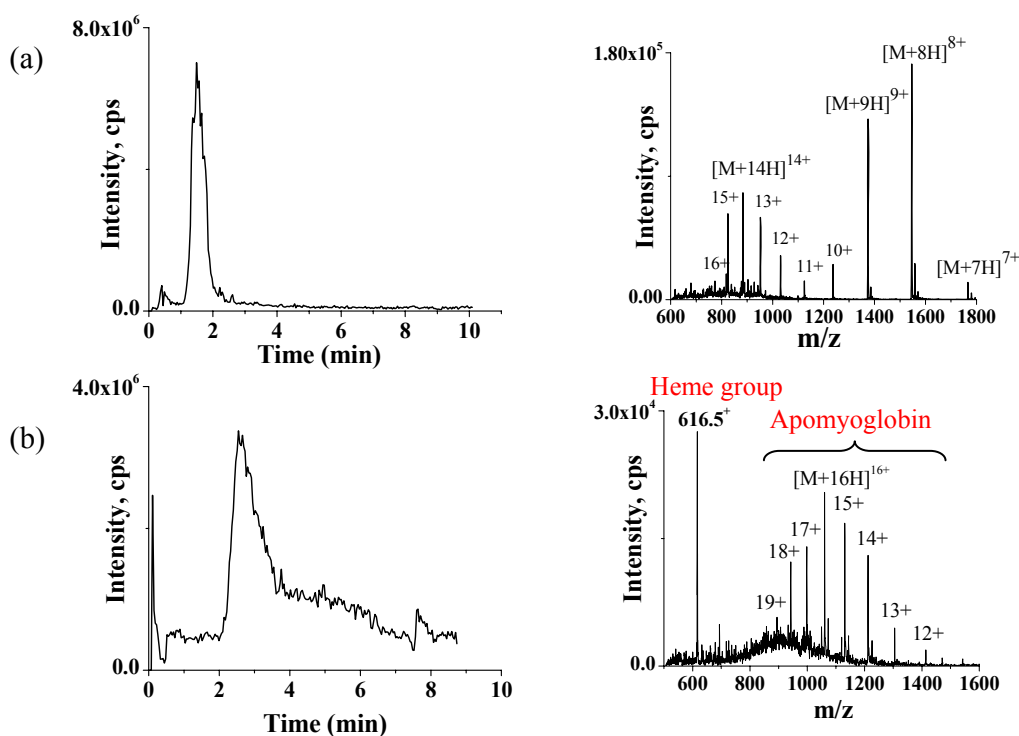


Figure 4.3 Total ion chromatograms for on-chip SPE preconcentration and elution of (a) cytochrome *c* and (b) myoglobin. Loading buffer: 5 mM formic acid, elution buffer: 5 mM formic acid with 60% ACN. Protein concentration: 1 μ M. All solutions were driven by electrokinetic force, with -2.5 kV at the sample reservoir and 3.2 kV on the electrospray tip. The right side shows the mass spectra with the charge states labeled for each mass peak. The microchannel was modified with PolyE-323 cationic coating. The positively-charged monolith was prepared according to #18 in Table 2.1.

The multiple charging phenomenon enables the determination of molecular weight of proteins. An average molecular weight of 12360.1 ± 1.4 Da is obtained for cytochrome *c*. The difference between this measured MW and the value calculated from the amino acid sequence (12360.3 Da) is 0.2 Da (16 ppm error). The molecular weight measured for myoglobin is 16953.5 ± 3.0 Da, and the difference from the value calculated from amino acid sequence (16952.5Da) is 1.0 Da (59 ppm error). Thus, ESI mass spectra of proteins provide rapid and accurate information on the molecular weight.

Another standard protein used to test the SPE performance of the monolith was BSA. This large protein is also strongly adsorbed onto the monolithic bed, and is later released using a 60% ACN buffer, resulting in the elution profile shown in Figure 4.4 (left). ESI-MS spectrum of BSA in Figure 4.3 (right) also displays the characteristic envelope of peaks with a typically bell-shaped distribution, each peak representing a different charge state from + 38 to +64.

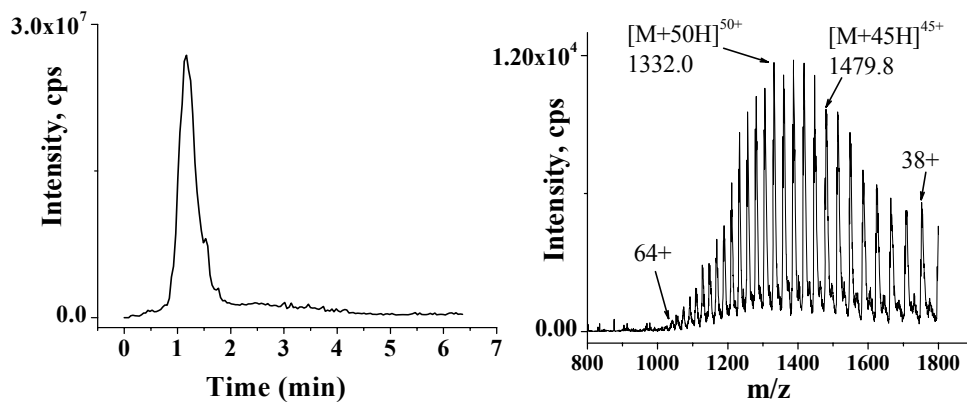


Figure 4.4 Total ion chromatograms (left) and representative mass spectrum (right) for on-chip SPE preconcentration and elution of BSA. The baseline shows a ‘hump’ of chemical noise under the spectrum. The microchannel was modified with PolyE-323 cationic coating. The positively-charged monolith was prepared according to #18 in Table 2.1.

It is worth noting that there is a broad hump in the baseline in the mass spectra of all three proteins. This background signal is most likely from chemical noise originating from solvent clusters and other species which are not part of the sample. Similar phenomena have been reported by O'Connor *et al.* [28], who showed that this chemical noise baseline hump could be reduced substantially by aggressive desolvation methods in the electrospray and nozzle skimmer regions of the instrument, using a home-built, heated metal capillary.

4.3.1.2 Different Cytochrome *C* Loads

The solid-phase extraction behavior of the monolithic bed was further evaluated by loading different amounts of cytochrome *c* onto the column. With - 2.0 kV at the sample reservoir and 3.2 kV at the electrospray tip, EOF was calculated to be 0.19 $\mu\text{L}/\text{min}$ from the EOF mobility and electric field in the channel. The loading times, cytochrome *c* concentrations and the final loads are summarized in Table 4.1.

Table 4.1 Different amounts of cytochrome *c* loaded onto the monolithic column.

	Flow rate	Loading Time	Concentration	Final Load
a	0.19 $\mu\text{L}/\text{min}$	5 min	0.00124 mg/mL	0.00118 μg
b	0.19 $\mu\text{L}/\text{min}$	5 min	0.0124 mg/mL	0.0118 μg
c	0.19 $\mu\text{L}/\text{min}$	10 min	0.0124 mg/mL	0.0236 μg

During the loading step, no sample breakthrough was observed. After each loading, the column was rinsed with 5 mM formic acid, and the adsorbed cytochrome *c* was eluted with 5 mM formic acid in 60% ACN. Figure 4.5 a-c shows elution traces with different cytochrome *c* loads.

The reproducibility of the preconcentration process was investigated and the experimental results with the same monolithic bed show reproducible extraction and elution of the analyte. The experiment with a cytochrome *c* load of 0.0236 μg was repeated four times, the RSDs for peak areas and peak heights are 4.5% and 7.6%. The repeatability of the elution time is also satisfactory with a RSD of 2.8%. Figure 4.5d presents peak areas versus protein loads; the linear relationship indicates that the monolithic bed is not saturated under these studied conditions.

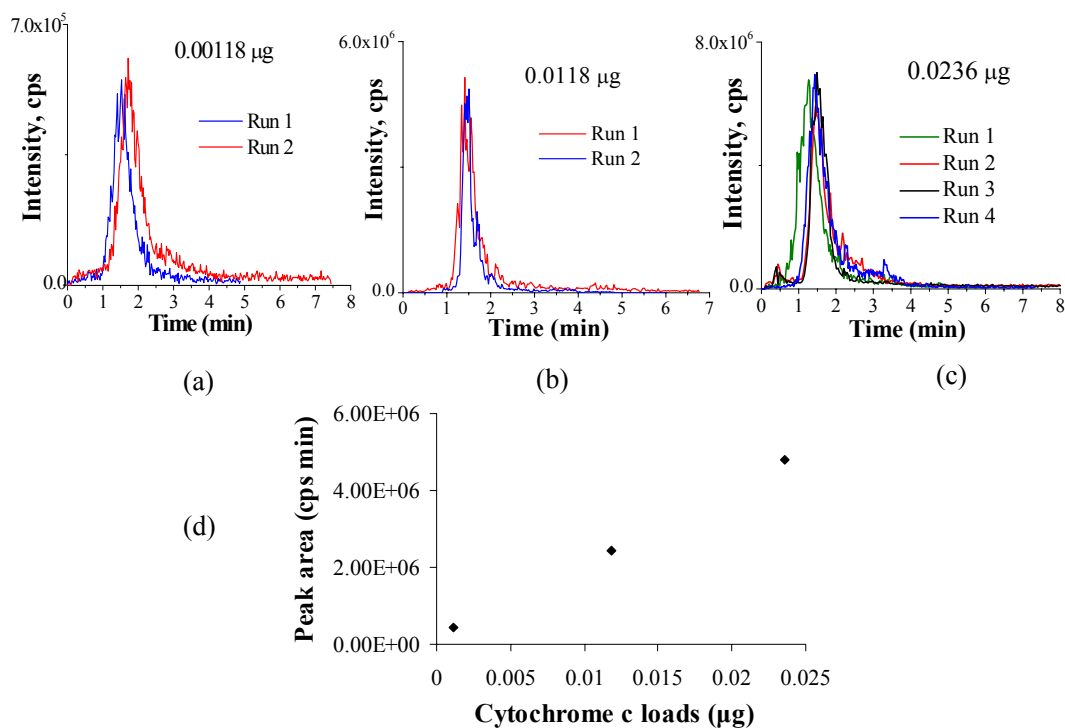


Figure 4.5 TICs for on-chip SPE preconcentration and elution of cytochrome *c* with three different sample loads. (a) 0.00118 μg ; (b) 0.0118 μg ; (c) 0.0236 μg . (d) peak areas versus three different cytochrome *c* loads. All the conditions are the same as those in Figure 4.3.

The total capacity of the monolithic SPE bed was determined using frontal analysis. The breakthrough curves were measured by continuously delivering 5 μM aqueous solution of cytochrome *c* through the bed at an EOF rate of 0.19 $\mu\text{L}/\text{min}$ with a voltage combination of -2.0 kV at the sample reservoir and 3.2 kV

at the electrospray tip (Figure 4.6, curve b). In order to account for the time needed for analyte to flow through the channel and capillary tip, the same sample solution was driven through an open channel without the monolithic bed and the signal was recorded by ESI-MS (Figure 4.6, curve a). The corrected breakthrough time was taken as the time needed for the signal to reach 50% of its maximum, subtracting the time required for the sample to reach the electrospray tip.

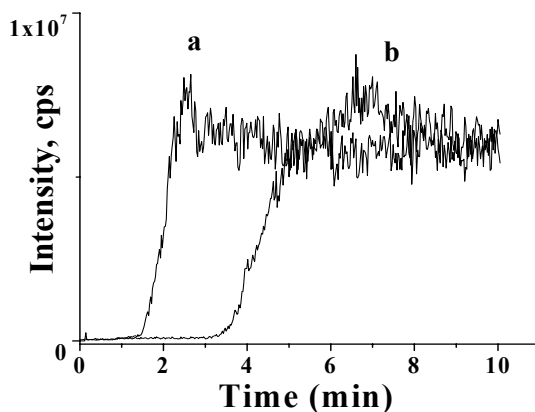


Figure 4.6 Breakthrough curve for sample capacity measurement. Conditions: test analyte solution: 5 μM cytochrome *c* in 5 mM formic acid; flow rate: 0.19 $\mu\text{L}/\text{min}$. The analyte solution was delivered through a channel without (curve a) and with (curve b) the monolithic bed. The microchannel was modified with PolyE-323 cationic coating. The positively-charged monolith was prepared following #18 in Table 2.1.

The overall capacity of the monolithic bed was calculated, based on the time delay to reach 50% of the ion intensity maximum, the flow rate, and the concentration, to be about 30 ng (2.4 pmol) of cytochrome *c*, corresponding to a specific capacity of 11.5 mg/mL of column volume or 0.92 mmol per liter of bed. A capacity of 7.6 pmol BODIPY was obtained for the BMA-based neutral monolith, as described in Section 2.3.4.1. In the same section, we also discussed the comparison of capacity of this neutral monolith to values reported for monoliths in the literature, and to capacities reported for alternative approaches

using either the modification of channel walls or the packing of beads in a portion of the channel, since all these SPE systems used small molecules as probes. A higher bed capacity can be achieved by increasing the bed volume; however, this relative low bed capacity had a beneficial effect on tryptic digestion where bed saturation is required, as will be discussed in the next section.

4.3.2 On-Bed Digestion of Proteins

After the initial SPE tests to ascertain the hydrophobic behavior of the monolithic bed, the next step is to perform enzymatic digestion, followed by the identification of the resulting peptide fragments using MS. The performance of this method was examined through on-bed protein digestion of melittin, cytochrome *c*, BSA, and myoglobin.

All Studies in this section were conducted in PolyE-323 coated single channel devices with a 1-mm-long hydrophobic monolithic polymer bed integrated in the microchannel. The following experimental protocol was used for all on-bed digestion experiments discussed in this section. The protein of interest in 5 mM formic acid buffer at desired concentrations (the protein concentrations are indicated in the captions of the corresponding figures) was flowed into the microdevice, followed by 5 min buffer flush with 20 mM NH_4HCO_3 . The channel was then filled with 0.31 mg/mL trypsin solution in 20 mM NH_4HCO_3 and digestion under stop-flow conditions was allowed to proceed for 30 min. To reduce the detection of trypsin by-product, the bed was washed with 5 mM formic acid for 5 min. And finally, the elution buffer (5 mM formic acid with 60% CAN)

was introduced into the channel to release peptides adsorbed on the bed for MS analysis. During all these steps, we implemented liquid pumping by EOF, and the EOF flow rate was estimated to be 0.22 $\mu\text{L}/\text{min}$ in aqueous buffer solution with -3.0 kV at the sample reservoir and 3.2 kV at the ESI tip, and EOF in the elution buffer containing 60% ACN was 0.13 $\mu\text{L}/\text{min}$ using the same voltage scheme as during sample loading and buffer rinsing.

4.3.2.1 Melittin

Melittin is a peptide consisting of 26 amino acids with the following sequence: GIGAVLKVLTTGLPALISWIKRKRQQ-NH₂. It possesses several basic amino acids which enable the formation of only a few tryptic peptide fragments. Xue *et al.* showed the use of melittin for probing the site specificity of trypsin as a function of time [29]. Here, we chose melittin as a model substrate to demonstrate the microchip performance in integrating the proteolysis digestion step, with direct analysis of the resulting peptides by ESI-MS.

Figure 4.7 shows a TIC (left) of elution of peptide fragments obtained from on-bed digestion of melittin and the corresponding mass spectrum (right). Melittin is digested to three main components, the T₁ and T₂ peptide products and a T₂R intermediate digestion component. The amino acid sequences and masses of these peptide fragments are presented in Table 4.2. After 30 min of digestion, no intact melittin is observed and 85% sequence coverage is obtained, meaning that the peptides identified from the mass spectrum account for 85% of the total amino acids present in the full sequence of the intact melittin.

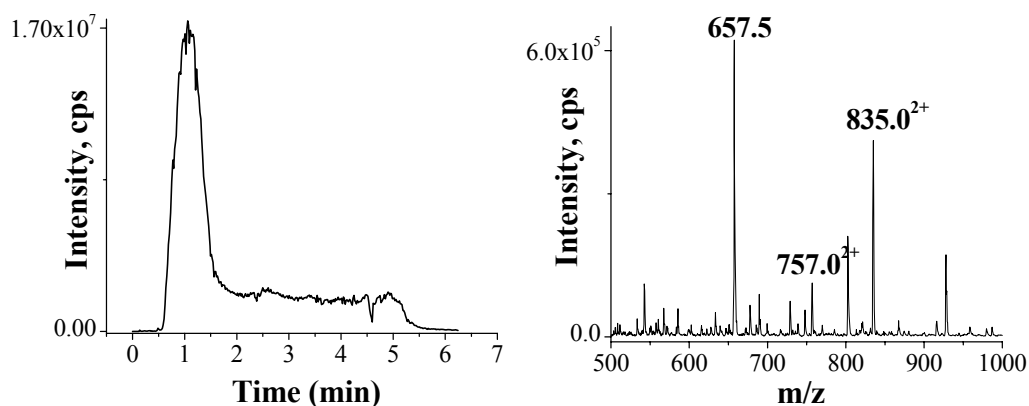


Figure 4.7 TIC (left) and mass spectrum (right) of elution of peptide fragments from on-bed tryptic digestion of melittin. The mass spectrum is an average of the data in the elution peak region in the TIC. Conditions: Loading: 0.1 mg/mL melittin in 5 mM formic acid to saturate the monolithic bed; washing: 20 mM MH_4HCO_3 (pH 8.0) for 5 min; digestion: 0.31 mg/mL trypsin solution in 20 mM MH_4HCO_3 under stop-flow conditions for 30 min; Washing: 5 mM formic acid for 5 min to remove trypsin solution left in the column; elution: 5 mM formic acid with 60% ACN.

Table 4.2 Amino acid sequences and masses of the peptide fragments of melittin

Fragment	Peptide sequence	m/z
T ₁	GIGAVLK	657.5
T ₂	VLTTGLPALISWIK	757.0 ²⁺
T ₂ R	VLTTGLPALISWIKR	835.0 ²⁺

The loss of several residues could be explained by the fact that some of the resulting peptide fragments are very short with masses out of our detection range. The extracted ion chromatograms (EICs) of the three components in Figure 4.8 show very small difference in elution time (± 4 s), indicating that these peptides experienced little chromatographic behavior in the bed and eluted at almost the same time in a single peak. The ability to achieve flash elution off the SPE bed within a short timeframe is very important in a multiplexed analysis platform, as will be discussed in more detail in the next section.

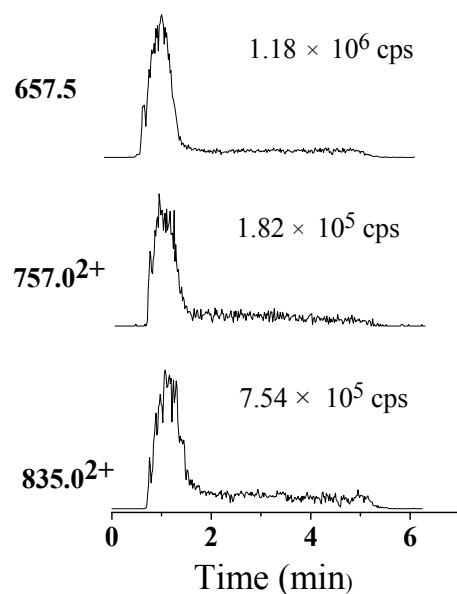


Figure 4.8 *Extracted ion chromatograms of the three tryptic peptide components of melittin.*

The column saturation during the initial sample loading stage is important to prevent enzyme denaturation and minimize trypsin autolysis for on-bed tryptic digestion. Aguilar *et al.* demonstrated that the incomplete coverage of the surface of the reversed-phase sorbent material resulted in adsorption of the trypsin, which in turn prevented digestion from occurring [30]. Thus, in our experiments, the monolithic polymer surface was saturated with the protein of interest before passing enzyme solution through the column. In this case, a short bed with a relatively lower bed capacity is a benefit, especially for analysis of low abundance proteins, as it requires less amount of sample to achieve complete coverage of the sorbent material.

4.3.2.2 Cytochrome *c*

The performance of the on-bed tryptic digestion system was further examined using a well-characterized model protein, cytochrome *c*, which is easy to work with, digest, and identify. The on-bed digestion procedure involves the following five steps and the detailed experimental procedure was outlined in Section 4.2.4.

1. Adsorption of protein onto the monolithic material;
2. Removal of nonbound protein;
3. Digestion of adsorbed protein with trypsin;
4. Removal of trypsin solution and nonbound peptide fragments;
5. Elution of bound peptides.

The whole process was monitored by observing the channel eluent using MS in each step, and the resulting TICs and mass spectra are shown in Figure 4.9. First, cytochrome *c* was loaded on the monolithic bed by continuously delivering a 10 μM protein solution through the microchannel at a flow rate of 0.22 $\mu\text{L}/\text{min}$. The TIC in Figure 4.9a demonstrates the breakthrough of protein sample, indicating the saturation of the monolithic SPE bed. The capacity of this positively-charged monolith was estimated from the breakthrough curve to be 2.2 pmol, which is close to the value we obtained in Section 4.3.1.3. The mass spectrum in the inset shows the charge state envelope of cytochrome *c*.

After sample loading, the bed was washed with 20 mM NH_4HCO_3 buffer at a flow rate of 0.22 $\mu\text{L}/\text{min}$ for 5 min to remove nonbound protein. The resulting TIC spectrum scanned over the range of 500-1200 is shown in Figure 4.9b. The m/z spectrum associated with the 3-5 minute region in the inset showed several

peaks from buffer impurities. The dramatic decrease of signal intensity at about 1 min gave an estimate of the required column wash volume of 0.22 μL . This indicates that a 5 min rinsing time is more than sufficient to remove proteins remaining in the solution.

A 0.31 mg/mL trypsin solution in 20 mM NH_4HCO_3 , was then flowed over the adsorbed protein in the microdevice, and digestion proceeded for 30 min under stop-flow conditions. The mass spectrum collected during this step shows several peptide peaks from trypsin autodigestion in the solution, marked by “T” in Figure 4.9c. Table 4.4 in the Appendix to this chapter shows a list of trypsin-related peaks.

To reduce the interference from trypsin autodigestion peptide peaks, the bed was washed with 5 mM formic acid buffer for 5 min at a flow rate of 0.22 $\mu\text{L}/\text{min}$, corresponding to a wash volume of 1.1 μL . After trypsin cleavage, some of the peptide fragments may not bind to the monolith, and in this washing step, these nonbound peptide fragments will be flushed out. This is confirmed through analysis of the ESI-MS signal during the washing step. As is shown in the mass spectrum in Figure 4.9d, three cytochrome *c* tryptic peptide peaks are observed, the 562.5 corresponds to peptide from position 99 to 104, 589.5 belongs to peptides from position 1 to 5, 817.5 is a doubly charged peptide from position 14 to 22. The results indicate that these sequence regions are not part of the hydrophobic binding domain, and thus are released during washing step after tryptic cleavage.

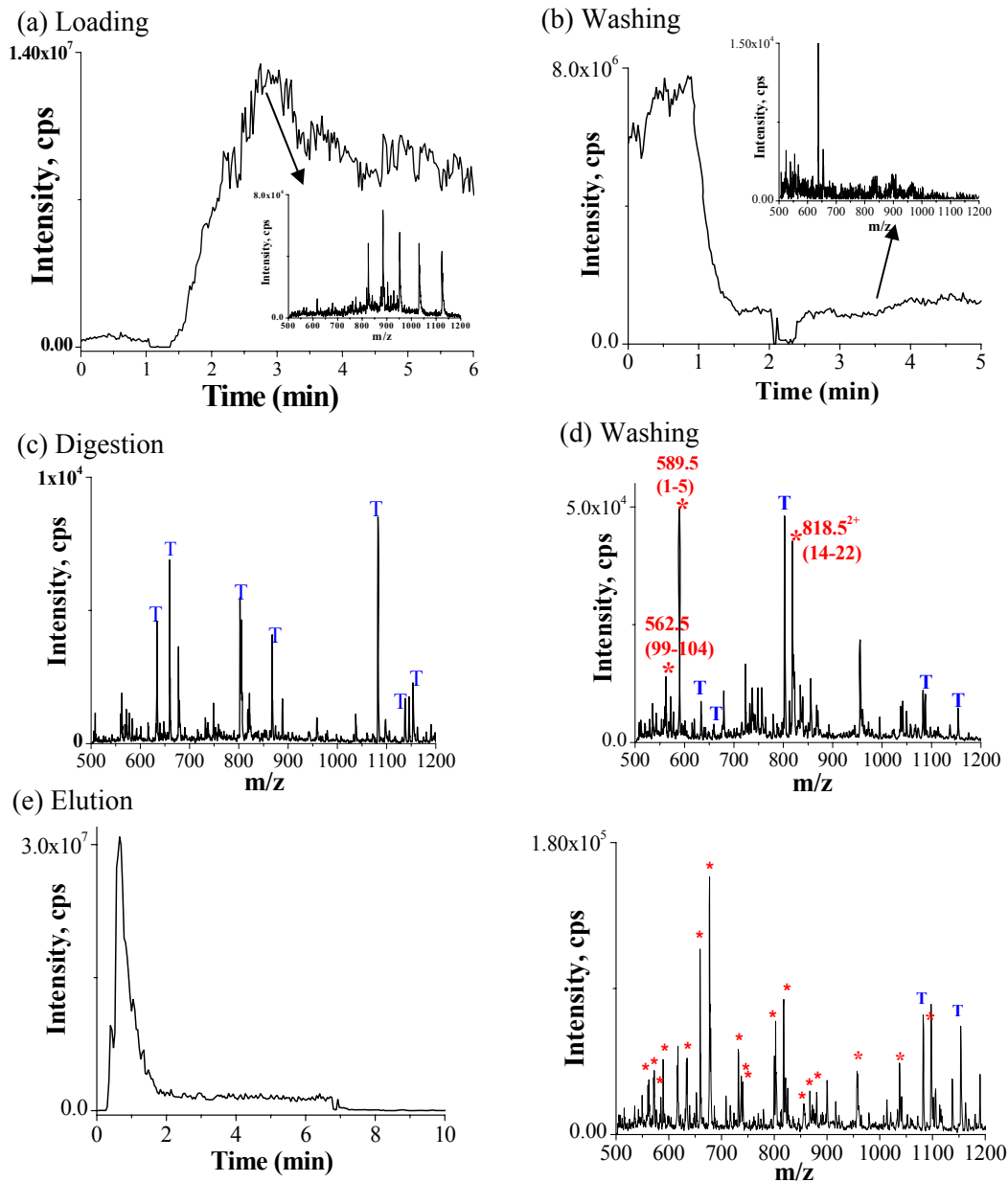


Figure 4.9 TICs and mass spectra obtained during each step of on-bed digestion of cytochrome c. (a) TIC obtained during sample loading step showing the saturation of the monolithic SPE bed. The mass spectrum in the inset shows the charge state envelope of cytochrome c; (b) TIC spectrum obtained during washing step showing the removal of nonbound cytochrome c. The mass spectrum in the inset shows signal from buffer impurities; (c) ESI-MS spectrum extracted when flowing trypsin solution through the column, showing peaks from trypsin autolysis; (d) ESI-MS spectrum extracted during the washing step showing signal from nonbound peptide fragments; (e) TIC spectrum obtained during elution. Mass spectrum is extracted from the peak region. T = peptide fragments from trypsin autolysis, * = peptide fragments from cytochrome c. All the other conditions are the same as those in Figure 4.7.

Finally, the remaining tryptic peptides bound to the monolith were eluted with 5 mM formic acid containing 60% ACN and detected by ESI-MS. The peak in the TIC in Figure 4.9e (left) shows the elution of the tryptic peptides. In the mass spectrum, “*” refers to tryptic peptide fragments from cytochrome *c*, “T” refers to peptides resulting from trypsin autolysis. Table 4.5 in the Appendix lists the identified cytochrome *c* peptides with their associated *m/z* values and amino acid sequences. The final percent coverage for the on-bed digestion of cytochrome *c* is 88%. This result compares well to data published by Craft *et al.* for on-bead cytochrome *c* digestion within a microcolumn, where 91% sequence coverage was obtained [23].

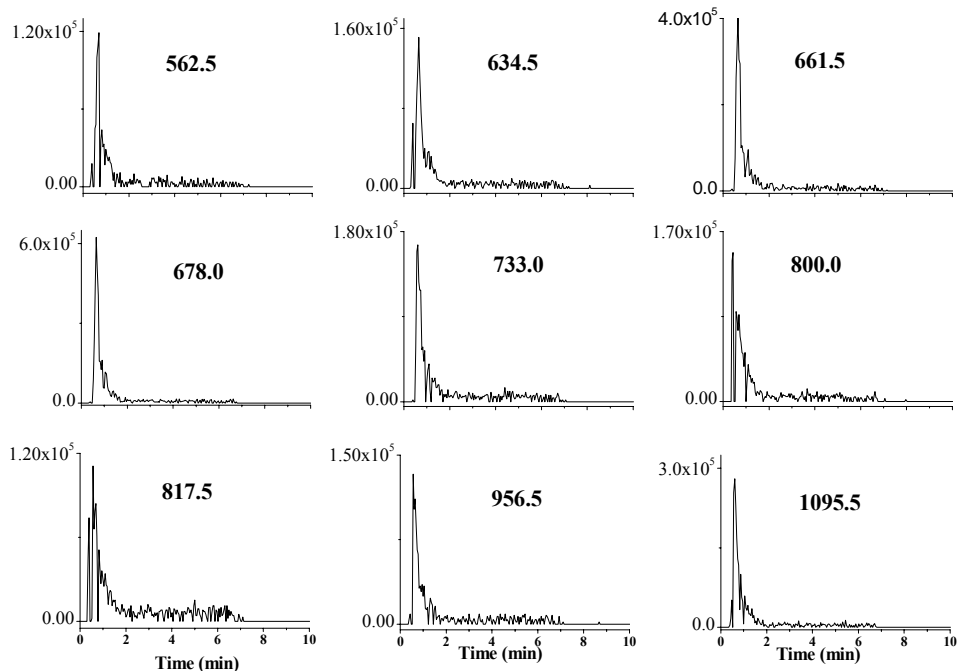


Figure 4.10 EICs for several of the most intense cytochrome *c* peptides. The *m/z* values of these peptides are noted above each plot.

The TIC of the tryptic digest elution demonstrates that all peptide fragments eluted in a single peak with a peak width of ~0.5 min (FWHM). EICs are extracted for several of the most intense cytochrome *c* peptides and are shown in

Figure 4.10. One can see that the various peptides exhibit similar elution profiles with differences of ± 7 s in the elution times.

This result is contrary to those obtained in earlier studies in a bead-based system [31]. In this system, the SPE bed was etched in the top wafer and aligned with the flow channels in the bottom wafer. The bed was designed to be 400 μm wide, 2 mm long and etched to 100 μm , resulting a bed volume of 0.111 μL . Oasis[®] HLB Plus beads (60 μm) from Waters were packed into the bed and served as sorbent material. The high SPE capacity of the bed resulting from the large bed volume leads to some adverse effects in peptide elution: peptides experienced chromatographic behavior in the 2-mm microbead bed and eluted as large, broad peaks with different elution profiles at different times, making pressure-driven analysis on the multiplexed platform difficult. By using a smaller SPE bed, as in our monolith-based system (100 μm wide, 20 μm deep, 1 mm long, with a bed volume of ~ 2.6 nL), the hydrophobic surface of the sorbent material is more readily saturated by small sample loads. The low bed capacity facilitates a flash elution off the column within a short timeframe, a desirable feature for multiplexed analysis.

An off-chip digestion in free solution was performed following the protocol outlined in section 4.2.4 to allow a comparison with on-bed digestion. Free solution digestion was performed under the optimized conditions discussed in Section 3.3.3.3 in Chapter 3 with a cytochrome *c*-to-trypsin ratio of 10:1, and digestion time of 2 h. As shown in the mass spectrum of Figure 4.11, a total of twenty peaks are assigned to peptide fragments of cytochrome *c*, representing

sequence coverage of 92% (see Table 4.6 in the Appendix for a list of peptide fragments identified for solution digestion of cytochrome *c*).

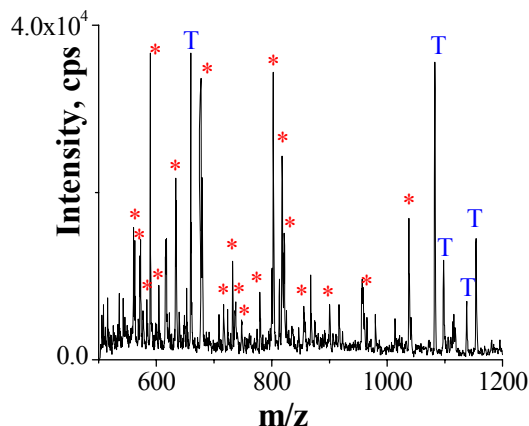


Figure 4.11 ESI spectrum showing the products of the digestion of cytochrome *c* in free solution. * = peptides from cytochrome *c*, T = peptides from Trypsin.

Comparison of the peptide mass maps obtained from in-solution digestion and on-bed digestion reveals significant differences in the digestion pattern. On-bed digestion generates less detectable peptide fragments in the m/z of 500-1200 than solution digestion. These differences could be attributed to partial digestion resulting from the surface-bound digestion, or loss of individual peptides from the support, as explained further below.

The tryptic digestion of proteins adsorbed to a hydrophobic surface tends to produce a greater number of larger, partially digested peptide fragments containing missed cleavages, compared to a solution digestion. This issue can be clearly seen by comparing the mass peaks obtained from on-bed digestion and in-solution digestion, which have been summarized in Table 4.5 and 4.6. As shown in these tables, most of the peptide fragments detected from the on-bed digestion have missed cleavage sites. Large peptide fragments containing up to 4 missed cleavages are observed. Most of these large peptides are not detected in the

solution digest. In contrast, most of the peptides detected in the solution digest have no, or only one missed cleavage.

The detection of peptides fragments with a high degree of missed cleavages for surface digestion has been reported by Doucette *et al.* [32] for bead-based protein digestion, in which proteins are captured onto reversed-phase chromatographic micro-beads and subjected to tryptic digestion within a microcolumn. They reported that large peptide fragments containing as many as nine missed cleavages were observed over the m/z of 750–2250 from the bead digests.

When a protein is adsorbed on a hydrophobic surface, it is expected to experience a conformational change to achieve maximum binding by orienting the hydrophobic domains to the sorbent material and leaving the hydrophilic domains facing the solution. A direct consequence of protein binding to a hydrophobic support is that certain cleavage sites of the protein become less accessible to tryptic cleavage, which in turn results in partial digestion of protein with a large number of missed cleavage sites, as is observed in our results.

Moreover, in on-bed digestion, not all resulting peptide fragments would remain bound to the monolith surface after tryptic cleavage, the peptides that are not bound to the hydrophobic support will be released into the solution phase and detected during the buffer flush following digestion, as is observed in Figure 4.9d. The peptide fragments that have been eluted out during the washing step should be in the sequence regions that do not form part of the hydrophobic binding domains. Doucette *et al.* [32] also explored the digestion of proteins adsorbed on

various types of hydrophobic supports with different chemistry (C4, C8, C18, and R2 beads). They concluded that although peptide mass maps obtained by direct MALDI show similar levels of sequence coverage for digestion of proteins on various supports, some notable small differences were observed in the peptide fragments recovered as a result of varying the surface. Thus, using a monolith with slightly different surface chemistry may retain peptide fragments lost during washing and increase the overall percent coverage, but this was not tested.

In our work, a 30 min digestion time was used and complete digestion of protein adsorbed on the monolithic polymer was achieved with no intact cytochrome *c* observed, indicating that the 30 min digestion time is sufficient to produce a complete digestion. On-bed digestion experiments with longer reaction times were carried out, and no significant differences were observed in the digestion pattern, indicating that longer digestion time did not result in more complete digestion with less missed cleavages. This is consistent with the results reported by Doucette *et al.* [32].

Although not tested in our monolith-based digestion method, a digestion time of less than 30 min may be enough to achieve a complete digestion based on the work reported by Craft *et al.* for bead-based protein digestion within a column [23]. They compared MALDI spectra obtained from the digestion of proteins on microbeads at various reaction times, and the results showed that similar sequence coverage and signal intensities were obtained for 5 and 30 min digestion time, but a 30 min incubation time gave a slightly higher number of detectable peaks. They

concluded that the 30-min digestion time was more than sufficient for most in-column digestion.

Therefore, the digestion of protein bound to a hydrophobic support is much faster than the conventional solution digestion, where digestion of 0.2 mg/mL cytochrome *c* will take at least 2 h to complete under optimized conditions. The speeding up of the digestion reaction could be attributed to the increase in protein concentration obtained by extracting the sample from solution onto a hydrophobic surface prior to digestion, which in turn improved the reaction kinetics.

4.3.2.3 BSA

BSA is a large protein with 583 amino acids, and it contains 17 intrachain disulfide bonds, making it a more difficult target for tryptic digestion. Reduction of the disulfide bonds is required to fully digest the protein, so BSA was treated with DTT to break disulfide linkages. To prevent the disulfide bonds from reforming, iodoacetamide was used to modify the reactive cysteine SH groups.

The pretreated BSA solution was loaded onto the monolithic bed and digested. Figure 4.12 shows the TIC (left) for the on-bed digestion of BSA. Although the peptide fragments of BSA are still eluted in a single elution peak with a peak width of ~2.2 min (FWHM), which is broader compared to that of cytochrome *c* and the peak shape presents severe tailing. The sudden loss of the signal in the TIC trace might be caused by degradation of electrospray performance.

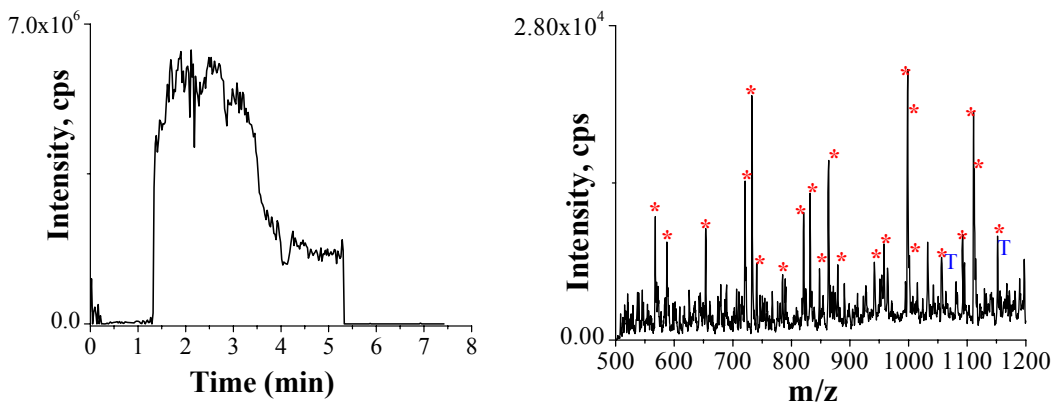


Figure 4.12 On-bed tryptic digestion of BSA. Left: TIC showing the peptide elution profile; Right: mass spectra averaged from the elution peak. * = peptides from BSA, T = peptides from Trypsin.

In an attempt to explain this elution behavior, EICs were extracted for several of the most intense BSA peptides and are shown in Figure 4.13 with their m/z values noted above each trace. Several peptides, e.g. peptides with m/z value of 863.5, 958.0, and 998.5, are eluted in a narrower peak within a shorter timeframe. Other peptides, such as those with m/z values of 732.5, 832.0, and 1111.0, are

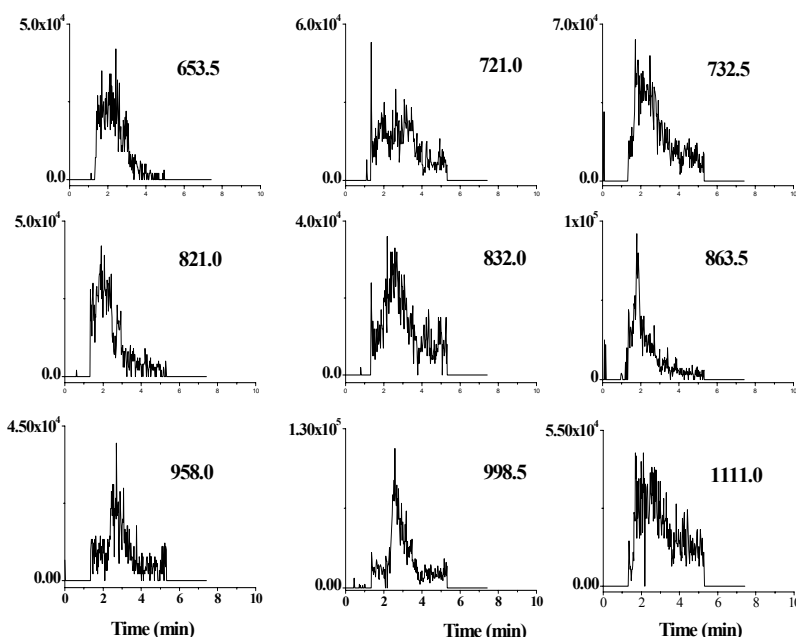


Figure 4.13 EICs for several of the most intense tryptic BSA peptides. The m/z values of these peptides are noted above each plot.

eluted in an extremely broad peak with a large amount of tailing. It is suspected that the differences in the elution behavior of the BSA peptides are probably related to their different affinity to the monolith.

A mass spectrum extracted from the peak region is shown in Figure 4.12 (right), in which 22 peaks are identified as the known peptide fragments of BSA and are labeled with “*”. Table 4.7 of Appendix lists the observed peaks and indicates the numbers of missed cleavages in each partially digested fragment (1–3 missed cleavages per fragment). The sequence coverage for the on-bed digestion of BSA is 56%. Craft *et al.* obtained 69% sequence coverage for BSA with their bead-based method in a microcolumn [23]. The lower sequence coverage obtained in our experiments is most likely due to the lower m/z scanning range of 500–1200 used in our experiments, compared to a mass range of 750–2250 in their work. Larger peptide fragments could have been detected in the m/z range between 1200 to 2250, contributing to a higher percent coverage.

For comparison, the protein was also digested with trypsin in free solution following the protocol outlined in section 4.2.4. The solution phase BSA digest was then infused through a single straight channel device (with no monolithic bed) coupled to a capillary tip at a flow rate of 0.21 $\mu\text{L}/\text{min}$ into MS for analysis. The resulting mass spectrum is shown in Figure 4.14. Tryptic peptide peaks identified for solution digestion of BSA are labeled with “*” and listed in Table 4.8 of the Appendix. A total of 41 peaks are assigned to peptide fragments of BSA, representing a sequence coverage of 68%. Similar to the results for cytochrome *c*, most peptide fragments generated by solution digestion have no, or only one

missed cleavages, as compared to the large peptide fragments containing 2 to 3 missed cleavages obtained in on-bed digestion.

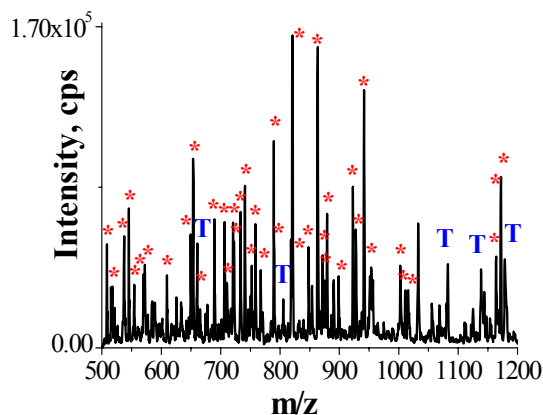


Figure 4.14 ESI spectrum obtained from the free solution digestion of BSA. * = peptides from BSA, T = peptides from Trypsin.

Although partial digestion with a great number of missed cleavages is observed as proteins are adsorbed to a solid support, it can still produce a peptide map containing a wide range of peptide fragments for protein identification. On the other hand, the generation of peptides containing a higher degree of missed cleavage sites in on-bed digestion is significant for protein identification. For a substrate containing closely spaced digestion sites, complete digestion results in very short peptide fragments with very low m/z values falling out of the detection m/z range, and thus leads to potential loss of structural information. In on-bed digestion, the partial digestion of protein enables formation of relative larger peptide fragments with overlapping sequences, and those small segments can be detected as portions of larger peptides with missed cleavages. This is particularly useful in the applications which require the detection of all residues, as in the case of determining the type and location of posttranslational modifications.

Compared to in-solution digestion, the on-bed digestion generates less trypsin autolysis products with lower intensity, which will not interfere with the detection of protein tryptic peptides. Therefore, this method reduced the extent of enzyme autolysis and improved digestion results.

4.3.2.4 Myoglobin

The third protein studied was myoglobin, which is a small protein containing 153 amino acid residues, devoid of disulfide bonds. On-bed digestion was initially performed and the resulting elution trace shows two unresolved peaks (Figure 4.15a). Mass Spectra extracted from the TIC for the two peak regions are shown in Figure 4.15b for the first peak and Figure 4.15c for the second peak. As shown, a spectrum extracted from the first peak is dominated by trypsin autolysis

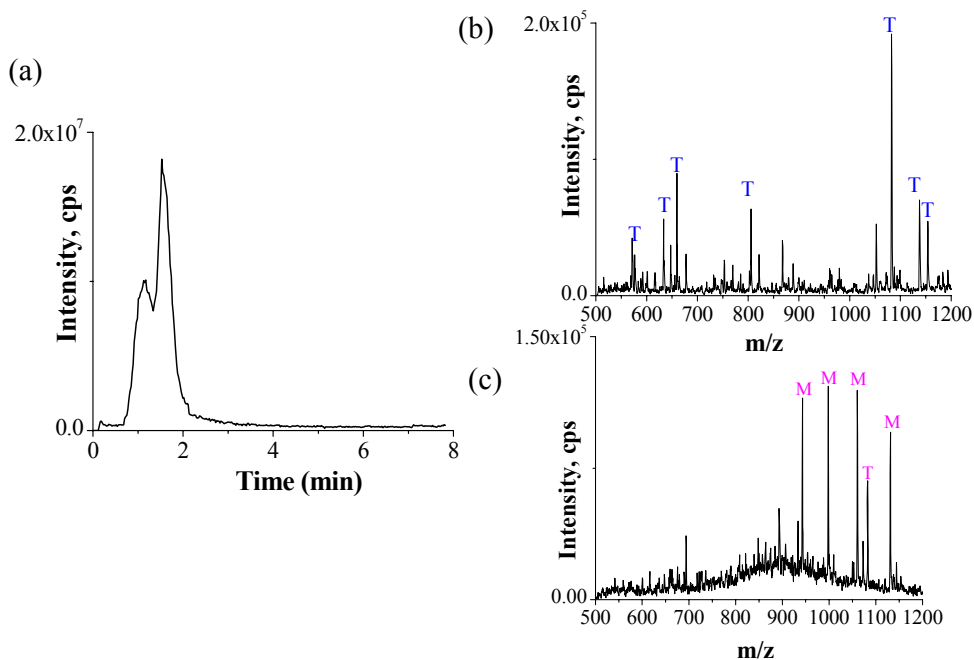


Figure 4.15 On-bed tryptic digestion of myoglobin. (a) TIC, (b) mass spectrum extracted at the first peak, and (c) mass spectrum extracted at the second peak. T = peptides from Trypsin, M = intact myoglobin charge states.

peaks, while the components eluted in the second peak result in a spectrum dominated by intact myoglobin charge states (labeled with “M”). No trace of tryptic peptides from myoglobin are observed, indicating that no detectable digestion has taken place.

Myoglobin digestion was then performed using a traditional aqueous solution phase protocol and Figure 4.16a presents the resulting mass spectrum of the solution digestion products. With 2 h solution digestion, there is still a significant amount of intact myoglobin present, as indicated by the charge state peaks of myoglobin, labeled with “M”. The solution digestion yielded relatively few tryptic peptide peaks (labeled with “*”) with low signal intensity, giving a 15% sequence coverage. These results indicate that this protein is resistant to proteolytic digestion, which is in agreement with results obtained by other researchers [33, 34].

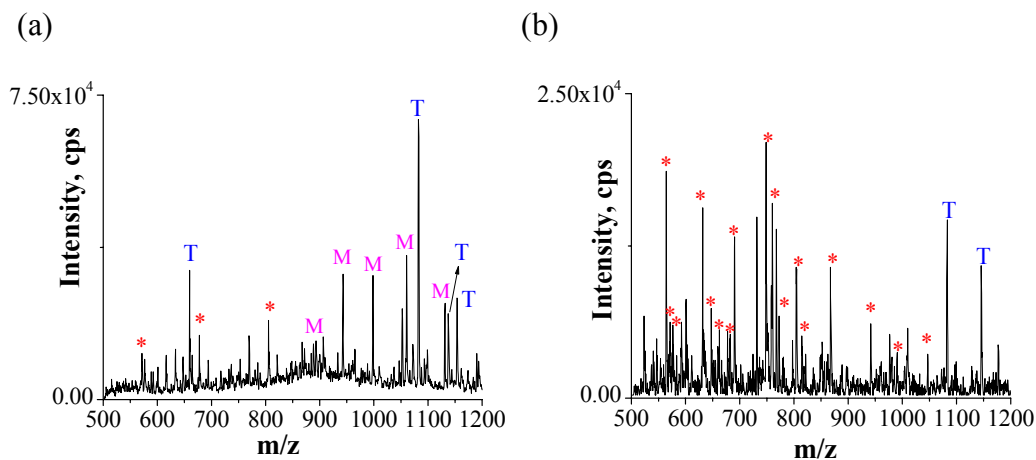


Figure 4.16 ESI mass spectra of myoglobin digested by trypsin for 2 h at 37 °C; (a) Nondenatured and (b) thermal denatured myoglobin. * = peptides from myoglobin, T = peptides from Trypsin, M = intact myoglobin charge states.

It was reported that enzymatic digestions of myoglobin can be significantly enhanced by denaturing the protein, either chemically [35] or thermally [36]. In our hands, the use of thermal denaturation significantly improved digestion efficiency with no traces of intact protein observed, as is shown in the m/z spectrum in Figure 4.16b. Table 4.9 in the Appendix lists the identified myoglobin tryptic digest peptides. While thermally denaturated protein could be tested for on-bed digestion, an integrated process would be substantially more complex to achieve, so we did not explore it.

4.4 Conclusion

A single channel microfluidic device is described in which an electrospray interface to a mass spectrometer is integrated with solid-phase extraction bed. An enlarged bed, 1 mm long, 140 μm wide and 20 μm deep, with a total bed volume of 2.6 nL, was created in the microchannel for *in situ* polymerization of hydrophobic monolith to act as a SPE sorbent material. The hydrophobic monolith, prepared from copolymerization of BMA, META, and EDMA was evaluated in terms of SPE behavior. Breakthrough curves for the 2.6 nL monolithic bed indicated an overall capacity for cytochrome c of 2.4 pmol, or 0.92 mmol per liter of bed. A cationic coating, PolyE-323, was used to modify the microchannel to generate an anodal EOF towards the MS and facilitate positive electrospray. A capillary tip (4 mm long, 50 μm I.D. with a tapered tip of 10 μm) was inserted into the exposed channel to act as an ESI emitter. EOF flow rate on this PolyE-323-coated chip-capillary device was calculated to be in the range of

1.8 to 2.2 $\mu\text{L}/\text{min}$ with -2.0 – -3.0 kV at the sample reservoir and 3.2 – 3.5 kV at the ESI tip. The combination of the hydrophobic monolith and the cationic coating in the single channel device allows the integration of on-chip SPE preconcentration, on-bed tryptic digestion, and on-line ESI-MS detection for peptide mass mapping.

On-bed digestion was conducted by capturing protein sample onto the hydrophobic monolithic support, followed by flowing a trypsin solution over the adsorbed protein, producing tryptic peptide fragments. The tryptic peptides were then eluted for MS detection. The performance of this system for on-bed digestion was tested using several model proteins. The use of solid-phase extraction to preconcentrate the sample prior to digestion improves the kinetics of enzymatic digestion and speeds up the reaction, allowing complete protein digestion to be achieved within 30 min. Although the tryptic digestion of protein adsorbed to a surface results in a large number of peptides containing missed cleavages, due to the partially block of some digestion sites, it still can produce a peptide map containing a wide range of peptide fragments for protein identification. Tandem mass spectrometry experiments can be performed on eluted peptides for further identification. This SPE and digestion system can be integrated into a multiplexed platform. Such a platform will allow for protein preconcentration, sample cleanup, and digestion, with on-line analysis of the digestion products by mass spectrometry. This chip design thus provides a convenient platform for protein sample processing for automated MS analysis in proteomic studies.

4.5 References

- 1 Ohno, K.; Tachikawa, K.; Manz, A. *Electrophoresis* **2008**, *29*, 4443–4453.
- 2 Lion, N.; Rohner, T. C.; Dayon, L.; Arnaud, I. L. Damoc, E.; Youhnovski, N.; Wu, Z. Y.; Roussel, C.; Josserand, J.; Jensen, H.; Rossier, J. S.; Przybylski, M.; Girault, H. H. *Electrophoresis* **2003**, *24*, 3533–3562.
- 3 Lazar, I. M.; Grym, J.; Foret, F. *Mass Spectrom. Rev.* **2006**, *25*, 573–594.
- 4 Lee, J.; Soper, S. A.; Murray, K. K. *J. Mass. Spectrom.* **2009**, *44*, 579–593.
- 5 DeVoe, D. L.; Lee, C. S. *Electrophoresis* **2006**, *27*, 3559–3568.
- 6 de Mello, A. J. *Lab Chip* **2001**, *1*, 7N–12N.
- 7 Sung, W. C.; Makamba, H.; Chen, S. H. *Electrophoresis* **2005**, *26*, 1783–1791.
- 8 Koster, S.; Verpoorte, E.; *Lab Chip* **2007**, *7*, 1394–1412.
- 9 Zhang, S.; Van Pelt, C. K. *Expert Rev. Proteomics*, **2004**, *1*, 449–468.
- 10 Quadroni, M.; James, P. *Electrophoresis* **1999**, *20*, 664–677.
- 11 Girelli, A. M.; Mattei, E. *J. Chromatogr. B-Anal. Technol. Biomed. Life Sci.* **2005**, *819*, 3–16.
- 12 Blackburn, R. K.; Anderegg, R. J. *J. Am. Soc. Mass Spectrom.* **1997**, *8*, 483–494.
- 13 Freije, J. R.; Mulder, P. P. M. F. A.; Werkman, W.; Rieux, L.; Niederlander, H. A. G.; Verpoorte, E.; Bischoff, R. *J. Proteomics Res.* **2005**, *4*, 1805–1813.
- 14 Thelohan, S.; Jadaud, P.; Wainer, I. W. *Chromatographia* **1989**, *28*, 551–555.
- 15 Wang, R.; Oleschuk, F.; Ouchen, J.; Li, P.; Thibault, D. J.; Harrison, J. *Rapid Commun. Mass. Spectrom.* **2000**, *14*, 1377–1383.
- 16 Slys, G. W.; Schriemer, D. C. *Anal. Chem.* **2005**, *77*, 1572–1579.
- 17 Calleri, E.; Temporini, C.; Perani, E.; De Palma, A.; Lubda, D.; Mellerio, G.; Sala, A.; Galliano, M.; Caccialanza, G.; Massolini, G. *J. Proteome Res.* **2005**, *4*, 481–490.
- 18 Calleri, E.; Temporini, C.; Perani, E.; Stella, C.; Rudaz, S.; Lubda, D.; Mellerio, G.; Veuthey, J. L.; Caccialanza, G.; Massolini, G. *J. Chromatogr. A* **2004**, *1045*, 99–109.
- 19 Peterson, D. S.; Rohr, T.; Svec, F.; Frechet, J. M. J. *J. Proteome. Res.* **2002**, *1*, 563–568.

- 20 Peterson, D. S.; Rohr, T.; Svec, F.; Frechet, J. M. J. *Anal. Chem.* **2002**, *74*, 4081–4088.
- 21 Feng, S.; Ye, M.; Jiang, X.; Jin, W.; and Zou, H. *J. Proteome Res.* **2006**, *5*, 422–428.
- 22 Doucette, A.; Craft, D.; Li, L. *Anal. Chem.* **2000**, *72*, 3355–3362.
- 23 Craft, D. ; Doucette, A. ; Li, L. *J. Proteome Res.* **2002**, *1*, 537–547.
- 24 Bings, N. H.; Wang, C.; Skinner, C. D.; Colyer, C. L.; Thibault, P.; and Harrison, D. J. *Anal. Chem.* **1999**, *71*, 3292–3296.
- 25 Lu, W.; Yang, G.; Cole, R. B. *Electrophoresis* **1995**, *16*, 487–492.
- 26 Kriger, M. S.; Cook, K. D.; Ramsey, R. S. *Anal. Chem.* **1995**, *67*, 385–389.
- 27 Zhu, X. F.; Thiam, S.; Valle, B. C.; Warner, I. M. *Anal. Chem.* **2002**, *74*, 5405–5409.
- 28 O'Connor, P. B.; Pittman, J. L.; Thomson, B. A.; Budnik, B. A.; Cournoyer, J. C.; Jebanathirajah, J.; Lin, C.; Moyer, S.; Zhao, C. *Rapid Commun. Mass Spectrom.* **2006**, *20*, 259–266.
- 29 Xue, Q. F.; Foret, F.; Dunayevskiy, Y. M.; Karger, B. L. *Rapid Commun. Mass Spectrom.* **1997**, *11*, 1253–1256.
- 30 Aguilar, M.; Clayton, D. J.; Holt, P.; Kronina, V.; Boysen, R. I.; Purcell, A. W.; Hearn, M. T. W. *Anal. Chem.* **1998**, *70*, 5010–5018.
- 31 Taylor, J. *Ph. D. Thesis*, University of Alberta, Edmonton, Alberta, Canada, 2004.
- 32 Doucette, A.; Craft, D.; Li, L. *J. Am. Soc. Mass Spectrom.* **2003**, *14*, 203–214.
- 33 Fontana, A.; Zambonin, M.; Polverino de Laureto, P.; De Filippis, V.; Clementi, A.; Scaramella, E. *J. Mol. Biol.* **1997**, *266*, 223–230.
- 34 Al-Lawati, H.; Watts, P.; Welham, K. J. *Analyst* **2006**, *131*, 656–663.
- 35 Russell, W. K.; Park, Z. Y.; Russell, D. H. *Anal. Chem.* **2001**, *73*, 2682–2685.
- 36 Park, Z. Y.; Russell, D. H. *Anal. Chem.* **2000**, *72*, 2667–2670.

4.6 Appendix

4.6.1 Myoglobin and Cytochrome *c* Charge States

Cytochrome *c* and myoglobin charge states and their corresponding *m/z* values are presented in Table 4.3. The *m/z* values were derived by dividing the protein's molecular weight, 12,360 g/mol for cytochrome *c* and 16,952 g/mol for myoglobin, by the corresponding charge state and adding 1 to represent $[M+nH]^{n+}$.

Table 4.3 Observed cytochrome *c* and myoglobin charge states.

Cytochrome <i>c</i>		Myoglobin	
+8	1546.0	+12	1413.5
+9	1374.5	+13	1305.0
+10	1237.0	+14	1212.0
+11	1124.5	+15	1131.0
+12	1031.0	+16	1060.5
+13	952.0	+17	998.0
+14	884.0	+18	942.5
+15	825.0	+19	893.0
+16	773.5		

4.6.2 Trypsin Autolysis Peptides

Trypsin autodigestion peaks were identified by database searching using the Swiss-Prot accession number for bovine trypsinogen [precursor], P00760, and then removing the first 20 residues which contain the signal information and the propeptide. The remaining sequence was then pasted into the database search. The database was searched using: trypsin digest, 3 missed cleavages, peptide N-terminus = hydrogen, peptide C-terminus = free acid, modifications considered = oxidation of methionine and protein N-terminus acetylated, cysteine unmodified. Peptides *m/z* values are listed for $[M+nH]^{n+}$, based on monoisotopic masses. The peptides listed in Table 4.4 were identified.

Table 4.4 Trypsin autodigestion peaks.

<i>m/z</i>	Position	Missed cleavages
577.5	126-136	0
633.5	218-223	0
659.5	44-49	0
805.5	92-99	0
1082.5 ²⁺	50-69	0
1097.5 ²⁺	150-170	0
1137.5 ²⁺	70-89	0
1153.5	126-136	0

4.6.3 Cytochrome *c* Tryptic Peptides

Cytochrome *c* peptides were identified by database searching using the SwissProt accession number for cytochrome *c*, P00004. Two databases were used, Peptide Mass by ExPASy (<http://us.expasy.org/>), and MS-Digest by Protein Prospector (<http://prospector.ucsf.edu/>). The databases were searched using: trypsin digest, 4 missed cleavages, peptide N-terminus = hydrogen, peptide C-terminus = free acid, modifications considered = oxidation of methionine (Met-ox) and protein N-terminus acetylated, cysteine unmodified. Peptides *m/z* values are listed for $[M+nH]^{n+}$, based on monoisotopic masses. Observed cytochrome *c* tryptic digest peptides are shown in Table 4.5 for on-bed digestion and in Table 4.6 for in-solution digestion.

Table 4.5 Cytochrome *c* peptides from on-bed tryptic digestion.

<i>m/z</i>	Position	Peptide Sequence	Missed cleavages
562.5	100-104	KATNE	1
571.5 ³⁺	40-55	TGQAPGFTYTDANKNK	1
585.0 ²⁺	28-38	TGPNLHGLFGR	0
589.5	1-5	Acetyl-GDVEK	0
634.5	9-13	IFVQK	0

661.5	87-91	KKTER	2
678.5	74-79	YIPGTK	0
733.0	1-7	GDVEKGK	1
737.0 ³⁺	56-73	GITWKEETLMEYLENPKK	2
740.0 ²⁺	89-100	TEREDLIAYLKK	2
800.0 ²⁺	39-53	KTGQAPGFTYTDANK	1
817.5 ²⁺	14-22	IFVQKCAQCHTVEK (Heme)	1
856.0 ²⁺	40-55	TGQAPGFTYTDANKNK	1
868.0 ²⁺	87-100	KKTEREDLIAYLKK	4
956.5 ³⁺	56-79	GITWKEETLMEYLENPKKYIPGTK	3
1041.5 ²⁺	56-72	GITWKEETLMEYLTNPK	1
1095.5 ²⁺	9-38	GKKIFVQKCAQCHTVEKGGK	4

Table 4.6 Cytochrome *c* peptides from tryptic digestion in free solution.

<i>m/z</i>	Position	Peptide Sequence	Missed cleavages
562.5	100-104	KATNE	1
571.5 ³⁺	40-55	TGQAPGFTYTDANKNK	1
585.0 ²⁺	28-38	TGPNLHGLFGR	0
589.5	1-5	Acetyl-GDVEK	0
604.5	56-60	GITWK	0
634.5	9-13	IFVQK	0
678.5	74-79	YIPGTK	0
717.5 ²⁺	26-38	HKTGPNLHGLFGR	1
733.0	1-7	GDVEKGK	1
737.0 ³⁺	56-73	GITWKEETLMEYLENPKK	2
748.5 ²⁺	61-72	EETLMEYLEBPK	0
779.5	80-86	MIFAGIK	0
800.0 ²⁺	39-53	KTGQAPGFTYTDANK	1
817.5 ²⁺	14-22	IFVQKCAQCHTVEK (Heme)	1
821.5 ²⁺	61-73	EETLMEYLENPKK	1

856.0 ²⁺	40-55	TGQAPGFTYTDANKNK	1
902.5	1-8	GDVEKGKK	2
964.5	92-99	EDLIAYLK	0
1041.5 ²⁺	56-72	GITWKEETLMEYLTNPK	1

4.6.4 BSA Tryptic Peptides

BSA peptides were identified by database searching using the Swiss-Prot accession number for bovine serum albumin [precursor], and then removing the first 24 residues which contain the signal information and the propeptide. The remaining sequence was then pasted into the database search. The MW of the protein was 66433 g/mol. The database was searched using: trypsin digest, 3 missed cleavages, peptide N-terminus = hydrogen, peptide C-terminus = free acid, modifications considered = oxidation of M and protein N-terminus acetylated, cysteine modified by carbamidomethylation. Peptides m/z values are listed for $[M+nH]^{n+}$, based on monoisotopic masses. Identified tryptic digest peptides for on-bed digestion and in-solution digestion are listed in Table 4.7 and 4.8, respectively.

Table 4.7 BSA peptides from on-bed tryptic digestion.

m/z	Missed cleavages	position	Modification
567.5	1	410-413	
587.5 ⁴⁺	1	276-294	3CAM-C
653.5 ²⁺	0	378-388	
721.0 ²⁺	1	336-347	
732.5 ²⁺	0	52-64	2CAM-C
741.0 ²⁺	0	397-409	
785.0 ²⁺	0	323-335	
821.0	1	205-211	
832.0 ²⁺	2	174-187	1Met-ox 1CAM-C
848.0	1	218-224	

863.5 ³⁺	0	445-458	
879.5 ²⁺	1	557-573	
941.5 ²⁺	0	484-499	1CAM-C
959.0 ³⁺	1	436-458	3CAM-C
997.5 ²⁺	2	466-483	
998.5 ⁴⁺	3	65-98	2CAM-C
1001.0 ²⁺	1	240-256	1CAM-C
1056.5 ³⁺	2	351-377	1CAM-C
1092.5 ²⁺	2	257-275	1CAM-C
1111.0 ³⁺	2	472-499	3CAM-C
1111.5 ²⁺	1	505-523	
1152.5 ³⁺	3	534-563	1CAM-C

Table 4.8 BSA peptides from tryptic digestion in free solution.

<i>m/z</i>	Missed cleavages	position	Modification
508.5	0	205-208	
517.5	0	257-261	
537.5	0	133-136	
545.5 ²⁺	0	77-81	
554.5 ²⁺	0	564-573	1CAM-C
570.0 ²⁺	0	475-483	2CAM-C
573.0	1	195-198	
609.5	0	500-504	
649.5	0	181-185	
653.5 ²⁺	0	378-388	3CAM-C
661.0	0	466-471	
690.0	0	212-217	
707.0	0	199-204	1CAM-C
711.0 ²⁺	0	65-76	1CAM-C
721.0 ²⁺	1	336-347	

723.0 ²⁺	0	262-273	1CAM-C
732.5 ²⁺	0	52-64	2CAM-C
741.0 ²⁺	0	82-93	2CAM-C
753.0	0	317-322	
759.0	0	174-180	1CAM-C
767.5 ²⁺	1	274-285	2CAM-C
789.5 ²⁺	0	115-127	1CAM-C
790.5 ²⁺	0	243-256	
819.0	0	538-544	
821 ²⁺	1	413-427	
848.0	1	218-224	
863.0 ²⁺	1	323-336	
871.0 ²⁺	0	445-458	1Met-ox 1CAM-C
875.0 ²⁺	0	160-173	2CAM-C
880.0 ²⁺	1	348-362	
899.0 ²⁺	1	363-377	1CAM-C
923.0	0	225-232	
927.5	0	137-143	
941.5 ²⁺	0	484-499	1CAM-C
951.0 ²⁺	1	397-412	1CAM-C
1002.0	1	209-217	
1011.0 ²⁺	1	82-98	
1016.0	0	286-294	
1164.5	0	42-51	
1172.0 ³⁺	2	286-316	2CAM-C
1178.5	1	378-396	1CAM-C

4.6.5 Myoglobin Tryptic Peptides

Myoglobin peptides were identified by database searching using the SwissProt accession number for myoglobin, P68082. Two databases were used, Peptide

Mass by ExPASy (<http://us.expasy.org/>), and MS-Digest by Protein Prospector (<http://prospector.ucsf.edu/>). The databases were searched using: trypsin digest, 3 missed cleavages, peptide N-terminus = hydrogen, peptide C-terminus = free acid, modifications considered = oxidation of methionine (Met-ox) and protein N-terminus acetylated. Peptides m/z values are listed for $[M+nH]^{n+}$, based on monoisotopic masses. Observed myoglobin tryptic digest peptides are shown in Table 4.9 for thermal denatured solution digestion.

Table 4.9 Myoglobin tryptic peptides from thermal denatured solution digestion.

m/z	Position	Peptide Sequence	Missed cleavages
564.0 ⁴⁺	119-139	HPGDFGADAQGAM(ox)TKALELFR	1
571.5 ⁴⁺	134-153	ALELFRNDIAAKYKELGFQG	3
577.5	48-62	HLKTEAEMKASEDLK	2
631.4	140-145	NDIAAK	0
650.0	148-153	ELGFQG	0
662.5	57-62	ASEDLK	0
677.0	51-62	TEAEMKASEDLK	1
690.0	64-77	HGTVVLTALGGILK	0
748.5	134-139	ALELFR	0
760.3	119-133	HPGDFGADAQGAM(ox)TK	0
772.5 ³⁺	32-50	LFTGHPETLEKFDKFKHLK	3
804.0 ²⁺	17-31	VEADIAGHGQEVLR	0
813.2 ⁴⁺	17-45	VEADIAGHGQEVLR LFTGHPETLEKFDK	2
867.8 ²⁺	97-118	HKIPKYLEFISDAIIHVLHSK	2
941.5	146-153	YKELGFQG	1
991.5 ²⁺	79-96	KGHHEAELKPLAQSHATK	1
1046.5 ³⁺	119-147	HPGDFGADAQGAMTKALELFRNDIAAKYK	3

Chapter 5

Electrokinetically Controlled Fractionator and Collector with Photopatterned Monolithic Polymer Beds for Protein Analysis

5.1 Introduction.....	157
5.2 Chip Design	159
5.2.1 Design Considerations	159
5.2.2 Final Chip Design	161
5.3 Impedance Simulation and Theoretical Calculation	166
5.4 Experimental Section	173
5.4.1 Chip Fabrication.....	173
5.4.2 Experimental Setup	174
5.4.2.1 Single Wavelength Detection System.....	174
5.4.2.2 Multi-Wavelength Detection System.....	175
5.5 Results and Discussion	178
5.5.1 Fabricated Devices.....	178
5.5.2 Fractionation and Collection.....	178
5.5.2.1 Measuring the Mobility of Fluorescein.....	178
5.5.2.2 Study of Sheath Effect on PolyE-323 Coated Devices.....	180
5.5.2.3 Study of Sheath effect on Devices with Monolithic Beds	191
5.5.2.4 Automatic Fractionation Using Three Delivery Sequences...	203
5.5.2.5 Theoretical Calculation of Pressure-Induced Flow.....	209
5.5.3 Elution.....	216
5.5.3.1 Study of Elution Profile	217
5.5.3.2 Sequential Elution with Single Wavelength Detection.....	222
5.5.3.3 Sequential Elution with Multi-Wavelength Detection.....	227
5.6 Conclusion	251
5.7 References.....	253

5.1 Introduction

Significant progress has been made in the development of microchip-based analytical technologies for proteomics research applications during the past decade [1, 2]. A protein fractionator that utilized electrokinetic sheath flow to prevent cross-contamination has been reported by our group [3]. Our new chip design built on this fractionator, aimed at developing a multiplexed platform to address the need for the integration of the steps of protein separation, fractionation and collection, preconcentration and desalting, and enzymatic digestion within a single microchip. Sheath-flow technology [4-6] was used to prevent leakage-induced cross-contamination, a common problem in electrokinetic systems. In this multi-channel device, multiple methacrylate-based monoliths were photo-patterned in an array of microchambers in a single step using photo-initiated polymerization to serve as solid-phase extraction (SPE) sorbent for protein preconcentration. We have also included an elution channel for the on-line coupling of the microfluidic device to ESI-MS utilizing an attached capillary emitter.

To investigate the performance of this microfluidic platform, we first demonstrate the sequential fractionation and collection of fluorescent samples onto the monolithic polymer beds to evaluate the ability to capture individual components into individual collectors without cross-contamination. After that, sequential elution of the adsorbed analytes was performed using timers and relays to sweep a sequential ground through each collection channel to drive elution buffer through the monolithic bed. A home-built multi-wavelength detection

system, which enables simultaneous recording of green and red fluorescence, was used to examine the potential sample carryover from one fraction to the next during the sequential elution process.

The design and fabrication of glass microfluidic devices, especially complex devices, is a time-consuming and costly process. Hence, it would be preferred to have an idea on what to expect before designing the chip. An impedance simulation can describe the flow behavior in the microchannels and give us useful information for device design, such as the selection of channel dimensions for each part of the device. So far, a few simulation tools for microfluidics are available, such as pSpice simulation, lumped-element approximation [7, 8], sheet resistance approximation [9, 10], and finite element analysis [11, 12]. In our study, we employed pSpice software to perform simulations of the multi-channel device designs. In this simulation tool, the device is treated as a combination of resistors and the simulation results give the current in each portion of the channel and the voltage at each intersection point, which allows us to make theoretical calculation of parameters such as electric field, volumetric flow rate, and transit time. A very important parameter for the operation of the fractionator is the sample stream width, as it indicates the extent of electrokinetic focusing and gives us instructions on the choice of voltages used in the experiments. Details on how to calculate the sample width can be found in Section 5.3. The results calculated from the simulation were compared with experimental data to determine if the simulation model is a reliable tool for predicting the performance of flow focusing inside the microchannel network.

5.2 Chip Design

5.2.1 Design Considerations

Previous work by Zhen Wang [13] in our lab demonstrated a protein fractionator and collector, which employed electrokinetic sheath flow to prevent leakage. The fractionator consists of a sample channel and two sheath channels, connected to several collection channels through the fractionation region. With such a design, the incoming analyte is surrounded by voltage-controlled sheath buffer flows, allowing a tightly focused sample stream to be delivered into the grounded channel without contaminating the other channels.

Based on Wang's work, we further improved this microfluidic system and made the following modifications in the mask design:

1. An unresolved issue in Wang's design was the interface to the ESI-MS for the fractionator. Several strategies were proposed by Wang regarding the on-line coupling of this fractionator to MS. One way she proposed is to use a single electrospray tip. As is shown in Figure 5.1a, all the collection channels are joined to a single outlet, from which a capillary ESI tip can be attached. The problem with this design is that it requires individual electrical and fluidic contacts for each collection channel if electrokinetic fractionation is to be performed. A simple solution to this problem is to place a collection reservoir before each SPE bed in each collection channel to provide electrical contact, where a voltage can be applied to move the solution electrokinetically. However, the addition of the collection reservoirs will introduce problems of sample dilution and electrolysis because the analyte are collected in the

reservoirs filled with buffer solutions. In addition, all the collection channels are connected through the joint point downstream of the bed. Thus when one of the collection reservoirs is held at ground during electrokinetic fractionation, the other channels also have paths to ground through a longer channel. While the majority of the flow will be fractionated into the grounded channel, there will also be a fraction of flow leaking into the other collection channels, depending on the resistance differences. This kind of multi-path flow will induce sample leakage into the undesired channels.

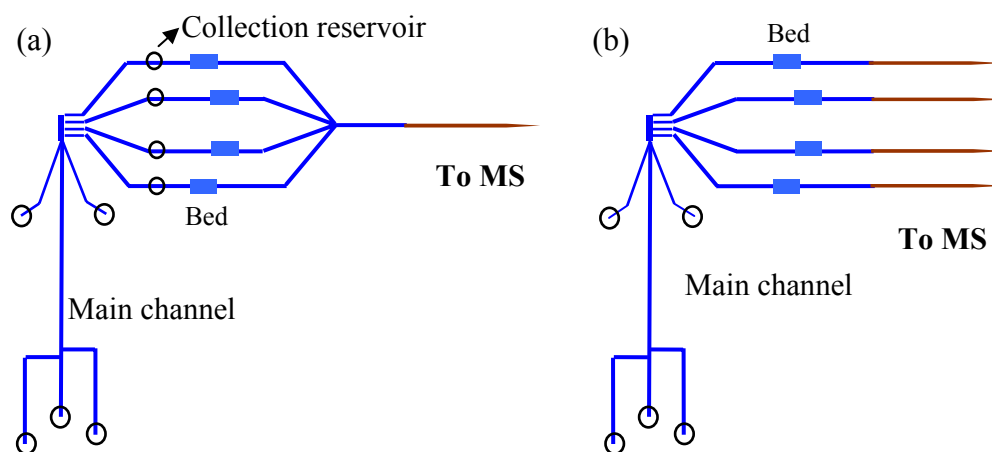


Figure 5.1 Schematic diagrams of the fractionator-ESI/MS interface. (a) Design with a single outlet for ESI-MS; (b) design with separate tips for each collection channel for ESI-MS.

An alternative way to build the interface is to use a separate tip for each collection channel (Figure 5.1b). Because we can not make all the capillary electrospray tips exactly the same, the optimal tip positions and ESI conditions for electrospray performance and sensitivity will be different for each emitter. Therefore, the main problem associated with this multiple-tip design is the difficulty in optimizing the tip position and ESI conditions for

each tip as we move the tips one by one to the MS inlet during the course of MS detection.

In order to overcome the aforementioned problems, we modified the design by adding an additional channel at the end of the fractionation zone to serve as a common elution pathway for all collection channels, from which an ESI capillary tip can be coupled for on-line ESI-MS.

2. A waste channel is added to collect the unwanted components during fractionation.
3. In one of the chip designs, we incorporate two reservoirs at the end of each collection channel, one for loading buffer and the other for elution buffer. This eliminates the need to change buffers during experiments, avoiding possible siphoning effect and solution disturbance from buffer switch.

5.2.2 Final Chip Design

Five multi-channel devices with different dimensions and various numbers of collection channels were designed in the masks. Figure 5.2a shows the device layouts and Figure 5.2b is an expansion of the corresponding rectangular area in Figure 5.2a, showing the detail of the fractionation regions.

The detailed structure of Device B is shown in Figure 5.3a as an example. Each device comprises a separation channel with three or four sample injection arms, two sheath channels surrounding the separation channel as it enters the fractionation region, a waste channel connected to the bottom of the fractionation region to collect unwanted components during fractionation, six or eight

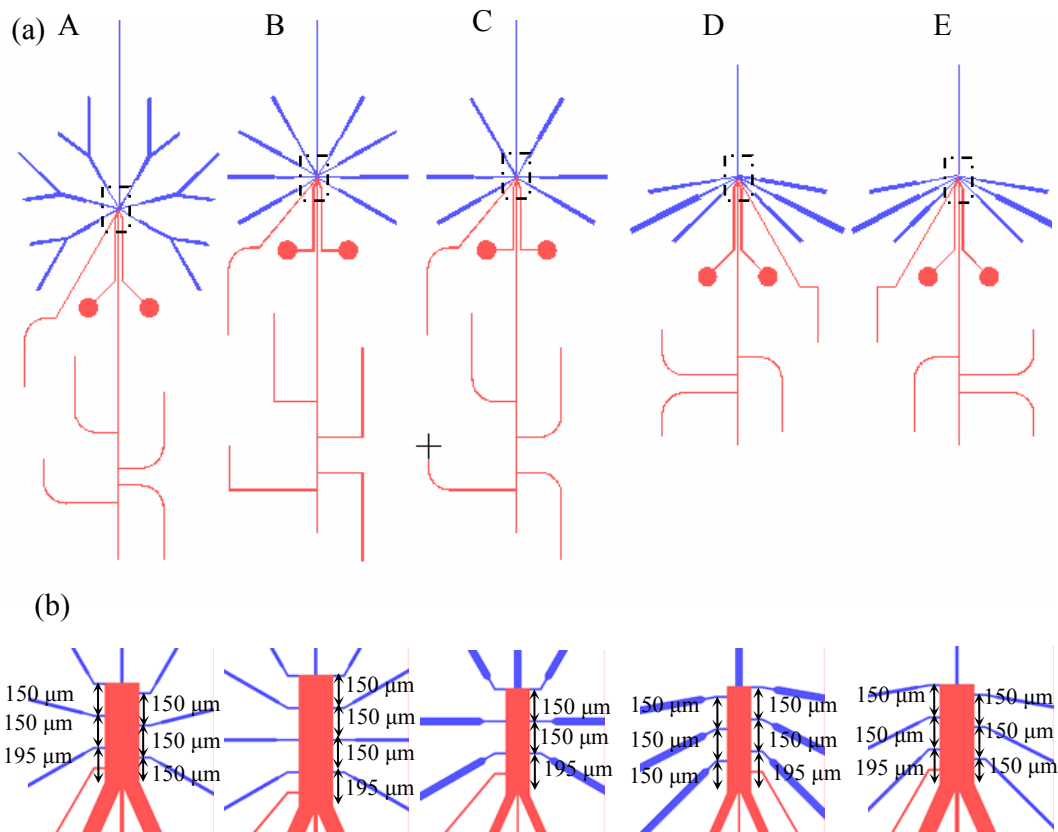


Figure 5.2 (a) Mask design for five devices with the fractionation zone highlighted by a dotted rectangle; (b) close-ups of the fractionation regions of the devices. The channel dimensions are summarized in Table 2.1.

collection channels evenly distributed on both sides of the fractionation zone for collecting the purified proteins, an elution channel at the end of the fractionation zone, through which analytes adsorbed on the SPE beds can be eluted and subjected to ESI-MS analysis. The detailed dimensions of each channel segment of the devices are summarized in Table 5.1. Compared to Devices A, B and E, Devices C and D have a narrower fractionation zone, narrower sample and sheath channels, but wider collection channels. Device D and E are designed to facilitate coupling of the microchip to ESI-MS. The injection element consists of three or four channels entering into the main separation channel to form different offsets,

allowing geometric definition of various sample plug volumes. The waste channel is 10 μm wide and 25 mm long.

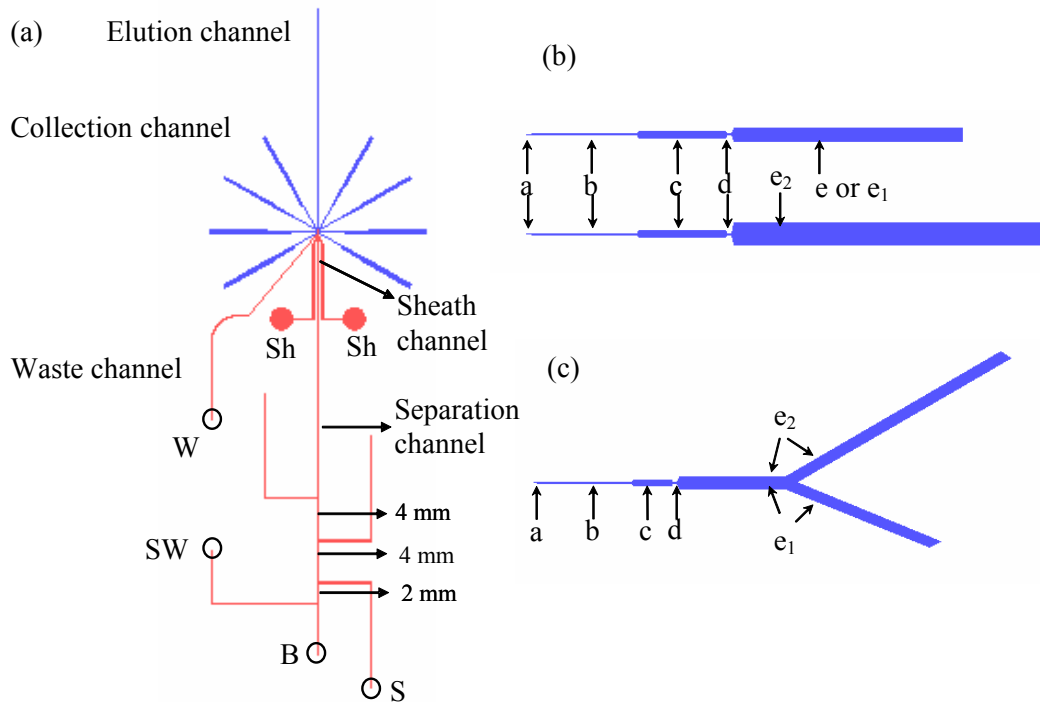


Figure 5.3 (a) The detailed structure of Device B. Reservoirs S, Sh, SW, B and W represent reservoirs for sample, sheath buffer, sample waste, separation buffer and waste, respectively; (b) a close-up of the layout of the collection channels in device B, C, D and E; (c) layout of the collection channels in device A. The detailed dimensions of each portion of the collection channels are given in Table 5.1.

Table 5.1 Detailed channel dimensions of Device A, B, C, D, and E on the mask.

	Fractionation zone	Sheath channel	Collection channel		Sample channel	Elution channel	Injection arms
A	$w = 162 \mu\text{m}$ $l = 500 \mu\text{m}$	$w = 78 \mu\text{m}$ $l = 11 \text{ mm}$	Segment a	Segment b	$w = 20 \mu\text{m}$ $l = 40 \text{ mm}$	$w = 16 \mu\text{m}$ $l = 21 \text{ mm}$	$w = 20 \mu\text{m}$ $l = 12.5 \text{ mm}$ $l_{\text{offset}} =$ 4 or 2 mm
			$w = 10 \mu\text{m}$ $l = 100 \mu\text{m}$	$w = 16 \mu\text{m}$ $l = 2.5 \text{ mm}$			
			Segment c	Segment d			
			$w = 160 \mu\text{m}$ $l = 1 \text{ mm}$	$w = 16 \mu\text{m}$ $l = 100 \mu\text{m}$			
			Segment e ₁	Segment e ₂			
			$w = 300 \mu\text{m}$ $l = 6.8 \text{ mm}$	$w = 300 \mu\text{m}$ $l = 9.3 \text{ mm}$			

B	$w = 162 \mu\text{m}$ $l = 650 \mu\text{m}$	$w = 78 \mu\text{m}$ $l = 10 \text{mm}$	Segment a $w = 10 \mu\text{m}$ $l = 100 \mu\text{m}$	Segment b $w = 16 \mu\text{m}$ $l = 2.5 \text{mm}$	$W = 20 \mu\text{m}$ $l = 40 \text{mm}$	$w = 16 \mu\text{m}$ $l = 17.5 \text{mm}$	$w = 20 \mu\text{m}$ $l = 15 \text{mm}$ $l_{\text{offset}} =$ 4 or 2 mm
			Segment c $w = 160 \mu\text{m}$ $l = 2 \text{mm}$	Segment d $w = 16 \mu\text{m}$ $l = 100 \mu\text{m}$			
			Segment e $w = 300 \mu\text{m}$ $l = 5.3 \text{mm}$				
C	$w = 114 \mu\text{m}$ $l = 500 \mu\text{m}$	$w = 46 \mu\text{m}$ $l = 10 \text{mm}$	Segment a $w = 10 \mu\text{m}$ $l = 100 \mu\text{m}$	Segment b $w = 36 \mu\text{m}$ $l = 2.5 \text{mm}$	$w = 10 \mu\text{m}$ $l = 40 \text{mm}$	$w = 36 \mu\text{m}$ $l = 17.5 \text{mm}$	$w = 10 \mu\text{m}$ $l = 14 \text{mm}$ $l_{\text{offset}} =$ 4 or 2 mm
			Segment c $w = 200 \mu\text{m}$ $l = 2 \text{mm}$	Segment d $w = 36 \mu\text{m}$ $l = 100 \mu\text{m}$			
			Segment e $w = 300 \mu\text{m}$ $l = 5.3 \text{mm}$				
D	$w = 114 \mu\text{m}$ $l = 500 \mu\text{m}$	$w = 46 \mu\text{m}$ $l = 11 \text{mm}$	Segment a $w = 10 \mu\text{m}$ $l = 100 \mu\text{m}$	Segment b $w = 36 \mu\text{m}$ $l = 2.5 \text{mm}$	$w = 10 \mu\text{m}$ $l = 30 \text{mm}$	$w = 36 \mu\text{m}$ $l = 12.5 \text{mm}$	$w = 10 \mu\text{m}$ $l = 12.5 \text{mm}$ $l_{\text{offset}} =$ 2 mm
			Segment c $w = 200 \mu\text{m}$ $l = 2 \text{mm}$	Segment d $w = 36 \mu\text{m}$ $l = 100 \mu\text{m}$			
			Segment e ₁ $w = 300 \mu\text{m}$ $l = 5.3 \text{mm}$	Segment e ₂ $w = 500 \mu\text{m}$ $l = 8.5 \text{mm}$			
E	$w = 162 \mu\text{m}$ $l = 500 \mu\text{m}$	$w = 78 \mu\text{m}$ $l = 11 \text{mm}$	Segment a $w = 10 \mu\text{m}$ $l = 100 \mu\text{m}$	Segment b $w = 16 \mu\text{m}$ $l = 2.5 \text{mm}$	$w = 20 \mu\text{m}$ $l = 30 \text{mm}$	$w = 16 \mu\text{m}$ $l = 12.5 \text{mm}$	$w = 20 \mu\text{m}$ $l = 12.5 \text{mm}$ $l_{\text{offset}} =$ 2 mm
			Segment c $w = 160 \mu\text{m}$ $l = 2 \text{mm}$	Segment d $w = 16 \mu\text{m}$ $l = 100 \mu\text{m}$			
			Segment e ₁ $w = 300 \mu\text{m}$ $l = 5.3 \text{mm}$	Segment e ₂ $w = 500 \mu\text{m}$ $l = 8.5 \text{mm}$			

All the collection channels are distributed evenly along the fractionation zone with a distance of $150 \mu\text{m}$ from center to center for channels on one side (Figure 5.2b). Each collection channel contains five segments. The structure of the collection channels is shown in Figure 5.3b and the detailed dimensions are given in Table 5.1. Segment a is a short and narrow channel ($10 \mu\text{m}$ wide and $100 \mu\text{m}$ long) used to connect the fractionation zone and the main part of the collection

channel in order to keep enough distance from edge to edge between collection channels. Segment b is slightly wider than segment a, and is the main source of electrical impedance of the collection channel. Segment c is designed as a bed structure with tapered geometries at both ends, where the hydrophobic monolith is to be prepared through *in situ* photo-initiated polymerization for protein preconcentration. Segment d is a small section of narrow channel used to define the bed structure. In Segment e, the channel is widened to 300 μm or 500 μm to lower the impedance of the collection channel. In Devices D and E, two types of collection channels with different lengths (1.0 cm or 1.3 cm) are designed to provide enough space for drilling access holes and attaching reservoirs. In Device A, a ‘Y’ shape collection channel is designed to enable the incorporation of two reservoirs, one for loading buffer and the other for elution buffer (Figure 5.3c).

From Wang’s work, a high electric field in the fractionation zone is desirable in order to generate a high velocity in this region, leading to shorter transit time and less radial diffusion of sample. Therefore, the electrical resistance of the collection channels is reduced by increasing the depth and width of the collection channels so that the voltage drop in the collection channel segment is lowered. Thus, instead of having the same depth in the whole chip, the collection channels and elution channels are etched to a depth of 20 μm , and all the other channels are etched to 5 μm .

With such a design, the samples can be fractionated and collected onto the SPE beds by applying voltages at the collection channel reservoirs, avoiding the sample dilution problem. After sample loading, elution buffer is placed in the

collection reservoir, and the adsorbed analytes are eluted in the opposite direction and directed towards the MS inlet through the common elution pathway at the end of the fractionation zone by reversing the potential polarity. This design allows the use of a single electrospray tip and eliminates the multi-path flow leakage problem, as the collection channels are not connected downstream of the SPE beds.

5.3 Impedance Simulation and Theoretical Calculation

It is well known that leakage at channel intersections is a notorious problem in electrokinetic systems [14-16]. In order to overcome this problem, we took advantage of electrokinetic focusing to pinch the sample stream. Figure 5.4a shows a cartoon illustrating the pinched sample flow profile in the fractionation region. The basic geometry of the microdevice is three inlet channels (one sample channel and two sheath channels) that meet and flow through the fractionation zone into individual collection channels. The sheath buffer, upon meeting the sample channel, pinches the sample stream and prevents the analyte from diffusing outwards and leaking into the other floating channel. The parameter of particular interest in our experiment is the sample stream width before entering the collection channel. Too wide a sample stream may contact the inlets of other collection channels, causing cross-contamination. Too narrow a sample stream will generate too much dilution of the sample by the sheath buffers.

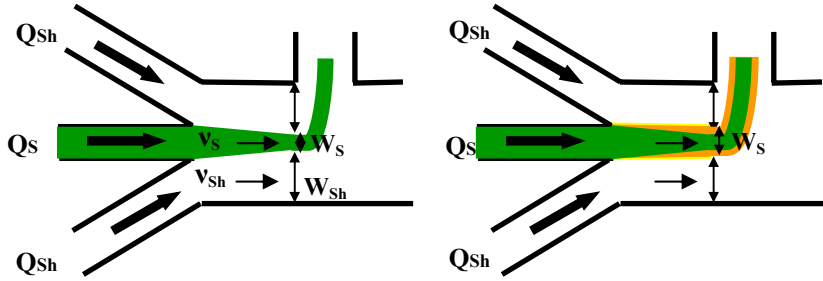


Figure 5.4 Cartoon illustrating the pinched sample stream profile. (a) Sample stream surrounded by two sheath streams; (b) Diffusion of sample across the boundary into sheath fluid streams. Arrows depict the direction of fluid transport, and the sheath streams are colored white, and sample stream is colored green. The widening regions due to diffusion between sheath and sample streams are indicated in orange.

The purpose of the simulation and theoretical calculation is to estimate the sample stream width under different conditions and investigate how it depends on factors such as applied voltages and channel dimensions. The simulation results will be compared to results obtained from real experiments to decide whether the simulated results are to be trusted. The calculation of sample stream width followed Wang's thesis work [13], and here we gave a more detailed derivation.

According to conservation of mass for incompressible liquids, the amount of fluid flowing into a point must be equal to the amount of fluid out of the point:

$$Q_{sh} + Q_s + Q_{sh} = Q_{out} \quad (5.1)$$

where Q_{sh} and Q_s are the volumetric flow rates of the sheath stream and sample stream respectively. Q_{out} is the total volumetric flow rate in the fractionation zone.

The volumetric flow rate, Q , is given by:

$$Q = vA \quad (5.2)$$

where v is the linear velocity, and A is the cross-sectional area of the flow, which is the product of stream width and channel depth.

In an electrokinetically-driven system, the bulk fluid flows are generated by EOF. The electroosmotic velocity, v_{eo} , is given by:

$$v_{eo} = \mu_{eo} E \quad (5.3)$$

where μ_{eo} is electroosmotic mobility and E is the electric field within the microfluidic channel.

Thus, the flow rate of sample stream (Q_s) and sheath stream (Q_{sh}) in the fractionation zone can be calculated by the following equations:

$$Q_s = v_{eo} A_s = \mu_{eo} E_f \times d_f \times W_s \quad (5.4)$$

$$Q_{sh} = v_{eo} A_{sh} = \mu_{eo} E_f \times d_f \times W_{sh} \quad (5.5)$$

where d_f and E_f are the channel depth and electric field in the fractionation zone, respectively, and W_s and W_{sh} are the sample stream width and sheath stream width in the fractionation region.

Different flow rates of sample stream and sheath stream result in different cross-sectional areas of these two flows in the fractionation zone. The cross-sectional area of the flow depends solely on the stream width because the channel depth in the fractionation zone is constant. Therefore, by dividing Equation (5.4) and Equation (5.5), a relation between the two widths as a function of flow rates is found in Equation (5.6).

$$\frac{W_s}{W_{sh}} = \frac{Q_s}{Q_{sh}} \quad (5.6)$$

In a complex manifold of channels, the electric field may differ within each portion of the channel due to differences in the cross-sections. Such changes can

be modeled by treating each channel segment as an electrical resistor with a resistance R given by:

$$R = \rho \frac{l}{A} \quad (5.7)$$

where A is the cross-sectional area of the channel, l is the channel length, and ρ is the solution's electrical resistivity. The flow rate in a branch channel can be calculated by:

$$Q = vA = \mu EA = \mu \frac{V}{l} A = \mu \frac{IR}{l} A = \mu \rho I \quad (5.8)$$

Thus the current in each channel can provide an estimate of the flow rate. In the sheath branch channel, the flow rate of the sheath buffer is proportional to the current in the sheath channel, I_{sh} as follows:

$$Q_{sh} = \mu_{eo} \rho I_{sh} \quad (5.9)$$

while in the sample branch channel, the flow rate of the sample is given by:

$$Q_s = \mu_{eo} \rho I_s \quad (5.10)$$

where I_s is the current in the sample branch channel. Because sample buffer is the same as the sheath buffer, the electrical resistivity ρ will be the same. Thus we have:

$$\frac{I_s}{I_{sh}} = \frac{Q_s}{Q_{sh}} \quad (5.11)$$

Combining Equation 5.6 and 5.11, we obtained:

$$\frac{W_s}{W_{sh}} = \frac{I_s}{I_{sh}} \quad (5.12)$$

The sample stream width relative to the width of the fractionation zone can then be calculated according to:

$$\frac{W_s}{W_{\text{fractionation zone}}} = \frac{I_s}{I_s + 2I_{\text{sh}}} = \frac{I_s}{I_{\text{fractionation zone}}} \quad (5.13)$$

By modeling the microfluidic device as a network of electrical resistors, upon application of voltage to each reservoir, the current in each channel can be calculated according to Kirchoff's law and Ohm's law. With an increasing complexity of the microfluidic device design, a simulation tool is necessary to predict the current in each channel.

PSpice is a powerful program that can perform functions such as creating a circuit design, running simulation and analyzing simulation results. With the help of this program, we can simulate the device designs, calculate and plot the voltages and currents of a circuit quickly and easily.

To do the simulation, an electronic circuit containing elements such as resistors and voltage sources was first built, and values such as resistances and voltage settings were then assigned to each part. In this simulation model, we converted the channels into equivalent resistances. In real experiments, all the channels were filled with the same buffer, i.e. the resistivity of the solution, ρ is constant in the whole device. Therefore, we used the relative impedance which equals R/ρ , instead of the true impedance of each channel. These values depend only on the channel dimensions, more specifically, on the ratios of channel lengths and the cross-sectional areas (l/A). With the circuit layout set up, running the simulation gives the voltage corresponding to every node and the current in each channel. The ratio of current flow in the sample channel to the total current

flow in the fractionation region ($I_s/I_{fractionation\ zone}$) is of particular importance, because it predicts the sample stream width in the fractionation zone relative to the total width of this region, as showed in Equation (5.13).

In order to make a more reliable simulation, we need to take into account the diffusion effect. Diffusion will transport material into adjacent fluid streams. Thus, there will not be an abrupt border between two fluids (Figure 5.4b). This effect can be described roughly by Fick's first law of diffusion, in which, the mean diffusion distance, d , is given by:

$$d = \sqrt{2Dt} \quad (5.14)$$

where D is diffusion coefficient and t is the time it takes for sample molecules to flow a distance l from the sheath point to the inlet of the collection channel at ground. The use $d = \sqrt{2Dt}$ to estimate the diffusion distance is a moderate approximation of the true error function distribution. This model is used for calculation of diffusion starting from an infinitely narrow zone, thus it is not physically accurate when used in estimation of diffusion from a sample band with a certain width, as is in our case. For simplicity, this model was used for most of the calculation of diffusion, while in several cases, the error function model in which the initial sample width is considered was used to predict the diffusion profile [17].

Charged analytes under an electric field are also driven by an electrophoretic force. The actual velocity of charged analytes, v_{app} , depends on the apparent mobility, μ_{app} , which is the sum of electroosmotic mobility, μ_{eo} and electrophoretic mobility, μ_{ep} .

$$v_{app} = \mu_{app} \times E = (\mu_{eo} + \mu_{ep}) \times E \quad (5.15)$$

Thus the transit time t can be calculated from the voltage drop as follows:

$$t = \frac{l}{v_{app}} = \frac{l}{\mu_{app} E_f} = \frac{l^2}{\mu_{app} V_{drop}} \quad (5.16)$$

where V_{drop} and E_f are voltage drop and electric field between the sheath point and the inlet of the grounded collection channel in the fractionation zone. Substituting for t in the diffusion equation, the diffusion distance is found to be:

$$d = \sqrt{2Dt} = \sqrt{\frac{2Dl}{v_{app}}} = \sqrt{\frac{2Dl}{\mu_{app} E_{fr}}} = \sqrt{\frac{2Dl^2}{\mu_{app} V_{drop}}} \quad (5.17)$$

The width of the sample stream would then be, when diffusion on both sides of sample stream is taken into account, as stated in following equation:

$$W_{sample} = \frac{I_s}{I_{fractionationzone}} \times W_{fractionationzone} + 2d = \frac{I_s}{I_{fractionationzone}} \times W_{fractionationzone} + 2\sqrt{\frac{2Dl^2}{\mu_{app} V_{drop}}} \quad (5.18)$$

The first term depends on the volumetric flow rate of sample relative to the total flow rate in the fractionation zone, which can be determined from the currents predicted by the simulation. The second part is the time dependent term due to diffusion. In order to calculate the distance the sample diffuse in the traveling time t , the apparent mobility μ_{app} of the sample was measured experimentally and diffusion coefficient D of the dye was obtained from literature ($3.3 \times 10^{-6} \text{ cm}^2/\text{s}$ for fluorescein [18]). The voltage drop V_{drop} can be easily calculated since the voltage at each intersection point can be obtained from pSpice simulation.

5.4 Experimental Section

5.4.1 Chip Fabrication

To produce channels with different depths, a two-mask approach was used. Two photomasks were designed using L-edit and were fabricated in the Nanofab. Mask A contains all the collection channels and the elution channel, and Mask B contains all the other channel patterns.

The fabrication of the multi-channel devices following the standard procedures produced microchannels with poorly-defined edges due to the non-uniform photoresist coating above an etched substrate during the second mask process, which is consistent with Wang's results [13].

The devices were then fabricated following a method improved by Zhen Wang [13]. In this method, all the collection and elution channels were first defined by Mask A using standard photolithography and etched to 20 μm using wet chemical etching. After removing the remaining photoresist and the metal layer, the etched wafer was coated with chrome and gold again. During the lithography process of the second mask layer, three layers of photoresist, instead of one layer, were spin-coated on the etched substrate, and the spinning speed was reduced from 4000 rpm to 1000 rpm. Briefly, the substrate was first coated with one layer of photoresist (500 rpm for 10 s, 1000 rpm for 40 s), soft-baked for 30 min, and left at room temperature for re-hydration for 15 minutes, and then this whole process (spinning–baking–re-hydration) was repeated twice.

Using this method, the substrate is covered with three layers of photoresist with a thickness of $\sim 6 \mu\text{m}$. No streaks appear on the substrate, indicating the

uniform distribution of photoresist on the etched substrate. The patterns on the second mask (Mask B) were then transferred to the substrate through UV exposure, followed by etching the exposed regions to 5 μm . Given that the photoresist is much thicker, the exposure time was increased from 4 s to 20 s, as was the developing time, which was extended from 25 s to 50 s. Finally, to form a closed network of the channels, a cover plate with access holes was thermally bonded to the etched bottom wafer.

5.4.2 Experimental Setup

5.4.2.1 Single Wavelength Detection System

Microchip performance is monitored by laser-induced fluorescence (LIF) using a CCD for imaging. The setup for fluorescence detection was similar to the one presented in Chapter 2 (Section 2.2.4) with a few modifications. To enable taking LIF images of large microdevice areas, the excitation light from the argon ion laser was expanded by passing the laser beam through a convex lens, allowing for a larger excitation region. The resulting beam covers the entire fractionation zone with sufficient intensity to excite detectable fluorescence emission. A 5 \times , 0.1 N.A. microscope objective (NeoDPlan 5, Olympus, Japan) was used in order to increase the field of view for detection. The fluorescence signal was collected by the objective, passed through a dichroic mirror (505DRLP, Omega Optical), and filtered by an orange glass absorption filter (OG515, Omega Optical) to remove the majority of the incident laser light. The resulting images or videos were captured with a SONY CCD-IRIS camera and recorded using Windows Movie

Maker. In-house written LabVIEW program (National Instruments, Austin, TX) was used for computer control of voltages required for chip operation. The power supply (blue box) used to provide the high voltage has been described previously in Chapter 2.

5.4.2.2 Multi-Wavelength Detection System

In order to investigate the potential sample carryover during sequential elution process, a multi-wavelength detection system, which enables simultaneous recording of green and red fluorescence, was used. This system was built by Jelena Dragoljic in this research group [19]. A critical part of the system was a home-built optical connector for two PMTs (Figures 5.5). This part has built in a 580DRLP dichroic mirror (Omega Optical, part #XF2018) to separate green and red fluorescence.

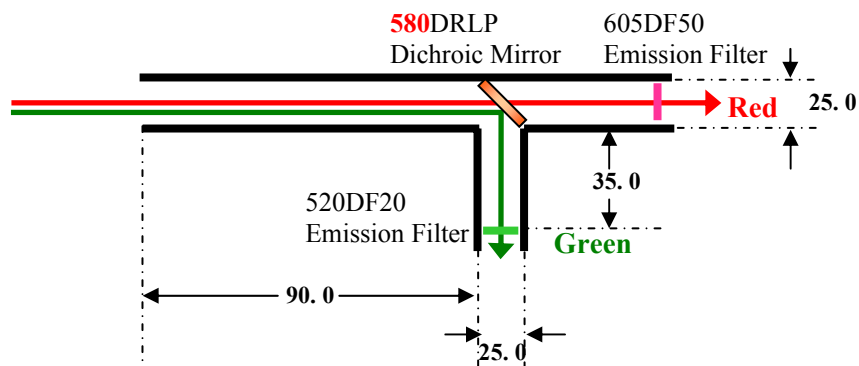


Figure 5.5 Schematic layout of the optical connection part for two PMTs in the multi-wavelength detection system. Dimensions of the connector are expressed in millimeter.

Figure 5.6 and Figure 5.7 depict the schematic drawing of the experimental setup and pictures of the final assembled platform for multi-wavelength detection. Two PMTs were used, one PMT (Hamamatsu, Photonica, Type No. H6780-02,

with a built-in gain of 10^6 Volts/Amp) with a high sensitivity for red fluorescence, was used with a 605DF50 emission filter, while the other PMT (Hamamatsu, Photonica, Type No. H5783, with a built-in 10^6 Volts/Amp gain) with a high sensitivity for green fluorescence was used with a 520DF20 emission filter. PMTs were connected to a home-built 0-10 V power supply with additional home-built amplifiers (293,333 times gain) and electronic filters with a 5th order low-pass Bessel filter with a frequency of 100 Hz. This was designed and built by Kim Nguyen-Do at the Chemistry Electronic Shop of University of Alberta. The signal was recorded using a PC computer (Celeron, 500 MHz) with National Instruments PC 1200 card (Celeron, 500 MHz) and a LabVIEW program. Collected data were analyzed in Origin 7.0. The LabVIEW program used to record data for the multi-wavelength detection system was designed by Randy Tsen.

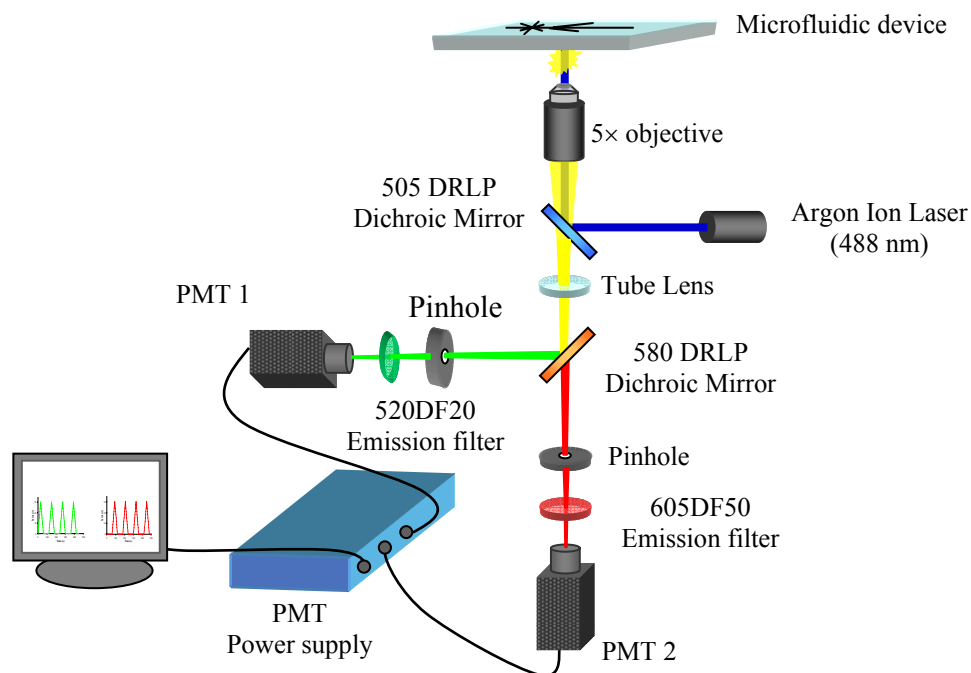


Figure 5.6 Schematic drawing of experimental setup.

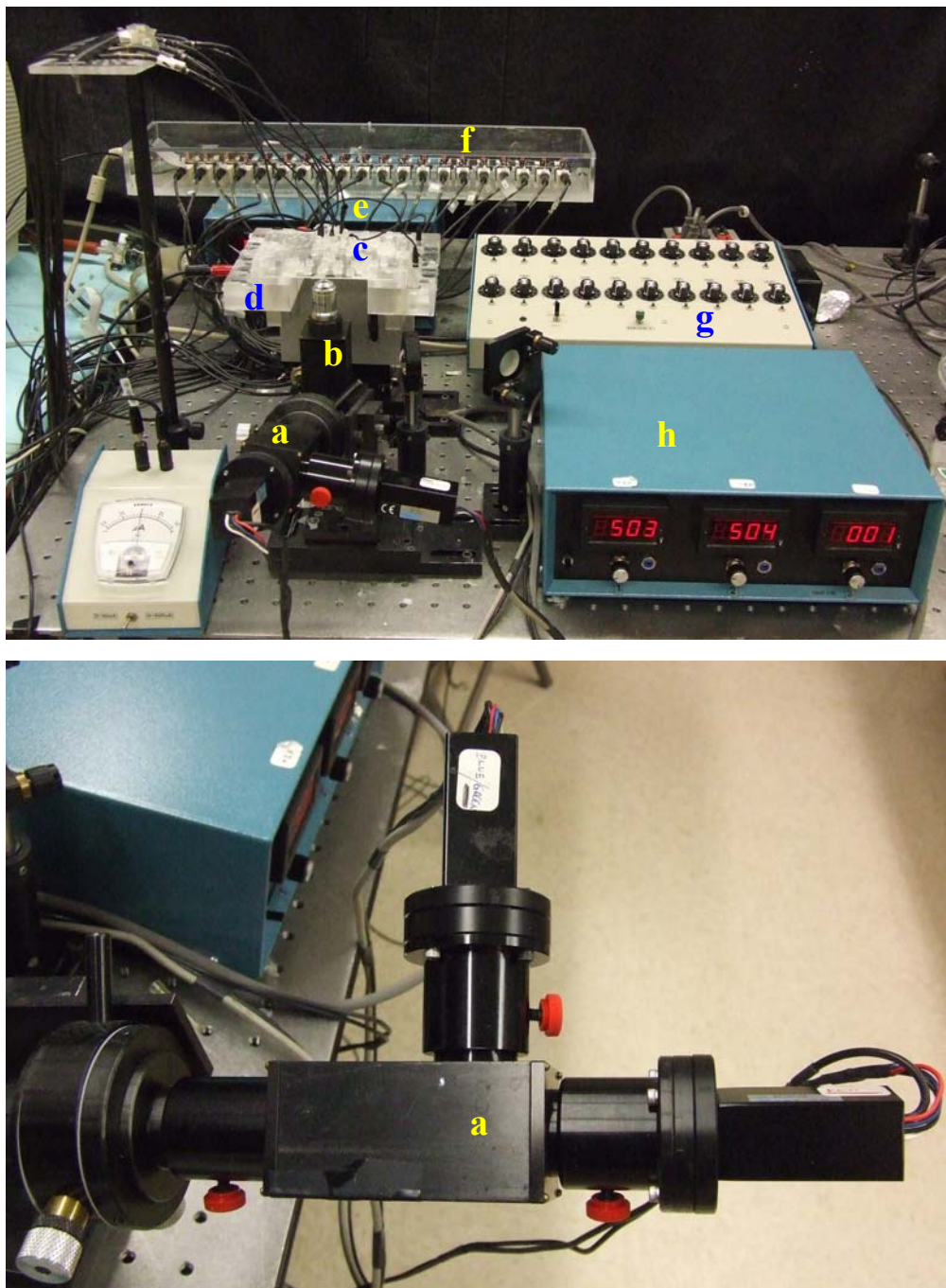


Figure 5.7 Final platform assembled for multi-wavelength detection. Entire assembled platform (top) and a closer view of the connection part (bottom). a: Connection part for 2 PMTs, b: Confocal epiluminescent microscope, c: Microchip, d: Chip holder, e: Power supply (blue box), f: Relay box, g: Timer, h: PMT power supply.

5.5 Results and Discussion

5.5.1 Fabricated Devices

The devices fabricated with the improved methods demonstrated nicely-defined channel edges, as is shown in Figure 5.8 for the fractionation zones of five etched devices.

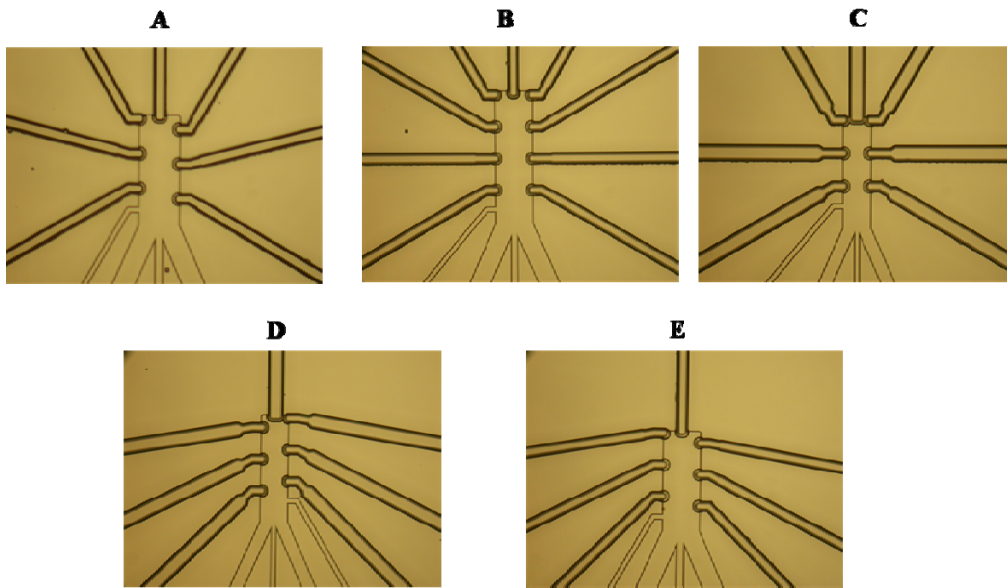


Figure 5.8 Images of fractionation zones of the five fabricated devices (A-E) with different dimensions showing well-defined channel edges.

5.5.2 Fractionation and Collection

5.5.2.1 Measuring the Mobility of Fluorescein

A fluorescent dye, fluorescein, was dissolved in 20 mM potassium phosphate buffer (pH 7) and was used as sample for sheath flow tests using LIF detection. To measure the mobility of fluorescein, a simple device with a double-T injector was used and the detector was positioned 2.2 cm from the intersection point along the main channel (Figure 5.9).

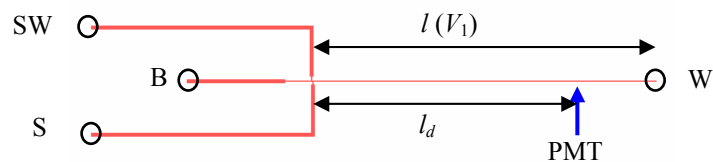


Figure 5.9 The layout of the microchip used for determination of analyte mobility. Sample reservoir (S) was loaded with fluorescein.

Voltage applied between sample (S) and sample waste (SW) reservoir draws sample into the channel and across the intersection point. Subsequent application of a voltage between buffer (B) and waste (W) reservoirs drives a small plug of sample along the main channel and past the detector, giving an electropherogram shown in Figure 5.10a.

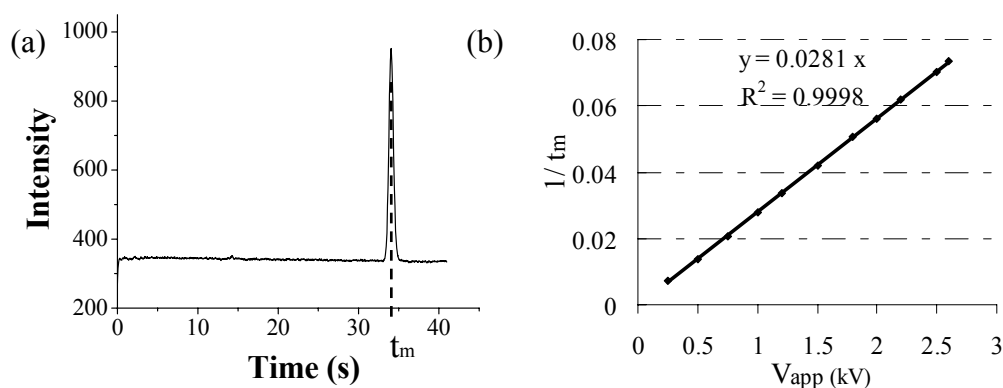


Figure 5.10 Determination of mobility of fluorescein. (a) Electropherogram obtained with an applied potential of 1.0 kV between reservoir B and W; (b) A plot of $1/t_m$ versus V_{app} gives a linear relationship.

Because the channel between reservoir B and W has two segments of different cross-sectional areas, the electric field in the narrow channel is calculated from the fraction (0.9523) of the V_{app} that drops between the intersection point and reservoir W. The length of this segment, l , is 6.9 cm. The overall mobility, μ_{app} , is related to the applied voltage by the following equation:

$$\frac{1}{t_m} = \frac{0.9523\mu_{app}}{l_d l} \cdot V_{app} \quad (5.19)$$

where l_d is the distance from the injection point to the detector and V_{app} is the total applied voltage. The migration times, t_m , were determined by applying a series of voltages over a range of 250-2600 V between reservoir B and W. Plotting l/t_m versus V_{app} gives a linear relationship with a correlation coefficient of 0.9998 (Figure 5.10b). The apparent mobility of fluorescein in a PolyE-323 coated channel was calculated from the slope to be $4.48 \pm 0.06 \times 10^{-4} \text{ cm}^2/(\text{V}\cdot\text{s})$.

5.5.2.2 Study of Sheath Effect on PolyE-323 Coated Devices.

5.5.2.2.1 Sheath Flow Tests

All studies in this chapter were carried out in polyE-323 coated microdevices, which are modified according to the coating procedure described previously in Chapter 3. Figure 5.11 demonstrates the necessity of using sheath flow to reduce leakage. In this experiment, sample was introduced into individual collection

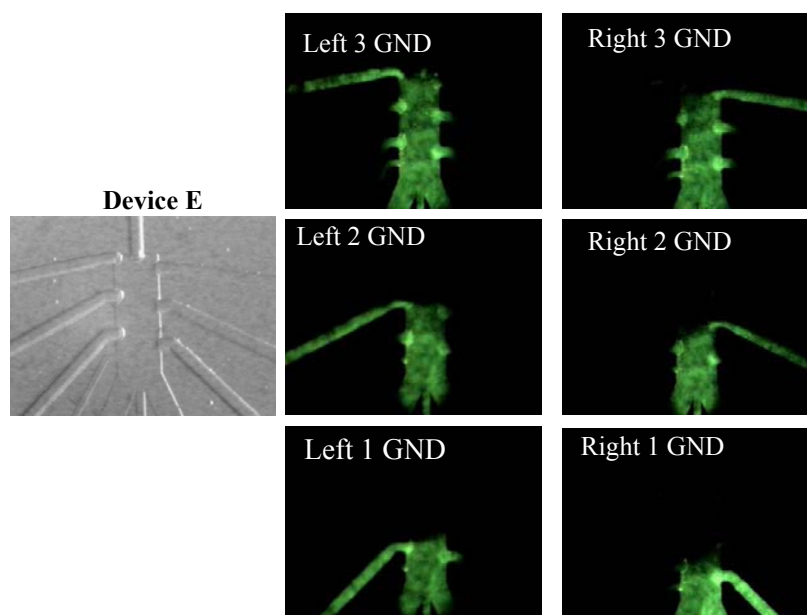


Figure 5.11 Images illustrating the flow profiles of dye stream into grounded collection channels without protection from sheath buffers. Left side: a picture of the fractionation zone of Device E. Sample channel: -1.0 kV , sheath channel: floating. Six collection channels were grounded individually.

channel by applying high voltage at the sample reservoir, with one of the collection channels held at ground and the other channels left floating. Without protection from sheath buffer, the sample stream spreads in the fractionation region and induces leakage into the other floating channels.

The sample stream can be electrokinetically focused by applying high voltages to the sheath reservoirs to drive sheath buffer into the grounded channel, as is shown in the sheath images in Figure 5.12.

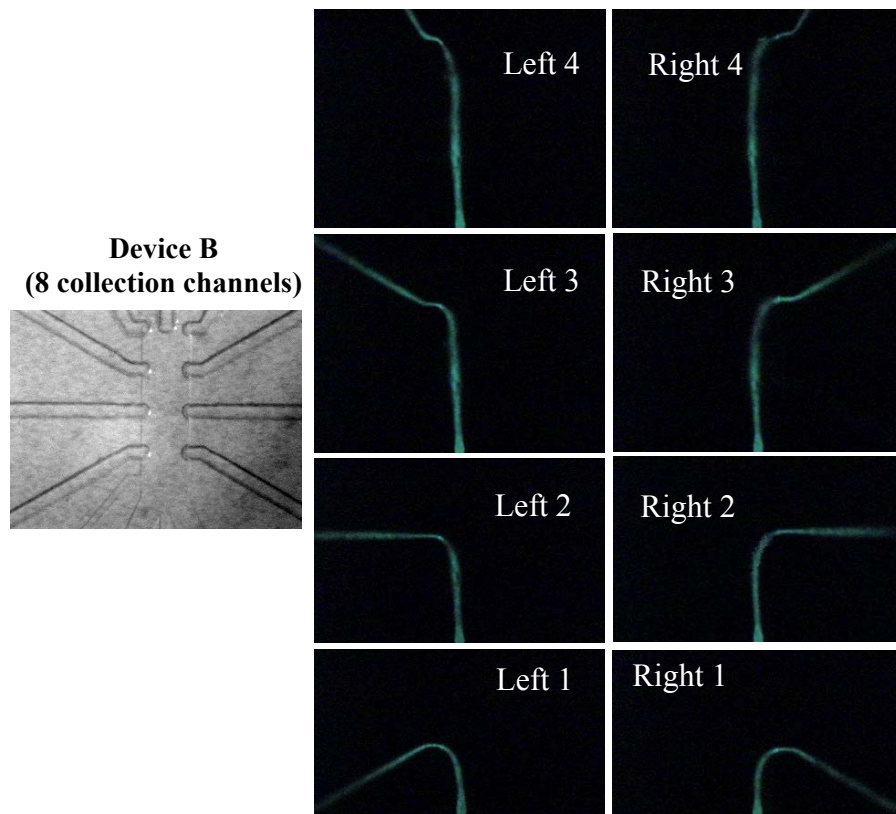


Figure 5.12 Sheath images illustrating that the focused fluorescein stream was delivered into individual collection channels under the protection of sheath buffers. On the left side of the sheath images is a picture of the fractionation zone of Device B. Sample voltage: -1.0 kV, sheath voltage: -1.5 kV. Collection channel was grounded individually.

With -1.0 kV applied on the sample reservoir and -1.5 kV applied on the sheath reservoir, while each collection channel grounded individually in Device B,

the fluorescein stream is nicely pinched and delivered into individual collection channels under the protection of sheath streams.

Signal intensity profiles can be extracted from the sheath images using ImageJ (NIH, Bethesda, MD). As shown in Figure 5.13, intensity profiles are extracted from the four right images in Figure 5.12, which illustrate that the sample streams enter into the four collection channels on the right side (Right 1 to Right 4). These profiles are taken at the channel inlet position. Sample stream widths at the inlet of each grounded collection channel are estimated from the extracted profiles by measuring the peak width at full width at half-maximum (FWHM). With the magnification of the microscope used in these experiments, the width of a pixel of the CCD camera corresponds to a length of 3.1 μm on the microchip. The sample stream widths estimated from the sheath images in Figure 5.12 are listed in Table 5.2 as *observed* W_{sample} .

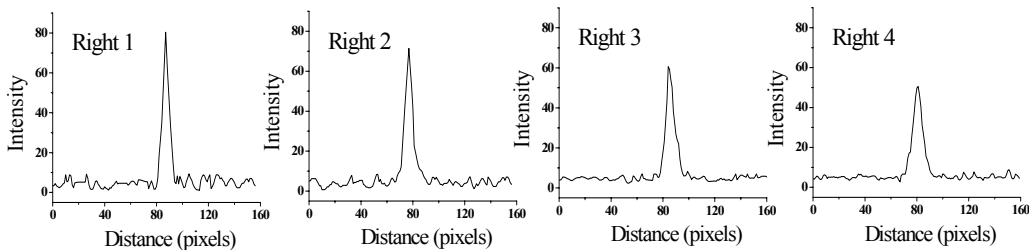


Figure 5.13 Intensity profiles extracted from sheath images for sample streams entering into the four collection channels on the right side of Device B.

We used pSpice software to do impedance simulation to predict the sample flow profile in the fractionation region in a pinched flow. Figure 5.14 shows an example of the circuit and the simulation result of the case when the fourth collection channel of Device B was grounded. Table 5.2 summarizes the simulation results and the values required for calculating the sample stream

widths in four different collection channels. The widths of the sample stream predicted from the simulation are referred to as *calculated* W_{sample} . The diffusion distance was calculated using the approximation model $d = \sqrt{2Dt}$.

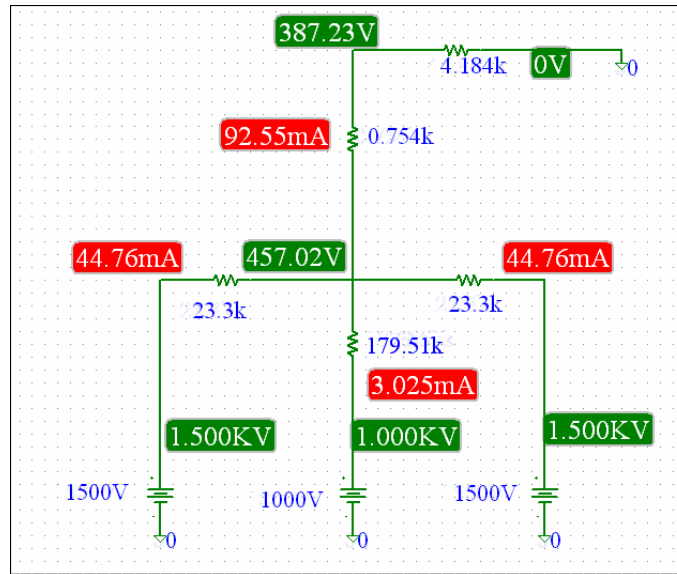


Figure 5.14 Simulation result of the case when the fourth collection channel of Device B was grounded. Sample voltage: -1.0 kV, sheath voltage: -1.5 kV.

The images in Figure 5.12 demonstrate that the sample stream becomes wider and wider as it is delivered into collection channels further downstream of the fractionation region, as predicted by the pSpice diffusion simulation. The theoretical expectation is compared with results from experiments, and differences in the range of 3–4 μm are observed between predicted and observed sample stream widths. The theoretical calculation from simulation does not deviate much from the experimental results considering the following factors. First, pSpice does not consider subtle changes in physical geometry of the microchannels, which could affect the prediction of currents and voltages. Second, the discrepancy might be related to hydrodynamic flow resistance, which is not considered in the simulation model. In addition, as mentioned in Section 5.3, the

use of the approximation model $d = \sqrt{2Dt}$ to estimate the diffusion distance is not accurate when used in estimation of diffusion from a sample band with a certain width.

Table 5.2 Simulation results for Device B when four collection channels were grounded separately.

Channel at ground	Right 1st	Right 2nd	Right 3rd	Right 4th
V_{sample} (V)	1000	1000	1000	1000
V_{sheath} (V)	1500	1500	1500	1500
$l_{travel\ distance}$ (μm)	190	340	490	640
$I_{sample\ channel}$ (mA)	3.22	3.154	3.089	3.025
$I_{fractionation\ zone}$ (mA)	95.75	94.66	93.6	92.55
V_{drop} (V)	21.44	37.86	54.00	69.78
$E_{fractionation\ zone}$ (V/cm)	1128.4	1113.5	1102.0	1090.3
μ [$\text{cm}^2/(\text{V}\cdot\text{s})$]	4.48×10^{-4}			
D (cm^2/s)	3.3×10^{-6}			
$t_{fractionation\ zone}$ (s)	0.038	0.068	0.099	0.131
d (μm)	4.98	6.71	8.09	9.30
$W_{fractionation\ zone}$ (μm)	172			
Calculated W_{sample} (μm)	15.8	19.2	21.9	24.2
Observed W_{sample} (μm)	19.3	22.8	25.7	28.1
ΔW_{sample} (μm)	3.5	3.6	3.8	3.9
$W_{sample}/W_{fractionation\ zone}$	0.092	0.111	0.127	0.141

V_{sample} and V_{sheath} , voltages applied to sample reservoir and sheath reservoir;
 $I_{sample\ channel}$ and $I_{fractionation\ zone}$, current in sample channel and fractionation zone;
 $l_{travel\ distance}$, V_{drop} , and $E_{fractionation\ zone}$ are the distance, voltage drop and electric field of part of the fractionation zone between the sheath point and the inlet of the collection channel at ground;
 μ and D are the mobility and diffusion coefficient of fluorescein;
 $t_{fractionation\ zone}$ and d are the transit time and diffusion distance for sample to travel from the sheath point to the inlet of the grounded collection channel;
Calculated W_{sample} , sample stream width calculated from pSpice simulation;
Observed W_{sample} , sample stream width measured from sheath images;
 ΔW_{sample} is the difference of observed and calculated sample stream width;
 $W_{sample}/W_{fractionation\ zone}$, the ratio of the observed sample stream width to the total width of fractionation zone.

Although pSpice impedance modeling can not give as accurate a simulation as more sophisticated simulation methods, such as Finite Element Analysis, it is simple and fast. This simulation method gives us enough information for our experiments, such as instructions on the choice of voltages and channel dimensions. It provides strong insight into our device and facilitates more complex design.

5.5.2.2.2 Error Function Model for Diffusion Profile

In most cases in practice, the initial distribution of the diffusing substance occupies a finite region. We can define the initial sample concentration as C_0 and the initial width as $2h$, meaning that the sample is initially confined in the region $-h < x < +h$. By solving the diffusion equation, the sample concentration distribution at time t is given by [17]:

$$C/C_0 = \frac{1}{2} \left\{ \operatorname{erf} \frac{h-x}{2\sqrt{Dt}} + \operatorname{erf} \frac{h+x}{2\sqrt{Dt}} \right\} \quad (5.20)$$

where D is the diffusion coefficient of the substance, erf is the error function defined as:

$$\operatorname{erf}(z) = \frac{2}{\sqrt{\pi}} \int_0^z e^{-y^2} dy \quad (5.21)$$

With these equations, the sample concentration distribution after a certain time can be obtained. We used a sample stream entering into the fourth collection channel on the left side of Device B as an example. As shown in Figure 5.15, the sample stream is tightly focused and reaches a minimum, and then disperses gradually due to the diffusion of dye sample into the adjacent focusing streams. Signal intensity profiles were extracted from the focused stream at five positions

(1-5), as indicated by the broken lines. The profiles are normalized and plotted in one graph in Figure 5.16 in order to compare the relative peak widths.

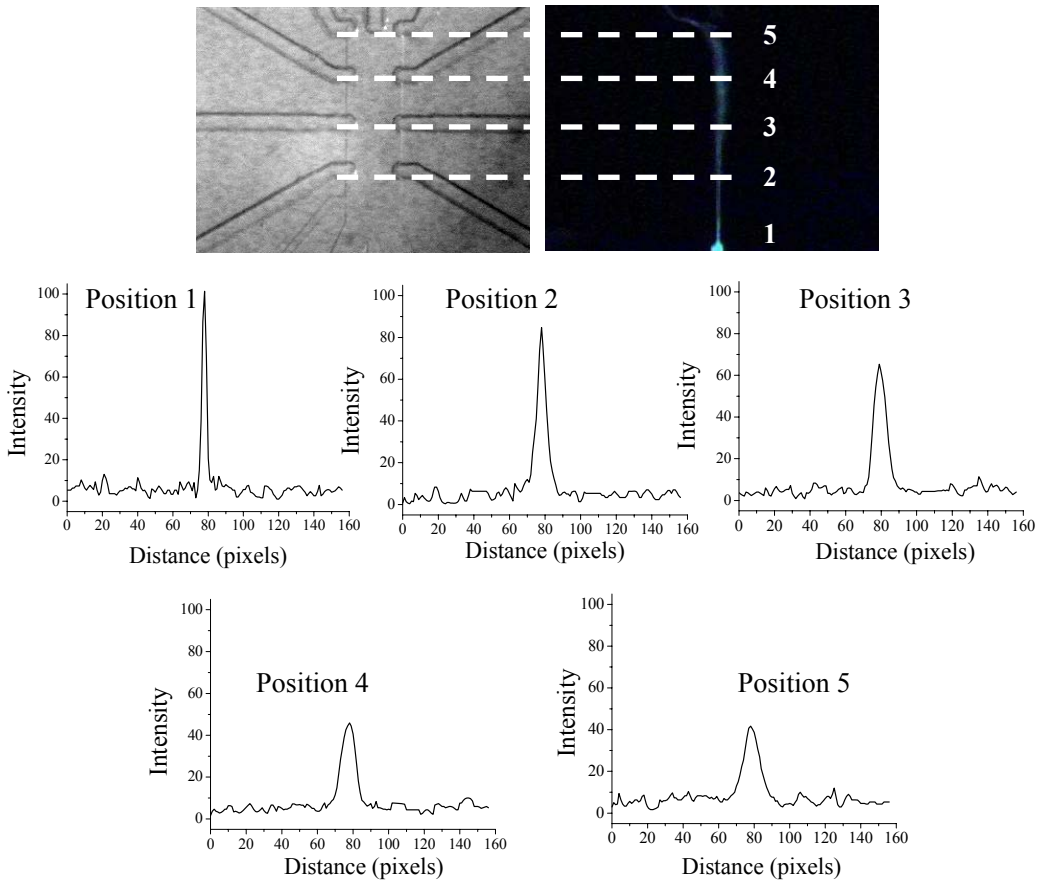


Figure 5.15 Signal intensity profiles extracted from the sheath images. The intensity profiles were obtained by scanning at the positions as indicated by the red lines using ImageJ.

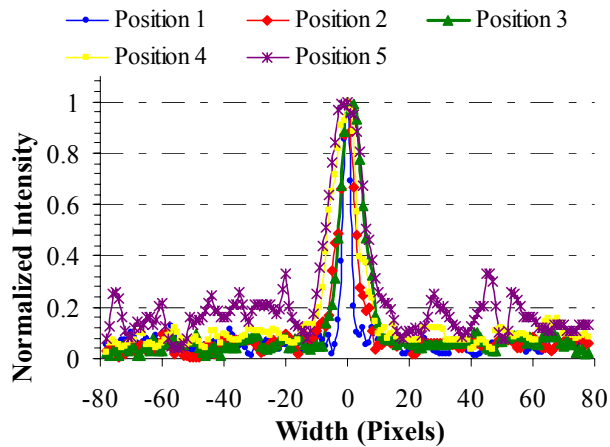


Figure 5.16 Signal intensity profiles with normalized intensity.

To study the diffusion effect in our system, position 1 was selected to represent the initial state. We considered that the diffusing substance was initially confined in a region with a width equal to the FWHM in the extracted profile at position 1 ($2h$). The peak signal intensity of the profile at position 1, which reflects the initial concentration C_0 , was used as the initial intensity (I_0). The diffusion coefficient is $3.3 \times 10^{-6} \text{ cm}^2/\text{s}$ for fluorescein [18] and the transit time t was calculated from pSpice simulation. Using Equation 5.20 and 5.21, the signal intensity distributions at position 4 and 5 were calculated and are plotted in Figure 5.17, where the X axis is displayed as the ratio of the distance from the center of the sample stream (x) to half of the initial width (h) and Y axis is displayed as the signal intensity normalized by the initial value (I/I_0).

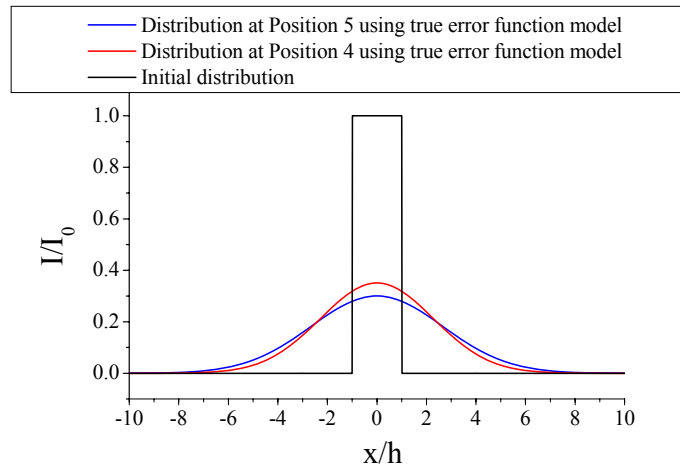


Figure 5.17 Calculated signal intensity distributions at the initial state, position 4 and 5. X axis is displayed as the ratio of the distance from the center of the sample stream (x) to half of the initial sample width (h) and Y axis is displayed as the signal intensity normalized by the initial value (I/I_0).

The signal intensity profiles extracted from the sheath images at position 4 and 5 were normalized by the initial intensity and initial width and fit to a Gaussian regression, as shown in Figure 5.18a and c, respectively. The fitted

Gaussian curves with baseline subtracted were compared with the theoretically predicted diffusion profiles and the results are illustrated in Figure 5.18b and d, which shows that the experimental results fit the theoretical prediction reasonably well. The differences in the FWHM between the calculated and fitted experimental curves are $\sim 1 \mu\text{m}$.

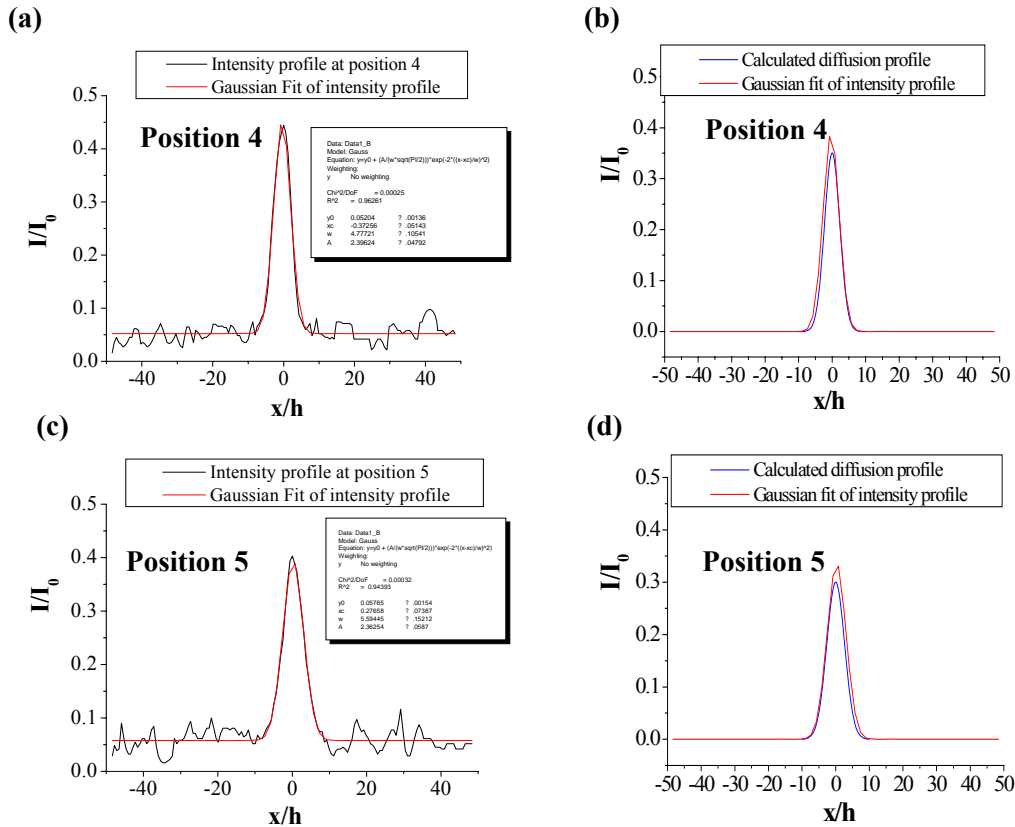


Figure 5.18 Comparison of fitted signal intensity profiles to the theoretically predicted diffusion profiles for position 4 (a, b) and position 5 (c, d). (a) and (c) Extracted profiles from the sheath images at position 4 and 5 were normalized by the initial intensity and initial width and fit to a Gaussian regression. (b) and (d) Comparison of the fitted Gaussian curves to the theoretically predicted diffusion profiles.

5.5.2.2.3 Impact of focusing voltage on the Sheath Effect

The impact of the sheath voltage on the focusing effect was studied by holding the sample voltage constant at -1.0 kV, while varying the sheath voltage from -1.0

kV to -2.5 kV. Figure 5.19 shows the sheath images and the corresponding extracted profiles for the third channel on the left side of Device C. Sample stream widths estimated from these profiles are listed in Table 5.3 as *observed* W_{sample} .

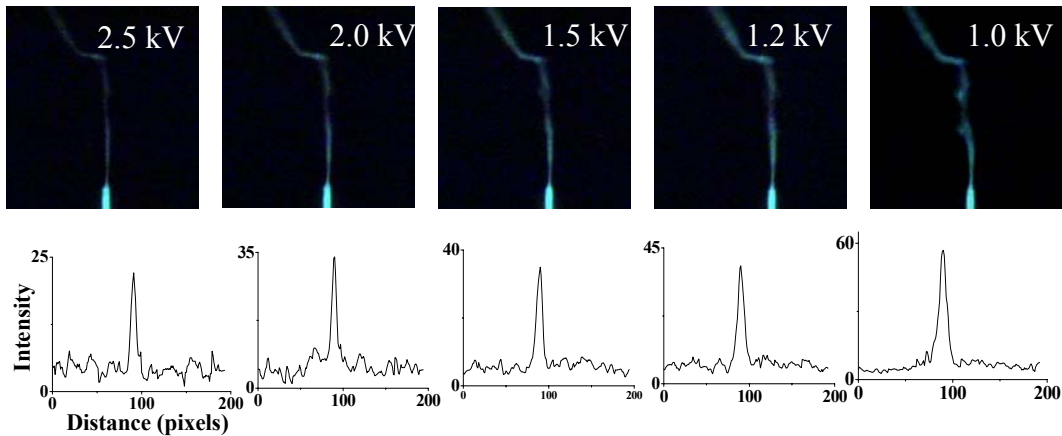


Figure 5.19 Images and extracted intensity profiles of the pinched sample streams at different sheath voltages. The third channel on the left side of Device C was grounded. Sample voltage: -1.0 kV, sheath voltage: from -1.0 kV to -2.5 kV.

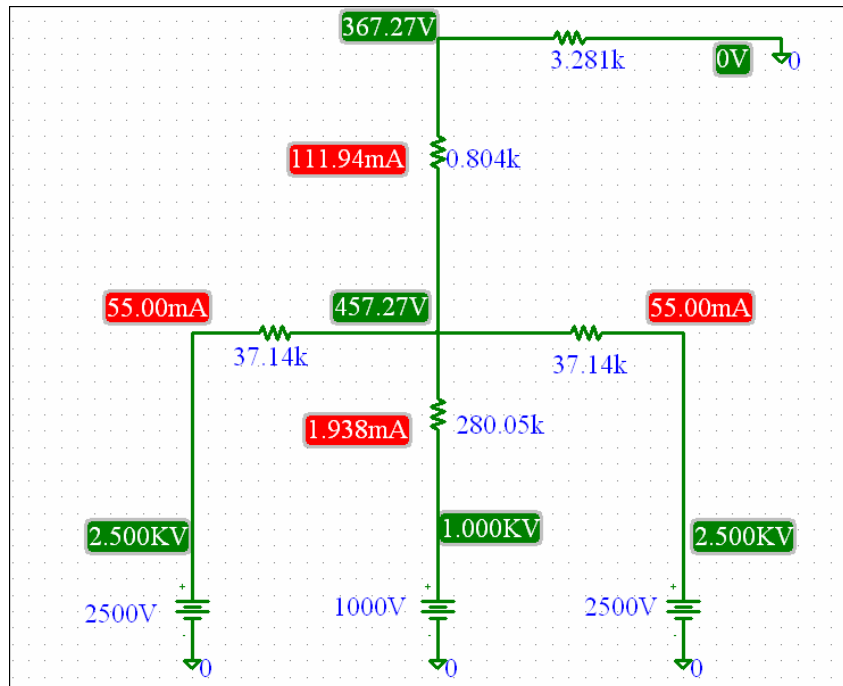


Figure 5.20 Simulation results for Device C when the third collection channel was grounded. Sample voltage: -1.0 kV, sheath voltage: -2.5 kV.

Figure 5.20 shows the simulation results for Device C when the third collection channel was at ground with a sheath voltage of 2.5 kV. Table 5.3 summarizes the data obtained from pSpice simulation and the calculation of sample width (*calculated* W_{sample}) using the approximation model. From the sheath images, it is obvious that the sample stream gets thinner as the pinching voltage increases, which is in agreement with the simulation results in Table 5.3. This indicates that as the sheath voltage increases, the degree of focusing increases. Discrepancies of 3–4 μm were observed between predicted and observed sample stream widths.

Table 5.3 Simulation results for Device C when the third collection channel was grounded at different sheath voltages.

Channel at ground	Left 3rd				
V_{sample} (V)	1000	1000	1000	1000	1000
V_{sheath} (V)	2500	2000	1500	1200	1000
$l_{Travel\ distance}$ (μm)	490				
$I_{sample\ channel}$ (mA)	1.938	2.256	2.574	2.765	2.892
$I_{fractionation\ zone}$ (mA)	111.94	90.13	68.32	55.24	46.51
V_{drop} (V)	90	72.46	54.93	44.41	37.4
$E_{fractionation\ zone}$ (V/cm)	1836.7	1478.8	1121.0	906.3	763.3
μ [$\text{cm}^2/(\text{V}\cdot\text{s})$]	4.48×10^{-4}				
D (cm^2/s)	3.3×10^{-6}				
$t_{fractionation\ zone}$ (s)	0.060	0.074	0.098	0.121	0.143
d (μm)	6.27	6.99	8.02	8.92	9.73
$W_{fractionation\ zone}$ (μm)	124				
Calculated W_{sample} (μm)	14.7	17.1	20.7	24.1	27.2
Observed W_{sample} (μm)	18.0	20.6	24.5	28.0	31.3
ΔW_{sample} (μm)	3.3	3.5	3.8	3.9	4.1
$W_{sample}/W_{fractionation\ zone}$	0.118	0.138	0.167	0.194	0.219

5.5.2.3 Study of Sheath effect on Devices with Monolithic Beds

5.5.2.3.1 Assembly of Monolithic Beds into the Multi-channel Device

The methacrylate-based monoliths were prepared within the microchannels to serve as SPE beds for protein preconcentration. In the multi-channel device, each collection channel contains a bed region (200 μm wide, 2 mm long) that accommodates the monolithic polymer. The use of UV-initiated polymerization to prepare the sorbent material enables simultaneous polymerization of monoliths in multiple locations in a single step.

Work done on a single channel device (Section 2.3.3.1) showed that the exposure window size had an impact on the polymerization reaction. Using a UV exposure window with the same size as the fabricated bed, a longer exposure time is required to fill up the entire bed with the polymer. On the other hand, with a 2-mm-long window for a 2-mm-long bed, the polymer may grow beyond the bed region into the narrower channel, increasing the flow resistance. For these reasons, a square window of 1.5 mm wide and 1.5 mm long is used for UV exposure (Figure 5.21). Another concern is the position of the window. Upstream of the bed region, there is a long narrow channel; while downstream of the bed, a very wide channel is connected to the bed through a small section of narrow channel. Therefore, instead of sitting in the middle of the bed, the window is aligned with the bed by leaving 400 μm space before the window and 100 μm space after the window. This will reduce the chance of plugging the narrow channel should the free radicals diffuse outside the bed region. Figure 5.22 shows the transparency

mask for UV exposure and the mask design layout of the whole wafer with five devices.

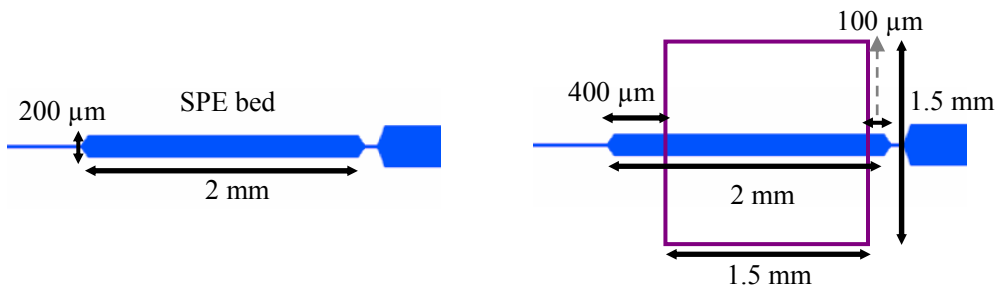


Figure 5.21 Schematic illustrating the bed region and the exposure window aligned with the bed.

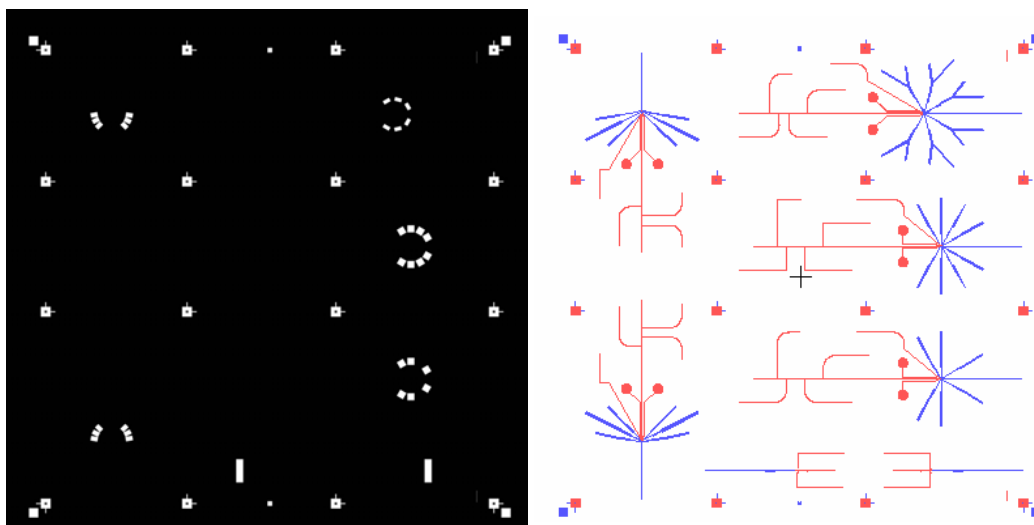


Figure 5.22 The transparency mask for UV exposure and the mask design of chip.

In order to be compatible with the PolyE-323 coated channels, monoliths with positively-charged functionalities (META) were used in all the studies in this chapter. The polymerization mixture compositions and reaction conditions were optimized for SPE in Chapter 2. For the preparation of the monoliths, three vacuum lines were attached to the sample reservoir and two sheath reservoirs, with all the other reservoirs loaded with freshly prepared monolith precursor

solution. The mixture was drawn through the channel by vacuum; after all the channels were filled, all the reservoirs were filled with 20 μL of water and sealed with parafilm to prevent evaporation of the mixture solution during polymerization. Care was taken to align the chip with the mask before UV exposure. After the polymerization process was completed, the unreacted polymerization mixture was removed by rinsing the channels with a 50:50 (v/v) MeOH/water mixture. During the rinsing process, all the other reservoirs must be filled with the rinsing solution to prevent drying out of the monoliths which will induce bubbles. Finally the channels were equilibrated with the running buffer before use.

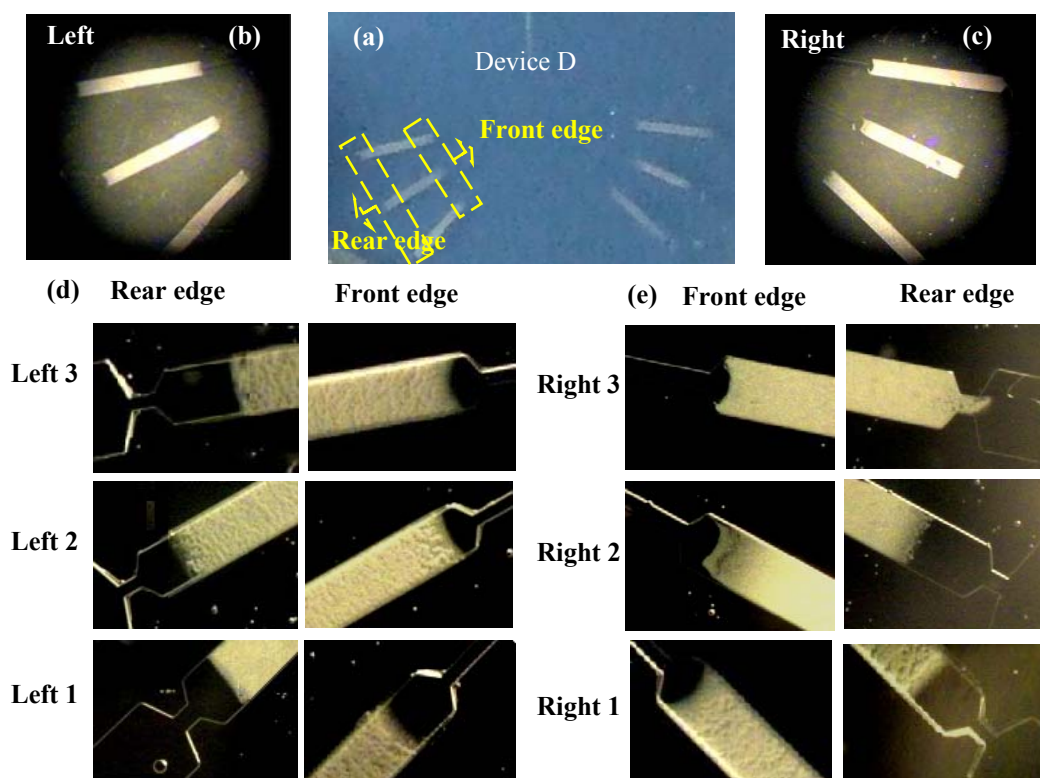


Figure 5.23 (a) Image of monoliths prepared in a 6-channel device D; (b) and (c) enlarged images of polymer beds on the left and right side, respectively; (d) and (e) images showing the front and rear edges of the polymer beds on the left and right side.

Figure 5.23 illustrates the monoliths prepared in a 6-channel device D and the polymers are all located in the bed region with sharply-defined edges. Figure 5.23a is the picture of the whole device with photopatterned monoliths (white); Figure 5.23b and c are enlarged images of monolithic beds on the left and right side, respectively. Pictures with higher magnification were taken to see the monolith structure more clearly, especially for the front and rear edges of the beds (Figure 5.23d and e).

5.5.2.3.2 Sheath Flow Tests on Devices with Monolithic Beds

Sheath flow tests were conducted in the devices with monolithic beds incorporated into the collection channels. The images in Figure 5.24 show that with a voltage combination of -1.0 kV at sample reservoir and -2.5 kV at sheath reservoir, the sample stream is focused tightly by the sheath streams and delivered into the grounded collection channel without contaminating other floating channels. This indicates that the incorporation of monolithic beds does not disturb the flow in the device significantly.

Table 5.4 summarized the sample stream width calculated from pSpice simulation and width estimated from the sheath images in Figure 5.24 for the six collection channels of Device D. The differences between the calculated and observed sample stream width are 5-6 μm , which are bigger compared to those obtained in a fractionator without polymer beds (3-4 μm). The accommodation of monolithic polymer beds into the collection channels may generate extra electrical resistance and flow resistance which was not introduced into the pSpice

simulation model, due to the challenge of estimating the effect on resistance. A flow rate change caused by the increase of channel resistance directly influences the sample travel time in the fractionation zone and the diffusion distance, which is the limiting factor in determining the sample dispersion, resulting in the bigger discrepancy of predicted and observed sample stream widths.

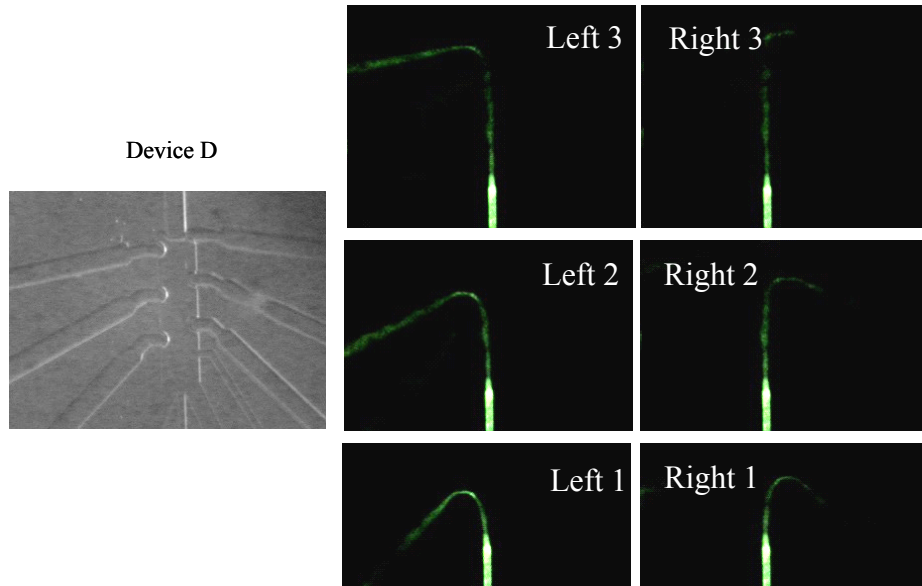


Figure 5.24 Images showing that the fluorescein stream was delivered into individual collection channels on Device D integrated with monolithic beds. On the left side of the sheath images is a picture of the fractionation zone of Device D. Sample voltage: -1.0 kV, sheath voltage: -2.5 kV; collection channel was grounded individually.

Table 5.4 Calculated and observed sample stream width for Device D when six collection channels were grounded separately.

Channel at ground	Left 1	Right 1	Left 2	Right 2	Left 3	Right 3
V_{sample} (V)	1000	1000	1000	1000	1000	1000
V_{sheath} (V)	2500	2500	2500	2500	2500	2500
$l_{Travel\ distance}$ (μm)	145	190	295	340	445	490
Calculated W_{sample} (μm)	9.3	10.3	12.3	13.1	14.6	15.3
Observed W_{sample} (μm)	14.7	15.9	18.0	18.8	20.5	21.6
ΔW_{sample} (μm)	5.4	5.6	5.7	5.7	5.9	6.3

The sheath effects were also studied at different voltage combinations for Device D and E, which have different channel dimensions. For comparison, the first left channel (Left 1st) of Device E and first right channel (Right 1st) of Device D were taken as examples because they are at the same level with a distance of 145 μm to the sheath point. Figure 5.25a and b show the sheath images at different sheath voltages for these two channels. For these images, the potential at the sample reservoir is held constant, while the voltage at the sheath reservoir was varied from 1.0 kV to 2.5 kV. Figure 5.26 shows the intensity profiles extracted from the images at the inlet of the grounded channel. Impedance simulation was performed for these two channels and sample field strengths and focusing field strengths were calculated from voltage drops predicted by pSpice model. The predicted and observed sample stream widths are summarized in Table 5.5.

As the sheath voltage increases, the focusing field strength increases, and the sample field strength decreases, resulting in a tighter focus of the sample stream. The variation of the sample stream width is plotted versus sample field strength. Experimentally observed widths expressed as FWHM are compared to calculated widths using the approximation model $d = \sqrt{2Dt}$ in Figure 5.27a. The change of the calculated and observed widths followed the same trends, but there is systematic shift that is almost identical at all voltages. Using the error function model (Section 5.5.2.2.2), a much better fit between the theoretical predictions and experimental results can be obtained, as is demonstrated in Figure 5.27b. The discrepancies of the observed width from width predicted using the error function

model are $\sim 2 \mu\text{m}$, as compared to discrepancies of 5-6 μm between observed width and width predicted using the Nernst diffusion thickness approximation.

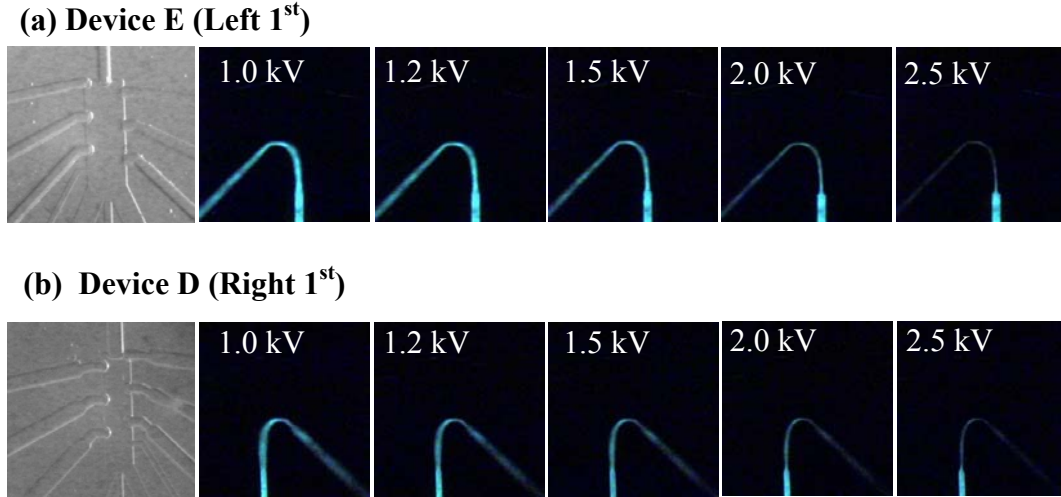


Figure 5.25 Sheath effect at different focusing voltages. The first channel on the left side of Device E (a) and the first channel on the right side of Device D (b) were grounded. Sample voltage: 1.0 kV, sheath voltage: 1.0-2.5 kV as marked.

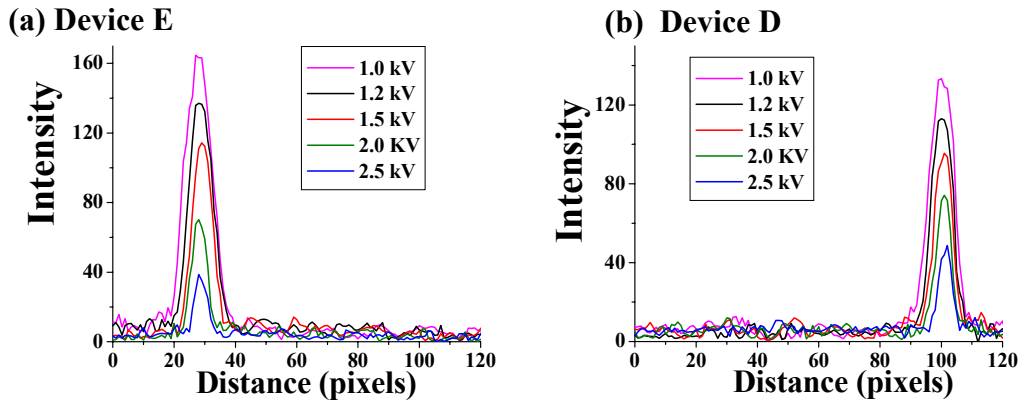


Figure 5.26 Intensity profiles extracted from images at different sheath voltages. The first channel on the left side of Device E (a) and the first channel on the right side of Device D (b) were grounded. Sample voltage: 1.0 kV, sheath voltage: 1.0-2.5 kV.

Table 5.5 Comparison of sample stream width in Device D and E. The first left channel Device E and the first right channel of Device D were grounded.

Device E					
Channel at ground	Left 1 st				
V_{sample} (V)	1000	1000	1000	1000	1000
V_{sheath} (V)	1000	1200	1500	2000	2500
l Travel distance (μm)	190				
$E_{sheath\ channel}$ (V/cm)	652.43	786.88	988.61	1324.8	1661
$E_{sample\ channel}$ (V/cm)	365.34	340.64	303.6	241.9	180.16
$I_{sheath\ channel}$ (mA)	28.01	33.78	42.44	56.87	71.3
$I_{sample\ channel}$ (mA)	5.088	4.744	4.228	3.369	2.509
$Q_{sheath\ channel}$ (nl/min)	70.91	85.53	107.4	144.0	180.5
$Q_{sample\ channel}$ (nl/min)	12.88	12.01	10.71	8.530	6.353
$Q_{fractionation\ zone}$ (nl/min)	154.71	183.07	225.61	296.51	367.42
Dilution factor	12.00	15.24	21.07	34.76	57.83
Calculated W_{sample} (μm)	26.9	22.8	18.6	14.0	11.1
Observed W_{sample} (μm)	32.8	28.3	23.8	19.2	16.4
ΔW_{sample} (μm)	5.9	5.4	5.2	5.2	5.3
$W_{fractionation\ zone}$ (μm)	172				
$W_{sample}/W_{fractionation\ zone}$	0.190	0.165	0.139	0.112	0.096
Device D					
Channel at ground	Right 1 st				
V_{sample} (V)	1000	1000	1000	1000	1000
V_{sheath} (V)	1000	1200	1500	2000	2500
l Travel distance (μm)	190				
$E_{sheath\ channel}$ (V/cm)	751.13	903.75	1132.59	1514.23	1895.68
$E_{sample\ channel}$ (V/cm)	420.61	406.06	384.24	347.93	311.61
$I_{sheath\ channel}$ (mA)	20.23	24.34	30.5	40.78	51.05
$I_{sample\ channel}$ (mA)	3.755	3.625	3.43	3.106	2.782
$Q_{sheath\ channel}$ (nl/min)	51.21	61.62	77.22	103.2	129.2

$Q_{\text{sample channel}}$ (nl/min)	9.507	9.178	8.685	7.864	7.043
$Q_{\text{fractionation zone}}$ (nl/min)	111.93	132.41	163.12	214.34	265.54
<i>Dilution factor</i>	11.77	14.43	18.78	27.26	37.70
<i>Calculated W_{sample}</i> (μm)	23.0	20.0	16.9	13.5	11.3
<i>Observed W_{sample}</i> (μm)	29.1	25.8	22.3	18.6	16.3
ΔW_{sample} (μm)	6.1	5.8	5.4	5.1	5.0
$W_{\text{fractionation zone}}$ (μm)	124				
$W_{\text{sample}}/W_{\text{fractionation zone}}$	0.235	0.208	0.180	0.150	0.131

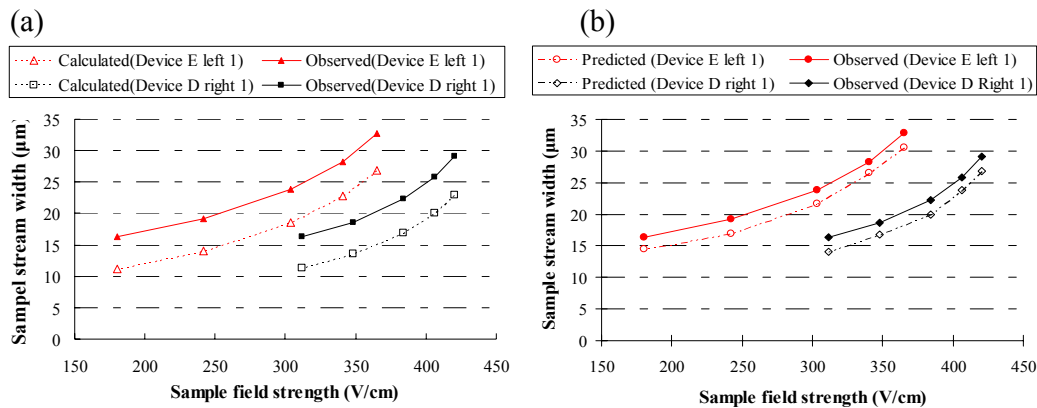


Figure 5.27 Variation of sample stream width versus sample field strength. (a) Calculated sample stream width using approximation model for Device D (\square) and E (Δ), sample stream width estimated from sheath images for Device D (\blacksquare) and E (\blacktriangle). (b) Predicted sample stream width using the error function model for Device D (\diamond) and E (\circ), sample stream width estimated from sheath images for Device D (\blacklozenge) and E (\bullet). The first channel on the right side in Device D and the first channel on the left side in Device E were grounded, with 1.0 kV applied to sample reservoir and 1.0-2.5 kV to sheath reservoirs.

Overall, the sheath flow effect functions well in all five devices with different channel dimensions. In comparison, due to the narrower fractionation zone, narrower sample and sheath channels, and wider collection channels compared to device E (Table 5.1), the sample streams in Device D are thinner than those in Design E at the same sample field strength, as can be seen from Table 5.5 and Figure 5.27. However, on the other hand, the fractionation zone of Device D (124

μm) is narrower than that of Device E (172 μm), resulting a higher ratio of the sample stream width to the total width of fractionation zone ($W_{\text{sample}}/W_{\text{fractionation zone}}$) for Device D, as compared in Table 5.5. A relatively narrower fractionation zone is beneficial as it makes the sample stream closer to the inlets of collection channels, which will reduce the distance and time required for sample to reach the inlets, and thus reduce spread of the sample stream by diffusion.

Another issue that is worth considering when comparing the focusing effect within difference devices is the dilution of sample by the sheath buffer. The dilution factors are calculated from the ratio of the total volumetric flow rate in the fractionation zone to the flow rate of sample stream ($Q_{\text{fractionation zone}}/Q_{\text{sample}}$). The sample dilution factors for the first left channel (Left 1st) of Device E and first right channel (Right 1st) of Device D at different sheath voltages are summarized in Table 5.5. In comparison, less dilution of the sample by the focusing streams is generated in the cases for Device D at the same applied voltages.

5.5.2.3.3 Adsorption of Dye into a Specific Polymer Bed

Since the sheath flow effect functions normally on the fractionator with monolithic polymer beds, we then studied a dynamic dye adsorption process onto a specific polymer bed under protection from sheath streams. A CCD camera was used to monitor the movement of fluorescein along the channel into the monolithic bed. The microchip was placed on top of an inverted microscope on an X-Y translation stage and the position of the device could be controlled through the use of the translation stage. At first, the laser spot was aligned at the fractionation region. Then the microchip was moved to bring the channel and bed

into the excited region for CCD imaging. The laser spot was expanded to cover the entire region.

Figure 5.28 presents a series of extracted frames from a video illustrating the dynamic adsorption process on the first bed on the right side. Frame A is a picture of the fractionation zone with white light, showing that the pinched dye stream is fractionated into the first channel on the right. Frames B-F show video images extracted as the field of view was moved along the channel to the bed region. The lack of an observable fluorescence signal for the channels downstream of the first channel indicates that no dye solution leaks into these floating channels. The bed glared brightly as the dye solution was adsorbed onto it, as can be seen from Frame G-L. A table lamp was then turned on in order to visualize the outline of

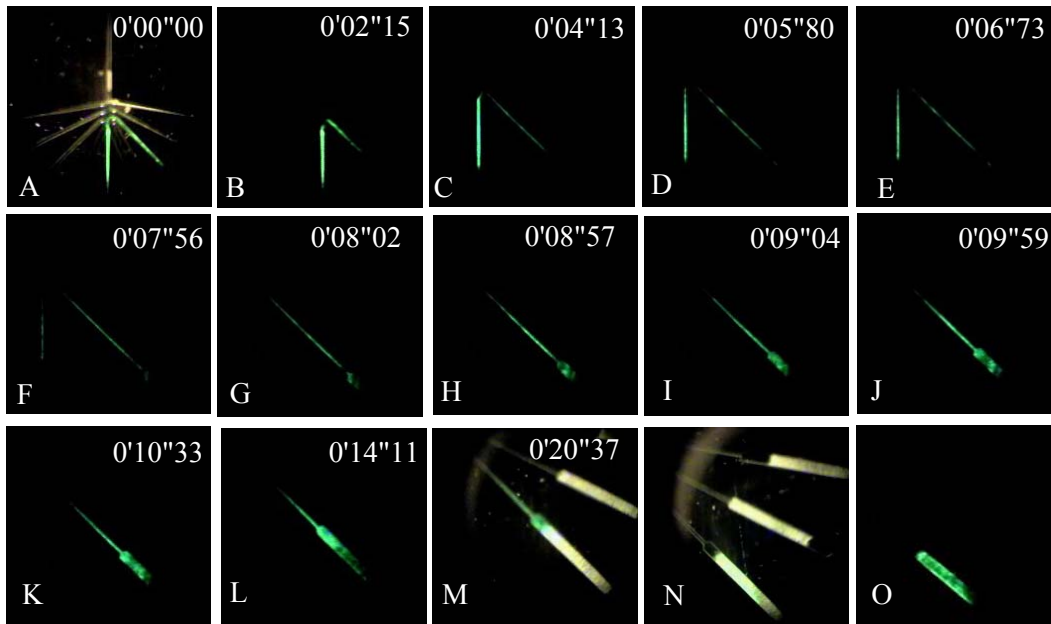


Figure 5.28 Frames A-M were extracted from a video demonstrating the dynamic dye adsorption process onto the first bed on the right side of Device E. Frame A is a photo of the fractionation region in full light. Frame M is a photo of the bed region with light on. Frame N and O are two Photos taken with the CCD camera showing the three beds region, one with light on and the other with light off.

the beds and channels (Frame M). The position of the device was moved to bring all three monolithic beds on the right side into the excited region, Frame N and O are two photos taken with the CCD camera showing the three beds, one with light on and the other with light off. With the table lamp off, we can see the fluorescence signal more clearly. No observable fluorescence in the beds of the two channels upstream provides further proof on the absence of leakage of fluorescein into these beds.

The images in Figure 5.29 show the selective adsorption of fluorescein onto the second bed on the left side and on the right side, respectively. The two beds in the two channels beside it (1st channel and 3rd channel) do not exhibit any fluorescence that could be detected by our sensitive instrumentation, which indicates that fluorescein is only adsorbed onto the desired beds, with no leakage into the other two beds.

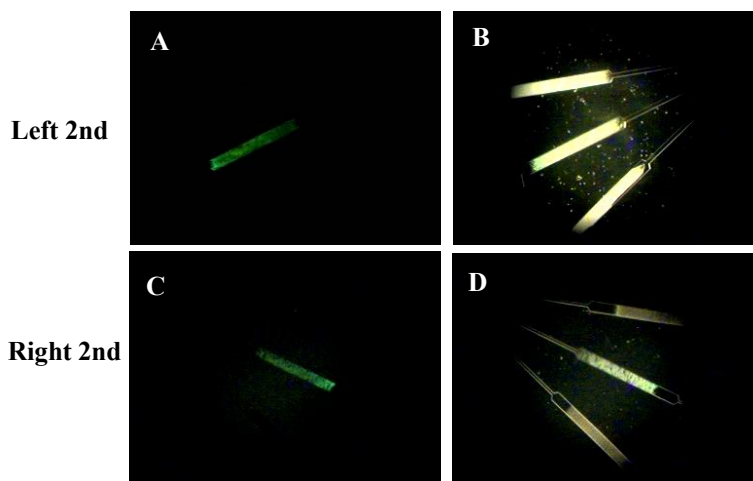


Figure 5.29 Selective adsorption of fluorescein onto the 2nd bed on the left (A, B) and on the right side (C, D) under protection from sheath streams. Images with light off (A, C), images with light on (B, D).

The assembly of monolithic polymer beds into the microfluidic device does not generate significant flow disturbance in the fractionation region and the sheath

effect functions properly to protect the incoming sample stream. Thus analytes can be delivered into individual collector and adsorbed onto a desired bed with no contamination of other beds.

5.5.2.4 Automatic Fractionation Using Three Delivery Sequences

For the experiments mentioned above, which involved the delivery of sample stream into a single collection channel, the collection channel was grounded individually via the blue-box power supply. In order to facilitate the automatic electrokinetic fractionation process, it is necessary to apply a sequential ground to each of the collection channels. An electrical system was designed by J. Taylor [20] to perform the sequential grounding process at a fixed time interval. The electrical components of this system are shown in Figure 5.30, which consists of timers, relays and platinum electrodes for each channel.

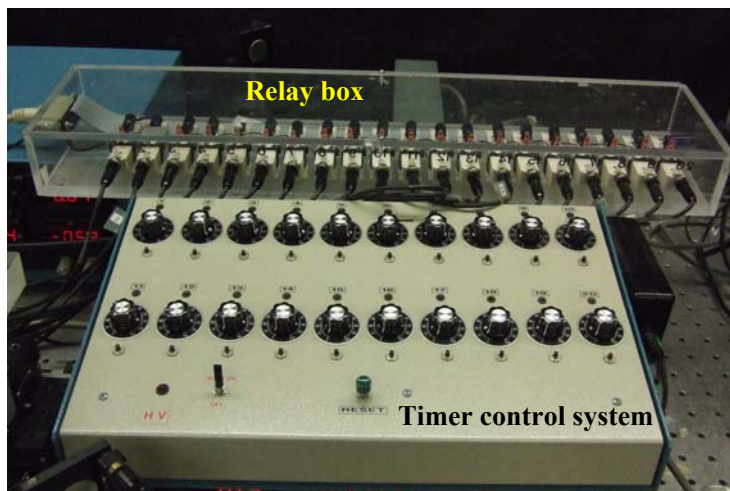


Figure 5.30 Electrical fractionation system. This system was designed and built by Ed Feschuk and Kim Do from the Electronics Shop in Department of Chemistry at the University of Alberta.

The relay box is connected to ground, hence, when a relay is activated it provides a path to ground. The timer control box is used to switch the relays and

control the entire electrical sequence. The timers and relay boxes step through each channel after initiating the grounding sequence. Because the high voltage source is a separate system that is not controlled by the relays, for safety reason we must ensure one of the channels is always at ground when the high voltage source is activated.

To perform automatic electrokinetic fractionation, the sample reservoir and sheath reservoirs received high voltages, while a ground is swept sequentially through each of the collection channels, driving the sample into the grounded channel by EOF. Sequential fractionation was performed in three modes with different delivery sequences and their performance in terms of potential leakage was compared. We labeled the channels on the left and right side from the bottom up as L1 to L4 and R1 to R4, respectively.

The first mode, Mode A, followed a switching order as indicated by the arrow in Figure 5.31a. The channels on the left side were first grounded sequentially from L1 to L4. Afterwards, the ground was switched to the fourth right channel R4, then sequentially from R4 to R1. Figure 5.31b presents a series of extracted frames from a video illustrating the electrokinetic fractionation into the eight channels following the switching order of Mode A, with the time indicated in each frame. In sequence, the dye stream was delivered from sample channel into channel L1 as the electrical system was initiated, and then fractionated into channel L2 as the ground was switched to L2, and so on. Using this method, the incoming flow from the sample channel was automatically fractionated into the eight collection channels.

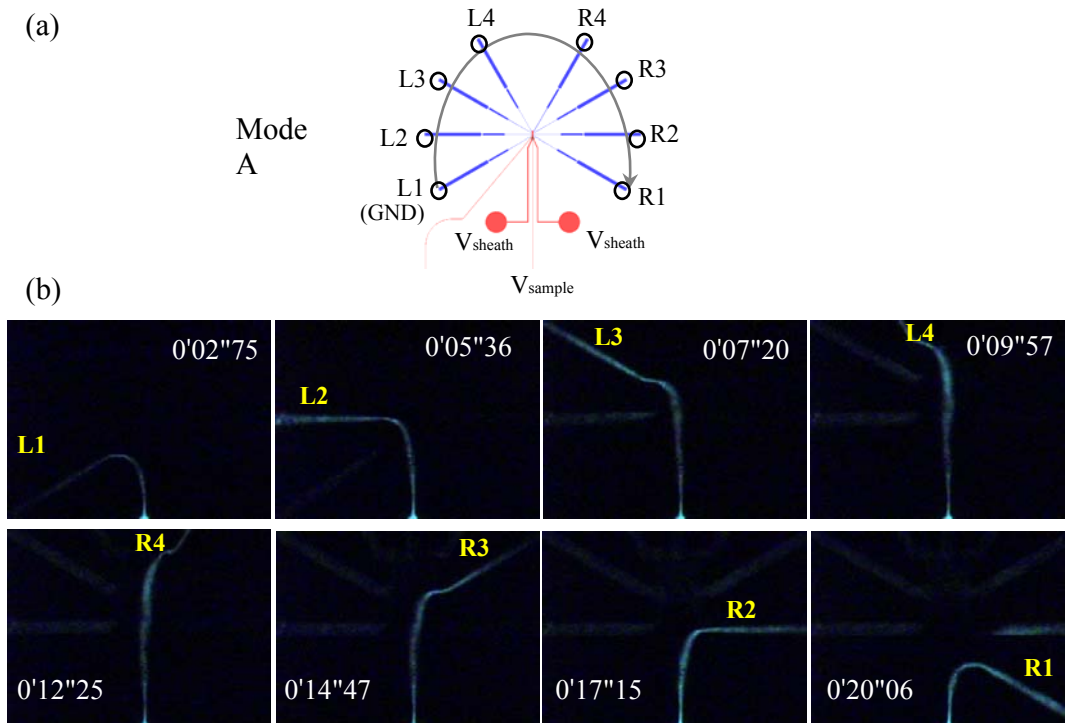


Figure 5.31 Sequential fractionation with Mode A. (a) Schematic illustrating the switching order in mode A. L1, L2, L3 and L4 refer to collection channel 1, 2, 3, 4 on the left side; R1, R2, R3 and R4 refer to collection channel 1, 2, 3, 4 on the right side from the bottom up. (b) Frames extracted from a video illustrating electrokinetic fractionation with the time indicated in each frame. Sample voltage: -1.0 kV, sheath voltage: -1.5 kV. Collection channel was grounded sequentially following the order indicated by the arrow in a.

In Mode B, ground was first applied sequentially to the left channels from L1 to L4, as in mode A, but then switched to the first right channel R1, and then sequentially from R1 to R4, as indicated in Figure 5.32a. In Mode C, the sequential grounding was accomplished in an order shown by the arrows in Figure 5.33a. The ground switches alternately between left and right side, starting from L1 to R1, then R2, followed by switching back to the left side L2, then L3, etc. Figure 5.32b and 5.33 b show the frames extracted from videos illustrating electrokinetic fractionation with Mode B and C, respectively.

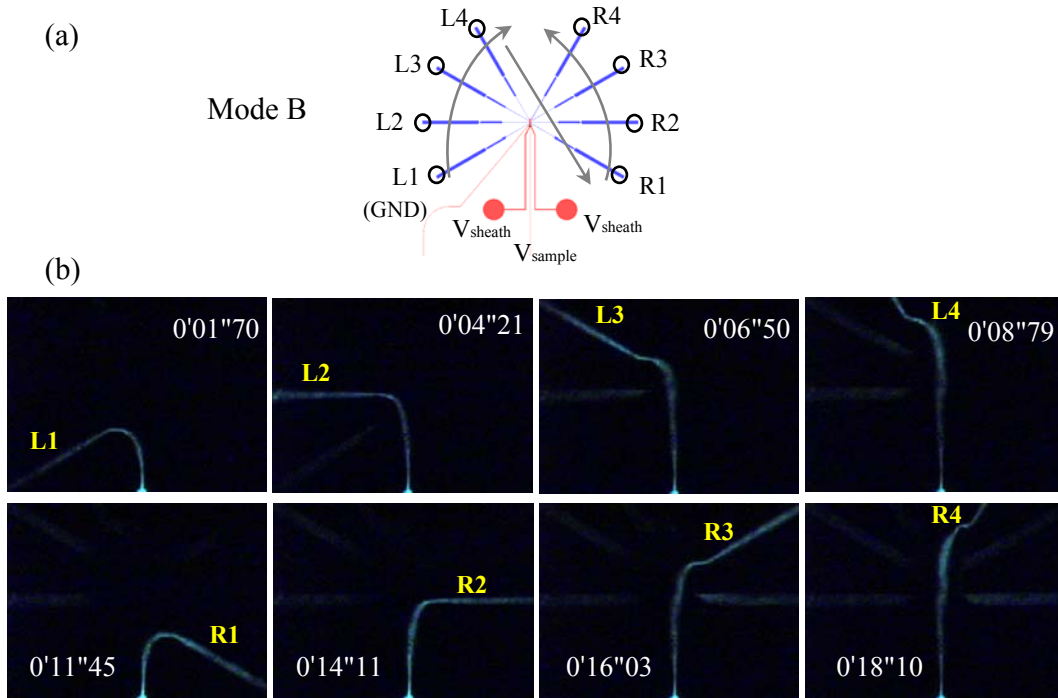


Figure 5.32 Sequential fractionation with Mode B. (a) Schematic illustrating the switching order in Mode B. (b) Frames extracted from a video illustrating electrokinetic fractionation with the time indicated in each frame.

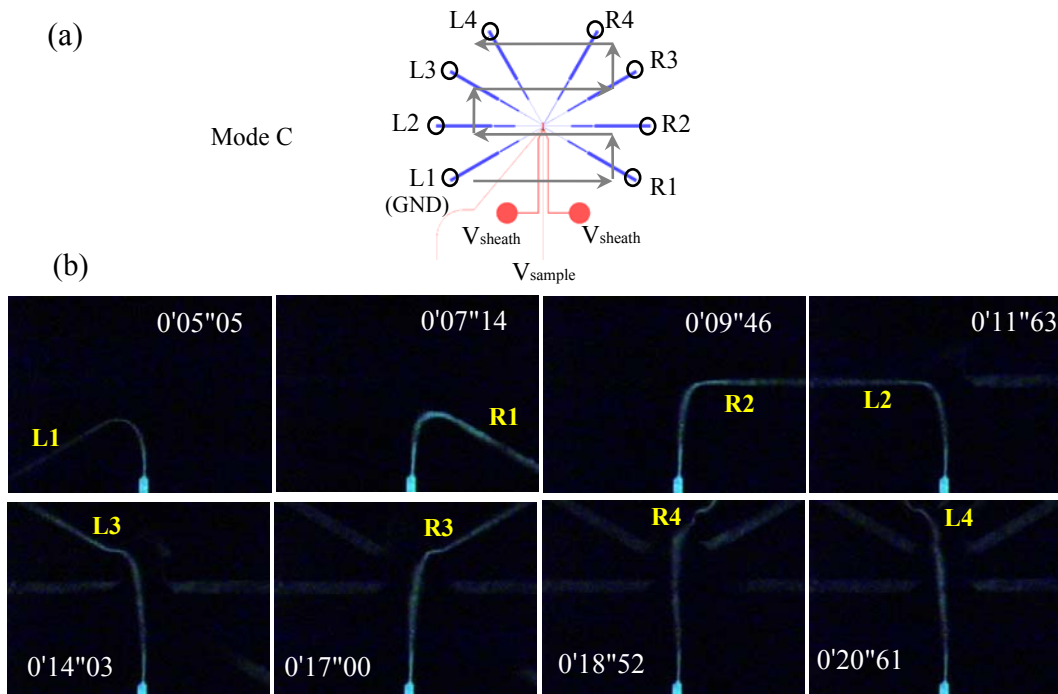


Figure 5.33 Sequential fractionation with Mode C. (a) Switching order in Mode C. (b) Frames extracted from a video illustrating electrokinetic fractionation.

As showed in Figure 5.31b, 5.32b, 5.33b, the fractionation process with all three switch modes proceeds smoothly; the focused dye stream is fractionated into all collection channels sequentially as the timers and relays step through each channel.

Special attention was paid to the sample flow when switching between the adjacent relays in order to monitor any leakage that may exist because this is an all-important issue to address to prevent leakage-induced cross-contamination. All three modes were explored and compared in terms of potential leakage during switching, and the results are summarized in Figure 5.34, where blue solid arrows indicate the switching order; red broken arrows indicate the switching that leads to obvious leakage, and the yellow-green lines show the leakage trace of the dye.

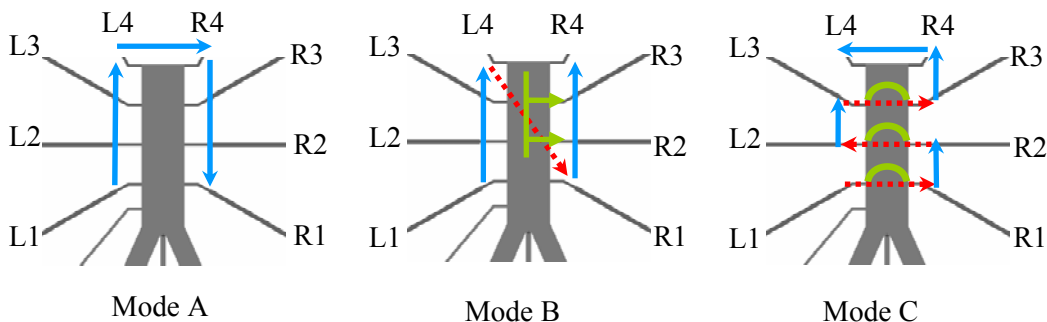


Figure 5.34 Comparison of the three switching modes in terms of the potential leakage when switching between adjacent relays. Blue solid arrows indicate the switching order; red broken arrows indicate the switching that leads to obvious leakage, and the yellow-green lines showed the leakage trace of the dye.

In mode A, there is no observable leakage. In mode B, there is obvious leakage when ground is switched from the fourth channel on the left side L4 to the first channel on the right side R1, the dye present in the fractionation zone is swept into other channels; mostly into R2 and R3, as can be seen from the frames extracted from the video during switch from L4 to R1 (Figure 5.35).

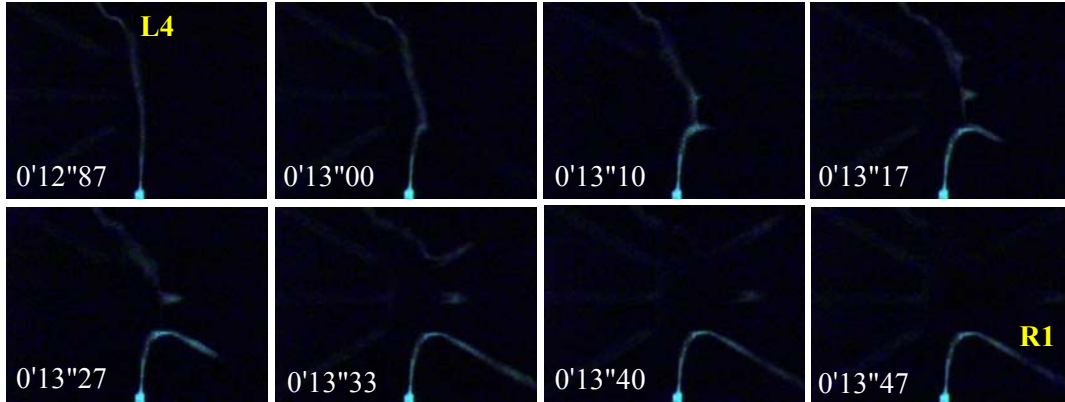


Figure 5.35 Frames extracted from a video illustrating the leakage during switch from L4 to R1 in switching mode B.

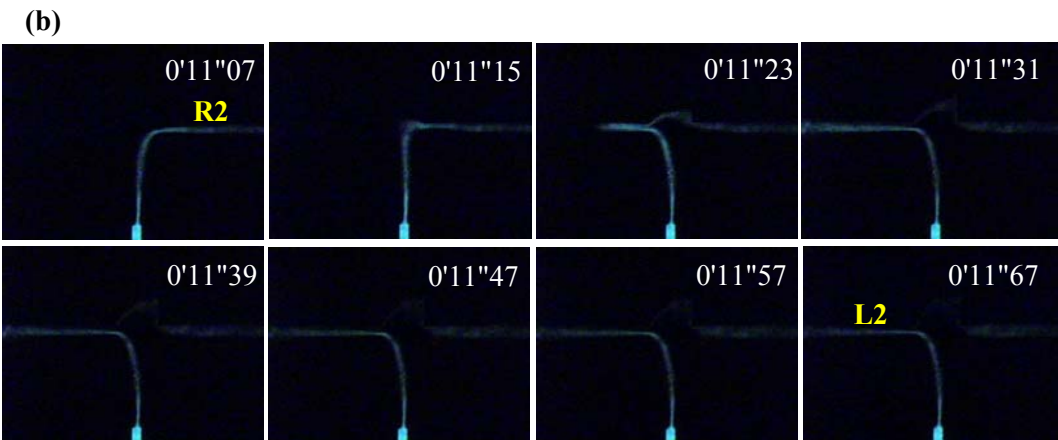
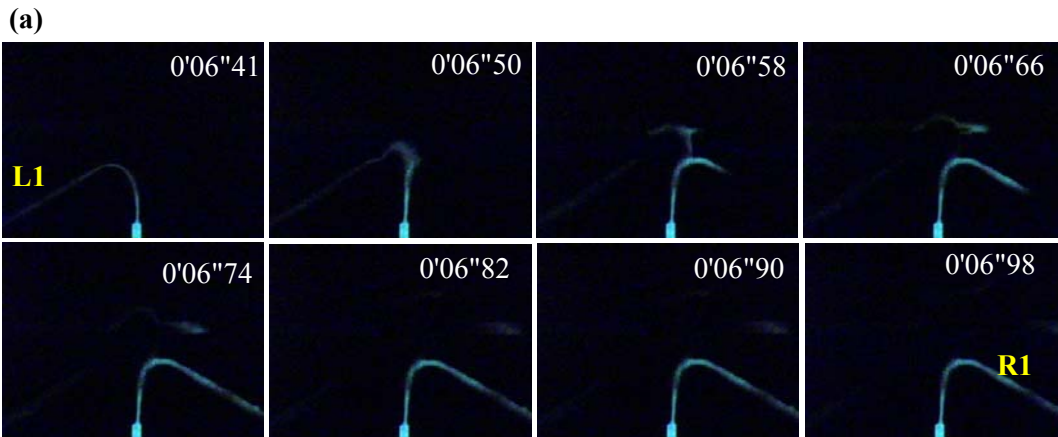


Figure 5.36 Frames extracted from a video illustrating the leakage during switch between left and right channels in Mode C, (a) switch from L1 to R1; (b) switch from R2 to L2.

In mode C, obvious leakage is observed when the relay is switched between left and right channels; dye is swept into the region downstream of the fractionation zone, as demonstrated in Figure 5.36a for switch from L1 to R1 and in Figure 5.36b for switch from R2 to L2. Therefore, switching Mode A should be used in the subsequent experiments or we should find a way to address the leakage present in Mode B and C. Solutions are proposed to overcome this leakage problem and will be discussed in Chapter 6.

5.5.2.5 Theoretical Calculation of Pressure-Induced Flow

Throughout the course of the sheath flow effect study, it was noted that this system was extremely sensitive to siphoning effects. Subtle differences in the buffer levels of each reservoir were enough to induce flow, which could lead to sample leakage. Therefore, great care was taken to ensure the liquid levels in all reservoirs were at the same height to avoid possible siphoning effects. However, as sample solution and sheath buffer are driven into the collection channels by EOF, the liquid levels at the sample and sheath reservoirs drop, while liquid levels at the collection reservoirs increase, resulting a height-induced pressure difference, which could generate hydrodynamic flow. A calculation was done in order to assess the magnitude of this pressure induced flow. The pressure-drive flow of a liquid through a straight channel is referred to as Hagen-Poiseuille flow [21-23] and is often characterized by the hydraulic resistance R_{hyd} as:

$$R_{\text{hyd}} = \frac{\Delta p}{Q} \quad (5.22)$$

where Δp is the pressure drop along the channel and Q is the volumetric flow rate through the channel. For rectangular channels, the hydraulic resistance R_{hyd} can be described by [24, 25]:

$$R_{\text{hyd}} = \frac{\Delta p}{Q} = \frac{4\eta L}{w^2 d^2 F} \quad (5.23)$$

where η is the viscosity of the fluid; L is the channel length, w is channel width, d is channel depth, and F is a geometric form factor related to d and w [26, 27]. We used the viscosity of water at 20 °C ($1.002 \times 10^{-2} \text{ g}\cdot\text{cm}^{-1}\cdot\text{s}^{-1}$) for our calculation. The detailed channel dimensions of Device B are listed in Table 5.1. Bao *et al.* [28] studied the F term in detail for the D-shape channel resulting from isotropic etching, and derived an empirical equation to calculate F as follows,

$$F = 0.3468\left(\frac{d}{w}\right) - 0.6230\left(\frac{d}{w}\right)^2 + 1.2466\left(\frac{d}{w}\right)^3 - 2.7916\left(\frac{d}{w}\right)^4 + 2.3696\left(\frac{d}{w}\right)^5 \quad (5.24)$$

The F factors for each section of Device B are calculated according to this equation and are listed in Table 5.6. The value of w is taken as the width at the top of the D-shape channel. The flow resistance for each segment of the device can thus be calculated according to Equation 5.23.

Table 5.6 Geometric form factors F for each segment of Device B.

Channel	Sample	Sheath	Waste	Fractionation	Elution
F Factor	0.0444	0.0179	0.0586	0.00958	0.0695
Collection channel	Segment				
	a	b	c	d	e
F Factor	0.0716	0.0695	0.0294	0.0695	0.0185

The volume of solution flowing into a single collection channel is calculated as the product of the EOF flow rate and the time period incoming flow is delivered into each collection channel, which is defined by the dwell time on each relay. The drop or increase of liquid level in each reservoir can be calculated by dividing the volume (V) of solution delivered out of or into the reservoir, by the base area (A_b) of the reservoir as follows,

$$\Delta h = V / A_b \quad (5.25)$$

The pressure drop across the flow path can then be calculated from the difference in the liquid levels of each reservoir. The static fluid pressure exerted by a column of liquid is defined by:

$$\Delta p = \rho g \Delta h \quad (5.26)$$

where ρ is the density of the fluid (1.0 g·cm⁻³ for water at 20 °C), g is the acceleration of gravity (980.7 cm·s⁻²) and Δh is the height difference of the liquid.

The volumetric flow rate Q can thus be calculated by dividing the height-induced pressure difference ΔP by the flow resistance R_{hyd} . However, for a device design as complex as ours, which has a channel network with many branches and junctions, a simulation tool is necessary to predict the flow in each channel. PSpice software can also be used to simulate the hydrodynamic flow by treating the pressure and flow resistance as an equivalent voltage and impedance, respectively.

As a first step, the EOF volume flow rate was calculated for flow into a single channel using pSpice, as described previously in Section 4.2.4. For, example, with 1.0 kV applied at sample reservoir and 2.5 kV applied at sheath reservoirs, while the first collection channel grounded and other collection channel left floating, the

electric field strength E in each channel segment can be predicted from pSpice simulation. Equation 5.27 is used to calculate the EOF flow rate Q_{EOF} (sheath channel as an example).

$$Q_{EOF} = \mu_{EOF} EA = (4.22 \times 10^{-4} \frac{cm^2}{V \cdot s})(1.81 \times 10^3 \frac{V}{cm})(429.3 \times 10^{-8} cm^2) = 3.26 \times 10^{-6} \frac{cm^3}{s} \quad (5.27)$$

where μ_{EOF} is the electroosmotic mobility, A is the channel cross-sectional area, and E is the electric field. The upper entries in Table 5.7 show the calculated results for the EOF driven process. In the next step, the volume transferred from the source reservoirs to the receiving reservoirs over a 30 s period was calculated. Equation 5.25 and 5.26 were then used to calculate the pressure this volume transfer created, shown as pressure entries in Table 5.7. Finally, these pressures were enter into pSpice as a “voltage” in units of $g/cm \cdot s^2$, and the hydraulic resistance of each channel was entered as an “impedance” in units of $g/cm^4 \cdot s^1$. The program then returned a “current” that is actually the volume flow rate in units of cm^3/s . This calculation indicates how much pressure-driven back flow is generated as the EOF moves liquid between reservoirs. The back flow is a function of time, but this method captures it only at a specific time.

Table 5.7 summarizes the values generated by the calculation of pressure-induced flow rate. Figure 5.37 demonstrates the simulation scheme for a case in which the sample and sheath streams were delivered into one individual collection channel (L1 as an example) for 30 s. In Figure 5.37, the calculated flow resistances and the pressure differences are displayed as “impedance” and “voltages”. For example, after delivering sample and sheath streams into collection channel L1 for 30 s, the liquid level in the collection reservoir L1 will

increase 2.79×10^{-3} cm, resulting in a positive pressure of $2.74 \text{ g/cm} \cdot \text{s}^2$. This pressure is displayed as a positive “voltage” at equal value, that is, 2.74 V at the collection reservoir L1 during simulation. The reservoirs with no liquid level changes are given a “voltage” of 0 V.

Table 5.7 Calculation of pressure-induced flows for one collection channel. Sample and sheath streams are delivered into one individual collection channel (L1) for 30 s.

Channels	Sample	Sheath	Collection
Voltage Applied	1 kV	2.5 kV	Ground
EOF flow rate($\text{cm}^3 \cdot \text{s}^{-1}$)	4.53×10^{-8}	3.26×10^{-6}	6.57×10^{-6}
Dwell Time (s)	30		
Delivered volume (cm^3)	-1.36×10^{-6}	-9.78×10^{-5}	1.97×10^{-4}
Base area of reservoir (cm^2)	0.07069	0.07069	0.07069
Increased/ decreased height (cm)	-1.92×10^{-5}	-1.38×10^{-3}	2.79×10^{-3}
Density of water ($\text{g} \cdot \text{cm}^{-3}$)	1.0		
Acceleration of gravity ($\text{cm} \cdot \text{s}^{-2}$)	980.0665	980.0665	980.0665
Pressure generated ($\text{g} \cdot \text{cm}^{-1} \cdot \text{s}^{-2}$)	-1.887×10^{-2}	-1.356	2.74
Hydraulic resistance ($\text{g} \cdot \text{cm}^{-4} \cdot \text{s}^{-1}$)	1.00×10^{12}	1.16×10^{11}	1.67×10^9
Pressure-induced flow rate ($\text{cm}^3 \cdot \text{s}^{-1}$)	8.10×10^{-13}	1.85×10^{-11}	1.14×10^{-9}
Pressure-induced flow/EOF	0.00179%	0.000567%	0.0174%

From the simulation, the liquid level change generated by a 30 s continuous flow of sample and sheath buffers into the collection channel L1 will result in a pressure-induced flow of 8.10×10^{-13} , 1.85×10^{-11} , $1.14 \times 10^{-9} \text{ cm}^3 \cdot \text{s}^{-1}$ in the sample channel, sheath channels, and the collection channel L1, respectively. Compared to the EOF flow which drives the fractionation process, the pressure-induced flows generated by the liquid level differences after 30 s operation are negligible (0.0006% to 0.0174%).

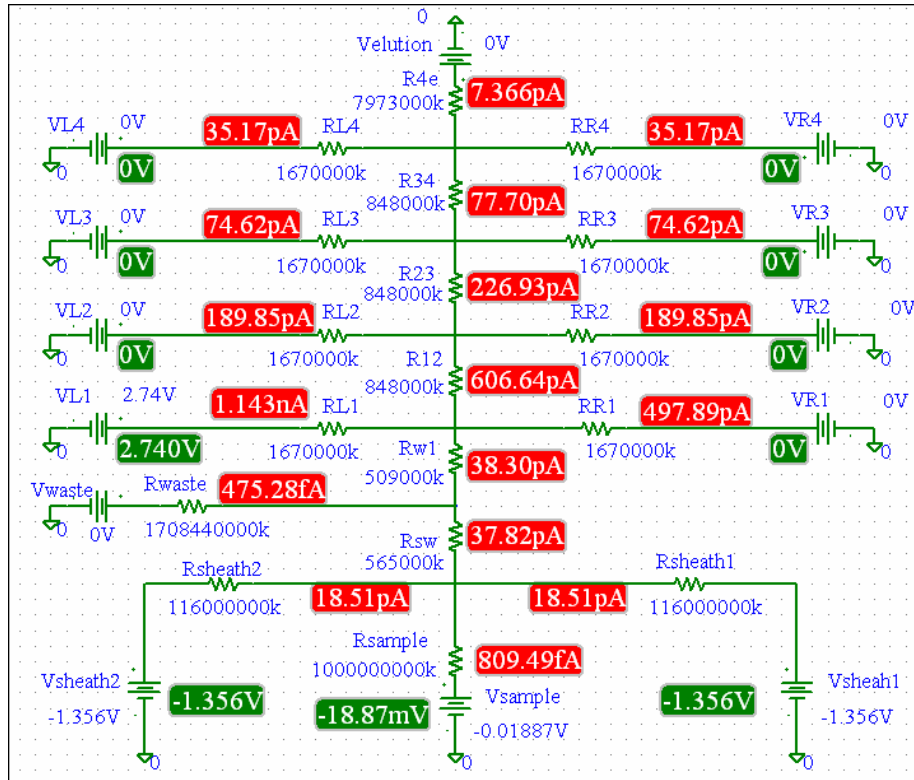


Figure 5.37 Simulation scheme of the pressure induced hydrodynamic flow for one collection channel. All the flow resistances are displayed as electrical impedances, and pressures are displayed as voltages. Sample and sheath streams were only delivered into the first collection channel on the left side for 30 s.

During the automatic electrokinetic fractionation process, sample solution and sheath buffer are directed into each of the eight collection channels in sequence, resulting in a greater decrease in the liquid levels in the sample and sheath reservoirs. Figure 5.38 demonstrates the simulation scheme for the case when the sample and sheath streams are delivered into all eight individual collection channels with a dwell time of 30 s for each channel. In this case, the liquid level in each collection reservoir will increase by 2.79×10^{-3} cm, corresponding to a positive pressure of $2.74 \text{ g/cm} \cdot \text{s}^2$, which is displayed as a positive “voltage” of 2.74 V in the pSpice program. The decreases of liquid level, and thus the displayed “voltages” in sample and sheath channel are eight times the

corresponding values in Figure 5.37 because they delivered 8 times more fluid. The calculated pressure-induced flow rates in the sample channel, sheath channels, and all the collection channels are summarized in Table 5.8 and compared to the EOF flow rates.

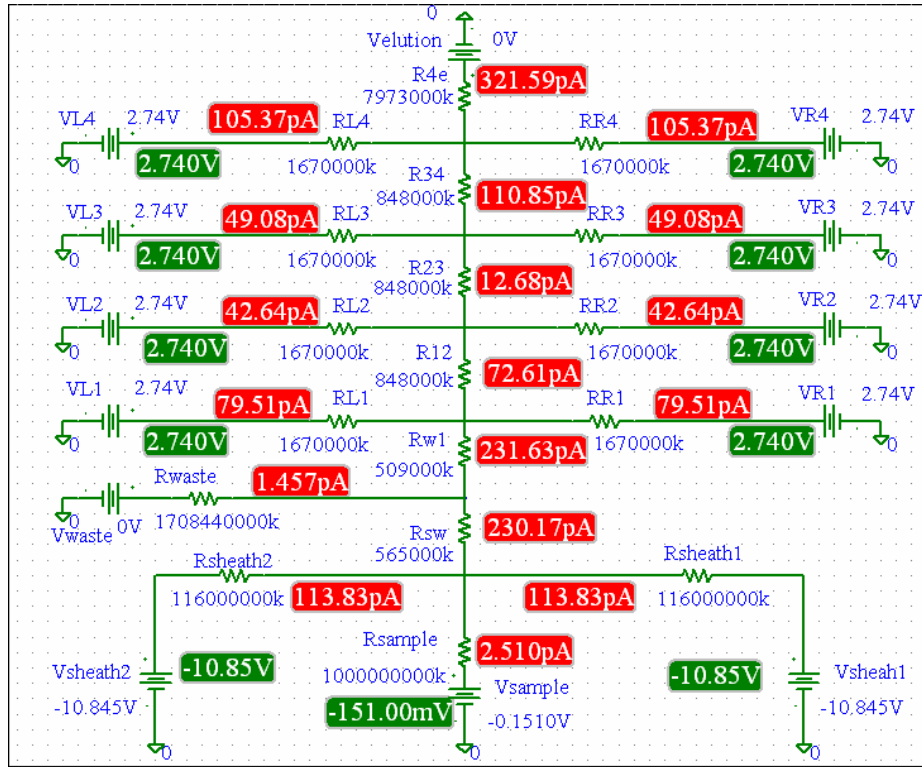


Figure 5.38 Simulation scheme of the pressure induced hydrodynamic flow for eight collection channels. Sample and sheath streams were delivered into each of the eight collection channels sequentially for 30 s.

The pressure-driven flow is still very small compared to the EOF, with ratios ranging between 0.0007% and 0.0055%. Therefore, delivering sample and sheath buffers into all eight channels did not generate liquid level differences which can induce a significant hydrodynamic flow under these conditions. These siphoning effects should not be a substantial issue in the real application of this device as the dwell time on each collection channel will be even shorter, typically a few seconds or less. Very long repetitive runs may require adjustments of the fluid

level, but buffer will likely be exhausted first. It should also be mentioned that the relatively small back flow rate indicates that the approximation we have made in these calculation of ignoring back flow during the run time is acceptable.

Table 5.8 Calculation of pressure-induced flows for all eight collection channels. Sample and sheath streams are delivered into each of the eight collection channels for 30.

Channel	Pressure induced flow rate ($\text{cm}^3 \cdot \text{s}^{-1}$)	EOF flow rate ($\text{cm}^3 \cdot \text{s}^{-1}$)	Pressure induced flow/EOF
Sample	2.51×10^{-12}	4.53×10^{-8}	0.00554%
Sheath	1.14×10^{-10}	3.26×10^{-6}	0.00350%
L1 or R1	7.95×10^{-11}	6.57×10^{-6}	0.00121%
L2 or R2	4.26×10^{-11}	6.57×10^{-6}	0.000648%
L3 or R3	4.91×10^{-11}	6.57×10^{-6}	0.000747%
L4 or R4	1.05×10^{-10}	6.57×10^{-6}	0.00160%

5.5.3 Elution

This electrokinetic sheath flow fractionator and collector provide an efficient design that overcomes leakage problems in electrokinetically pumped devices, allowing tightly focused sample streams to be distributed into individual channels and selectively adsorbed onto a desired bed without leaking into the other beds. Using this method, protein samples can be preconcentrated and cleaned-up on the SPE beds, and on-bed enzymatic digestion can then be performed by flowing trypsin solution through the Beds. The step after digestion is to elute the adsorbed peptides from the polymer beds for detection by MS. In this section, we explore the elution behavior in these multi-channel microfluidic devices in terms of the elution profile, sequential elution and sample carryover evaluation.

5.5.3.1 Study of Elution Profile

Theoretically, the elution of analytes from a SPE bed can be achieved by applying voltage between the desired collection reservoir and the elution channel reservoir to drive eluent through the bed. However, we were concerned that without spatial confinement the sample eluted from the collection channel would spread in the fractionation zone, leading to sample leakage. With this concern in mind, we studied the elution stream profiles by continuously delivering fluorescein sample from the collection reservoir towards the elution channel. The fluorescein sample was dissolved in elution buffer, so that it would not be retained on the monolithic bed. These experiments were conducted on polyE-323 coated devices integrated with positively-charged monoliths and an imaging CCD camera was used to monitor the motion of the fluorescent dye along in the fractionation region.

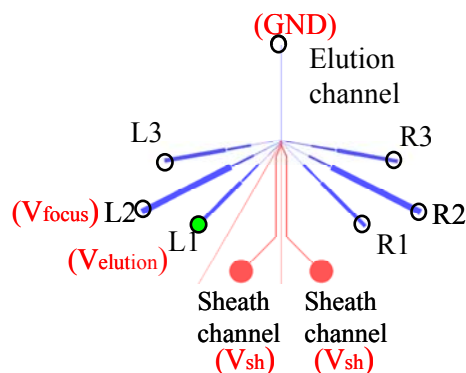


Figure 5.39 Voltage program for sequential elution for Device D. Elution channel was grounded (GND); one of the collection channel received high negative voltage ($V_{elution}$); Sheath channels received negative voltages to define the elution stream from the bottom (V_{sh}); an extra negative voltage (V_{focus}) is applied to the channel above the desired collection channel for elution to confine the elution stream from the top.

Figure 5.39 shows the chip layout of Device D used for these experiments. The elution channel reservoir was grounded (GND), while one of the collection channel reservoirs received a negative voltage to drive dye solution towards the elution channel, this voltage is defined as $V_{elution}$.

Figure 5.40 illustrates the images of the elution streams for each collection channel when voltage is only applied between the desired collection channel and elution channel. One can see that, with no electrical sheath confinement, the sample stream spreads in the fractionation zone and gradually enters the other collection channels, as well as flowing into the elution channel.

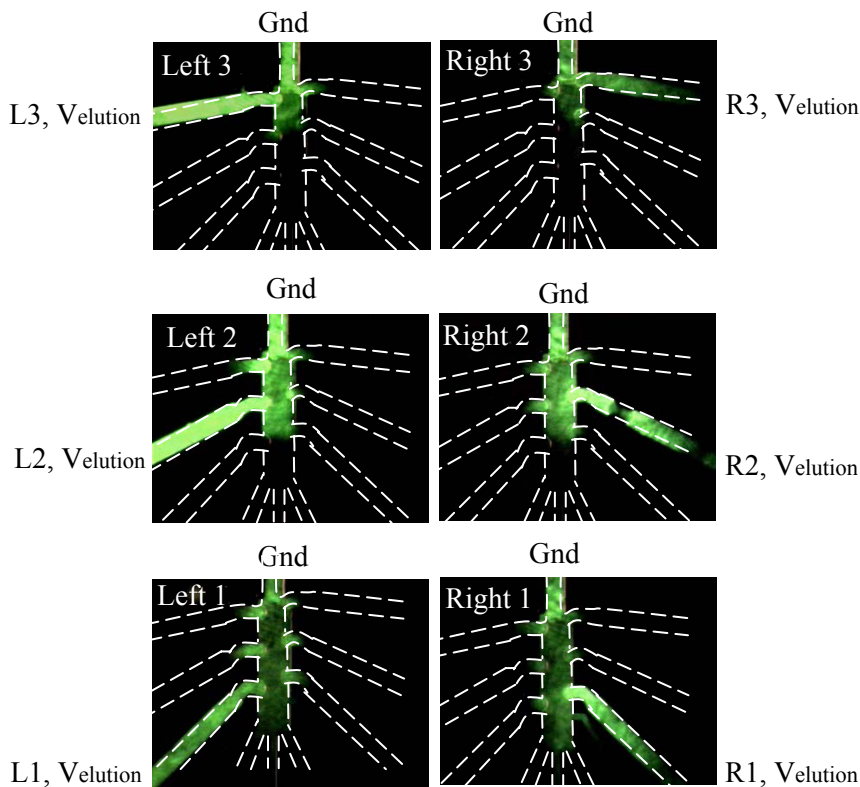


Figure 5.40 CCD Images showing the elution stream profiles with no spatial confinement. Voltage is only applied between the desired collection channel and elution channel. The channels are outlined for clarity.

This leakage problem can be solved by applying voltages on the other channels to transport fluid to spatially confine the elution stream, similar to the

sheath flow technology used in fractionation. In choosing channels to provide the focusing streams, common channels that can be used for all collection channels are preferred. Thus, we first applied voltages on the sheath channels (V_{sh} in Figure 5.39), and Figure 5.41 shows the images of the resulting dye stream profiles. Applying focusing voltages on sheath channels drives buffer towards the elution channel, effectively controlling the flow profile upstream of the collection channel.

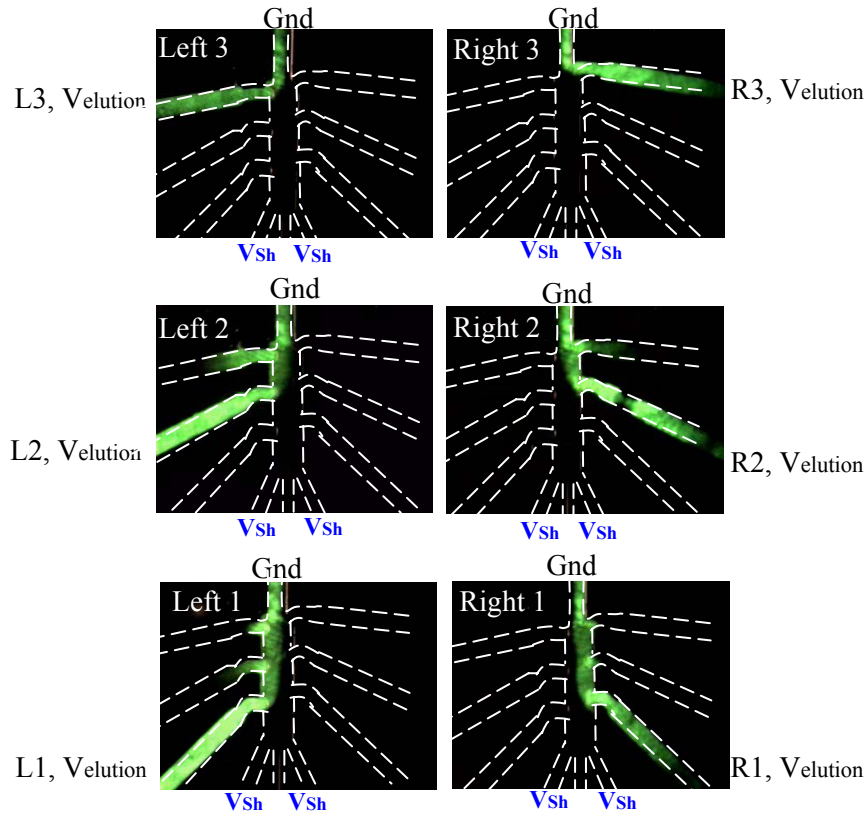


Figure 5.41 CCD Images showing the elution stream profiles with focusing voltages on sheath channels (V_{sh}). The channels are outlined for clarity.

However, there is still leakage of dye into the channels downstream of the desired channel, as seen for four bottom channels (L1, L2 and R1, R2). An extra focusing voltage is required to further confine the elution stream. We added voltage on the channel downstream of the desired channel to geometrically define the dye stream from the top, which is referred to as V_{focus} , as marked in Figure

5.39. That is, for the first channel L1, focusing voltage was added on the second channel L2, and for the second channel L2, focusing voltage was added on the third channel L3. With this additional voltage, well-defined elution profiles are obtained, as is demonstrated in Figure 5.42.

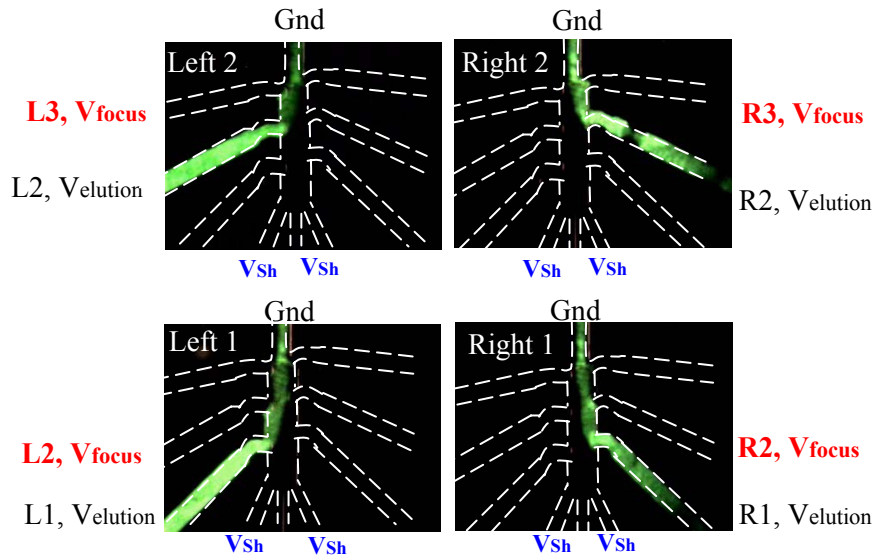


Figure 5.42 CCD Images showing the elution stream profiles when an extra focusing voltage was applied on the channel downstream of the desired collection channel (V_{focus}). The channels are outlined for clarity.

The effect of focusing voltages on the sheath channels on confinement of the elution stream was studied (Figure 5.43). Consider the second channel on the left side (L2) as an example. In this experiment, the elution channel was grounded; dye solution was placed in the reservoir of L2 and the voltages at reservoir L2 was fixed at 0.5 kV to continuously deliver the dye solution. The potential at reservoir L3 was also held constant at 0.5 kV to control half of the stream geometry, while the voltages at the sheath channels were varied from 0.4 to 1.0 kV. It is obvious that the dye stream gets thinner as the pinching sheath voltage increases (Figure 5.43).

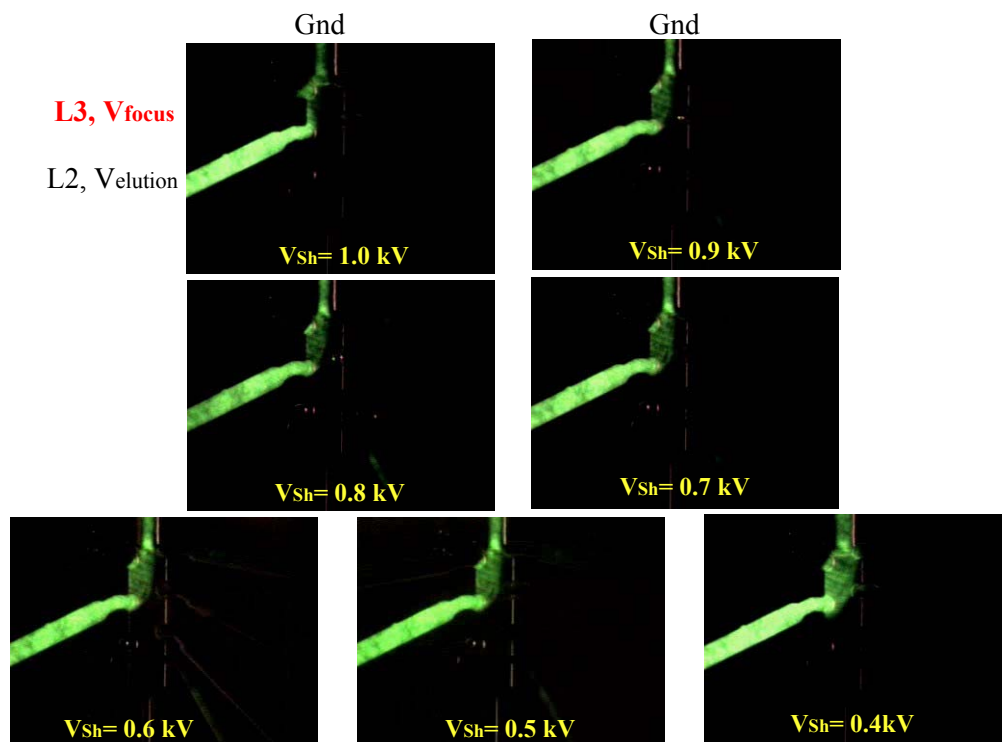


Figure 5.43 CCD Images showing the elution stream profiles at different focusing voltages at the sheath channels. Elution channel: ground; collection channel reservoir L2 and L3: 0.5 kV, sheath reservoirs: 0.4 kV -1.0 kV. Dye solution was placed in collection channel reservoir L2.

When choosing the focusing voltage, we must make sure the focusing voltage is high enough that the sample eluted from one channel won't leak into the other collection channels. On the other hand, the focusing voltage at the sheath channels and the focusing collection channel must be tuned to balance the fluid transport from both sides. With a high sheath voltage of 1.0 kV (Figure 5.43, first image), dye solution pushes into collection channel L3. Further increasing the sheath voltage meant the dye stream could not be driven into the fractionation zone. If the focusing voltage is too high, it will produce too much dilution of the sample by buffer solution, which could be a problem for MS detection of low abundance analyte, as both sample and focusing solution will be sprayed into the MS orifice. Therefore, a voltage combination that can produce a sample stream narrow

enough not to touch the inlets of the other collection channels should be chosen. From Figure 5.43, with an elution voltage of 0.5 kV ($V_{elution}$) on the desired collection reservoir to be eluted, and focusing voltages of 0.5 kV on the sheath channels and the focusing collection channel are optimal.

5.5.3.2 Sequential Elution with Single Wavelength Detection

5.5.3.2.1 Sequential Fractionation and Elution

With the leakage problem solved by applying focusing voltages on sheath channels and one of the collection channels to transport buffer to geometrically define the elution stream, we studied sequential elution from the monolithic polymer beds, which is the final aim of the fractionator. The adsorption and elution was carried out in three steps. Sample was placed in the sample reservoir and sequentially delivered onto the monolithic bed in each channel under the protection of sheath flow. The loading time was held constant at 30 s for each bed. After sample loading, the sample flow was stopped and sheath buffer was delivered into each channel for 1 min to flush the remaining unretained sample. Finally, elution buffer was placed in the collection reservoir to elute the adsorbed sample towards the elution channel.

To perform sequential elution, the elution channel reservoir was biased at a positive voltage via the blue-box power supply, while the collection channels were sequentially grounded using the sequential grounding system. The sheath reservoirs were grounded via the blue box. In the application of the switching system to sequential fractionation, once the first timer is initiated, the relays are

activated automatically and step through each channel controlled by setting the dwell time on the timer. That is, one relay is off and the next relay is on. However, in the application here, the focusing collection channel also needs to be sequentially grounded. In other words, two relays must be activated at the same time. Therefore we have to control the relays manually by turning the knobs of the timer. It will be necessary to design a switching system and program to control the entire process automatically in future work.

PolyE-323 coated devices with monolithic beds incorporated in the collection channels were used in these experiments and a PMT was positioned in the elution channel to record the elution traces. The sample used here is a fluorescent dye labeled protein FITC-BSA. Since the channel immediately downstream of the desired channel to be eluted is used to provide the focusing stream, the sample adsorbed on the SPE bed in this focusing channel must be eluted before it can serve as the focusing channel. The sequential elution was performed in the order shown in Figure 5.44a by the arrows, in which the collection channels on one side were grounded sequentially from L4 to L1, and then switched to the other side, and grounded sequentially from R4 to R1. Figure 5.44b shows the elution profile, where the eight peaks indicate the sequential elution of FITC-BSA off eight monolithic SPE beds in an 8-channel Device B.

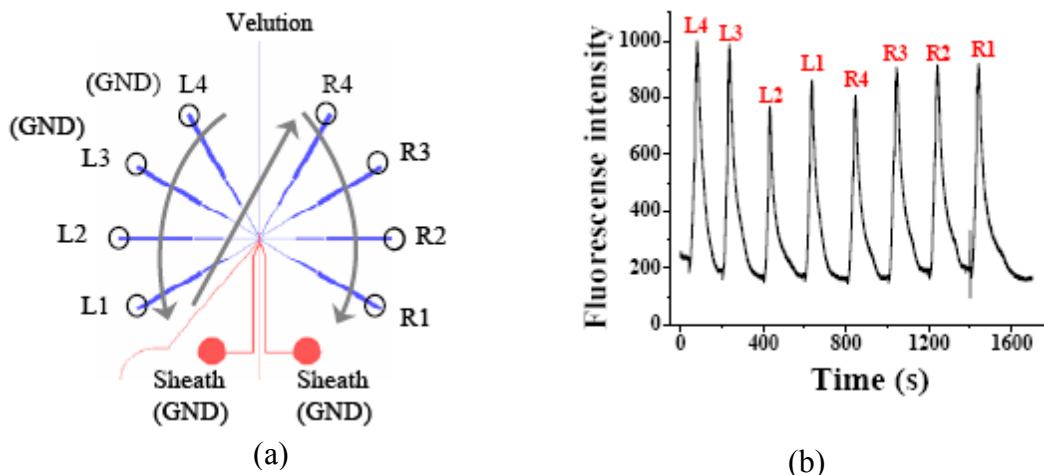


Figure 5.44 Sequential elution from an 8-channel Device B. (a) Schematic illustrating the elution order; (b) Elution trace illustrating the sequential elution of FITC-BSA from eight monolithic SPE beds. Elution channel: 0.5 kV; collection channel for elution and focusing: ground, sheath reservoirs: ground. The corresponding channel is labeled above each peak.

The eluted peak areas were estimated using Origin software and variations in the peak areas of $\pm 11.4\%$ RSD were observed for the eight elution peaks. As discussed in the next section, the reproducibility of the bed capacity was ± 7 to 8% RSD. An important factor that could account for the greater variation is differences in flow rates between each collection channel during the sample loading step. The monolithic beds in the channels may change both the electrical resistance and flow resistance, leading to flow rate changes. Mei He [29] in our lab demonstrated that monoliths can be reproducibly patterned in a microfluidic device with a bed-to-bed variation of flow resistance within a single wafer of $\pm 5.3\%$ RSD ($n=3$). The results she obtained were all from single channel studies. In our multi-channel device, the complex channel network may have an effect on the monolith formation, changing the structure and interface. In particular, subtle

differences in the liquid levels of each reservoir may induce small fluid flows, leading to larger variations in bed-to-bed reproducibility.

5.5.3.2.2 Reproducibility Study

In order to study the peak area reproducibility for sequential elution from a multi-channel device, a different strategy was used by continuously delivering sample through the channels to saturate the monolithic SPE bed. For simple operation and easy detection, sample was placed in the collection reservoirs and electrokinetically driven towards the elution channel. A PMT was located in the elution channel to monitor the sample breakthrough which indicated the saturation of the monolithic beds. The monolithic beds were loaded in the opposite order to sequential elution, that is, from L1 to L4, and then from R1 to R4, to enable the use of the focusing channel before it was filled with sample solution. Each channel was flushed to remove the sample that remained within the channel before loading the next channel. This method eliminates the effect of the flow rate. Thus the reproducibility of the sequential elution process can be assessed based on the elution peak areas.

Figure 5.45 shows the sequential elution traces from four different runs using this loading method. The peak areas estimated from the elution traces show better reproducibility, with peak-to-peak reproducibilities ranging between 6.8%-8.0% RSD for the six peaks in one sequential elution trace. The run-to-run reproducibilities were 2.4%-6.7% RSD for the elution peaks from the same SPE bed in four different runs (Table 5.9).

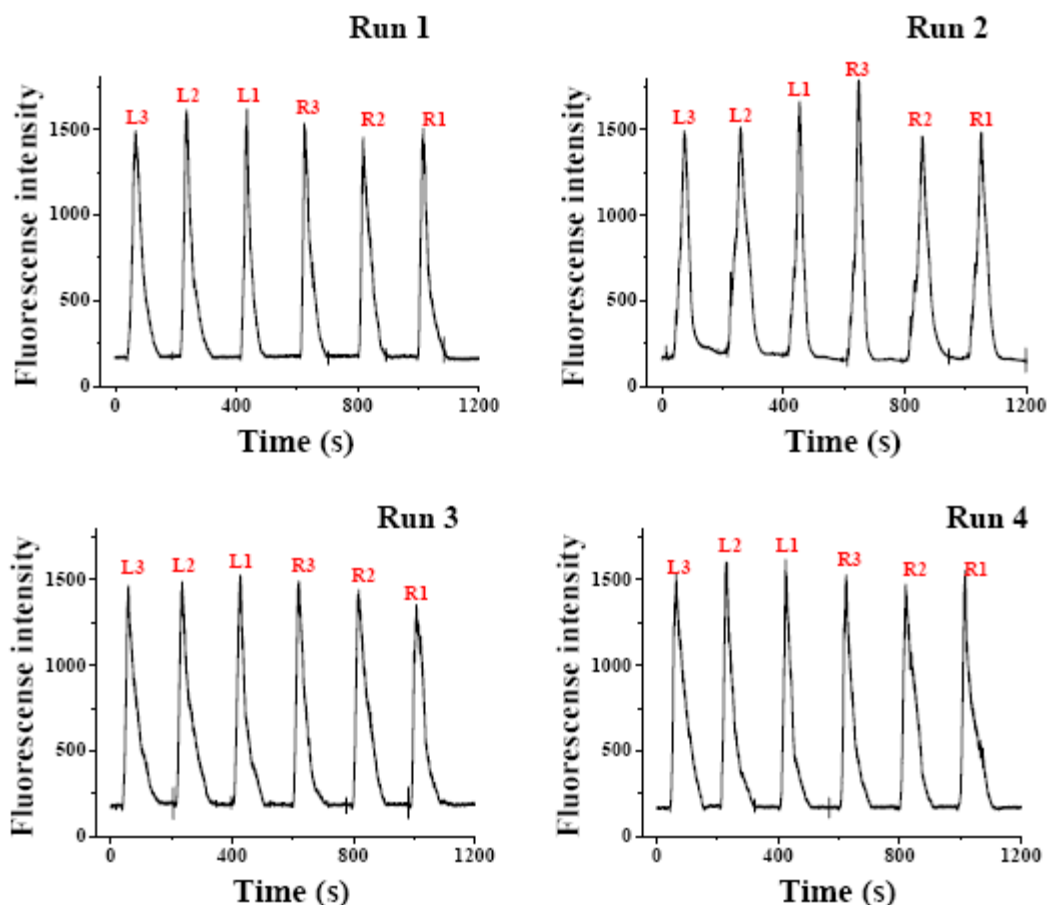


Figure 5.45 *t* of four different runs illustrating the sequential elution of FITC-BSA off six monolithic SPE beds in a 6-channel Device D. Elution channel: 0.5 kV; collection channel for elution and focusing: ground, sheath reservoirs: ground. The corresponding channel is labeled above each peak.

Table 5.9 Peak area reproducibility in the sequential elution for four separate runs.

Peak Area	Peak L3	Peak L2	Peak L1	Peak R3	Peak R2	Peak R1	Peak-to-peak (RSD)
Run 1	52211	49120	41780	44803	47341	44029	8.1%
Run 2	49158	57380	47721	47300	54328	49603	7.9%
Run 3	50697	52982	47369	45278	53850	47645	6.9%
Run 4	55571	50959	45999	46087	52453	51229	7.4%
Run-to-Run (RSD)	5.3%	6.7%	6.0%	2.4%	6.2%	6.4%	

The elution peaks in Figure 5.42 and 5.43 are very broad, with peak widths of ~50 s (FWHM), which could be attributed to the low electric field during elution. Using pSpice simulation, the electric field strength in the collection channel is estimated to be ~100 V/cm. To facilitate a flash elution, higher electric fields should be applied in subsequent experiments. The flash elution with a peak width of ~10 s shown in Section 2.3.4.1 was achieved with an electric field of ~ 600 V/cm.

5.5.3.3 Sequential Elution with Multi-Wavelength Detection

5.5.3.3.1 Sample Carryover Evaluation

Since one of the collection channels is always used to provide the focusing stream, a question arises regarding the issue of sample carryover from the SPE bed in the focusing channel. As an example, if we are going to elute the sample from the monolithic bed in the third channel L3, the fourth channel L4 will be used to drive buffer into the fractionation zone to define the sample stream. Even though the samples adsorbed on the monolithic bed in L4 will have been eluted already, the presence of any residual retained compound will be carried over as samples are eluted from L3.

In order to investigate this sample carryover effect, we used a multi-wavelength detection system, previously built by Jelena Dragoljic in our research group [19]. This system records green and red fluorescence at the same time, as described in Section 5.4.2.2.

Figure 5.46 illustrated a schematic of the experiment designed to evaluate sample carryover. A green fluorescent dye and a red fluorescent dye were loaded onto the monolithic polymer beds alternately, as demonstrated by green and red bars, respectively. Following rinsing all the beds to remove unretained sample, elution buffers were placed in the reservoir to release samples adsorbed on the beds. Ideally, no analyte signal should be observed in the green fluorescence PMT during release of the red fluorescent dye, and vice versa. Sample carryover from the focusing channel can thus be detected by monitoring both red and green fluorescence simultaneously. We define this sample-carryover induced signal leakage as chemical leakage, as compared to two other possible signal leakages, optical leakage and electrical leakage, which will be discussed in the following sections.

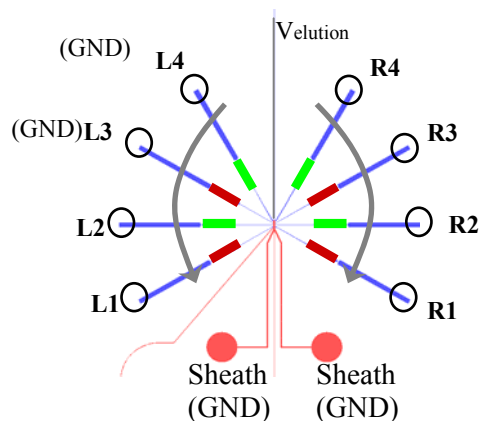


Figure 5.46 Schematic of the experiment designed for sample carryover evaluation.

5.5.3.3.2 Selection of Sample

The selection of the two fluorescent dyes, one giving green fluorescence and the other giving red fluorescence, requires several criteria be met. Both must be

efficiently excited by a 488-nm argon ion laser; they should have a minimum degree of overlap in the emission spectra in order for the signal from each fluorophore to be effectively separated with bandpass emission filters. They should also show some affinity for the hydrophobic monolith.

Unfortunately, we did not find two dyes that perfectly match our precise requirements. By accepting a bleed-through of fluorescence emission, or optical leakage, between channels to be less than 10% of maximum emission, two fluorescent dyes were identified: fluorescein and 5-(and-6)-carboxy SNARF®-1.

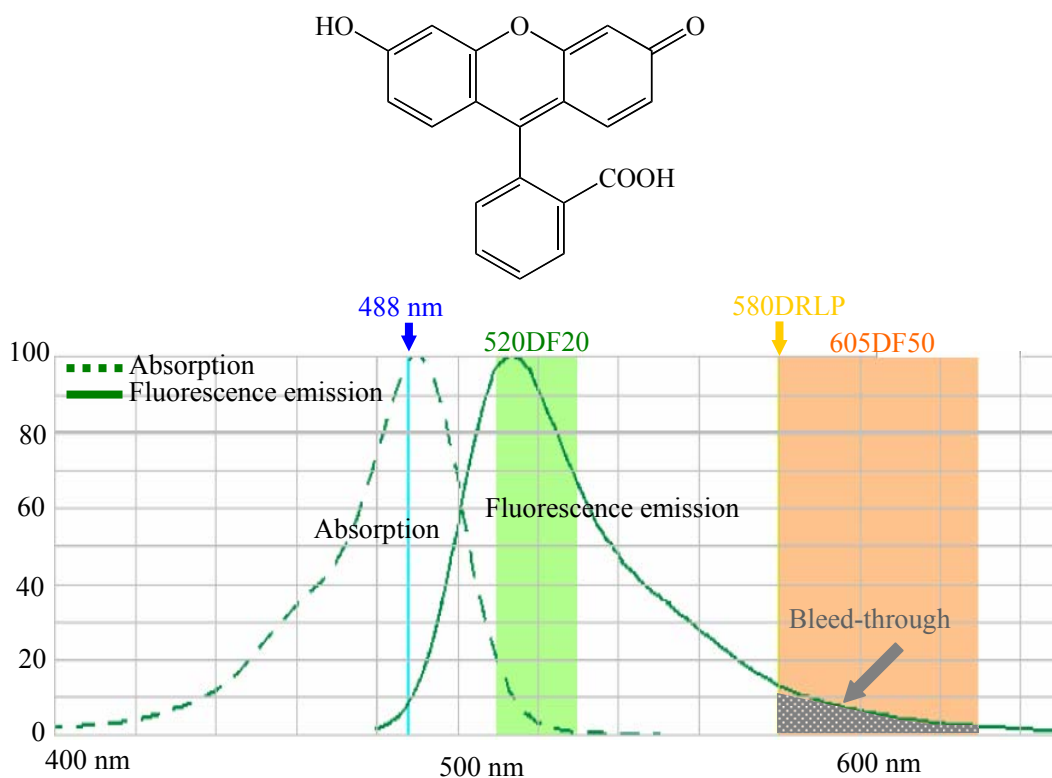


Figure 5.47 Chemical structure, adsorption spectrum and emission spectrum of Fluorescein. Dashed line indicates the absorption spectrum and the solid line indicates the emission spectrum. Blue line: 488 nm excitation laser; yellow line: dichroic mirror used to separate green and red fluorescence; green and orange regions: two bandpass filters; grey shades: bleed-through of emission signal.

Figure 5.47 shows the chemical structure of fluorescein and its absorption and green fluorescence emission spectra (<http://www.invitrogen.com>). The blue line

indicates the 488 nm excitation laser, the yellow line indicates the dichroic mirror used to separate green and red fluorescence, the green and orange regions represent the two bandpass filters. We can see that there is some bleed-through of emission into the channel for red fluorescence detection, as indicated by gray shading.

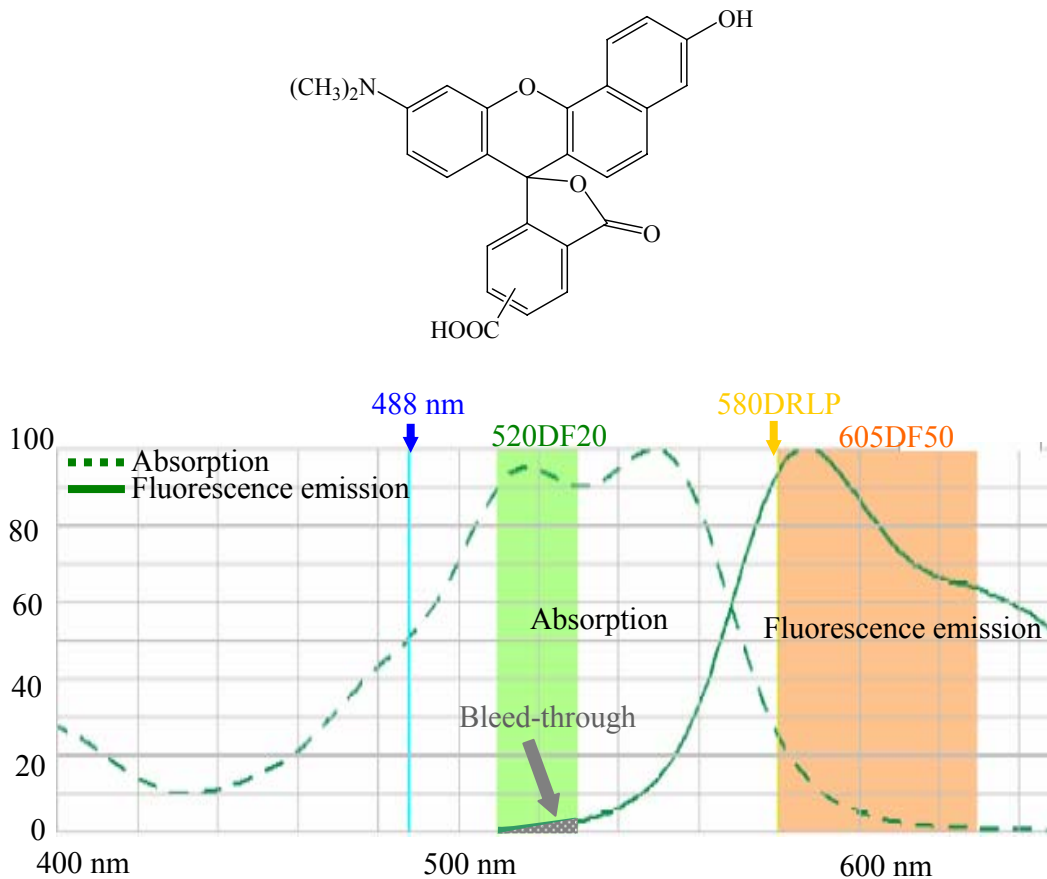


Figure 5.48 Chemical structure, adsorption spectrum and emission spectrum of Carboxy SNARF-1 (<http://www.invitrogen.com>).

Carboxy SNARF-1 is a red fluorescent dye with the chemical structure shown in Figure 5.48. The spectra shows it can also be efficiently excited at 488 nm, with a small amount of bleed-through of fluorescence signal into the green fluorescence channel. This optical leakage, together with the electrical leakage,

can be quantified through a calibration curve which is created by measuring signal response using standard solutions of each dye.

5.5.3.3.3 Software Testing

The output signal from the PMTs was converted into digital data with a National Instruments LAB PC 1200 data acquisition board and recorded with a LabVIEW program. The LabVIEW program was written by Randy Tsen to facilitate simultaneous recording of red and green fluorescence emitted from the two dyes with the multi-wavelength detection system. Figure 5.49 shows the interface of the LabVIEW program.

Several parameters such as the input channel number, the board sample rate and the number of points to average must be addressed when using this software because the software was not properly annotated. Two signal input channels, named as channel 0 (CH0) and channel 2 (CH2), are connected to the board. While there are three windows where the signals can be displayed, labeled as A, B and C, respectively, in Figure 5.49, and the data will be automatically save as three files, DataG, DataR, and DataL after a designated file name “Data”. In order to determine the corresponding display windows and data files for the two signal input channels, two function generators were used to generate the required signals: one function generator generates a square waveform, which is fed into CH0; the other generates a triangular waveform, which is fed to CH2.

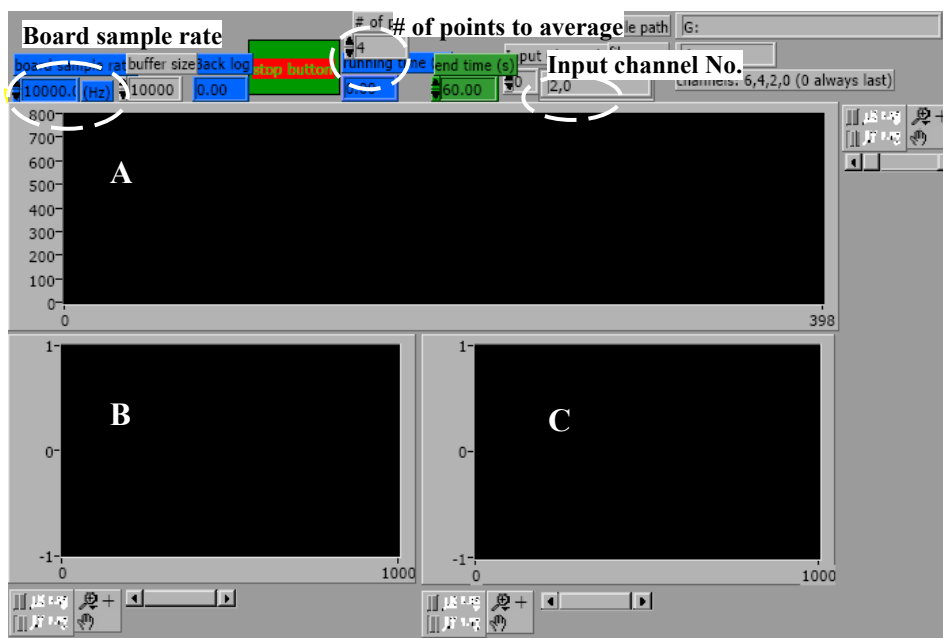


Figure 5.49 Interface of the LabVIEW program for collecting data with the multi-wavelength detection system

With an input channel setting of 2, 0 in the input channel No., signal from CH0, the square wave, is displayed in Window B and saved as DataG; and signal from CH2, the triangular wave, is displayed in Window A and saved as DataR; nothing is shown in window C and the file DataL is empty since there is no input signal.

A proper sampling rate is very important when collecting data. Too low a frequency may result in missing data points and distortion of the peak, too high a frequency will generate big files that may cause computer crashes. We designed experiments to help us pick up an optimized frequency for collecting data and the proper averaging rate of the data collected. A square wave and a triangular wave from the function generators were used in these experiments. The elution peaks obtained in previous experiments is about 50 s wide, thus the square wave is set to have a pulse width of 10 s and the triangular wave with is set to have a scan rate

of 100 mV/s, resulting in a period of 10 s for the waveform to sweep from 0 V to 1 V. Different sampling frequencies of 10, 100, 500, 1000, 10000 Hz and averaging rates of 2, 4, 10, 20 data points were tested. Figure 5.50 shows several examples.

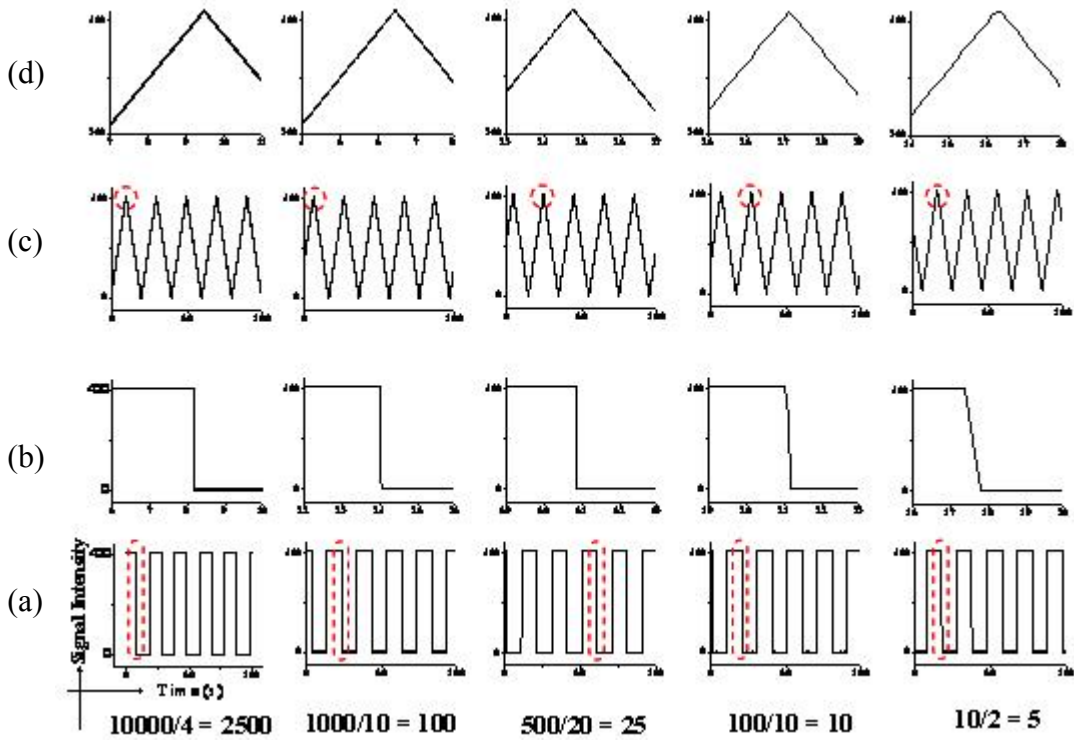


Figure 5.50 Optimization of sampling frequency, averaging rate, and overall writing frequency for data collection. Input signal: a square waveform is fed into CH0 (a, b); a triangular waveform is fed to CH2 (c, d). (b) and (d) a closer look at individual data points in the region marked with dashed lines.

A 10000 Hz sample frequency with 4 data points averaged, gives a writing frequency of 2500 Hz; a 1000 Hz sample frequency with 10 data points averaged, gives a writing frequency of 100 Hz, and so on. Although, as expected, the highest sampling frequency 10000 Hz with four data points average generates the best quality data, the other combinations also showed proper description of the original signal. By zooming the X-axis and Y axis to take a closer look at

individual data points where the signal flips from 0 V to 1V for the square wave (Figure 5.50b) and the maximum position for the triangular wave (Figure 5.50d), we notice some distortion for the two lowest writing frequencies (a sampling frequency of 100 Hz with 10 data points average and a sampling frequency of 10 Hz with 2 data points average). These results suggested we employ a sampling frequency of 500 Hz with 20 data points averaged, giving a writing frequency of 25 Hz. This combination offers good quality data with a satisfactory signal-to-noise ratio, compromising between the size of the data file and proper description of the data recorded.

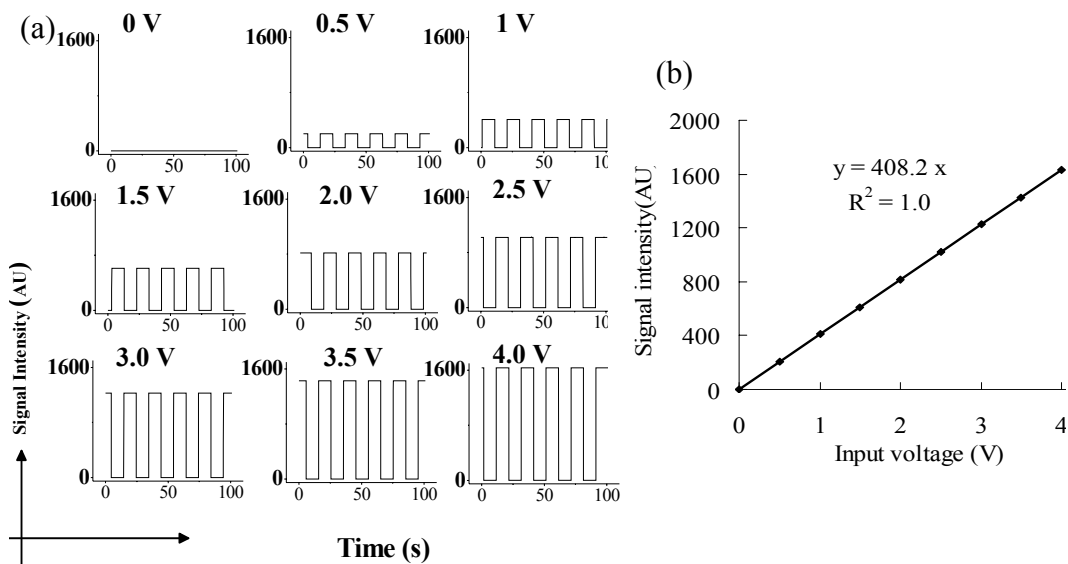


Figure 5.51 Response of recorded signal intensity to the change of amplitude of input signal. (a) Data recorded with square wave input at different amplitudes from 0 V to 4 V, all graphs are plotted on the same scale. (b) Signal-response curve.

In order to check if the collected data respond to the change of input signal correctly, the amplitudes of the square wave were varied from 0 V to 4 V and the signals recorded are shown in Figure 5.51a. The signal intensity was presented as arbitrary units with the same scale. A signal-response curve gives a linear

relationship between the magnitudes of the responses versus the amplitudes of the input signals, as is demonstrated in Figure 5.51b.

Another practical concern with the data acquisition system is the potential electrical leakage of signal between the two channels due to the parallel circuits existing in the data acquisition interface. In order to test the presence of any signal leakage between CH0 and CH2, experiments were designed as one of the two channels was fed with a square wave signal, while the other channel had no signal feeding in.

When the square wave signal was fed into CH0 with no input to CH2, the window for CH0 displays the square waveform signal, while the window for CH2 also shows a signal change, indicating that signal in CH0 leaks slightly into CH2 (Figure 5.52).

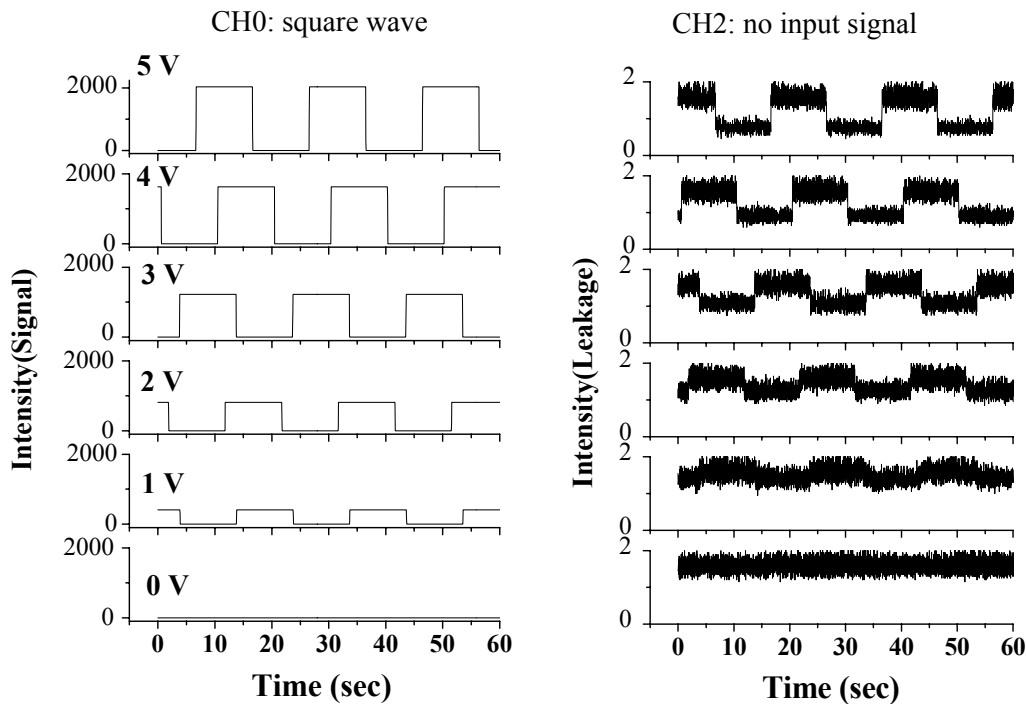


Figure 5.52 Electronic Leakage of signal from CH0 to CH2. Input Signal: square waveforms with different amplitude from 0 V to 5 V.

Similar results are observed when the square wave signal was fed into CH2 (Figure 5.53). The amount of electrical leakage, i.e. the signal intensity in the undesired channel, is plotted versus the intensity of the input signal, giving a linear response for both channels, as shown in Figure 5.54.

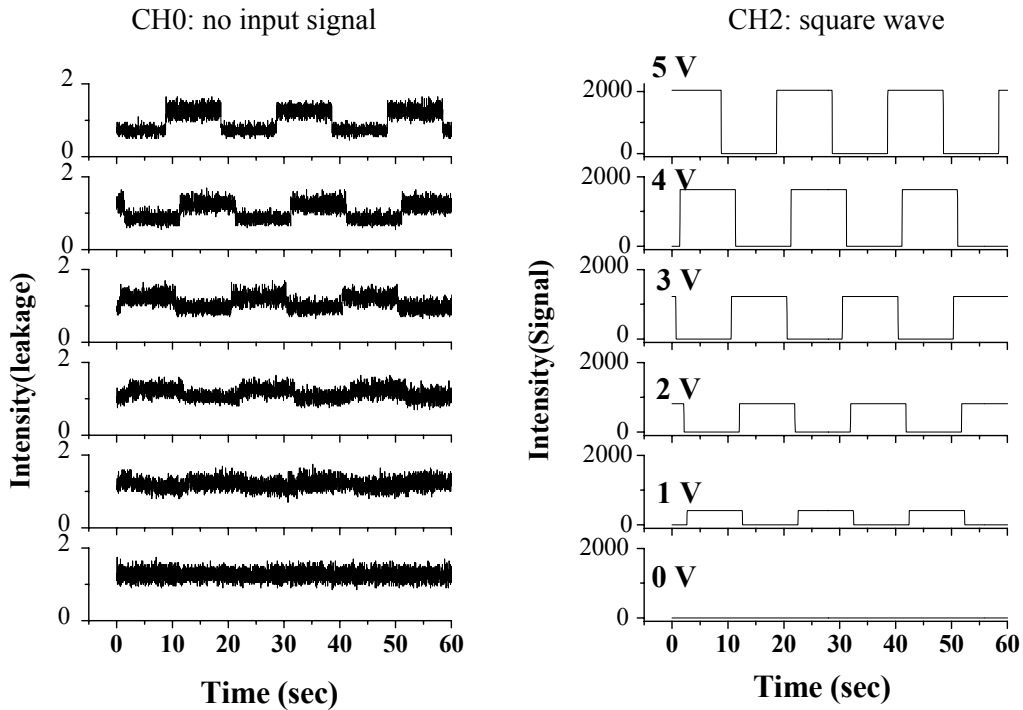


Figure 5.53 Electronic Leakage of signal from CH2 to CH0. Input Signal: square waveforms with different amplitude from 0 V to 5 V.

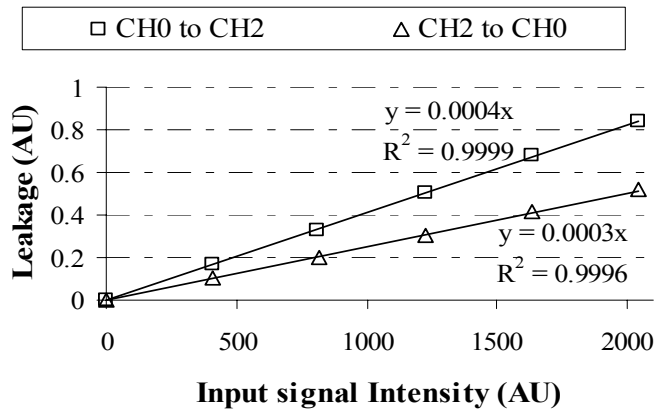


Figure 5.54 Plot of electrical leakage in the undesired channel as a function of input signal intensity.

5.5.3.3.4 Quantification of Optical and Electrical Leakage

To determine the amount of chemical leakage (sample carryover) during the elution process, it is necessary to quantify the optical and electrical leakage first. Calibration curves were obtained by measuring signal responses in both detection channels using the standard solution of each dye. A series of standard solutions of fluorescein with a concentration range of 0.3 to 9.0 μM were prepared in 20 mM potassium phosphate buffer (pH 6.5). The dye solution was placed in the sample reservoir and delivered continuously through a straight open channel with the PMT detector located in the middle of the channel. The fluorescence signals were recorded simultaneously in both detection channels: signal from the PMT for green fluorescence was fed into CH0 (green); while signal from the PMT for red fluorescence was fed into CH2 (red).

Figure 5.55 presents several traces of the fluorescence signal detected in green (a) and red (b) fluorescence channel with constant infusion of fluorescein solution at difference concentrations.

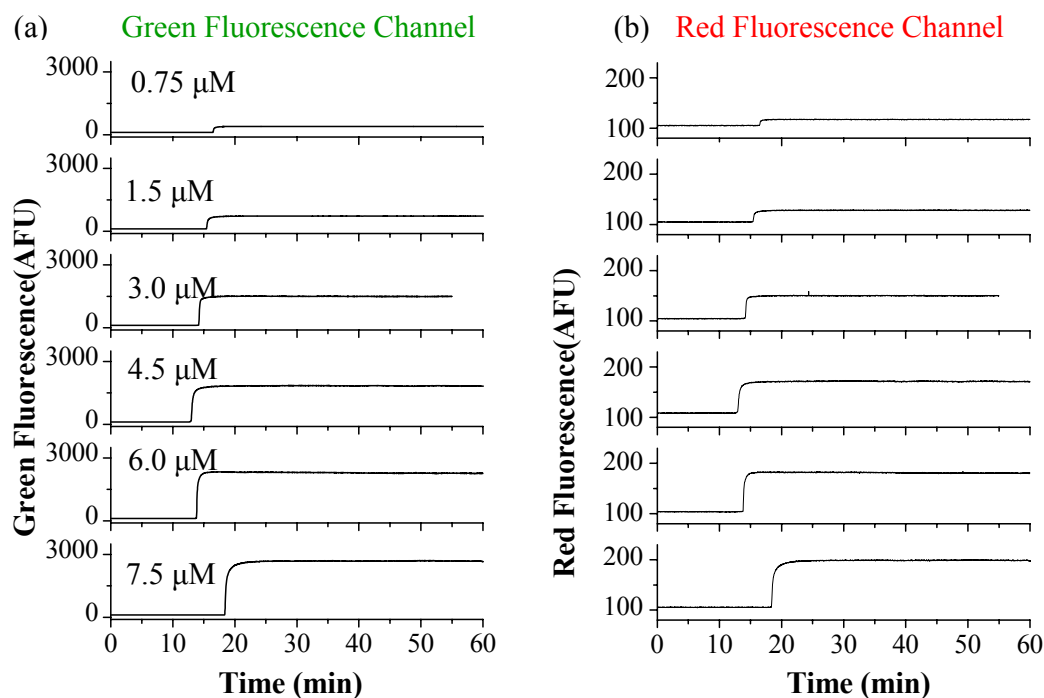


Figure 5.55 Traces of the green (a) and red (b) fluorescence detected with constant infusion of Fluorescein solution at difference concentrations. (a) Normal green fluorescence signal; (b) Optical and electrical leakage of signal into the red fluorescence channel. Fluorescein sample concentration is indicated above each trace.

The intensities of the fluorescence signal seen in both green and red channels are shown in Figure 5.56a and b. The intensity of the fluorescence signal was quantitatively presented as arbitrary units of fluorescence and was baseline corrected. Both calibration curves give a linear response in the concentration range tested. Figure 5.56c shows the red fluorescence intensity (leakage) versus the green fluorescence intensity (normal signal). A linear relationship was observed with a slope of 0.0364. This slope indicates the ratio of leakage (optical and electrical) to signal, thus it is an important parameter for later evaluation of the chemical leakage. Figure 5.56d shows the plot of red/green intensity ratio versus green fluorescence intensity, illustrating the leakage-to-signal ratio is signal strength independent.

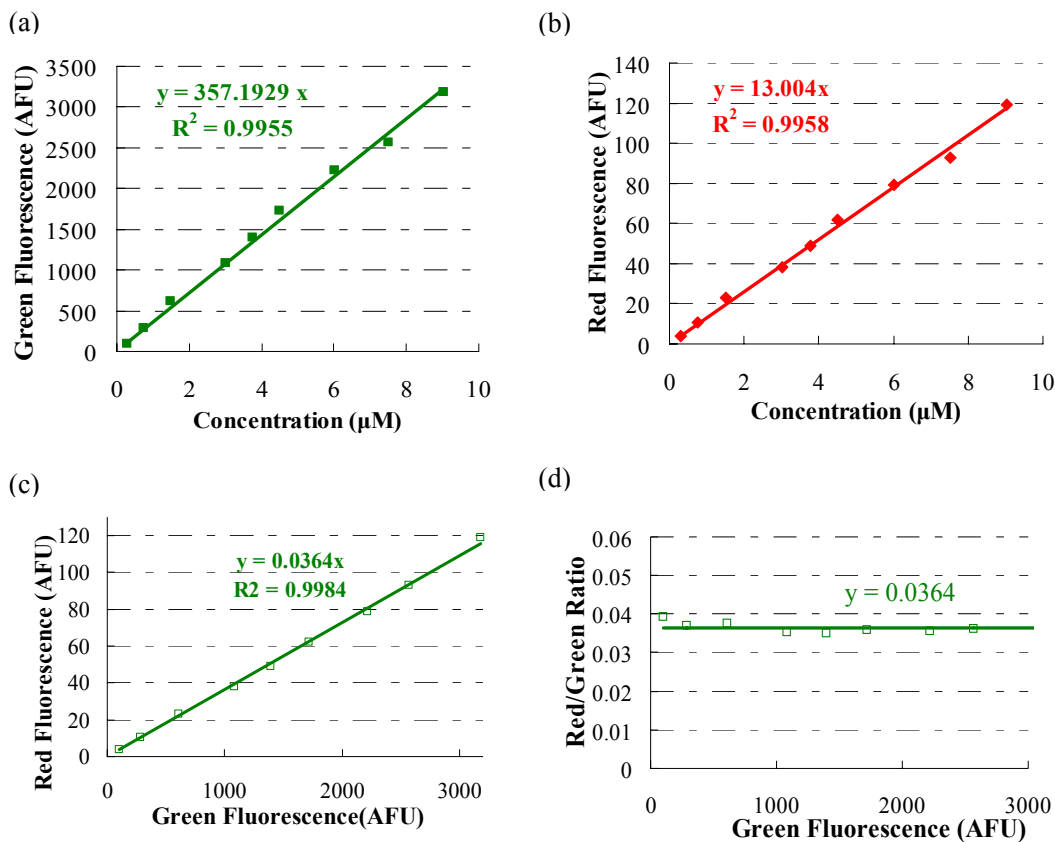


Figure 5.56 Quantification of optical and electrical leakage into red fluorescence channel. (a) Plot of intensities of the green fluorescence (normal signal) versus sample concentrations; (b) Plot of intensities of the red fluorescence (leakage) versus sample concentrations; (c) plot of red fluorescence(leakage) versus green fluorescence (normal signal); (d) plot of red/green intensity ratio versus green fluorescence intensity.

Similar experiments were conducted by infusing red fluorescent dye carboxy SNARF solutions with a concentration range of 0.45–13.2 μM through the flow channel to determine the optical and electrical leakage into the green fluorescent channel. The results are shown in Figure 5.57 and 5.58. A slope of 0.0117 in the plot of green fluorescence intensity versus red fluorescence intensity (Figure 5.58c) gives the ratio of leakage (optical and electrical) to signal.

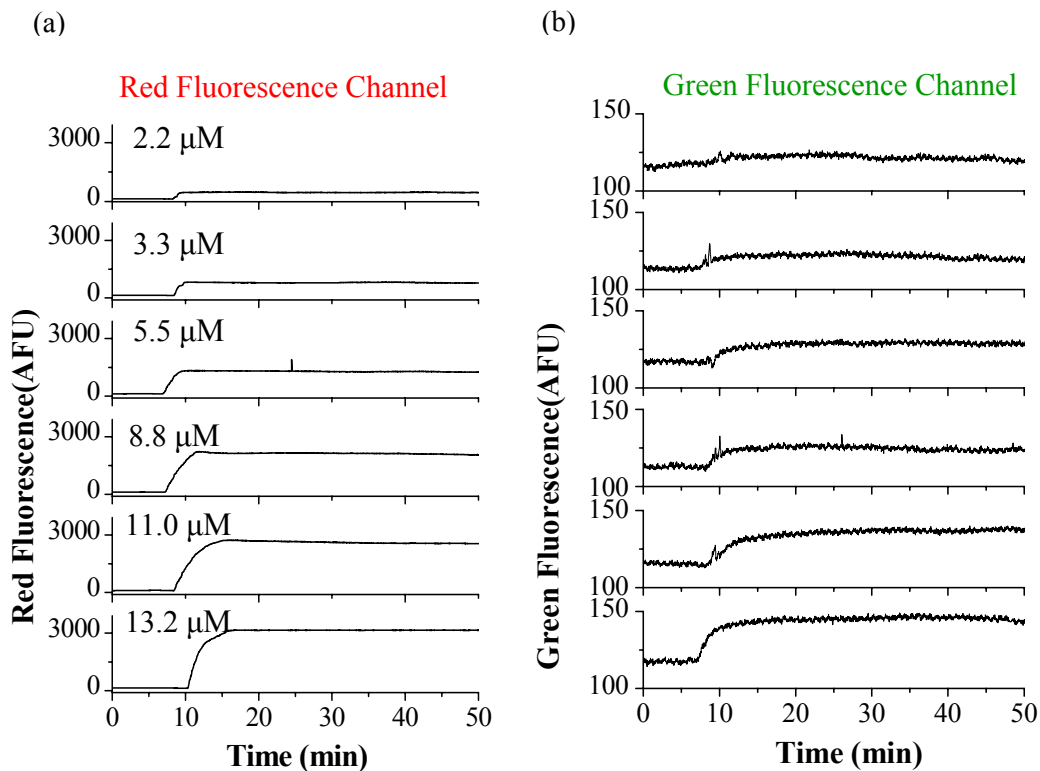


Figure 5.57 Traces of the red (a) and green (b) fluorescence obtained with constant infusion of Carboxy SNARF solution at difference concentrations. (a) Normal red fluorescence signal; (b) Optical and electrical leakage of signal into the green fluorescence channel. SNARF sample concentration is indicated above each trace.

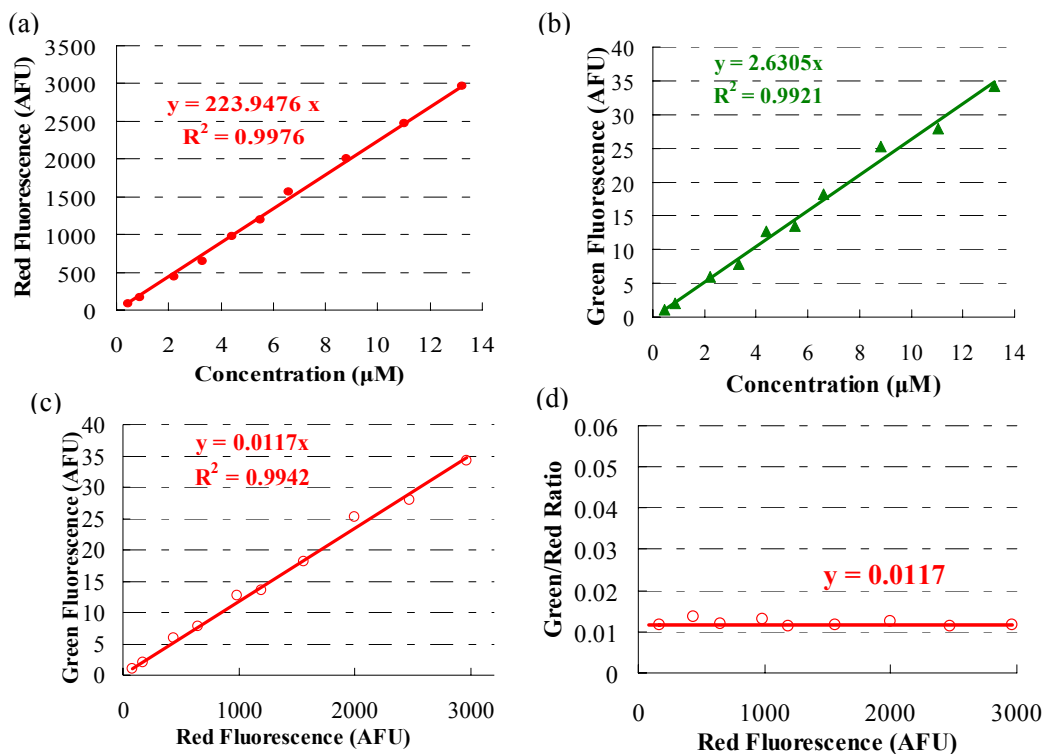


Figure 5.58 Quantification of optical and electrical leakage into green fluorescence channel. (a) Plot of intensities of the red fluorescence (normal signal) versus sample concentrations; (b) Plot of intensities of the green fluorescence (leakage) versus sample concentrations; (c) plot of green fluorescence (leakage) versus red fluorescence (normal signal); (d) plot of green/red intensity ratio versus red fluorescence intensity.

5.5.3.3.5 Determination of Chemical Leakage

Adsorption and elution experiments were performed on the multi-channel device using the multi-wavelength system. Fluorescein and carboxy SNARF were loaded alternately onto the monolithic polymer beds in an 8-channel Device B, with fluorescein adsorbed in the SPE beds in channel L4, R4, L2, R2 and carboxy SNARF adsorbed in SPE beds in Channel L3, R3, L1, and R1. Sample loading was conducted with the method used in the sequential elution reproducibility study (Section 5.5.3.2.2). That is, the respective dye solutions were placed in the

collection reservoirs and electrokinetically driven towards the elution channel until the monolithic beds were saturated.

After extensive buffer rinsing to remove the dye sample existing in solution, elution buffer was placed in the collection reservoirs to perform sequential elution. The elution was conducted following the elution order and voltage program described in Section 5.5.3.2.1. Samples in the four beds on the left side were first eluted by grounding the channels from the top down sequentially controlled by the relay box, with positive voltage on elution channel and sheath channel grounded. Afterwards, the four channels on the right side were grounded sequentially to elute samples in these beds. The resulting elution profiles are shown in Figure 5.59, where green traces represent signal recorded in the green fluorescence channel and red traces represent signal recorded in the red fluorescence channel.

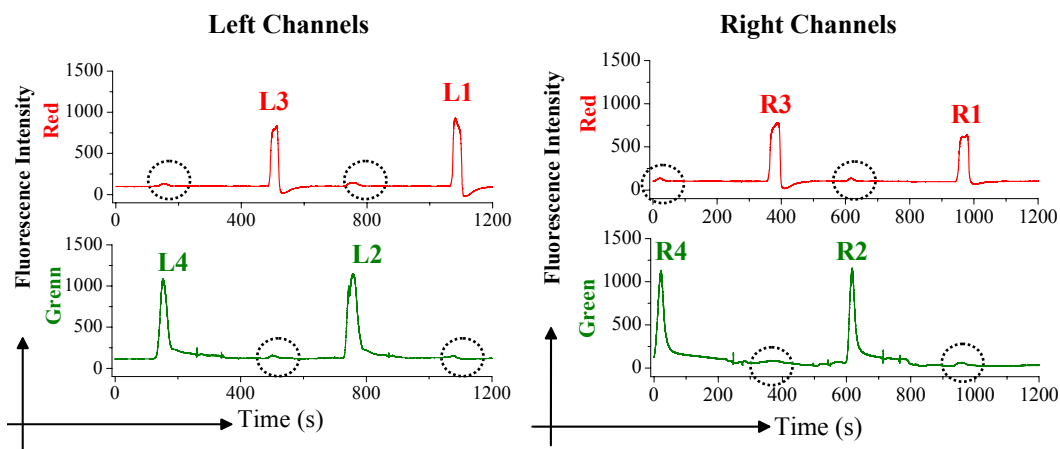


Figure 5.59 Sequential elution from an 8-channel Device B with multi-wavelength detection. Elution profiles illustrating the sequential elution of fluorescein (Green trace) and carboxy SNARF (red) from the eight monolithic SPE beds. Elution channel: 1kV; collection channel for elution and focusing: ground, sheath reservoirs: ground. The corresponding channel is labeled above each peak.

Eight peaks with high intensities represent the elution of samples from the eight SPE beds with detection at the elution channel, among them four are from elution of fluorescein and the other four are from elution of carboxy SNARF. Besides the big elution peak recorded in the desired detection channel, small peaks are also observed at the same position in the other detection channel, as marked by circles in Figure 5.59.

Figure 5.60 presents elution traces of two more repetitive runs showing similar peak patterns. The presence of the small peaks indicates the simultaneous detection of signal in the undesired channel, which originates from optical and electrical leakage, and possibly, chemical leakage.

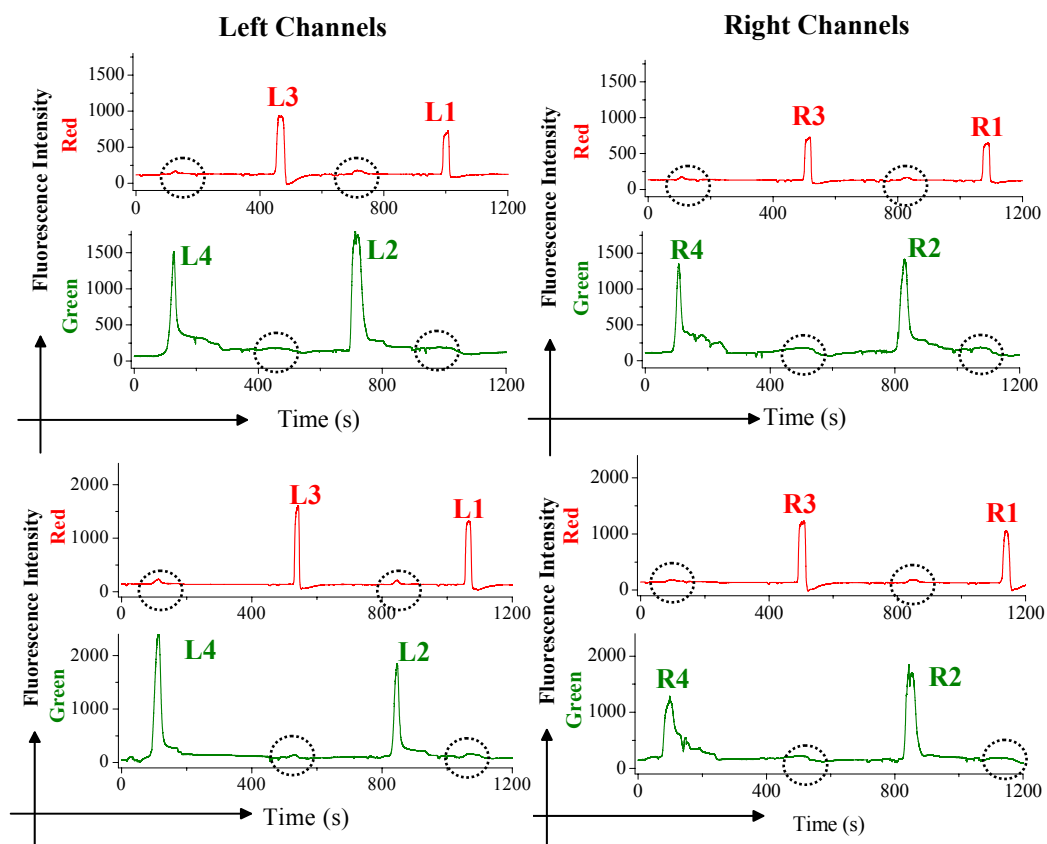


Figure 5.60 Elution traces of two repetitive runs showing the sequential elution of fluorescein and SNARF. All the conditions are the same as those in Figure 5.59.

Determination of the contribution of each of these factors requires further calculations. The intensity of the small leakage peak maximum was measured, as was the intensity of the big elution peak coincident with the leakage peak. The ratio of these values indicates the total leakage-to-signal ratio. The amount of leakage due to optical and electrical leakage could be determined from the ratio of optical and electrical leakage to signal obtained in the previous section and the intensity of the elution peak. The extra leakage can be attributed to chemical leakage due to sample carryover from the focusing channel.

Leakage can be more clearly evaluated by plotting the red versus green signals in the elution study along with the optical and electrical leakage calibration data obtained in Section 5.5.3.3.4. As demonstrated in Figure 5.61a, the green line with open square symbols indicates the plot of red fluorescence intensity due to optical and electrical leakage versus green fluorescence intensity from fluorescein (same as Figure 5.56c); the red solid diamonds represent the experimental elution data points from 10 separate runs. Each run is defined as a complete elution of eight channels in Device B. Thus, each run will give four elution peaks for fluorescein and four elution peaks for Carboxy SNARF. The 40 data points in Figure 5.61 are from the elution peaks for fluorescein. In Figure 5.61b, the green line with open square symbols represents the amount of optical and electrical leakage by the ratio of red/green fluorescence intensity (same as Figure 5.56d). The ratios of peak intensities in the elution study (red/green ratio) are also plotted in this graph. From the two graphs in Figure 5.61, one can see that the data points are evenly

distributed along the green lines, indicating that no significant chemical leakage (sample carryover) of carboxy SNARF was observed.

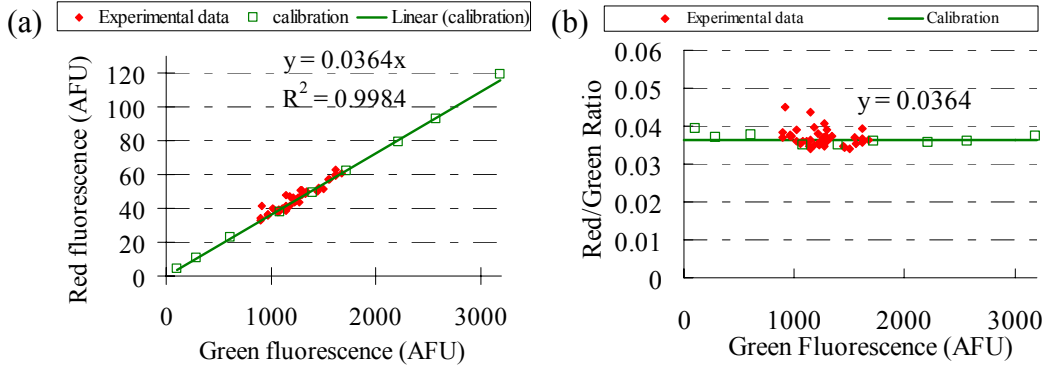


Figure 5.61 Graphical interpretation of possible presence of sample carryover of carboxy SNARF for elution of Fluorescein from the SPE beds. (a) Plot of red fluorescence (leakage) versus green fluorescence (normal signal from elution of Fluorescein); (b) Plot of red/green fluorescence intensities ratio versus green fluorescence intensity. The green line with open square symbols represents the amount of optical and electrical leakage; the red solid diamonds represent 40 experimental data points from 10 separate runs.

The ratio of the amount of residual red fluorescent compound to the total amount of SNARF sample that was loaded on the monolithic bed can be calculated by the following equation:

$$SNARF_{residual} \% = \frac{\left(\frac{I_{R,leakage}}{I_{G,Fluor_elution}} - 0.0364 \right) \times I_{G,Fluor_elution}}{I_{R,SNARF_elution}} \times 100\% \quad (5.28)$$

where $I_{R,leakage}$ and $I_{G,Fluor_elution}$ are the intensity of red fluorescence (the total leakage including electrical, optical and chemical leakage) and green fluorescence recorded during the elution of fluorescein, respectively. 0.0364 represents the ratio of optical and electrical leakage to signal obtained in Section 5.5.3.3.4. $I_{R,SNARF_elution}$ is intensity of the SNARF elution peak. The residual SNARF in the monolithic bed is estimated to be $0.08 \pm 0.23 \%$ ($n = 40$) of the total loaded SNARF sample.

Similar graphical interpretation and data analysis were conducted for the elution of carboxy SNARF. The red lines with open circles in Figure 5.62a and 5.62b represent the optical and electrical leakage from the green to the red fluorescence channel (same as Figure 5.58c and Figure 5.58d). The 40 data points shown in green solid triangles in these graphs are from the elution peaks for carboxy SNARF in the separate 10 runs.

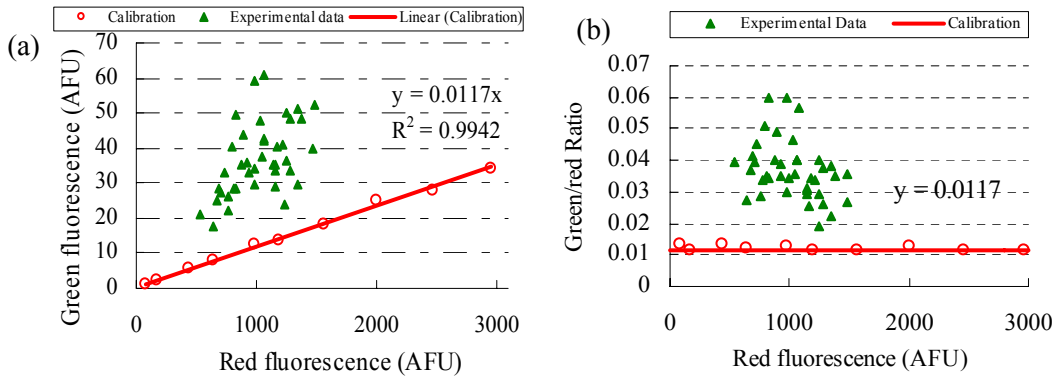


Figure 5.62 Graphical interpretation of possible presence of sample carryover of Fluorescein for elution of carboxy SNARF from the SPE beds. (a) Plot of green fluorescence (leakage) versus red fluorescence (normal signal from elution of Carboxy SNARF); (b) Plot of green/red fluorescence intensities ratio versus red fluorescence intensity. The red line with open circle symbols represents the amount of optical and electrical leakage; the green solid triangles represent the 40 experimental data points from 10 separate runs.

Most of the data points fall in a region well above the line, indicating that there is obvious chemical leakage from residual fluorescein. Sample carryover induced chemical leakage was calculated as follows:

$$Fluorescein_{residual} \% = \frac{\left(\frac{I_{G,leakage}}{I_{R,SNARF_elution}} - 0.0117 \right) \times I_{R,SNARF_elution}}{I_{G,Fluor_elution}} \times 100\% \quad (5.29)$$

where $I_{G,leakage}$ $I_{R,SNARF_elution}$ are the intensity of green fluorescence (the total leakage including electrical, optical and chemical leakage) and red fluorescence recorded during the elution of SNARF. 0.0117 represents the ratio of optical and

electrical leakage to signal obtained in Section 5.5.3.3.4. $I_{G,Fluor_elution}$ is intensity of the fluorescein elution peak. The residual fluorescein in the monolithic bed is estimated to be $2.5 \pm 1.3 \%$ ($n = 40$) of the total loaded fluorescein sample.

The different behavior of fluorescein and carboxy SNARF in terms of sample carryover may be attributed to the difference in their affinity to the monolithic bed. Fluorescein exists in four ionization states: H_3F^+ , H_2F , HF^- , F^{2-} , with three dissociation constant of $K_{a1, H_3F^+} = 6.61 \times 10^{-3}$, $K_{a2, H_2F} = 3.98 \times 10^{-5}$, $K_{a3, HF^-} = 4.36 \times 10^{-7}$ [30]. At a pH of 6.5 in our study, fluorescein is 58% dianionic (F^{2-}) and 42% monoanionic (HF^-). Carboxy SNARF also has four prototropic forms, and the dissociation constants of each ionization transition are $K_{a1, H_3F^+} = 3.98 \times 10^{-5}$, $K_{a2, H_2F} = 3.16 \times 10^{-8}$, $K_{a3, HF^-} = 1.58 \times 10^{-9}$. At pH 6.5, 91% are present in the neutral form, and 9% are in monoanionic form. The negative charge on the fluorescein dianion and monoanion leads to strong retention on the positively-charged monolith containing META. The eluted peaks of fluorescein are broad with significant peak tailing, indicating slow elution of this probe. In contrast, rapid desorption of carboxy SNARF results in sharp elution peaks with no tailing. This also explains the difference in the extent of sample carryover for these two dyes. For Carboxy SNARF, complete elution is readily achievable and the occurrence of carryovers is negligible. While for fluorescein, the slow elution property could leave some residual fluorescent probe in the monolithic bed that will be carried over as we are eluting samples in the next channel.

It is clear that the amount of sample carryover will depend on the nature of the analytes. Since we are attempting to use this platform to analyze a variety of

samples including proteins and peptides which will have different properties in terms of hydrophobicity, *pI* values, it is preferable to redesign the platform to accommodate focusing channels, instead of using a collection channel, to provide a focusing stream to avoid cross-contamination between fractionated samples.

An alternative solution to this sample carryover problem is to design three outlet channels at the end of the fractionation zone. With this design, eluted sample stream from the desired connection channel can be delivered into the middle outlet channel, while the focusing streams from both sides are guided into the two side outlet channels. Thus, the focusing stream from the collection channel is separated from the elution stream, and interference from residual samples desorbed from the SPE bed in the focusing channel is eliminated.

Simple experiments were conducted in our current device design in order to evaluate the possibility of using voltage manipulation to control the flow of sample and focusing streams into different outlet channels. These experiments were carried out on an 8-channel Device B, the two top collection channels L4 and R4 were used to collect the focusing streams. Figure 5.63a shows a picture of the fractionation region of the device with the channels labeled. Dye solution was placed in one of the collection reservoirs and continuously delivered towards the elution channel under the protection of buffer solution from both sides, with one focusing stream from the sheath channel and the other from the channel downstream of the desired channel. Three channels (elution channel, L4, and R4), instead of one, were grounded to guide the streams into three outlet ports. An

imaging CCD camera was used to monitor the movement of the fluorescent dye along the fractionation region.

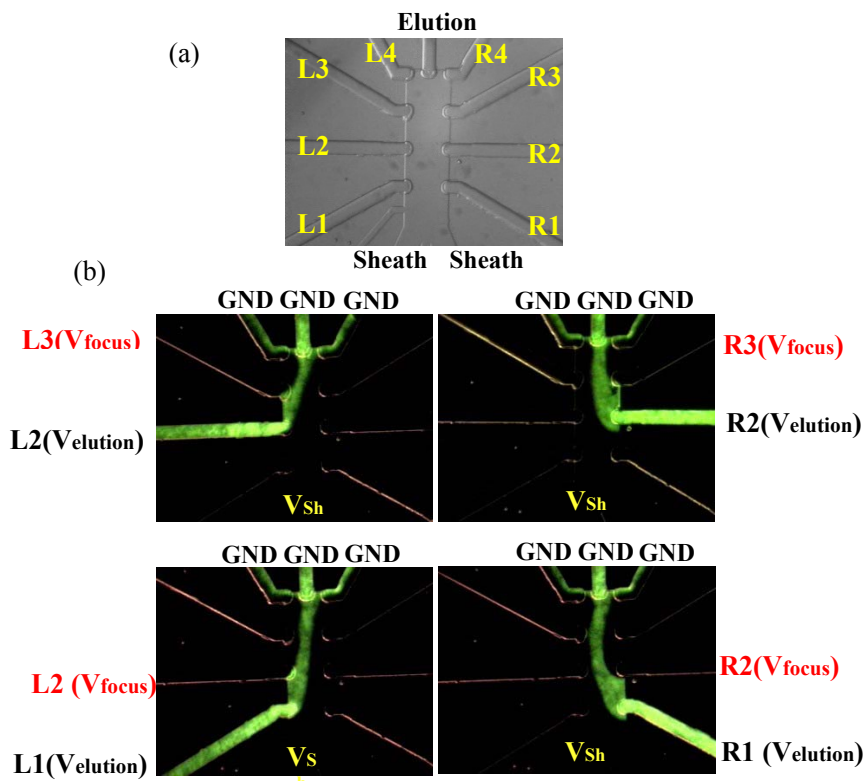


Figure 5.63 CCD Images illustrating that the focusing streams are guided to the top two grounded collection channels. (a) a picture of the fractionation region with the channel labeled; (b) Pictures showing that focused sample flow is delivered to the middle elution channel, while the focusing buffer streams are guided into the top two grounded collection channels (L4 and R4) without leaking into the elution channel. Voltage combination: $V_{elution}$ in desired channel: -500 V ; V_{focus} at focusing collection channel: -550 V ; V_{sh} at sheath channels: -1000 V ; Elution channel, collection channel L4 and R4 were grounded.

With a voltage combination of -500 V on the desired elution channel, -550 V on the focusing collection channel and -1000 V on the sheath channels, the focusing buffer streams from both sides are guided into the top two grounded collection channels without leaking into the elution channel (Figure 5.63b). The majority of the sample stream is delivered into the middle elution channel with a small amount of sample flowing into the two side outlet channels.

Figure 5.64 shows a pSpice simulation for the case when dye solution is delivered from the first collection channel reservoir. The simulation results show a current of 40.99 mA in the first collection channel where the dye sample flows out, as compared to a current of 17.96 mA in the elution channel, indicating that sample is distributed into the center elution channel, as well as going into the two side channels. Since streamlines do not cross in laminar flow, no sheath fluid is entering into the center elution channel.

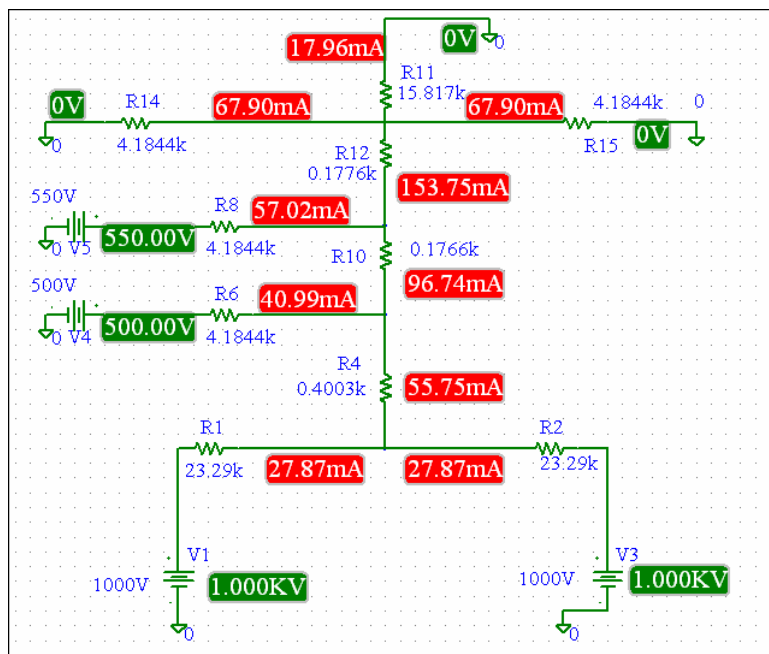


Figure 5.64 PSpice simulation scheme for the case when dye solution is delivered from the first collection channel reservoir. Voltage combination: $V_{elution}$ in desired channel: 500 V; V_{focus} at focusing collection channel: 550V; V_{sh} at sheath channels: 1000 V; Elution channel, collection channel L4 and R4 were grounded.

These experiments provide proof of the feasibility of using multiple outlet channels to separate the focusing streams and sample elution streams to eliminate sample carryover-induced cross-contamination. Suggestions for re-designing the multiplexed device will be presented in Chapter 6.

Another advantage of this method is that it eliminates dilution by the focusing buffer, which occurs when sample and buffer streams are delivered into the same outlet. Compared to the adverse effect of sample carryover and analyte dilution, the loss of a small amount of sample into the side channels is a minor issue. The leakage of sample into the side channels can be minimized via the manipulation of voltages for elution and focusing, making this less of a concern.

5.6 Conclusion

In this chapter, we present the design and fabrication of multiplexed microfluidic platforms addressing the need for integration of multiple analytical steps involved in the process of protein sample preparation for ESI-MS analysis. Each microfluidic pattern employed a series of features including a separation channel, a fractionator and collector, SPE columns, and an elution channel for the detection of eluted sample using fluorescence detector or mass spectrometer. Using photo-initiated polymerization, multiple BMA-META-EDMA-based monoliths were photopatterned in an array of microchambers in a single step to serve as SPE sorbent for protein preconcentration.

The performance of the microfluidic fractionator was evaluated with sequential fractionation of incoming sample flow from the main channel into branch channels. The introduction of sheath flow serves to prevent leakage-induced cross-contamination, allowing tightly focused sample streams to be distributed into individual channels and selectively adsorbed onto a desired bed without contaminating other beds. Automatic electrokinetic fractionation was

successfully achieved with three different delivery sequences using timers and relays to control flow switching at fixed time intervals.

PSpice impedance simulation was used to predict the sample stream width in the fractionation region. The calculation of the sample width using this model includes two parts: the first term is a constant width depending on the volume flow rate ratios of sample stream and sheath streams; the second is a time dependent term due to diffusion. Using an approximation model to calculate the diffusion term, which is a dominant term in the spread of sample stream in the fractionation zone, discrepancies of 3-6 μm were observed between the predicted widths and the widths estimated from the sheath images, indicating the limitation of this diffusion simulation model. Using the error function model to calculate the sample diffusion, a much better fit between the theoretical estimation and the experiment results can be obtained.

Sequential elution of adsorbed analytes from the multiple monolithic beds has also been accomplished through the use of electrokinetic focusing to spatially confine the elution stream. Peak areas estimated from the elution traces showed peak-to-peak reproducibilities of 6.9-8.1% RSD for six peaks from six monolithic beds in one sequential elution and run-to-run reproducibilities of 2.4-6.7% RSD for the elution peaks from the same SPE bed in four different runs. The sample carryover from a collection channel which provides the focusing stream was evaluated by alternately eluting fluorescein and carboxy SNARF using a multi-wavelength detection system. Quantification of the optical and electrical leakage before elution experiments allows the determination of sample carryover induced

chemical leakage. The residual retained compound is estimated to be 0.08 ± 0.23 % and 2.46 ± 1.31 % of the total loaded sample for the carboxy SNARF and fluorescein, respectively.

The multiplexed microchip presented in this chapter introduces an attractive strategy for the integration of multiple steps, including separation, fractionation, preconcentration, purification, digestion, elution, and on-line analysis of the digestion products by MS within a single microfluidic platform. The entire system can potentially be automated for high-throughput parallel processing of protein samples for large-scale proteomics analysis.

5.7 References

- 1 Moschou, E. A.; Nicholson, A. D.; Jia, G.; Zoval, J. V.; Madou, M. J.; Bachas, L.G.; Daunert, S. *Anal. Bioanal. Chem.* **2006**, *385*, 596–605.
- 2 Spesny, M.; Foret, F. *Electrophoresis* **2003**, *24*, 3745–3747.
- 3 Wang, Z.; Harrison, D. J. *Proc. μ TAS 2005*, Boston, USA, **2005**, 1549–1551.
- 4 Jacobson, S. C.; Ramsey, J. M. *Anal. Chem.* **1997**, *69*, 3212–3217.
- 5 Schrum, D. P.; Culbertson, C. T.; Jacobson, S.C.; Ramsey, J. M. *Anal. Chem.* **1999**, *71*, 4173–4177.
- 6 Stiles, T.; Fallon, R.; Vestad, T.; Oakey, J.; Marr, D.W.M.; Squier, J.; Jimenez, R. *Microfluidics and Nanofluidics* **2005**, *1*, 280–283.
- 7 Dym, C. L. *Principles of mathematical modeling* **2004**, Boston: Elsevier Academic Press.
- 8 Senturia, S. D. *Microsystem design* **2002**, Boston : Kluwer Academic.
- 9 Van Zant, P. *Microchip Fabrication* **2002**, New York: McGraw-Hill.
- 10 Jaeger, R. C. *Introduction to Microelectronic Fabrication* **2001**, New Jersey: Prentice Hall.
- 11 Krishnamoorthy, C. S. *Finite element analysis: theory and programming* **1995**,

- India: Tata McGraw-Hill.
- 12 Narasaiah, G. L. *Finite element analysis* **2009**, Boca Raton: CRC Press.
 - 13 Wang, Z. *Ph. D. Thesis*, University of Alberta, Edmonton, Alberta, Canada, **2006**.
 - 14 Harrison, D. J.; Fluri, K.; Seiler, K.; Fan, Z. H.; Effenhauser, C. S.; Manz, A. *Science* **1993**, *261*, 895–897.
 - 15 Seiler, K.; Fan, Z. H.; Fluri, K.; Harrison, D. J. *Anal. Chem.* **1994**, *66*, 3485–3491.
 - 16 Fan, Z. H.; Harrison, D. J. *Anal. Chem.* **1994**, *66*, 177–184.
 - 17 Crank, J. *The Mathematics of Diffusion* **1975**, Oxford University Press.
 - 18 Harrison, D.J; Manz, A.; Fan, Z.H.; Ludi, H.; Widmer, H. M. *Anal. Chem.* **1992**, *64*, 1926–1932.
 - 19 Dragoljic, J. *M. Sc Thesis*, University of Alberta, Edmonton, Alberta, Canada, **2004**.
 - 20 Taylor, J., *Ph. D. Thesis*, University Of Alberta, Edmonton, Alberta, Canada, **2004**.
 - 21 Zengerle, R.; Richter, M. *Journal of Micromechanical and Microengineering* **1994**, *4*, 192–204.
 - 22 Ahn, J. J.; Oh, J. G.; Choi, B. *Microsystem Technologies* **2004**, *10*, 622–627.
 - 23 Aumeerally, M.; Sitte, R. *Simulation Modeling Practice and Theory* **2006**, *14*, 82–94.
 - 24 Mortensen, N. A; Okkels, F.; Bruus, H. *Physical Review E*, **2005**, *71*, 057301.
 - 25 Mortensen, N. A; Bruus, H. *Physical Review E*, **2006**, *74*, 017301.
 - 26 Attiya, S.; Jemere, A. B.; Tang, T.; Fitzpatrick, G.; Seiler, K.; Chiem, N.; Harrison, D. J. *Electrophoresis* **2001**, *22*, 318–327.
 - 27 Longwell, P. A. *Mechanics of Fluid Flow* **1966**, McGraw Hill, New York.
 - 28 Bao, J. B.; Harrison, D. J. *AIChE Journal* **2006**, *52*, 75–78.
 - 29 He, M. *Ph. D. Thesis*, University Of Alberta, Edmonton, Alberta, Canada, **2008**.
 - 30 Diehl, H.; Horchak-Morris, N. *Talanta* **1987**, *34*, 739–741.

Chapter 6

Conclusions and Future Work

6.1 Summary of the Thesis	256
6.2 Future Work	258
6.2.1 Improvement of Fractionation Process	258
6.2.2 Device Re-design for Sequential Elution.....	260
6.2.3 Separation in Sample Channel	261
6.2.4 Protein Digestion on Polymer Beds	262
6.2.5 Protein Identification	263
6.3 References.....	264

6.1 Summary of the Thesis

In this thesis work, I demonstrated the preparation of monolithic material with hydrophobic surface chemistry within microfluidic channels by photo-initiated polymerization of butyl methacrylate (BMA) and ethylene dimethacrylate (EDMA). META, which contains quaternary ammonium groups, was added as a co-monomer to provide the monolith with positively-charged functionalities. Various parameters, such as composition of the porogenic system, initiator, concentration of the META, and reaction time were studied in order to optimize the composition of the monolithic beds. The optimized monolith precursor solution was found to produce mechanically stable monoliths with uniform structures and sharply-defined edges, allowing transport of liquid through the monoliths at low back pressure.

We described a straightforward and effective method using a newly presented polymer coating, PolyE-323, to modify the microchannel surface. This physically adsorbed coating shows excellent coating properties including high stability and durability, a robust EOF of high magnitude, fast and reproducible preparation, capability of regeneration, tolerance towards organic modifiers, and good compatibility with sheathless ESI-MS. The positively charged wall coating will not only generate an anodal electroosmotic flow to facilitate the detection of proteins and peptides in positive ESI-MS, but also hinder analyte-wall interactions. It is also compatible with the polymerization mixture used for preparation of monoliths.

The application of monolithic polymer for on-chip solid-phase extraction and on-bed tryptic digestion was demonstrated using model proteins with on-line ESI-MS detection. Comparison of the peptide mass maps obtained from on-bed digestion and in-solution digestion of cytochrome *c* and BSA reveals significant differences in the digestion pattern, as demonstrated in Table 6.1. On-bed digestion generates less detectable peptide fragments in the *m/z* of 500-1200 than solution digestion. And the digestion of protein adsorbed on a surface results in a large number of peptides containing a higher degree of missed cleavages, presumably due to the partially block of some digestion sites. However, the digestion products obtained with on-bed digestion and in-solution digestion show similar levels of protein sequence coverage. The method of preconcentration and digestion of proteins on the hydrophobic monoliths produces peptide maps containing a wide range of fragments for protein identification.

Table 6.1 Summary of digestion products detected by ESI/MS resulting from on-bed digestion and solution phase digestion.

		cytochrome <i>c</i>		BSA	
		On-bed digestion	Solution phase digestion	On-bed digestion	Solution phase digestion
Number of peptides detected		17	19	22	41
Sequence coverage		88%	92%	56%	68%
Number of missed cleavages	0	4	8	6	28
	1	7	9	9	12
	2	3	2	5	1
	>3	3	0	2	0

We also demonstrated the development of multiplexed microfluidic devices for protein analysis which integrate a series of microfluidic features. The electrokinetic sheath flow fractionator and collector provide an efficient design to overcome the leakage problems in electrokinetically pumped systems. An array of monolithic polymer beds was polymerized *in situ* on the multi-channel devices using UV-initiated polymerization for on-chip solid-phase extraction and preconcentration. The performance of the multiplexed devices as multi-task microfluidic platforms for integration of multiple sample preparation steps was evaluated with sequential fractionation and collection of fluorescent sample onto the monolithic polymer beds, evaluating the ability to trap individual fractions without cross-contamination. Sequential elution of adsorbed analytes was achieved with the aid of electrokinetic focusing to spatially confine the elution stream. The sample carryover from a collection channel which provides the focusing stream was evaluated using a multi-wavelength detection system.

As an initial prototype, this multiplexed chip design is useful in determining the components that are successful and those needed re-design. Suggestions for future work and chip re-design are presented in the following section.

6.2 Future Work

6.2.1 Improvement of Fractionation Process

In Chapter 5, we demonstrated the possibility to control fluid flow within multi-channel manifold using electrokinetic force. An issue to address in the

electrokinetic fractionation is the potential leakage when the sample flow is switched from one channel to the next, as described in Section 5.4.1.4.

During the automatic sequential fractionation process, sample solutions will stay in the collection channels until buffer solution is later introduced into each channel to remove them. Sample solution left at the channel inlet may diffuse back or be pulled by the convective flow into the fractionation during switches. This fluid leakage will ruin the protective effect of sheath flow and contaminate the solution moving toward other channels.

The introduction of a short sample flow pause during switches may serve to eliminate this problem. The experimental procedure of this approach is illustrated in Figure 6.1. First, the sample stream is delivered into the grounded collection channel under the protection from sheath flow, and then the sample flow is stopped by reducing the sample voltage while sheath buffers continue to be delivered into the same channel to clear away the sample solution at the inlet. Afterwards, we switch ground to the next collection channel and only sheath buffer is driven into this channel at this moment. And finally we restart the sample flow by increasing the sample voltage to the original value.

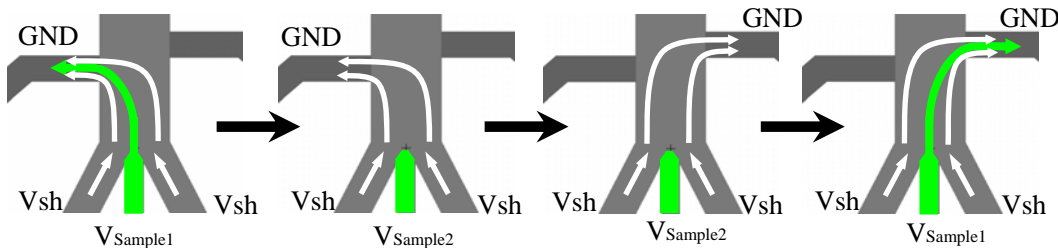


Figure 6.1 Schematic illustrating the procedure of sample flow pause experiment. The flow paths are indicated by arrows, and the sheath streams are colored white and the dye stream are colored green. $V_{sample1}$ is sample voltage at which sample is delivered into grounded channel, $V_{sample2}$ is sample voltage at which sample flow is stopped at the sheath point.

In analyzing real sample, the sample flow from the main channel must resume before detrimental effects on the separation efficiencies achieved on the separation channels occur. Thus the pause of sample flow can only last for a very short time (several ms). Therefore, it is necessary to design an electrical system and write a program to control the whole process automatically.

6.2.2 Device Re-design for Sequential Elution

As discussed in Chapter 5, the amount of sample carryover depends on the nature of the analytes. Since this platform is designed to analyze a variety of samples with different properties, it is necessary to re-design the platform to eliminate this adverse carryover issue. One way to overcome this problem is to incorporate focus channels, instead of using collection channels, to provide the focusing stream. Channels for collecting analytes and channels for providing focusing stream can be designed to be distributed alternately along the fractionation region. However, this approach will greatly increase the complexity of the microfluidic device design and reduce sample throughput.

An alternative way is to design three outlet channels at the end of fractionation region. A rough draft of such a design is shown in Figure 6.2a. With the three outlet channels grounded, upon application of proper voltages at the sheath channels, the collection channel for focus and elution, sample can be delivered into the middle outlet channel, while focus streams from both sides are guided into the two side outlet channels (Figure 6.2b). With this design, the focus stream from the collection channel is separated from the elution stream, and interference

from residual samples desorbed from the SPE bed in the focus channel is eliminated, avoiding cross-contamination between fractionated samples.

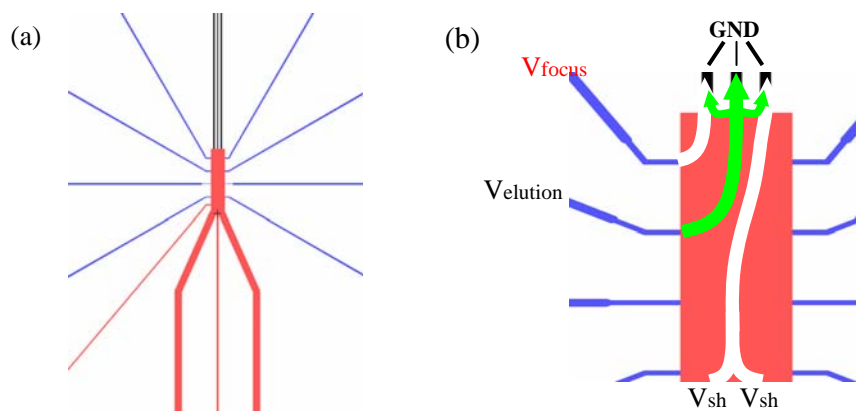


Figure 6.2 Microfluidic device with three outlet channels. (a) Rough sketch of a fractionator with three outlets at the end of fractionation zone. (b) Schematic illustrating that the sample stream is delivered into the middle outlet channel and the focus buffer streams on both sides are guided into the two side outlet ports. The flow paths are indicated by arrows, and the focus streams are colored white and the dye stream are colored green.

6.2.3 Separation in Sample Channel

For protein separation in the sample channel, several options are available. One choice would be capillary isoelectric focusing (CIEF). CIEF is categorized into two-step and one-step CIEF. In two-step CIEF, the proteins are focused into individual zones according to their pI values, followed by mobilization out of the channel by hydrodynamic force [1-3] or chemical mobilization [4-6]. While in one-step CIEF, the proteins are simultaneously focused and mobilized [7, 8].

In our application, EOF is the driving force to transport flow in the device, hence, we have to use one-step CIEF. However, there are still challenges with one-step CIEF. Firstly, One-step IEF is not as stable as two-step IEF because of the disturbance of focusing by the mobilization force in the separation channel. Typically, EOF is reduced so that the main driving force for focusing is

electrophoretic mobility, while the residual EOF serves as the mobilization force. In our case, coating all the channel surfaces to reduce EOF is not feasible, because a strong anodal EOF is required to sustain a stable electrospray. A possible solution is to selectively coat the sample channel with coating materials to reduce EOF, while coating all the other channels with PolyE-323 to provide the strong anodal EOF for elution and MS detection. This kind of selective modification is not easy to accomplish in a complex design. Moreover, the non-uniform EOF will induce pressure difference and thus pressure-induced flow. Second, some reagents or additives used in CIEF, such as ampholyte, anolyte, and catholyte are not compatible with trypsin digestion or ESI-MS. With a SPE monolithic bed assembled in each collection channel, this may not be a concern since a cleanup step can be integrated to remove unwanted components.

If CIEF are not compatible with this electrokinetically controlled fractionator, other separation methods can be considered as well. One choice would be capillary zone electrophoresis (CZE). Although CZE is not as powerful as CIEF, the operation of CZE is much simpler, making it easier to integrate with the other parts and more compatible.

6.2.4 Protein Digestion on Polymer Beds

The fractionator integrated with polymer beds is basically ready for the next trypsin digestion step. As mentioned in Chapter 4, the saturation of the monolithic beds during protein loading step is critical for on-bed tryptic digestion. However, in application of this multiplexed device for analyzing real proteomic samples, protein in each fraction may not be sufficient to saturate each monolithic polymer

bed, resulting in incomplete coverage of the sorbent material. A promising solution presented in the literature [9] is to use a hydrophobic substance to block the extra exposed sites on the monolith surface. Future work will study the feasibility of this method and explore the suitable blocking reagent, which should have known mass and should not interfere with the subsequent digestion and detection.

6.2.5 Protein Identification

The step after enzymatic digestion of the adsorbed proteins is to elute the resulting peptide fragments from the monolithic beds for detection by ESI-MS. Without a direct interface to the MS, much more work will be involved to collect the digestion mixture and introduce it into the MS. We will employ the coupling strategy involving the attachment of a tapered capillary emitter to the chip. An elution channel has been included in our fractionator design for the direct coupling of the device to a capillary tip. A problem associated with this design is the difficulty in modifying the channel segment that connects the fractionation zone and the tip.

To avoid this problem, Device D and E, which has been demonstrated in Chapter 5, are designed to facilitate the coupling of microchip to ESI-MS. With all the collection channels arranged below the end of the fractionation region, we can cut the elution channel at a point very close to the fractionation zone, then drill a hole and attach the electrospray tip directly to the fractionation zone (Figure 6.3). However, with this design, the collection channels can not extend

cross the end of the fractionation zone, which limit the number of collection channels that can be accommodated and reduce the fractionator's throughput.

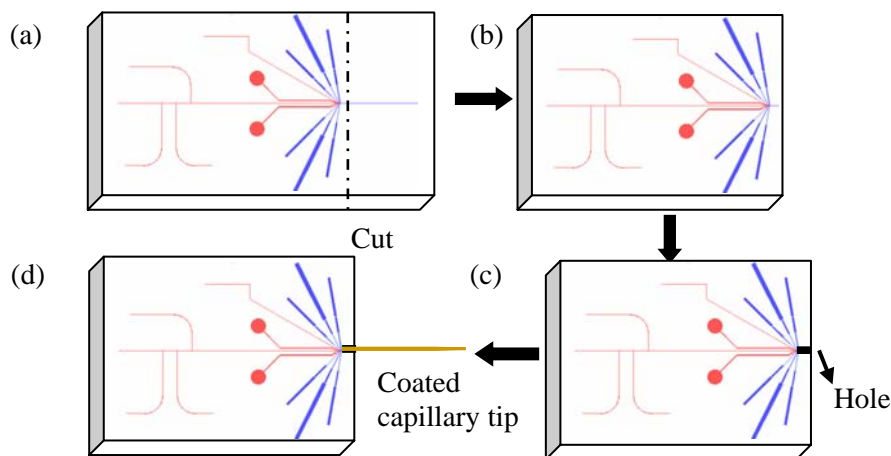


Figure 6.3 Microchip-ESI-MS interface for easy modification of the whole device. (a) Chip layout of a Device D; (b) the elution channel is cut at a point very close to the end of the fractionation zone; (c) a hole is drilled at the channel outlet; (d) a capillary tip is inserted into the hole.

6.3 References

- 1 Chen, S. M.; Wiktorowicz, J.E. *Analytical Biochemistry* **1992**, *206*, 84-90.
- 2 Minarik, M.; Groiss, F.; Gas, B.; Blaas, D.; Kenndler, E. *J. Chromatogr. A* **1996**, *738*, 123-128.
- 3 Zhang, C.X.; Xiang, F.; Pasa-Tolic, L.; Anderson, G.A.; Veenstra, T.D.; Smith, R.D. *Anal. Chem.* **2000**, *72*, 1462-1468.
- 4 Hjertén, S.; Zhu, M. *J. Chromatogr.* **1985**, *346*, 265-270.
- 5 Kilar, F.; Hjerten, S. *J. Chromatogr.* **1989**, *480*, 351-357.
- 6 Kilar, F.; Hjerten, S. *Electrophoresis*, **1989**, *10*, 23-29.
- 7 Hiraoka, A.; Tominaga, I.; Hori, K. *J. Chromatogr. A* **2002**, *961*, 147-153.
- 8 Moorhouse, K.G.; Eusebio, C.A.; Hunt, G.; Chen, A.B. *J. Chromatogr. A* **1995**, *717*, 61-69.
- 9 Craft, D. ; Doucette, A. ; Li, L. *J. Proteome Res.* **2002**, *1*, 537-547.